COMPUTATIONAL MODELING TO EXPLORE SOLVENT AND DYNAMIC EFFECTS IN MOLECULAR, NANO AND SOLID CATALYSIS

Antoni Salom Català

UNIVERSITAT ROVIRA i VIRGILI

Computational Modeling to Explore Solvent and Dynamic Effects in Molecular, Nano and Solid Catalysis

ANTONI SALOM CATALÀ

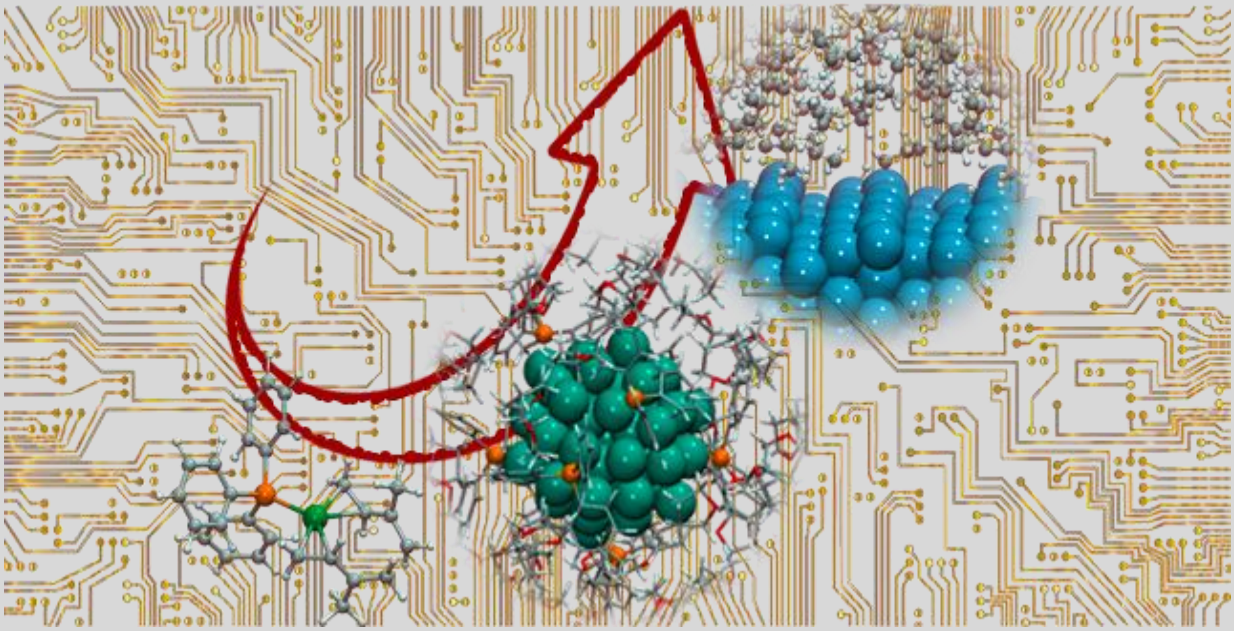

DOCTORAL THESIS
2022

UNIVERSITAT ROVIRA I VIRGILI
COMPUTATIONAL MODELING TO EXPLORE SOLVENT AND DYNAMIC EFFECTS IN MOLECULAR, NANO AND SOLID CATALYSIS
Antoni Salom Català

UNIVERSITAT ROVIRA I VIRGILI
COMPUTATIONAL MODELING TO EXPLORE SOLVENT AND DYNAMIC EFFECTS IN MOLECULAR, NANO AND SOLID CATALYSIS
Antoni Salom Català

Antoni Salom Català

Computational Modeling to Explore Solvent and Dynamic Effects in Molecular, Nano and Solid Catalysis

DOCTORAL THESIS

Supervised by
Prof. Jorge Juan Carbó Martín and Prof. Josep Manel Ricart Pla

UNIVERSITAT ROVIRA i VIRGILI

Departament de Química Física i Inorgànica

Tarragona, maig 2022

UNIVERSITAT ROVIRA I VIRGILI
COMPUTATIONAL MODELING TO EXPLORE SOLVENT AND DYNAMIC EFFECTS IN MOLECULAR, NANO AND SOLID CATALYSIS
Antoni Salom Català

UNIVERSITAT ROVIRA i VIRGILI

Jorge Juan Carbó Martín, Catedràtic del Departament de Química Física i Inorgànica de la Universitat Rovira i Virgili, i Josep Manel Ricart Pla, Catedràtic del Departament de Química Física i Inorgànica de la Universitat Rovira i Virgili

FEM CONSTAR que aquest treball, titulat

"Computational Modeling to Explore Solvent and Dynamic Effects in Molecular, Nano and Solid Catalysis"

que presenta Antoni Salom Català per a l'obtenció del títol de Doctor, ha estat realitzat sota la nostra direcció al Departament de Química Física i Inorgànica d'aquesta universitat.

Tarragona, 29 de març de 2022

Els directors de la tesi doctoral

Jorge Juan Carbó Martín

Josep Manel Ricart Pla

UNIVERSITAT ROVIRA I VIRGILI
COMPUTATIONAL MODELING TO EXPLORE SOLVENT AND DYNAMIC EFFECTS IN MOLECULAR, NANO AND SOLID CATALYSIS
Antoni Salom Català

Contents

UNIVERSITAT ROVIRA I VIRGILI
COMPUTATIONAL MODELING TO EXPLORE SOLVENT AND DYNAMIC EFFECTS IN MOLECULAR, NANO AND SOLID CATALYSIS
Antoni Salom Català

List of Publications

The following scientific publications have been achieved during the Ph. D.

- Álvarez-Ruiz, E.; Carbó, J. J.; Gómez, M.; Hernández-Prieto, C.; Hernán-Gómez, A.; Martín, A.; Mena, M.; Ricart, J. M.; Salom-Català, A.; Santamaría, C. "**N=N Bond Cleavage by Tantalum Hydride Complexes: Mechanistic Insights and Reactivity**" *Inorg. Chem.* **2022**, *61*, 474-485 DOI: 10.1021/acs.inorgchem.1c03152.

- Colavida, J.; Lleberia, J. A.; Salom-Català, A.; Gual, A.; Collado, A.; Zangrando, E.; Ricart, J. M.; Godard, C.; Claver, C.; Carbó, J. J.; Castillón, S. "**Regioselectivity Control in Pd-Catalyzed Telomerization of Isoprene Enabled by Solvent and Ligand Selection**" *ACS Catal.* **2020**, *10*, 11458-11465 DOI: 10.1021/acscatal.0c02911.

- Carbó, J. J.; Gómez-Pantoja, M.; Martín, A.; Mena, M.; Ricart, J. M.; Salom-Català, A.; Santamaría, C. "**A Bridging bis-Allyl Titanium Complex: Mechanistic Insights into Electronic Structure and Reactivity**" *Inorg. Chem.* **2019**, *58*, 12157-12166 DOI: 10.1021/acs.inorgchem.9b01505.

UNIVERSITAT ROVIRA I VIRGILI
COMPUTATIONAL MODELING TO EXPLORE SOLVENT AND DYNAMIC EFFECTS IN MOLECULAR, NANO AND SOLID CATALYSIS
Antoni Salom Català

Summary of the Thesis

This PhD thesis presents computational investigations on different catalytic systems, from homogeneous organometallic complexes, to heterogeneous metallic surfaces, going through the bridge between them, homogeneous nanocatalysts. Catalysis, as an important industrial process, has been known for many years, but its impact in chemical industry and basic research is still growing nowadays.

In Chapter 1, we show the impact and the growth of the catalysis field in scientific research, as well as its challenges to achieve greener and more sustainable processes. Computational chemistry applied to catalysis, also known as computational catalysis, is younger than other chemicals fields, but in just a few years it has become a fundamental and promising pillar in catalysis research. We present some achievements of computational catalysis in the field of homogeneous- and nano-catalysis, and the importance of some aspects in modelling catalysis such as the conformation of the ligands, the solvent modelling, the topology of the nanocatalysts and the effect of the capping ligands on the catalytic activity of the nanoparticles (NPs). The future challenges of computational catalysis, closely related with the prediction and formulation of new catalysts and processes, using Machine Learning (ML) and Quantitative Structure-Activity Relationship (QSAR) models or the use of reactive force fields are presented below. Finally, we summarize the theoretical background of the computational methodologies used in this thesis, such as, Density Functional Theory (DFT), the modelling of solvation, the microkinetic analysis, molecular dynamics (MD) techniques including *ab initio* molecular dynamics (AIMD), classical MD and reactive MD focusing on the ReaxFF approach, and the Basin Hopping Parallel Excitable Walkers (BH-PEW) global optimization algorithm. After this introduction, the next section presents the goals of the thesis.

In Chapter 2 we used DFT and microkinetic analysis to computationally rationalize the regioselectivity control of the isoprene telomerization catalyzed by Pd-phosphine complexes observed in the experiments of Castillón *et al.* Among all the reaction conditions studied, two of them showed the major impact on the selectivity: the acidity of the solvent and the structure of the phosphine ligand. To understand the origin of the solvent control of the selectivity, we computed the reaction mechanism using Et_2NH as nucleophile, and three alcohol solvents with different acidity: TFE, *t*BuOH and MeOH. The atomistic and kinetic simulations showed that the selectivity-determining step switches from C-C oxidative coupling at low pK_a (TFE), with a preference for the telomer head-to-

head, to protonation at high pK_a (*t*BuOH), with a preference for the telomer tail-to-tail. Moreover, we computed the mechanism with an aprotic solvent DMF, for which the reaction cannot proceed, due to the lack of acidic protons, but microkinetic analysis revealed that the traces of water were the responsible of the selectivity observed. To understand the origin of the ligand control on the selectivity, we analyze the reaction mechanism with two different phosphine ligands: PPh_3 and a sterically hindered monophosphine (**P2**). The results showed that the selectivity towards tail-to-head telomer can be directed in moderately acidic solvents by selecting a bulky ligand that exerts steric control on the protonation step. At the end, this study provides the tools and the knowledge to select an appropriate Pd/Ligand/Solvent system to predict and obtain three of the four linear telomers of isoprene telomerization.

Chapter 3 is divided in two sections, both related to the study of Rh NPs used as catalysts for hydrogenation reactions. In the first part we studied bare Rh nanoparticles in terms of morphology and electronic structure. We used the Basin Hopping Parallel Excitable Walkers (BH-PEW) optimization algorithm to find the global minima of Rh NPs with different sizes: Rh_{49}, Rh_{55}, Rh_{75} and Rh_{147}. We also consider the Rh(111) surface. For all of them, all minima corresponded to high symmetric structures, such as quasi-icosahedron for Rh_{49}, icosahedron (ICO) for Rh_{55} and Rh_{147}, and Marks-decahedron for Rh_{75}. To ensure the minimum nature, we performed classical MD simulations using the Gupta potential, and LoDiS program developed by Baletto *et al*. Then we computed the cohesion energy and the d-band center of the minima structures, and both descriptors revealed that the stabilization of the NPs increases as the size also increases, either structurally (with an increase of the cohesion energy from -4.1 eV for Rh_{49} to -4.8 eV for a slab mimicking the Rh(111) surface) and electronically (with a decrease of the d-band center of the occupied states from -2.24 eV to -2.63 for Rh_{49} and Rh(111), respectively).

The second section of Chapter 3 is devoted to the characterization and analysis of the effect of phosphines as capping ligands. We selected PPh_3 as a model phosphine, but the adsorption of P(*o*-tolyl)$_3$, $P(OPh)_3$ and $OPPh_3$ are also studied. For the NP, we selected the Rh_{55} ICO structure because there is experimental evidence that the NPs exhibit spherical shapes and diameters around 1.5 ± 0.2 nm (1.3 nm for the computed Rh_{55} ICO NP). Firstly, we calculate the adsorption of PPh_3 on all symmetry-inequivalent sites of Rh_{55} ICO and cuboctahedral (CUB) nanoparticles (the latter included for sake of comparison), and the results showed that PPh_3 bounds through the P electron lone pair to an edge Rh atom, one phenyl ring adsorbed onto the (111) face with η^6 mode and a second phenyl substituent interacting via η^2 through the *ortho* and *ipso* C atoms on a vertex Rh atom. This adsorption mode is supported by indicative geometric parameters

such as C-Rh bonding distances of 2.17 or 2.30 Å, or H-C-C-H phenyl dihedral angles of 12º, and by a charge density difference analysis that showed zones of electron accumulation between the P and the two phenyl rings and the Rh atoms. Moreover, a decomposition analysis of the adsorption energy revealed that the P-Rh and the phenyl-η^6 interactions are the responsible for the strong adsorption energy of -2.96 eV. Secondly, we computed the adsorption energy of PPh_3 onto the other sized Rh NPs and the Rh(111) surface, and we found that the adsorption energy of PPh_3 decreases as a function of the NP size, from -3.06 to -1.52 eV for Rh_{49} and Rh(111), respectively. Then, with all the computed structures, we built a simple regression model using the Generalized Coordination Number (GCN) as local and the d-band center as a global descriptor to predict the adsorption energy of PPh_3 on Rh NPs. After that, we analyzed the effect of the PPh_3 coverage on the Rh_{55} ICO NP, and we placed up to 10 PPh_3 ligands on the NP surface. The results revealed that the adsorption energy decreases for each molecule that is added up to eight ligands, the eighth with an adsorption energy of -0.46 eV that competes with the adsorption of one THF solvent molecule. The adsorptions of the ninth and tenth PPh_3 ligands are not favorable. Electronically, the d-band center of the surface Rh occupied states decreases with each new PPh_3 that is adsorbed up to eight phosphines, when the d-band center remains constant. This fact reveals that the adsorption of more than eight PPh_3 molecules is unfavorable due to steric rather than electronic effects. Afterwards, we used AIMD simulations to study the behavior of 2 different systems in solution (THF as solvent): Rh_{55} ICO NP with one and seven PPh_3 molecules adsorbed, respectively. The analysis of the two AIMD showed that the adsorption of PPh_3 is stronger than THF, and PPh_3 was linked to the NP surface during the simulations. Moreover, we found that the THF molecules interact weakly and preferentially with the Rh corner atoms, with a constant adsorption and desorption due to a weaker O-Rh interaction than Rh-P one. Finally, we inspect the adsorption mode and energy of the other phosphine ligands: P(*o*-tolyl)$_3$, $P(OPh)_3$ and $OPPh_3$. The strongest adsorption mode of P(*o*-tolyl)$_3$ corresponds to the P linked to a vertex Rh atom, with a mode practically isoenergetic where the P atom is linked to an edge Rh atom with one tolyl moiety adsorbed in η^2 manner with the *meta* and *ortho* C atoms to a corner Rh atom with an adsorption energy of -1.03 eV, revealing a steric hindrance of the methyl groups that decrease the adsorption strength respect PPh_3. The $P(OPh)_3$ showed a high adsorption energy of -4.15 eV because besides coordinating the P to an edge Rh atom, the flexibility given by the bridge O atoms allowed the adsorption of two phenyl rings in η^6 mode onto two different 111 faces. The most favorable adsorption mode of $OPPh_3$ presents a structure equivalent to PPh_3, but linked to the edge Rh atom through the oxygen electron lone pairs. Its adsorption energy was -2.43 eV, that is 0.53 eV lower in energy than the analogous PPh_3 adsorption

supported by an adsorption energy decomposition analysis that revealed that the O-Rh interaction is weaker than the P-Rh one.

In Chapter 4, we proposed a plausible mechanism, by means of DFT investigations to understand the selective deuteration of specific positions of different phosphine ligands catalyzed by Rh- and Ru-based metal NPs decorated by N-heterocyclic carbenes (NHC) or polyvinylpyrrolidone (PVP) performed by Prof. Castillón and Godard groups. As model phosphines, we selected PPh_3 and P(*o*-tolyl)$_3$, due to their different and unexpected deuterations. PPh_3 was selectively deuterated in the ortho positions of the phenyl rings, while P(*o*-tolyl)$_3$ was deuterated on the methyl groups and *meta* position of the aromatic ring. The calculations showed a high influence of the phosphine geometry on the selectivity, and the need of defects on the nanoparticle surface. Based on the adsorption studies shown in Chapter 3, we found that the PPh_3 is deuterated on the *ortho* position coordinated in η^2 mode on a Rh corner atom via a dissociation mechanism with a moderate energy barrier of +0.6 eV. The energy barriers for the positions of the phenyl adsorbed in η^6 mode were also computed, but they were too high to be affordable at working conditions (+1.5, +2.3 and +2.1 for *ortho*, *meta* and *para* positions, respectively). In addition, an associative mechanism was also analyzed but resulted in a higher energy barrier than the dissociative pathway. In the case of P(*o*-tolyl)$_3$, the activation of aliphatic C_{sp3}-H bonds had low energy barrier (+0.2 eV), but the activation of the *meta* position presented a prohibitive energy barrier of +1.9 eV due to a high distortion over the aromatic ring. Thus, we propose a mechanism in three steps to activate the *meta* C-H bond: 1) decoordination of the P atom, 2) activation of the C-H methyl bonds at NP edge, and 3) the meta C-H bond activation, resulting in an overall energy barrier of +1.3 eV. The activation of the 5-*meta* position was also evaluated, and showed an energy barrier of +1.5 eV, too high to be affordable in the reaction conditions. However, we observed a significant drop of the adsorption of P(*o*-tolyl)$_3$ using more realistic NP covered by NHC and hydride species, that make the cost of the activation process lower.

The last chapter, Chapter 5, is devoted to developing a reactive force field (ReaxFF) able to simulate the propane dehydrogenation reaction (PDH) catalyzed by Pt surfaces and nanoparticles. Firstly, we expose a general strategy to re-parametrize a ReaxFF force field, in which the most important steps are the assessment of the transferability of a ReaxFF parameters from the literature, the optimization of parameters and the validation. Secondly, we show the assessment of the transferability of three ReaxFF force field candidates from the literature (**2016-Pt/Ni/C/O/H**, **2016-Pt/H/O** and **2008-Pt/C/H**). We found important discrepancies between the three candidates and DFT data in the description of the relative energies and the geometries of some key

intermediates in PDH, and the need to re-optimize one of this force fields to be used in the study of PDH. To this end we used the Covariance Matrix Adaptation Evolution Strategy (CMA-ES) as a multivariable optimization algorithm. Before achieving the final force field, called **2022-Pt/C/H**, we generate 4 different versions. From **2016-Pt/H/O** to the first **2021a-Pt/C/H** version, we improved notably the relative energies of the PDH intermediates, but any reactive event was detected when we performed reactive MD simulations due to the high energy barrier required to activate the first C-H bond. In **2021b-Pt/C/H** version, we tried to lower the energy barrier changing the energy profile for the first C-H activation (from propane to 1-propyl). After optimization, the first C-H activation barrier was decreased from ~75 kcal mol^{-1} to 17 kcal mol^{-1}, showing a better fitting with the DFT reference data. However, we inspect the reaction kinetics of other processes, and we noted that they were not well reproduced. To optimize the third version, called **2021c-Pt/C/H**, we added 5 more energy profiles in the training set. This led to a good description of the PDH reaction kinetics, but when we performed a reactive MD simulation with a model system, we detected the segregation of Pt atoms from the surface to the gas phase, forming Pt-hydride clusters, indicating that the Pt-Pt bond was too weak. In the **2021d-Pt/C/H**, we changed the Pt-Pt E_σ parameter value in the training set, and we solved the issue of the Pt diffusion, but using this force field in a MD simulation, the products detected were CH_3 and CH_2 produced by a C-C single bond breaking from propane, without any previous C-H bond activation that is more accessible thermo- and kinetically. To overcome this, we added one more C-C bond breaking energy profile in the training set, and after force field optimization we obtain the last version of our ReaxFF force field: **2022-Pt/C/H**. The internal validation revealed a good fitting between the DFT reference data with a Mean Absolut Error (MAE) of 3.4 kcal mol^{-1} for the relative energies of PDH intermediates, and a maximum MAE of 5 kcal mol^{-1} and 0.2 Å for the energy barriers and the key C-H and C-C distances of the transition states. The external validation also showed promising results with a maximum MAE for the energy barriers and key distances of 2.3 kcal mol^{-1} and 0.08 Å, respectively. Afterwards, we used the ReaxFF **2022-Pt/C/H** force field to study PDH catalyzed by Pt(111) and Pt(211) surfaces and Pt_{55} NP. The reactive MD simulations indicated that the Pt(211) surface was more reactive with a 0.88% of conversion than Pt(111) surface with a 0.5 % of propane conversion. Moreover, all the reactive events on Pt(211) undergo on atoms of the steps. The mechanistic analysis of the MD simulations showed that the preferential path to obtain propene is via 1-propyl, rather than 2-propyl. The Pt_{55} NP showed higher activity than the surfaces with a 2.6 % of propane conversion, but with a higher degree of side products with a 37 % of selectivity towards propane. At the end, we present an assessment of the cost of parameterize a ReaxFF force field with CMA-ES algorithm, revealing a

dependency of several parameters, such as the job performed on each structure during the error function evaluation or the number of entries in the training set, and an assessment of the performance of ReaxFF program to simulate large systems and long times showing the real power of the ReaxFF tool. Finally, the main conclusions and achievements of this thesis are presented.

UNIVERSITAT ROVIRA I VIRGILI
COMPUTATIONAL MODELING TO EXPLORE SOLVENT AND DYNAMIC EFFECTS IN MOLECULAR, NANO AND SOLID CATALYSIS
Antoni Salom Català

UNIVERSITAT ROVIRA I VIRGILI
COMPUTATIONAL MODELING TO EXPLORE SOLVENT AND DYNAMIC EFFECTS IN MOLECULAR, NANO AND SOLID CATALYSIS
Antoni Salom Català

Chapter 1:

Introduction.

Computational Catalysis

UNIVERSITAT ROVIRA I VIRGILI
COMPUTATIONAL MODELING TO EXPLORE SOLVENT AND DYNAMIC EFFECTS IN MOLECULAR, NANO AND SOLID CATALYSIS
Antoni Salom Català

Chapter 1:
Introduction.
Computational Catalysis

In this initial chapter we introduce the topics related to this thesis, which are closely connected with the field of catalysis. Firstly, the impact and the growth of catalysis in research is shown, as well as its challenges and future role as a crucial tool to achieve efficient catalytic processes for a more sustainable world. Then, computational catalysis is introduced as promising field to solve some of the today's issues of catalysis, and some examples of how computational catalysis has helped to understand and improve homogeneous and nanocatalytic processes. It then discusses current and future challenges, mostly involved into the design and prediction of new and more efficient catalysts and materials, showing also some of novel and powerful methodologies to achieve those goals, such as the use of descriptors and data-driven techniques, or reactive force fields. Finally, the theoretical background of the computational methods used in this thesis to model the catalytic processes studied will be presented, focusing on different approaches such as Density Functional Theory (DFT), the quantum mechanical treatment of solvation, microkinetic analysis, ab Initio, classical and reactive molecular dynamic simulations, the latter within ReaxFF framework, or the Basin Hopping-Parallel Excitation Walkers global optimization algorithms for the conformational search protocol of nanoparticles.

1.1 The impact of catalysis

The phenomenon of catalysis was recognized and used since the early 19th century, but it was in 1836, that Berzelius first defined the term catalysis.[1] Since then, this concept started to be understood but, it was from the middle of XX century when catalysis was applied in a wide range of chemical transformations,[2] becoming a fundamental pillar for a growing and competitive industry, to supply the needs of a modern and overpopulated society.[3]

The impact of catalysis is reflected by the growth in the number of articles published over the years (Figure 1.1), or the number of journals interested in this field (Figure 1.2). Note in Figure 1.2, only the 20 scientific journals with more publications are represented, but the total number of journals according to the database is 20798. Moreover, leading countries and institutions decided to pay special attention to catalysis by the creation of specific societies and

organizations aimed to promote the research and knowledge transfer between catalysis community in academia, industry, research institutes, even policy institutions, such as the European Cluster on Catalysis created by the European Comission in 2015,[4] the German Catalysis Society (GeCatS)[5] in Germany, the North American Catalysis Society[6] founded in 1956, or here in Spain the Sociedad Española de Catálisis (Secat)[7] created in 1995. In addition, nowadays, catalysis has become an interdisciplinary research area with contributions coming from engineering, biology, physics and chemistry. Figure 1.3 shows the 21st main disciplines which are working on catalysis.

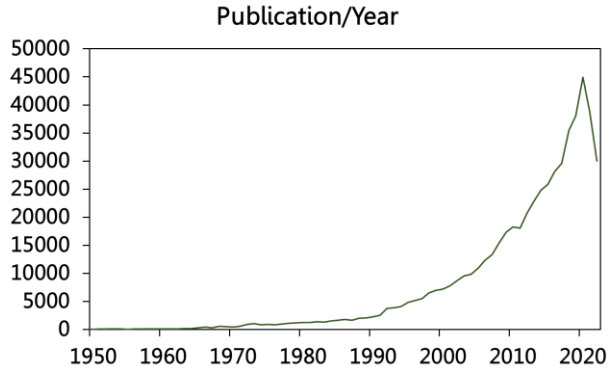

Figure 1.1 Catalysis-related publications by year during the last 50 years. Source: Web of Science.

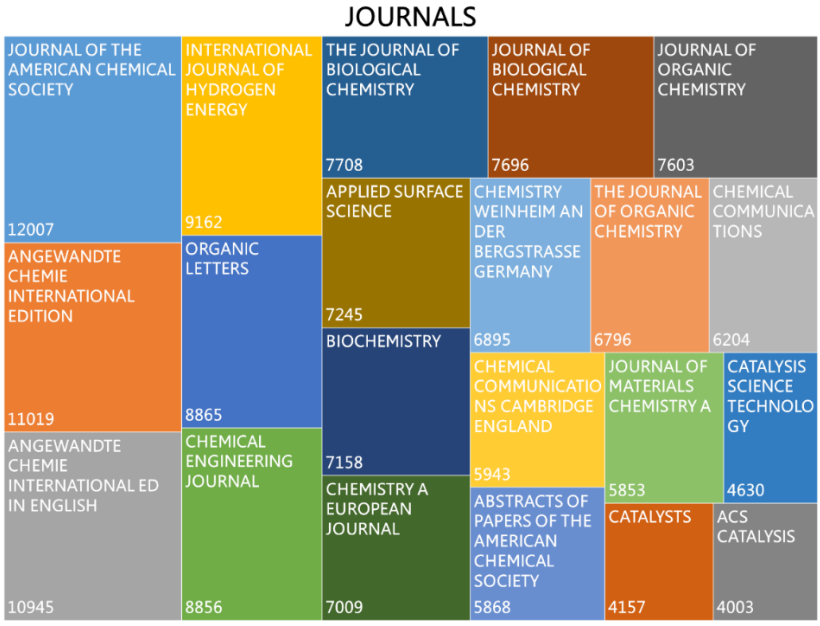

Figure 1.2. Scientific journals and number of their publications about catalysis. Source: Web of Science.

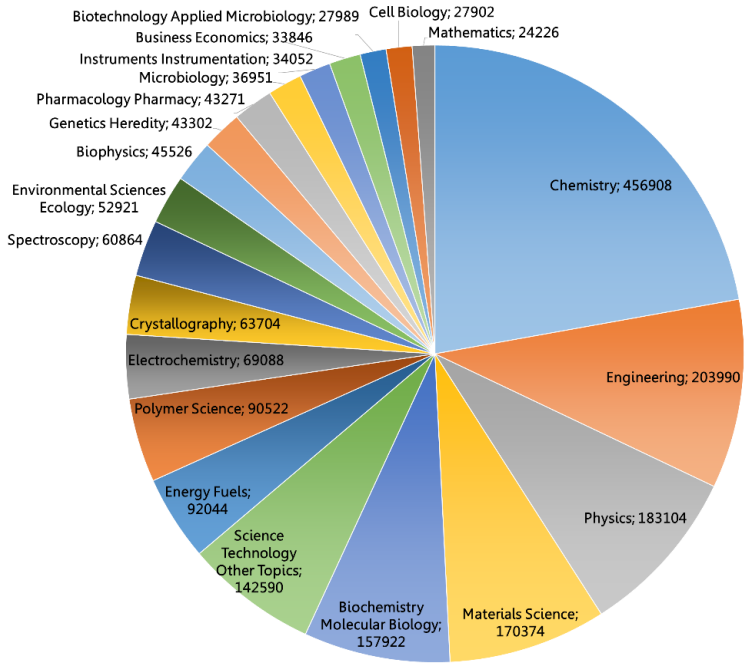

Figure 1.3. Research disciplines with the highest number of publications in catalysis. Source: Web of Science.

The importance of catalysis grew up exponentially, and nowadays, around of the 85-90% of products of the chemical industry are produced in catalytic processes.[8] Despite catalysis provided the way to more and new chemicals and materials that supplied the needs of the population and made their lives more comfortable, the catalytic processes are not free of some drawbacks. Due to the lack of efficient catalytic materials, a huge amount of energy must be provided to perform some chemical transformations. Moreover, the fact that the catalysts are not selective enough towards desired chemicals, generates undesirable byproducts, which many of them cannot be reused or recycled, and at the end, they become undesirable waste. In addition, with the world's population growing steadily, in contrast to the rapid depletion of our fossil fuels, as well as other metals and minerals, and global climate change driven by the greenhouse gasses as CO_2, CH_4, and others, we are forced to transition to a sustainable economy, with renewable energy sources and more efficient and selective catalytic processes.[9]

Along these lines, a new philosophy of chemistry emerged in the late 1990s, known as Green Chemistry. This new field requires the application of a group of principles to reduce or remove the use or generation of hazardous materials in the design, synthesis and application of chemicals. Green Chemistry follows the

twelve principles proposed by Paul Anastas and John Warner in 1998,[10,11] some of them are involved in the processes studied in this thesis:

- 1st principle: do not make waste
- 2nd principle: atom economy
- 6th principle: energy consumption should be minimized
- 8th principle: reduce derivatives
- 9th principle: use of highly active and selective catalysts

Catalysis is called to be a fundamental pillar for the transition to a sustainable and greener chemistry and society.[12] Thus, some of the current challenges of catalysis are devoted:

- To produce base chemicals from renewable sources such as biomass than the traditional cracking of naphtha.[13] The composition of plant biomass can vary, but it is mainly composed by cellulose (30-50%), hemicellulose (20-40%), lignin (15-25%), plant oils (2-7%), proteins and a few percent of minerals.[9] These components are highly functionalized materials, and to utilize them, selective de-functionalization and functional group transformation catalysts must be developed. For instance, in the case of lignin, some studies were focused on the controlled de-polymerization to give less complex product mixtures.[14,15,16]
- To deal with energy from different fronts: 1) saving energy by making chemical processes more efficient, avoiding the need of high temperatures or pressures, 2) producing new forms of energy with new procedures, such as H_2, more abundant and greener than the traditional carbon-based fossil fuels energy sources, that can be produced by photocatalytic water splitting, even mimicking the biological photosystem II[17,18,19] and, 3) storage and transportation of that H_2, using the liquid organic hydrogen carriers, LOHCs, that are hydrocarbons that can be hydrogenated and dehydrogenated reversibly, such as *N*-ethylcarbazole[20] or *N*-propylcarbazole, over supported ruthenium catalyst.[21]
- To generate selective and efficient catalysts to prevent waste. Examples are the catalytic substitution of alcohols by N-nucleophiles by the so-called "borrowing hydrogen" approach,[22] where the metal catalyst dehydrogenates the alcohol, and stores hydrogen as hydrides to then hydrogenate the imine intermediate with water as the only by-product (Figure 1.4). However, the turnover numbers of these reactions are too low for practical applications and more detailed mechanistic insights are needed to improve catalyst performance.[23]

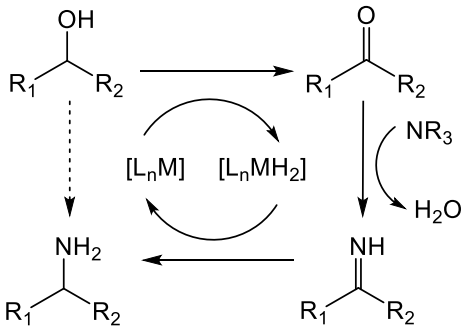

Figure 1.4. Schematic representation of the direct amination of alcohols mechanism by the borrowing hydrogen approach

Within this context, new types of catalysis rapidly emerged such as organocatalysis, nanocatalysis, photocatalysis, electrocatalysis or biological catalysis. Nevertheless, as in all fields of chemistry, catalysis benefits from one approach due to its power to explain and understand at atomistic level the experimental data, even as a predictive tool, for instance, to catalyst design. It is computational catalysis. Computational catalysis has been one of the most expanded and dynamic research field over the last decade. The growth of this area has been possible due to the improvement in computational speed and software development. The computational catalysis is the frontier between theory and experiments and it has become an indispensable and a routine tool for all fields in catalysis research.

1.1.1 Computational Homogeneous Catalysis

Nowadays, quantum chemistry based calculations are usually used to suggest or explain mechanistic insights to observed experimental facts.[24] Computational investigations can shed light on structural and energetic features of molecular catalysts that are hard to assess by experiments, such as conformation variability, metal-ligand or metal-metal cooperation or non-innocent roles of solvent molecules or additives.[25] Also, thanks to theoretical calculations, plausible mechanisms have been proposed for different reactions of interest, such as the activation of small molecules, oxidations or cross coupling reactions, providing an atomistic understanding and the guide to improve them in terms of yield or selectivity.[26]

Nevertheless, one of the most important aspects regarding homogeneous catalysis modelling is to choose the right chemical model, as the reaction media involves several actors, such as metal catalysts, ligands, solvent or additives. The

simplest chemical model consists of the organometallic catalyst with the corresponding ligand (actually, without further simplifications), and one molecule of each reagent. Even when such a model is reliable, several things need to be taken into account. For instance, the structure, the conformational space and the orientation of the ligand respect the metal center of the catalyst. An example of this is the study of Pd catalyzed Suzuki-Miyaura cross-coupling performed by Besora *et al.*[27] where the error bars associated with the conformational diversity range, when $[(PPh_3)_2Pd]$ was used as catalyst, were between 0.3 and 6.7 kcal mol^{-1}, whereas they grew to between 10.2 and 11.4 kcal mol^{-1} when the more flexible $[(P(i\text{-}Pr)_3)_2Pd]$ was used. Another illustrative example of the importance of ligand conformational exploration is the recent study of the Buchwald-Hartwig amination of aryl halides using Pd-Josiphos complex carried out by Gómez-Orellana *et al.*[28] They performed an extensive conformational search of all species involved in the mechanism and they found that the energy difference between two conformations of the same intermediate was 2.7 kcal mol^{-1}, but the more stable intermediate had not the appropriate disposition to undergo the bromine substitution process. Thus, they consider the highest intermediate in energy to propose the mechanism. In Figure 1.5 are shown the commented conformers of Pd-Josiphos catalyst. Other examples corroborate that the first coordination sphere of the active site is crucial for the computational modelling of homogeneous catalysis.[29] Fortunately, nowadays we have several methodologies that enable fast ligand conformational explorations such as, Molecular Mechanics (MM) approaches, low-level, semiempirical, DFT calculations or QM/MM and metadynamics simulations.[30]

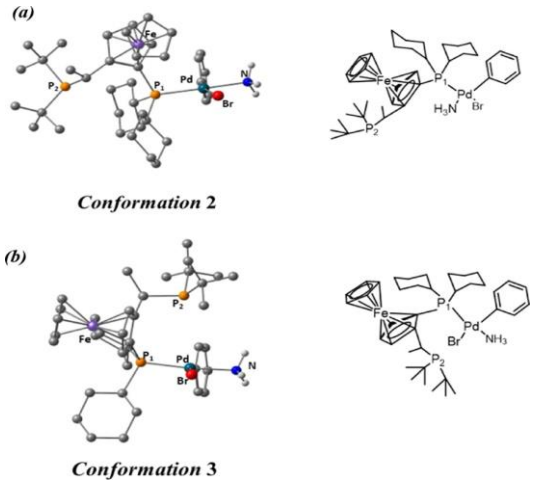

Figure 1.5. Optimized structures of the two most stable conformers used in the work of Gómez-Orellana *et al.* Reproduced from ref. 28 with permission. Copyright 2021 American Chemical Society.

In many cases, the simplest model commented above is not sufficient to achieve reliable and accurate energy profiles, or some steps of the mechanism may be left out. Then, an extended model is needed to properly reproduce the experimental conditions, as the one shown in Figure 1.6 for ketone hydrogenation catalyzed by Ir-hydride complex in alcohol solvent in presence of NaOMe additive.

This extended model can comprise: 1) additional molecules of one reagent that could interfere in the reaction,[31] 2) counterions when ionic species are present,[32,33] and 3) solvent effects. There are three main approaches to include solvent in the calculations: i) implicit solvent model, where the solvent molecules are replaced by a polarizable continuum media characterized by its dielectric constant, ii) hybrid implicit-explicit model, which a few molecules of solvent are explicitly added surrounding the catalyst, and the rest is described by a continuum model, and iii) explicit solvent model, where a huge number of molecules are placed around the organometallic complex.

The simplest and most used model to account for solvent effects is the implicit one, especially when one is dealing with low polar, no coordinating solvent or does not actively participate in the reaction. Initially, the implicit solvent was included after geometry optimization in gas phase and then the energy was computed by single point calculations, to reduce the computational cost. Fortunately, today's computer power allows the fully optimization and characterization of stationary points in solution, to properly compute a reliable catalytic mechanism. However, when solvent molecules participate in the reaction, for instance transferring protons or coordinating with the metal center, continuum models are not enough to explicitly describe the solvent-solut interactions. In such cases, hybrid or explicit solvation models are the most adequate. For example, the importance of the solvent was demonstrated for two well-known reactions, the Wacker process[34] and Grignard reactions,[35] where explicit model shed light on their mechanisms. Nevertheless, situations with solvent involved processes, such as charge separation, are hard to accurately describe, and other strategies must be considered.

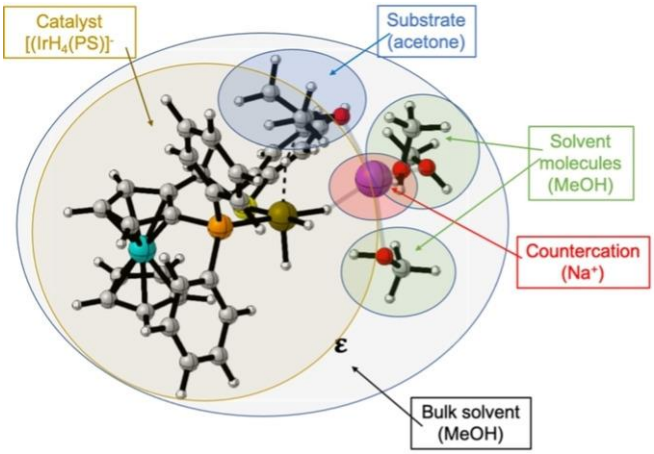

Figure 1.6. Extended chemical model for ketone hydrogenation catalyzed by Ir-hydride complex in alcohol solvent and in presence of NaOMe. Reproduced from ref. 24.

Computational homogeneous catalysis has been mainly concerned with calculating Gibbs free energy profiles. However, in experiments in solution the magnitude measured is the evolution of the concentration of key species, such as reactants, intermediates or products. In addition, in the case where the Potential energy Surface (PES) is flat and hard to characterize, where the energy barrier of two selectivity-determining steps are quite similar, where the concentration of one species is orders of magnitude different from others or complex reaction networks are involved, the concentration of key species must be taken into account. Within this context, microkinetic analysis has been proved to be a simple, useful and cheap model to introduce concentration effects.[36] Actually, there are several examples where microkinetic analysis has been applied successfully. One example is the study of the C-H activation catalyzed by palladium catalysts performed by Clot *et al.* that demonstrates the influence of base (HCO_3^-) dissociation directing the reaction towards either C-C coupling or H-β elimination (Figure 1.7),[37] or the investigation about Pd-catalyzed decarboxylative C-C bond formation carried out by Maseras *et al.* where they denoted a dependency of product distribution related with the nature of the substituents of the substrate.[38]

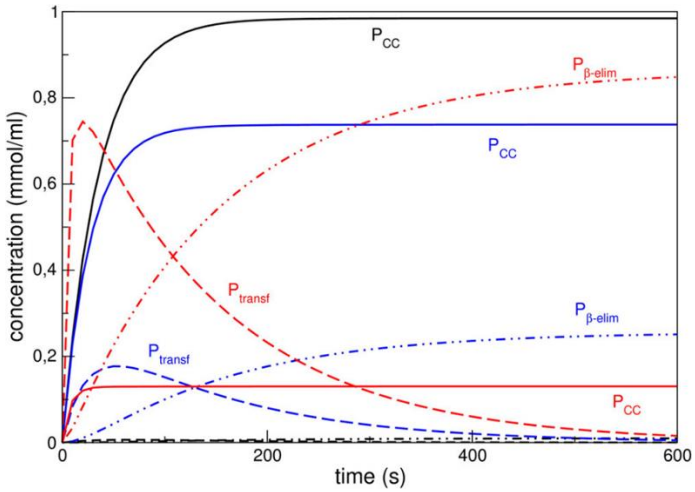

Figure 1.7. Example of microkinetic analysis done by Clot *et al.* Comparison of the evolutions of concentrations of P_{CC} (product of C-C coupling), P_{transf} (product of H transfer) and $P_{\beta\text{-elim}}$ (product of β-elimination) with time, associated with different values of the activation barrier for HCO_3^- dissociation (Black, 6 kcal mol^{-1}; blue, 9 kcal mol^{-1}; red, 12 kcal mol^{-1}). Reproduced from ref. 37 with permission. Copyright 2014 American Chemical Society.

1.1.2 Computational Nanocatalysis

Metallic nanoparticles have been used for a long time in ancient civilizations of China and Egypt for many uses, mainly for curative and aesthetic purposes or for the elaboration and decoration of glasses and ceramics.[39] However, metallic nanoparticles in catalysis were not reported until 1941, when Rampino and Nord published the synthesis of platinum and palladium nanoparticles by metal salts reduction by H_2 and their use as hydrogenation catalysts.[40] The alliance between nanoscience and catalysis is devoted to achieving a new generation of catalysts with high activity and high selectivity, and in addition, there is an economic and environmental interest and benefit in reducing the amount of precious-metal, and here is where computational catalysis can provide important contributions.[41]

For small nanoparticle, size and shape become critical features that determine the electronic structure and the catalytic performance. Since Haruta in 1987 discovered that the catalytic performance of gold nanoparticles for the oxidation of CO to CO_2 and O_2 was boosted when the nanoparticles used were smaller than 5 nm,[42] computational chemists an physicists have led their efforts to sample the morphological space of nanoparticles, and analyze their catalytic, electronic, optical and magnetic properties.

DFT is still the most used approach to explore the conformational PES of small nanoparticles and nanoclusters. For example, Ferrari *et al.* investigated the size

and shape dependence of Pd doping small gold nanoclusters of up to ten atoms.[43] Although DFT is useful when dealing with small nanoclusters and preselected structures, other strategies have to be considered when a large PES space is going to be explored, or when the number of metal atoms forming the nanoparticles makes DFT calculations unfeasible due to technical considerations. For example, Xiang *et al.*[44] used a simulated annealing algorithm, to successfully sample the conformational space of Ni nanoparticles from 2 up to 55 atoms, and showing that besides icosahedral-like structures, Ni nanoparticles could take decahedron-like or fcc crystal fragments as stable geometries, revealing Ni_{13}, Ni_{38} and Ni_{55} nanoparticles to be very stable. Genetic Algorithm (GA) is another useful approach to explore complex and large PES. Zhao *et al.*[45] developed a GA-based program, which with first principle calculations determined the lowest energy structures of different metal clusters, such as Na, Ca, Ga, PtSn, among others. A third convenient method is the Basin Hopping algorithm with Parallel Excitable Walkers (BH-PEW) developed by Rossi and Farrando.[46,47] Baletto *et al.* reported the computational study on the adsorption of O_2 on different sized PtNi alloys (clusters of 13, 19, 38 and 55 atoms) varying the ratio Pt/Ni in the nanocluster. To compute the global minimum structures of these alloys, they used the BH-PEW methodology with an empirical potential to describe the metal-metal interactions. In addition, they checked the BH-PEW results by means of first principle calculations, showing good agreement between both approaches.[48] These results indicate BH-PEW as a powerful tool exploring the conformational space of metal nanoparticles. Figure 1.8 shows the putative global minimum found for all sizes and compositions studied, as well as the energy comparison between BH-PEW and QM results. Note that, many of these algorithms are coupled with ab initio calculations[49] and there are other global optimization algorithms suitable to explore the morphological space of metal nanoparticles.[50,51] Combinations of the approaches discussed above have also been used.[52]

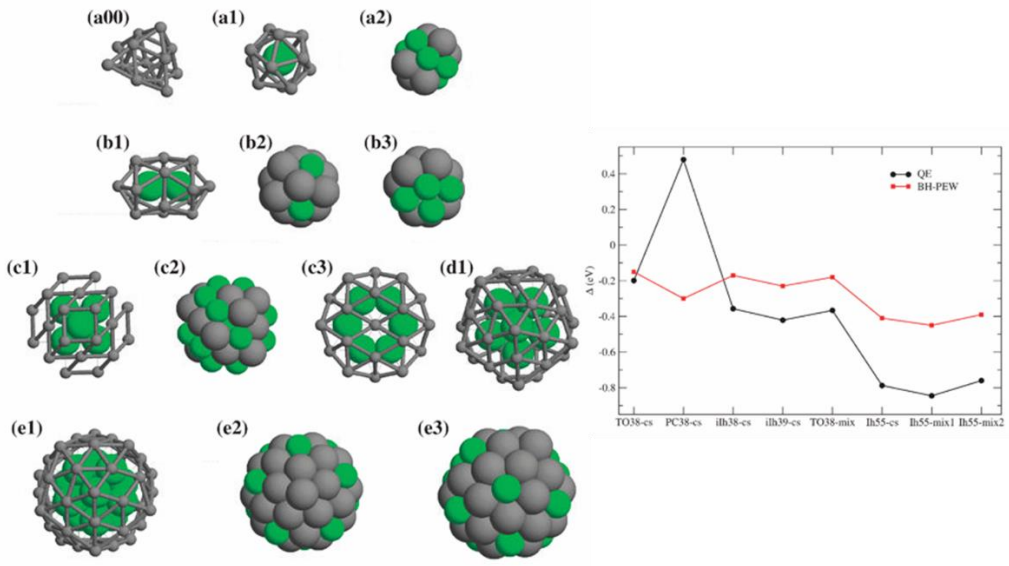

Figure 1.8. Global minima of different sized PtNi alloys obtained by BH-PEW method (Left). Comparison between the energies of PtNi Systems calculated with DFT (black) and BH-PEW (red) (Right). Reproduced from ref. 48 with permission from the Royal Society of Chemistry

Although size and shape constitute a critical part to modulate the nanoparticles catalytic activity, those features could not be controlled without the presence of surface species. Nanoparticles in chemistry, are often synthetized using the chemical or "bottom-up" approach shown in Figure 1.9. First, an organometallic complex of the desired metal is reduced or hydrogenated and then, the metallic atoms start to nucleate forming small nanoparticles and clusters. At that moment, species called stabilizers are added to the solution to stop the nanoparticles growth and prevent sintering that would result in a bulk material. With this technique, one has more control over the size and dispersion of the synthetized nanoparticles.

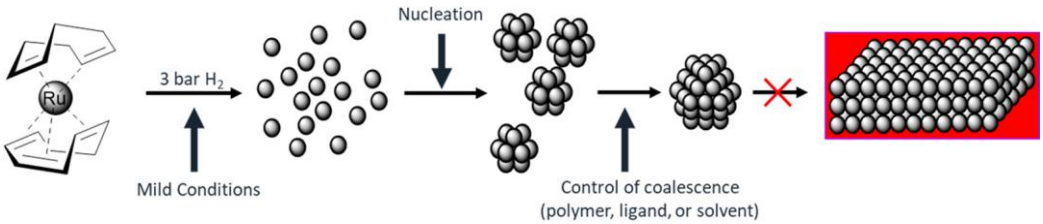

Figure 1.9. Schematic representation of the synthesis of Ru nanoparticles by the "bottom-up" approach. Reproduced from ref. 53 with permission. Copyright 2018 American Chemical Society.

Besides the role of the stabilizers in preventing sintering of the nanoparticles, they can also modify the electronic, optical and magnetic properties of the nanoparticles, as well as enhance their activity and also improve or change their selectivity. In other words, the stabilizers can modulate the catalytic performance of the nanoparticles,[53,54] thus, an atomistic understanding of the interaction stabilizer-NP is needed. The stabilizers can be polymers, solvent molecules or ligands. Among the latter, the variety studied computationally is of considerable size: N-based ligands such as aminoacids,[55,56] pyridines,[57] amines,[58,59] or aminidates;[60] S-based ligands;[61,62,63,64] and other ligands such as carboxylic acids.[65] However, here we want to pay special attention to the C-based ligands, specially NHC carbenes, and P-based ligands.

Among C-based capping ligand, NHC are of great interest due to their unique electronic and structural features.[66] One of these features is the great σ-donation capability. Ernst *et al.* reported the synthesis and DFT study of Pd NPs covered by NHC ligands.[67] The electron density injection to the NPs lowered the activation energy of the bromobenzene. Moreover, by changing the substituent of the NHC ligands, this energy barrier can be modified. Figure 1.10 shows three molecular orbitals of the NHC@Pd_{13} nanocluster studied that illustrate the interaction between the NHC ligand and the Pt_{13}. Another computational study about NHC stabilizing NPs was performed by Narouz *et al.* They reported that the stability of gold nanoclusters increases when phosphine and thiolate ligands are substituted by NHC ligands. In addition they found a correlation between the stability of these NHC@Au NPs and their performance in the electrocatalytic CO_2 reduction.[68]

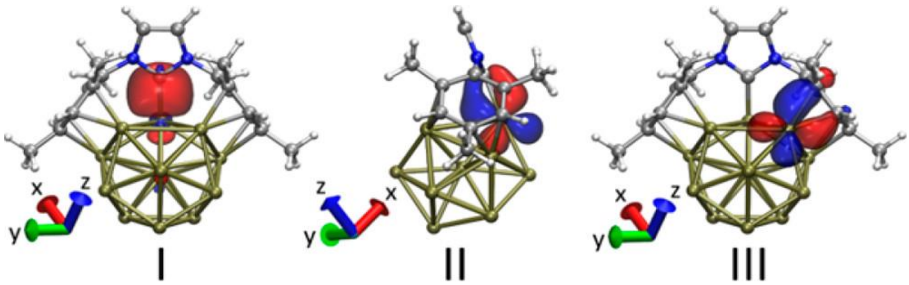

Figure 1.10. Representation of three molecular orbitals of NHC@Pd_{13} system. I) σ bonding orbital between carbene carbon and Pd. II) π bonding orbital between carbene carbon and Pd. III) Bonding combination of aromatic π and Pd 4d orbitals. Reproduced from ref. 67 with permission. Copyright 2017 American Chemical Society.

Phosphine compounds are commonly used ligands in homogeneous catalysis due to their fine-tuning properties, and they also have a great ability to modulate

the catalytic performance of small nanoparticles. Lambert *et al.* reported the synthesis of PPh_3 stabilized gold NPs $[Au_{55}(PPh_3)_{12}Cl_6]$ for selective styrene oxidation by O_2.[69] Then, Zeng *et al.* performed DFT calculation to study the ligand effect, nanoparticle shape and the mechanism of that reaction.[70] First, they explore the morphology of different Au_{55} nanoparticles by means of DFT and basin hopping methods. Finally, they found a quasi-icosahedral structure as the most stable configuration, and they also demonstrated that the ligands not only stabilized the Au_{55} core, but affected its electronic structure. The electron back-donation from the ligands made Au_{55} negatively charged that facilitates the O_2 activation. Furthermore, the spatial confinement by the ligands allowed a high yield of benzaldehyde product via a superoxo-like intermediate, containing two C-O bonds. Figure 1.11 shows the model NP and the reaction studied.

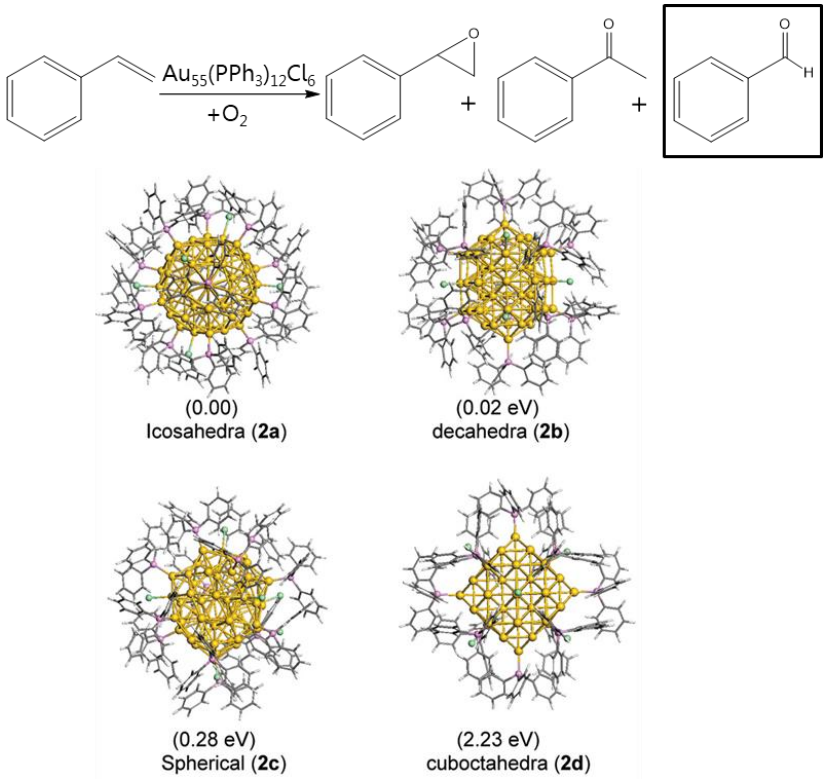

Figure 1.11. Schematic representation of the reaction and model Au_{55} nanoparticles decorated by PPh_3 molecules used in the work performed by Zeng *et al.* Reproduced from ref. 70 with permission. Copyright 2010 American Chemical Society.

Other phosphine ligands, such as the secondary phosphine oxide (SPO) Ph_2PO or the bidentate phosphine DPEphos have been studied computationally by López

et al.[71] First, they wanted to rationalize the experimental results on SPO stabilized Au nanoparticles for the selective hydrogenation of α,β-unsaturated aldehydes obtained by van Leeuwen *et al.*[72] The model used was a Au_{55} nanoparticle decorated by 27 Ph_2PO molecules. They observed a decrease in the energy barrier of H_2 activation of 0.24 eV compared with the clean surface, changing the reaction energy from endothermic to exothermic. They attribute this energy difference to the active role of the ligand, promoting a concerted transfer hydrogenation mechanism. Regarding bidentate phosphines, they use a Pd(111) surface model to simulate the NP surface. Nevertheless, they could explain the difference on the yield of fatty acid deoxygenation catalyzed by Pd NPs[73,74] when a mono- or di-phosphine were used, due to the decoordination of one arm of the di-phoshine, creating a transient cavity which was able to capture the reactants (Figure 1.12).[75] Furthermore, the steric hindrance exert by the ligands, prompted the release of the products, preventing further isomerization or side reactions.

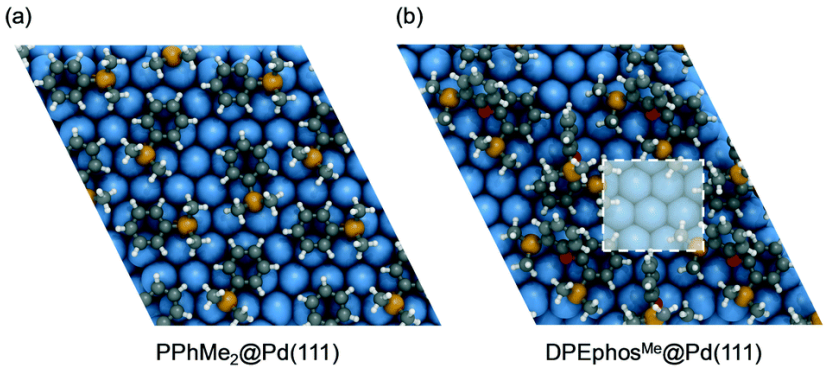

Figure 1.12. Pd(111) surface covered by monophosphine $PPhMe_2$ (a) and biphosphine DPEphos (b). The cavity formed by the labile DPEphos is marked in white. Reproduced from ref. 54 with permission from the Royal Society of Chemistry.

1.1.3 Current Challenges and Future Perspectives of Computational Catalysis

Traditional computational catalysis relies on the description of elementary reaction steps through the characterization of minima and transition states on the potential energy surface (PES) using quantum mechanics (preferentially DFT) methods and theoretical calculations have been used to understand and give an explanation of experimental results after their acquirement. However, simulations are mature enough to considered their predictive power in the catalyst and reaction design. For that reason, computational catalysis community orients its

efforts to develop efficient strategies to predict catalytic properties and to formulate new catalysts.[76]

One of these computational strategies is deriving mathematical models with parameters (descriptors) that can be fitted to reproduce (experimental or computational) data. In fact these methodologies have been known for decades (from the 60s),[77] and have been usually referred to as Quantitative Structure-Activity Relationship (QSAR) or -Property Relationship (QSPR) approaches, which are based on the so-call Hansch hypothesis:[77] "It is possible to obtain functions correlating mathematical description of molecules (molecular descriptors) with the activity of the compounds".

QSAR approaches were born in the field of biology, and along all this time they have been an essential part of drug discovery in both academia and pharmaceutical industry. At the turn of the 21st century, the portfolio of computational catalysis has routinely incorporated QSAR-like methodologies, initially and mostly in molecular catalysis,[78,79] but also in heterogeneous catalysis.[80,81] By analogy with Hansch hypothesis, it is possible to correlate the mathematical features of the catalyst structure (descriptors) with its activity or selectivity. In principle, these mathematical models enable the prediction of the activity and selectivity without prior experimentation synthesis and lead to the design of new compounds.

More recently, the proliferation of data technologies in diverse areas of science has also influenced computational heterogeneous catalysis, as reflected by the numerous review articles published during the last years that focus on the use of Machine Learning (ML) in catalysis (homogenous and heterogeneous) and material science.[82] ML methods, which include QSAR approaches, are considered one of the most powerful strategies within Artificial Intelligence (AI), consisting of mathematical algorithms to learn from data and detect patterns. In general, the evolution from "QSAR" to "ML" modeling means in practice less control in the selection of chemically meaningful descriptors, more complex (non-linear) relationships between descriptors and target properties, and larger data sets. According to recent reviews, while there are a number of successful examples for the prediction of physical properties of catalytic materials, the prediction of rates and selectivities of catalytic processes, especially heterogeneous, has had a limited success. The reasons for the small impact of data-driven design of novel catalysts are: (1) the lack of universal datasets for catalytic activities and selectivities, (2) the existence of few reactivity descriptors for heterogeneous catalysts, and (3) the complex web of factors affecting catalytic outcome, including side reactions, catalyst deactivation, and the dynamic nature of catalytic species. Thus, further developments in this area are expected for the next years.

The general working protocol of the so-called ML and QSAR approaches can be divided into three common stages: (1) selection and definition of the dataset, (2) calculation of different descriptors for catalytic species, and (3) model building and validation of predictive models using machine learning mathematical algorithms. The Figure 1.13 shows the general workflow of model development and catalyst design, incorporating the interplay between *in silico* and *in vitro* experiments.

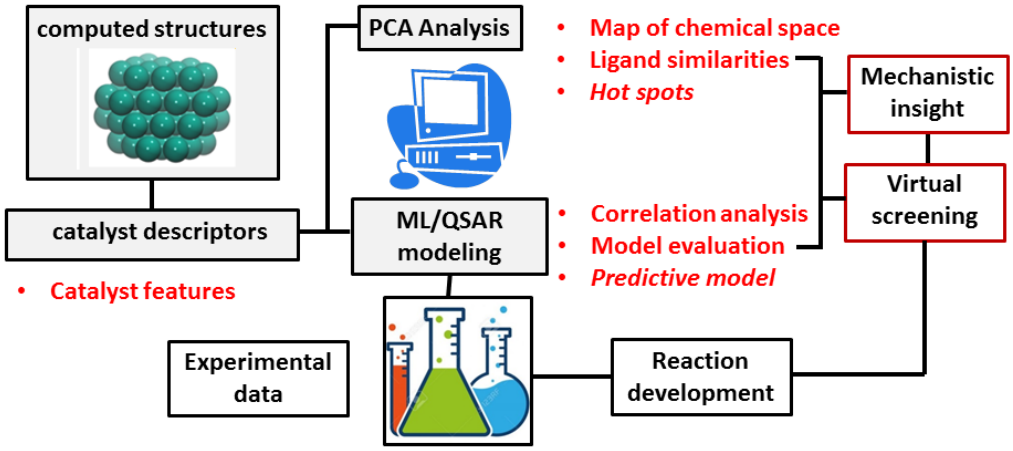

Figure 1.13. General workflow of ML or QSAR approaches procedure.

Step 1. Selection of data sets and computational databases. Machine learning is based on *data-driven* algorithms, which means that ML models are defined only by feeding a training data set into them, and therefore, the quality and extent of data sets are essential prerequisites for the development of reliable models. Thus, selection should cover the range of properties that may affect the catalytic outcome (response variable, *y*). The size of data set cannot be too small to be relevant, neither too large for practical reasons; while the range of values should be broad and uniformly distributed, avoiding imbalanced or biased data sets. The *good practices* in data selection have been defined in the literature.[83] In addition, there are experimental design techniques (for example, D-optimal design or fractional factorial design) whose goal is to catch all important properties affecting activity and selectivity using the minimal number of compounds in data set. Within this context, the development of computational databases might beneficiate ML modeling and accelerate the discovery of novel catalyst.[84] It is possible to find initiatives such as CatApp[85] and Catalysis-Hub.org,[86] which collect data within the field of heterogeneous catalysis, although one has to recognize the difficulties to provide accurate data due to the varieties of methods employed

and the complexity of the phenomena. A joint project between URV and ICIQ institutions has recently developed ioChem-BD (Input/Output Chemistry Big Data) platform[87] as a multiheaded tool aimed to manage large volumes of quantum chemistry results that also provides tools for data curation and post-processing.[88]

Step 2. Calculation of descriptors in heterogenous catalysis. Even before the popularization of supervised machine learning algorithms, DFT and other theoretical studies have investigated scaling relationships between the properties of catalytic systems and catalytic trends, allowing to construct reactivity descriptors.[80] In the literature one can identify different type of descriptors that could help designing *in silico* new catalyst materials:

- **Geometrical descriptors**. The generalized coordination number (**GCN**) proposed by Sautet *et al.* has been successfully applied as a quantitative metrics of the local structure of surface sites (also referred to as ensembles) in solid catalysts.[89,90] Later, this simple descriptor has been evolved to simultaneously capture the coordination and surface strain of the active sites (**GCN***).[91] An illustrative example is shown in Figure 1.14, where Baletto *et al.* used **GCN** as a descriptor to derive geometric genome that distinguishes, catalogues, and counts the variety of adsorption sites available on different NP isomers with a diameter up to 10 nm.[92]
- **Binary descriptors**. These descriptors take into account both geometrical and electronic effects. The orbital-wise coordination number (**CN^{α}**) has been developed for nanocatalysis and quantifies the degree of coordinative saturation of metal atoms and their tendency to form bonds via the α orbital (*s* or *d*) of a specific adsorption site.[93] The bond-energy-integrated orbital-wise coordination number (**CN^{sd}**), in contrast to **CN^{α}** evaluates the bond energy of *s* and *d* orbitals, and has been proposed for transition-metal oxides.[94] An interesting example was reported for graphene-based single-atom catalysts, for which the activity in electrochemical reactions was correlated with a descriptor that combines the coordination number with the electronegativity of the nearest-neighbor atoms.[95]
- **Electronic descriptors**. The electronic descriptors of metal extended surfaces have such a diverse spectrum, covering both the adsorption energies of key reaction species[96] and the d-band model,[97] as well as other examples such as charge polarization,[98] the average *2p*-state energy,[99] and the *p*-band center for metal-oxides. Based on the Sabatier principle, the absorption energies have been largely used for setting scaling relationships (volcano plots) and for more sophisticated machine learning approaches. For example, the selective hydrogenation of

acetylene by NiZn alloys,[100] and the CO_2 reduction to methanol by NiGa catalyst.[101] The d-band center, average energy of d band, was defined for transition metal catalysis; and within the same model, related descriptors such as the width and the shape of d-band (ε_u) are also proposed.[102]

- **Universal descriptors**. Most of the employed descriptors are not transferable to different reactions, and therefore there is an interest to develop universal descriptors that can be applied to different catalyst families, reactions and properties. Different classes of methods approaching the problem have been discussed recently.[103] Among them, atom-density based descriptors connect with the use 3D functions such as the local density of states (LDOS) as local electronic descriptors for different types of catalysts. Another approach could be the use of several topological features of the electron density (or electrostatic potential) of the ensemble and use unsupervised machine learning techniques to classify materials for their use as catalysts.

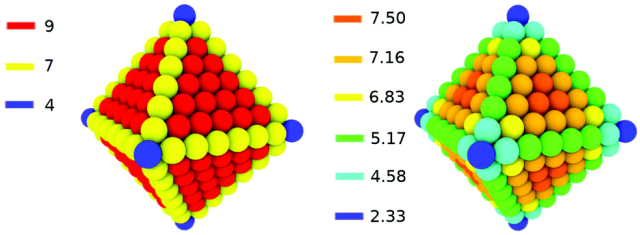

Figure 1.14. Color mapping of an atop adsorption site in a regular octahedron by the nominal coordination number (left) or the GCN (right). The value of the descriptor is reported at the left of each structure. Reproduced from ref. 92 with permission from the Royal Society of Chemistry.

Step 3. Methods for building predictive models. Methods for building the mathematical models from data include a number of different tasks and algorithms which can be classified as methods of supervised and unsupervised learning.[82h,82k,104] Methods based on supervised learning are commonly used in catalysis. They are able to build functions that map the path from input to output using only training data, and without providing explicit modelling. In supervised learning, we can distinguish between linear and non-linear regressions:

- Linear regression methods allow an ease interpretation of the modelled relationship between the independent (descriptors) and dependent (activity or selectivities) variables, and this is the option of choice for small data sets. Popular methods include multilinear least square regression, principal components regression, or partial least square (PLS) regression. If the number of descriptors is large (similar or larger than the size of

dataset) we have to use methods such as principal components or PLS regression, which reduce the dimensionality of descriptors space in order to avoid the overfitting phenomena.

- Non-linear regression methods are employed for big data sets where complex (non-linear) relationships may exist between the descriptors and the target property. Normally, the resulting models are more difficult to interpret, and provide less insight into the relative importance of the different descriptors and how they influence the target. The most popular method in Machine Learning for catalysis is the artificial neural network (ANN) regression, while other methods such as support vector machines (SVMs), genetic algorithms (GA), K nearest-neighbour (KNN), decision trees, or random forests have been also used to model material catalysts. The selection of one or another method has pros and cons. For example, SVMs methods are easier to interpret than ANN but they are very sensitive to selection of parameters and functions. Decision tree methods are suitable when data set has lost an attribute value of the catalysts, but they show a tendency to overfitting.

While software for linear regression methods have been available for long time (Unscrambler[105] or COSAN[106]), the software for non-linear regression has become available only recently. Open-source software such as scikit-learn,[107] TensorFlow,[108] PyTorch,[109] or Chainer[110] have substantially popularized the use of machine-learning methods in scientific community.

Classical potentials, especially reactive force fields, also can be useful to investigate a catalytic reaction, the catalyst morphology and composition at atomistic level, in a realistic large-scale dynamic environment of temperature, solvent or pressure with low computational cost.[111] ReaxFF[112] formalism has become very popular in the last twenty years, and it has been proved a powerful tool in many fields,[113] such as biology,[114] energy,[115] materials,[116] etc. In the field of catalysis, numerous examples used the ReaxFF approach. For instance, Chenoweth *et al.* developed a ReaxFF force field for the oxidation of propene over $BiMoO_x$ surfaces,[117] or for the methanol oxidation and dehydrogenation catalyzed by vanadium oxide surfaces.[118] However, not only surfaces and materials can be modelled by ReaxFF, but also nanocatalysts. For example, one can study the oxidation processes of benzene[119] or methane[120] catalyzed by palladium nanoparticles. In the work performed by Mao *et al.* they found that O_2 molecules adsorbed faster than CH_4 and block the adsorption sites. Moreover, they observed that the activation of CH_4 on bare Pd nanoparticles takes place at much higher temperature than on oxygen-coated Pd nanoparticles, and the conversion rate increases with the temperature and is sensitive to the level of oxygen coverage. In addition, they conclude that first, the Pd nanoparticle is

oxidized to PdO, and the coexistence of PdO and Pd on the surface leads to lower energy barriers for the adsorption and dissociation of the methane molecules, that accelerates their ignition. Figure 1.15 shows some snapshots of different simulations of the work performed by Mao *et al.*

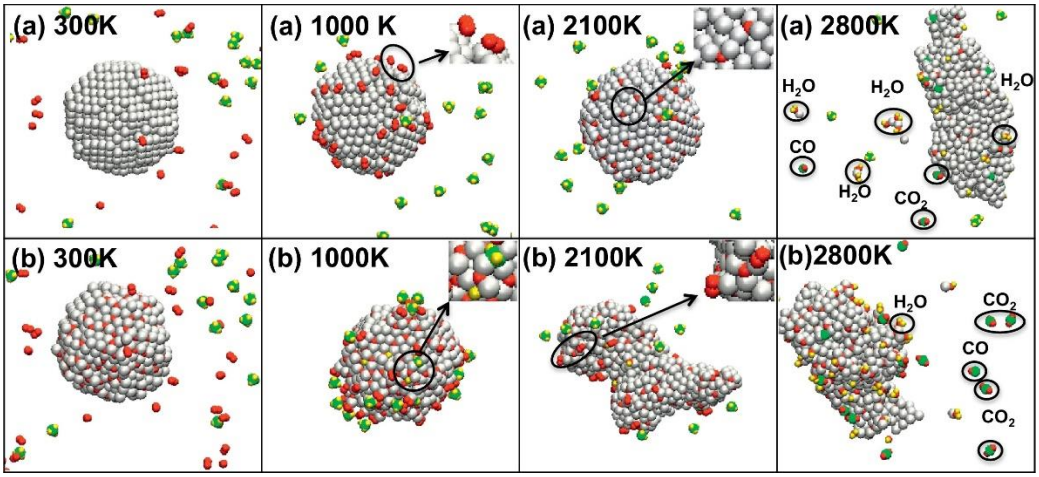

Figure 1.15. Snapshots of ReaxFF MD simulations at different temperatures of CH_4/O_2 mixture over bare (a) and oxygen-coated (b) Pd nanoparticles. Reproduced from ref. 120.

Computational catalysis has become a crucial tool to understand and improve catalytic reactions, and in the last years the first steps to design and propose new catalytic materials have been done. Although great advances have been achieved in this field, there are room for improvement, for instance, with methodologies including the entire complexity of a catalytic system. In this context, computational catalysis has been called to be a fundamental pillar to predict and design better and new materials and the novel computational techniques open the door to a more sustainable world.

1.2 Computational Approaches for Modelling Catalysis

1.2.1 Density Functional Theory for Molecules and Periodic Systems

By far the most widely used methodology in computational catalysis research is the Density Functional Theory approach, due to its balance between accuracy and computational cost. Since the formulation of its basic theorems in 1964 by Hohenberg and Kohn,[121] and the subsequent proposal of equations by Kohn and

Sham in 1965,[122] DFT has become a routine tool in chemistry and catalysis research. The DFT energy can be expressed as:

$$E_{DFT}[\rho] = T_{ref}[\rho] + V_{ne}[\rho] + V_{ee}[\rho] + E_{xc}[\rho] \quad (1)$$

Where $T_{ref}[\rho]$ represents the electronic kinetic energy of a reference system of non-interacting electrons that has the same density as the real system, $V_{ne}[\rho]$ is the classical electrostatic nucleus-electron attraction potential, $V_{ee}[\rho]$ refers to the classical Coulomb electron-electron repulsion potential of the reference non-interacting electrons system and $E_{xc}[\rho]$ is the so-called exchange-correlation functional and encapsulates the unknown factors: 1) the kinetic energy deviation from the real system, and 2) the electronic exchange potential and the correlation energy.[123]

A critical point about DFT calculations is the selection of the computational model paying special attention to the accuracy of the methodology employed. The exchange-correlation functional has a cornerstone role in the accuracy of DFT methodologies, and it cannot be determined exactly. Thus, the selection of the functional is crucial in any computational chemistry study. There are different types of functionals, differing between them in the degree of accuracy.[25] Nevertheless, more sophisticated is the functional, higher the computational cost. Local Density Approximation (LDA) functionals are the simplest, but also cheapest ones. This approximation considers that a molecule property at any point of the space only depends on the electron density at that point. LDA has been successfully applied to solids and materials, but gives poor results for molecular systems. Next, the Generalized Gradient Approximation (GGA) corrects the locality of the uniform electron density by adding a gradient to the energy density of the LDA, and further meta-GGA functionals also consider the second derivative of the density, including the kinetic energy density. Functionals of these groups such as, BP86,[124] BLYP[124,125] and PBE[126] (GGA) and TPSS[127] or M06-L[128,129] (meta-GGA) have been extensively and successfully used in many chemical applications, and probably, GGA functionals such as PBE, are the most frequently used functionals to model periodic systems. The next rung in the called "Jacob's ladder" are the hybrid functionals, that are nonlocal, where the energy functional expression contains a percentage of exact Hartree-Fock (HF) exchange. Nowadays, functionals such as B3LYP,[125,130] PBE0[131] and M06[128,129] are the most used to calculate molecular systems, and although these kind of functionals were not used to simulate periodic systems in the past due to their high computational cost, thanks to the evolution of computer technologies, some studies about periodic systems with hybrid functionals have been reported.[132,133] Although the

choice of the functional is not as relevant as one might think when dealing with closed-shell species (the difference can be as little as a few kcal mol^{-1} between two different functionals), special attention has to be paid to the percentage of Hartree-Fock exchange, if working with open-shell species using hybrid functionals.[24] For instance, Álvarez *et al.*[134] investigated the oxidation of C-H bonds by copper centers, and they reported also a comparison between the energy differences of Cu(II) (triplet) and Cu(III) (singlet) intermediate isomers using several functionals, showing a highly functional dependence. To illustrate that, taking three widely used hybrid functionals, such as B3LYP-D3, ωB97XD and TPSSh-D3, the two isomers differ 15.4, 5.4 and 9.4 kcal mol^{-1}, respectively. Nevertheless, in any case, before choosing any functional to be applied to a computational catalysis study based on DFT, a previous benchmarking is highly recommended. See also, for example, the interesting work of Illas *et al.* in which different functionals are considered to calculate several bulk properties of transition metals.[135]

In many cases, non-covalent interactions are involved in a reaction mechanism, thus, a precise description of the dispersion forces is needed. Some of the functionals commented before have the dispersion or long range correction in their formulations, such as ωB97XD, but in the non-dispersed-corrected functionals, empirical dispersion parameters must be incorporated. There are several articles benchmarking the different dispersion correction approaches,[136,137,138] and they conclude that the choice of the dispersion scheme depends on many factors, such as the functional or the system (organometallic complexes, oxides, metallic nanoparticles, etc.). Grimme's D3 correction (GD3),[139] or GD3 with the Becke-Johnson damping function scheme[140,141] (GD3BJ) have been used extensively in DFT calculations.

Additional parameters that should be considered are the basis sets used to describe the molecular orbitals (wavefunction). Normally, a double-ξ is enough to get reliable geometries, however, is common and highly recommended to refine the energy values with a large basis set. An efficient scheme that does not introduce significant errors is to perform a geometry optimization with a computationally less expensive level of theory, such as GGA or meta-GGA functionals with small basis set, followed by a single-point calculation with a more demanding functional and basis set.[25] However, thanks to the technical evolution, nowadays it is affordable to use directly a triple-ξ basis set with a hybrid functional in a geometry optimization or transition state search of organometallic complexes. Moreover, other kind of functions can be added to the basis sets, such as polarization and diffusion functions.[123]

In the case of periodic systems, both atomic basis set[142,143] and plane waves (more common) are used, derived from Bloch's theorem (2),[144] in order to take

advantage of the periodicity and the translation symmetry.[145] The plane waves are expressed as:

$$\Psi_n(r) = \sum_G c_{n,(k+G)}\, e^{i(k+G)r} \qquad (2)$$

Where $c_{n,(k+G)}$ are the plane waves coefficients, G are the reciprocal lattice vectors and k is the wave vector that is confined into the first Brillouin zone. However, to fully describe the wavefunction, an infinite number of plane waves functions in the sum is needed, and to devise a computational implementation, one must choose a finite end to the sum. This finite point is referred to as the plane wave kinetic energy cutoff. At the same time, the k space is infinite, and hence, impossible to cover it. For that reason, the symmetry features of the Brillouin zone are taken into account to study a limited number of k points. In practice, pre-stablished meshes are used. Probably, the most popular meshes are the ones generated by Monkhorst-Pack[146] or also the meshes generated by Evarestov-Smirnov[147] for cubic packing or Chadi-Cohen[148,149] for hexagonal packing. Nevertheless, a convergence test with different plane waves energy cutoff and k-points mesh schemes is highly recommended before productive periodic DFT calculations.

1.2.2 Solvent Modelling

As commented in Section 1.1.1, to improve the description of a catalytic system, the solvent effects must be introduced in the model, because solvent molecules can directly or indirectly affect the evolution of a catalytic reaction. Also mentioned in Section 1.1.1, there are three main approaches to deal with model solvation: [123]

Explicit model. In this case some solvent molecules are placed around the catalytic site, treating both of them, solvent and solute, at the same level of theory. Typically, the explicit model is used in classical molecular dynamics simulations using classical forcefields, especially when the solute is a big molecule like a protein and the number of solvent molecules needed to completely surround it is big. However, when the solvent is directly involved in the reaction, for instance in acid-base processes, the explicit model is used in Ab Initio Molecular Dynamics (AIMD) simulations, since Molecular Mechanics (MM) potentials are not able to simulate reactive events, such as bond formation and breaking. The advantage of this methodology relies in an explicit description of the solvent molecules, allowing the detection of active participation of solvent in

the reaction, but the counterpart is that the computational cost increases exponentially with the number of solvent molecules.

Hybrid model. To decrease the computational expenses of the explicit model, one can define regions, and treat them at different level of theory. Typically, the catalytic site and the first solvation sphere are described at high level of theory, and the bulk solvent with less accurate functionals or basis sets, at MM level, even as continuum solvent.

Implicit model. The main idea behind the implicit solvent model is to put the solute inside a cavity of a continuum solvent, defined with its dielectric constant, and then to compute the interaction between the cavity and the solute. This continuous media can be taken as a homogeneous average of the effect of a large number of explicit solvent molecules surrounding the solute, represented by a perturbation factor added to the solute Hamiltonian *in vacuo*, which in turns, polarizes the wave function.

The crucial step on the implicit model is the calculation of the size and shape of the cavity. The simplest cavity model is the spherical one, in which the molecule is placed in a sphere, and a bit more complex it is the ellipsoid cavity. However, the molecules are not as simple as a sphere or ellipsoid and this models are very unrealistic and not really accurate. More precise schemes, called molecular models, use the van der Waals surface as a cavity, that is the superposition of the van der Waals atomic radii of the elements forming the solute. Then, the Gibbs free solvation energy can be expressed as a sum of different terms Equation (3): 1) the energy needed to build the cavity, 2) the energy of the solute-solvent dispersion interactions and 3) the electrostatic stabilization by the electric charge distribution.

$$\Delta G_{solvation} = \Delta G_{cavity} + \Delta G_{dispersion} + \Delta G_{elec} \quad (3)$$

Many computational solvation schemes have been proposed in the literature such as the conductor-like screening model (COSMO),[150] or the Solvent Model (SMx) methods.[151,152] However, one of the methods widely used and has gained increasing attention over the last decades is the Polarizable Continuous Method (PCM)[153,154], based on the fact that charge distribution of the solute polarizes the cavity wall, that in turn polarizes again the charge density of the solute, and so on. For that reason, the final interaction energy must be calculated iteratively, procedure known as Self Consistent Reaction Field (SCRF) calculations.

1.2.3 Microkinetic Analysis

Normally, the catalytic reactions are carried out in solution, and experimentally it is not the free energy difference that is measured, but the evolution of the concentration of the species involved in the process. Computationally, kinetic analysis is a cheap and powerful tool to consider the concentration effects with time.[36] The macroscopic expression for the rate of a reaction with the form n_aA + n_bB ⟷ n_cC + n_dD is shown in Equation (*4*):

$$\text{rate} = \frac{1}{n_c}\frac{d[C]}{dt} = \frac{1}{n_d}\frac{d[D]}{dt} = -\frac{1}{n_a}\frac{d[A]}{dt} = -\frac{1}{n_b}\frac{d[B]}{dt} = k_{forward}[A]^{\alpha}[B]^{\beta} \quad (4)$$

where α and β are the partial orders of reaction. For an elemental step, the partial orders are the stoichiometric coefficients. The magnitudes to be computed for the kinetics analysis are the free energy barriers ($\Delta G^{\ddagger}$) measured as the difference between the free energies of a transition state and the corresponding intermediate. Both variables, $\Delta G^{\ddagger}$ and rate constant, are related by the Eyring-Polanyi equation (Equation (*5*))[155] within the Transition State Theory (TST):

$$k = \frac{\kappa k_b T}{h}\exp\left(\frac{-\Delta G^{\ddagger}}{RT}\right) \quad (5)$$

Where k is the reaction rate constant, κ is the transmission factor, k_b is the Boltzmann's constant, T is the temperature, h is the Planck's constant, $\Delta G^{\ddagger}$ is the activation free energy and R is the ideal gas constant. In practice, all catalytic processes involve multiple steps, each of them with its own reaction constant that can contribute in more or less extent to the kinetics of the process, such as the formation of a catalyst from a pre-catalyst, catalyst deactivation products, side reactions, etc. To build up a microkinetic model, one must first consider all possible reactions involved in the entire catalytic cycle, and the corresponding kinetic equations, as the generic one shown in Equation (*4*). The idea is to consider all the processes leading to the formation or consumption of each single species, as well as all forward and reverse chemical equations. That leads to a system of differential equations that must be solved introducing the initial concentrations of each species and the rate constants, that can be obtained from $\Delta G^{\ddagger}$ by Equation (*5*). The result of solving these differential equations is the evolution of the species concentration with time. Useful softwares are available to solve the differential equations, such as Tenua,[156] Copasi,[157] or Acuchem.[158] In

this thesis we have used Acuchem thanks to previous successful experience in our group.[159]

1.2.4 Modelling Dynamic Behaviour

Ab initio molecular dynamic simulations

The AIMD technique rapidly evolved during the last decades and became one of the most important theoretical tool thanks to the exponentially growing computational power. The motivation for the AIMD development was the need of one technique able to account for the microscopic dynamic behaviour of the systems in a condensed phase, including the bond breaking and formation phenomena considering the electronic polarization effects.[160] The main idea behind the AIMD approach is to calculate the static electronic structure of the system at a fixed nuclear position by solving the time-independent electronic Schrödinger equation propagating the nuclei according to classical mechanics.[161] The classical dynamics of the nuclei is given by the Newton's equation of motion:

$$\mathrm{M_I}\ddot{\mathbf{R}}_\mathrm{I} = -\nabla_\mathrm{I}[\varepsilon_0(\mathbf{R}) + \mathrm{V_{NN}}(\mathbf{R})] \quad (6)$$

where $\mathrm{M_I}$ is the mass of the nucleus I, $\ddot{\mathbf{R}}_\mathrm{I}$ is the second derivative of the position of the nucleus I respect to time, $\varepsilon_0(\mathbf{R})$ is the electronic ground state energy at nucleus position $\mathbf{R}$ and $\mathrm{V_{NN}}(\mathbf{R})$ is the nuclear-nuclear Coulomb repulsion at nuclear configuration $\mathbf{R}$. The procedure to solve the electronic time independent Schrödinger equation depends on the method used, but nowadays the most popular approach is DFT. There are two different types of QM dynamics: in Born-Oppenheimer MD, the electronic structure is calculated at each step. In Car-Parrinello MD (CPMD)[162], the wavefunction is calculated only once at the beginning of the dynamics, and then is propagated during the whole simulation. Also there are technical differences between both methodologies. In general, in any molecular dynamic approach, the time step must be one order of magnitude lower than the fastest movement that exists in the system. Since in CPMD, the electrons have associated a fictitious mass, their movement becomes the fastest, forcing very small time steps, while in BOMD one can use bigger time steps because the fastest movement is the nuclear dynamics.

Classical molecular dynamic simulations. LoDis framework.

Classical Molecular Dynamics (MD) approaches, are based on Molecular Mechanics (MM) formalism. The atoms are considered as rigid balls linked

together by springs representing the bonds and neglecting the electrons. The energy of the system is treated as a sum of different energy contributions as shown in Equation (7):[123]

$$E = \sum_{bonds} E_{stretch} + \sum_{angles} E_{bend} + \sum_{dihedrals} E_{torsion} + \sum_{pairs} E_{nonbond} \quad (7)$$

The different terms in Equation (7) are the bond stretching energy ($E_{stretch}$), angle bending energy (E_{bend}), the rotation energy of dihedral angles ($E_{torsion}$) and the interaction energy between atoms not directly bonded ($E_{nonbond}$). The mathematical expression of this terms and their parameters constitutes a forcefield. Examples of popular and widely used forcefiels are the Universal force fields[163] (UFF), CHARMM[164], AMBER[165] or GROMOS[166] among others[167].

Low Dimensional System molecular dynamics (LoDiS) software was developed by Baletto *et. al.* at King's College London. The program mainly focuses on investigations into growth, coalescence, phase transition and free energy sampling of mono- and bi-metallic nanoclusters.[168] The interatomic potential is modelled according to the Gupta or Rosato-Guillope-Legrand formulation[169] presented in Equation (8). The potential energy form consists in two well differentiated terms, the repulsion part written as a Born-Mayer term (left) and the attractive part written as a many-body term derived according to the second moment tight binding approximation framework (right):

$$E_i = \sum_{j \neq i}^{n_v} A_{ab} e^{-p_{ab}\left(\frac{r_{ij}}{r_{ab}^0}-1\right)} - \sqrt{\sum_{j \neq i}^{n_v} \xi_{ab}^2 \, e^{-2q_{ab}\left(\frac{r_{ij}}{r_{ab}^0}-1\right)}} \quad (8)$$

The sum runs up to the number of atoms n_v where r_{ij} is the distance between the atoms i and j. The labels a and b have been introduced to distinguish between the homoatomic and the heteroatomic interactions, a being the chemical species of atom i, and b of the jth atom. r_{ab}^0 is the nearest neighbour distance, that for homoatomic pair, it coincides with the pure bulk metal nearest neighbour distance, while for heteroatomic pair it is given by their average distance $r_{ab}^0 = \frac{r_{aa}^0 + r_{bb}^0}{2}$. The parameters A_{ab}, ξ_{ab}, p_{ab} and q_{ab} are fitted to the bulk experimental values of cohesive energy, lattice parameter and elastic constants for the pure

elements for homoatomic interactions, while for heteroatomic, the geometrical average of the homoatomic values are considered.[48]

Reactive force fields. ReaxFF framework.

Classical forcefields are not able to simulate reactive processes, with bond breaking or formation, since they do not consider the electrons and are based in fixed force constants and charges. To cover that issue, reactive force fields emerged as powerful tool to simulate dynamics of large-systems allowing reactive events during the simulation with very low computational cost. Nowadays there are many examples of reactive force fields such as AIREBO[170], COMB[171] or ReaxFF[172] methods. The last one has been used in this thesis.

The main idea behind the ReaxFF approach, developed by Adri van Duin in 2001,[172a] is that the interatomic potential allows reactive events through a bond-order concept, initiated by Abell[173], Tersoff[174,175] and Brenner[176], where the bond order is calculated empirically at each simulation step from the interatomic distances. The ReaxFF potential energy of the system is defined as a sum of different energy contributions:

$$E_{system} = E_{bond} + E_{over} + E_{angle} + E_{tors} + E_{vdWaals} + E_{Coulomb} + E_{specific} \quad (9)$$

The first four terms stand for the covalent contributions and are the bonding energy between two atoms (E_{bond}), an energy penalty to prevent the over coordination of atoms (E_{over}), the three-body angle strain energy (E_{angle}) and the four-body dihedral strain energy ($E_{vdWaals}$). $E_{vdWaals}$ and $E_{Coulomb}$ are the non-bonded interactions and they are the dispersive and electrostatic contributions calculated over all the atoms regardless of connectivity and bond-order. The last term is related to some specific energy contributions, calculated only in especial cases, such as lone pair energy, conjugation, hydrogen binding or C_2 corrections.

All the covalent terms in Equation (9) are bond-order-dependent, and since the bond orders are calculated in each step, allowing their change, the bonds can break or form during the simulation. The bond orders are calculated by the following empirical expression directly from the interatomic distances:

$$BO_{ij} = BO_{ij}^{\sigma} + BO_{ij}^{\pi} + BO_{ij}^{\pi\pi} = \\ = \exp\left[p_{bo1}\left(\frac{r_{ij}}{r_0^{\sigma}}\right)^{p_{bo2}}\right] + \exp\left[p_{bo3}\left(\frac{r_{ij}}{r_0^{\pi}}\right)^{p_{bo4}}\right] + \exp\left[p_{bo5}\left(\frac{r_{ij}}{r_0^{\pi\pi}}\right)^{p_{bo6}}\right] \quad (10)$$

In Equation (10), BO is the bond order between the atoms i and j, r_{ij} is the interatomic distance between atoms i and j, r_0 is the equilibrium bond length, p_{bo} are different empirical parameters and σ, π and ππ are related with single, double and triple bond orders, respectively.

The internal workflow of the ReaxFF program is shown in Figure 1.16. The total energy of the system is calculated in two parts, starting both from the atomic positions. On one hand, the covalent, bond-order-dependent terms are calculated from the bond orders calculated by Equation (10). On the other hand, bond-order-independent terms are calculated from charges and polarization energies deducted by the electronegativity equalization method (EEM) proposed initially by Mortier *et al.*[177]

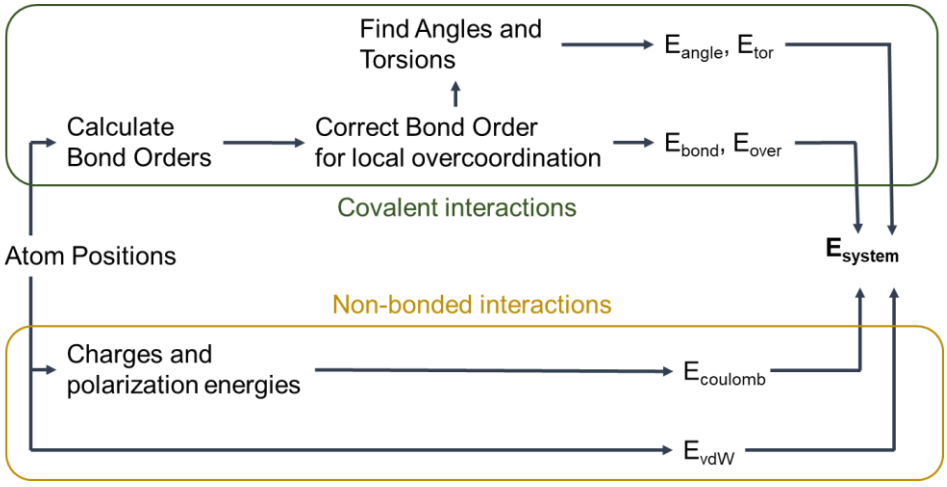

Figure 1.16. General workflow of ReaxFF program.

Comparison among molecular dynamic approaches.

All MD approaches are useful in certain circumstances, but all of them have their own limitations and they cannot be used indistinguishably.

Table 1.1. Summary of differences among the three MD methodologies used in this thesis.

Ab initio MD	ReaxFF framework	Classical MD
Computationally expensive	Computationally cheap	Computationally much cheaper
Reactive events	Reactive events	No reactive events
System size: small	System size: large	System size: large
Very accurate	Training dependence	Training dependence
No training is needed	Training is needed	Training is needed
Fully transferable	Not fully transferable	Not fully transferable

The first difference one has to note is the time needed to carry out one of these MD simulations. In AIMD simulations the Schrödinger equation has to be solved with a well converged wave function to ensure high accuracy, and this procedure takes a long time making the *ab Initio* MD very computationally expensive. However, in Reactive or Classical MD, the electrons are not taking into account, avoiding the Schrödinger equation resolution and the SCF procedure, using much less sophisticated mathematical expressions allowing much longer simulations with the same clock time than AIMD. Table 1.2 shows a comparison of the computational cost to perform typical production runs with the different methods commented above, in the study of the protonation state of $[Mo_6O_{19}]^{2-}$ Polioxometalate (POM) carried out in our group. The system was the same for the three simulations and it was composed with 335 water molecules, 2 H^+ and the POM in a simulation box of 22 Å of lattice. The results of Table 1.2 clearly indicate the superior computational cost of the AIMD, and the cheap cost of classical MD, with ReaxFF MD representing a reasonable balance between the two extremes. Moreover, since in AIMD, the electrons are important, the system under study must be small, just a few atoms, to make the simulations affordable. On the other hand, with reactive and classical MD, the number of atoms involved in the simulation can be of the order of thousands. Nevertheless, despite these issues around AIMD, it has some advantages respect ReaxFF and Classical MD. For instance, due to the QM basis of ab initio MD, these simulations are very accurate, but in the case of reactive and classical MD, their accuracy depends to a large extent on their parameterization, most of the times being this parameterization very challenging. That constitutes a handicap of MM methods against *ab Initio* MD, because to get a reliable force field, a huge amount of empirical or QM data is needed, unlike *ab Initio* methods that no previous training is needed. Another consequence of the methodology used is that *ab Initio* methods are fully transferable. They can be used on any kind of element

and any atomic environment. For example, with the same method of *ab Initio* MD one can simulate the O in gas phase as O_2, as well as the O in water without prior training whereas, in classical MD, the force field needs to be parameterized for all the atoms of interest and needs all the parameters for all the chemical species that one element can form. In the case of ReaxFF the force field is composed by just one kind of atoms per element (only one atom for O, O_2, H_2O or Al_2O_3), and the treatment during the simulation depends on the environment surrounding the atom, but the training data must include all the chemical species of that atom you want to simulate. For that reason, with classical MD or ReaxFF, one cannot transfer the force field directly from one chemical system to another, and needs to test it prior usage in productive simulations. Finally, the similar point between AIMD and ReaxFF is that both can perform reactive simulations, where bond breaking and bond formation can be observed, due to its QM nature or its bond-order formalism. Unfortunately, with Classical MD, no reactive events can be observed and only electrostatic and Van der Waals interactions are present. All three approaches have their advantages and their disadvantages, and the conclusion is that one method is not better than the others, but they must be used in the correct situation and the correct moment, and most of the times all three methodologies are complementary and they can elucidate different important things of the same problem.

Table 1.2. Comparison of the computational cost between CPMD, ReaxFF and Classical MD methods for $[Mo_6O_{19}]^{2-}$ anion in a water solvent box 22 Å of lattice.

System	Method	Simulated time	n atoms	CPU cores	Clock time	Relative time cost[a]
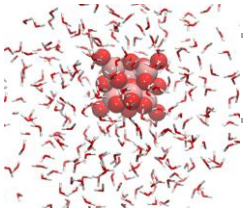	CPMD	5 ps	1032	100	880 h	$2.4 \cdot 10^6$
	ReaxFF	2ns	1032	32	66 h	$1.4 \cdot 10^2$
	Classical MD	100 ns	1032	32	23 h	1.0

[a] The relative computational cost (rcc) is calculated as: rcc = (clock time x number of cores x simulation time^{-1})/rcc classical MD

1.2.5 Basin Hopping-Parallel Excitable Walkers Global Optimization Algorithm.

Basin Hopping (BH) optimization algorithm[178] belongs to the so-called deformation methods family, which alter the shape of the PES by a transformation that reduces the number of local minima or changes their appearance. The BH modified landscape is obtained by applying a local minimization procedure to every point in the configurational space:

$$\widetilde{\mathrm{E}}(\mathbf{X}) = \min\{\mathrm{E}(\mathbf{X})\} \tag{11}$$

That means that the point $\mathbf{X}$ assumes the energy of $\mathbf{X}_{\mathrm{min}}$ which corresponds to the closest local energy minimum on the PES, transforming the energy function into a staircase function as shown in Figure 1.17. During the optimization, BH uses a Monte Carlo (MC) sampling approach, that generates random initial configurations by changing the atomic coordinates. The moves from starting position can be accepted or refused according to a standard Metropolis algorithm:

$$\text{if } \widetilde{\mathrm{E}}_{\mathrm{D}} \leq \widetilde{\mathrm{E}}_{\mathrm{S}} \rightarrow \mathrm{p} = 1 \tag{12}$$

$$\text{if } \widetilde{\mathrm{E}}_{\mathrm{D}} > \widetilde{\mathrm{E}}_{\mathrm{S}} \rightarrow \mathrm{p} = \mathrm{e}^{-(\widetilde{\mathrm{E}}_{\mathrm{D}} - \widetilde{\mathrm{E}}_{\mathrm{S}})/\mathrm{k_b T}} \tag{13}$$

Where p takes values between 0 and 1 and indicates the probability of acceptance, T is the fictitious temperature of the system and $\mathrm{k_b}$ is the Boltzmann's constant. Here, the BH PES transformation gain importance as illustrated in Figure 1.17. For example, without the local minimization of the PES, the move from S to D could be rejected with a probability of $1 - \mathrm{e}^{-(\mathrm{E_D} - \mathrm{E_S})/\mathrm{k_b T}}$ because $\mathrm{E_D} > \mathrm{E_S}$. However, thanks to the BH local minimization $\tilde{E}_{\mathrm{D}} < \tilde{E}_{\mathrm{S}}$, thus the move is accepted with probability of 1 (Figure 1.17).

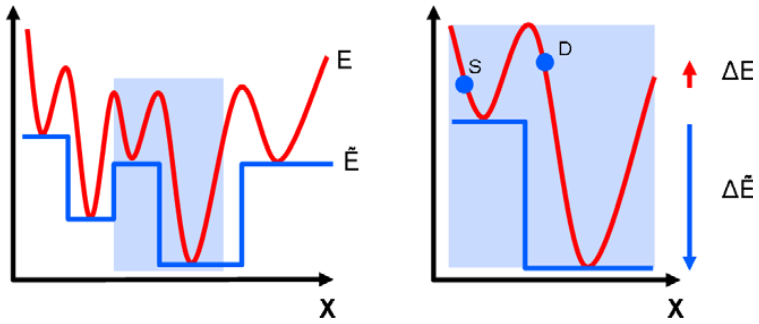

Figure 1.17. On the left, the PES (E) and its BH transformation in a staircase surface ($\tilde{E}$). On the right, zoom in the highlighted area. Reproduced from ref. 47 with permission from IOPScience.

The BH algorithm is extremely efficient reaching the lowest minimum in a given funnel of the PES, however, it can have difficulties to overcome the energy barriers that separate different funnels.[46,178] To be able to explore multiple funnels of the PES within the BH approach, and to improve its performance Rossi and Farrando developed the Parallel Excitable Walkers (PEW) algorithm.[46,47] The idea behind the PEW methodology is that one walker (**k**) is in its starting position (S) and if it has at least one neighbor walker (**z**) in the transformed PES, the walker **k** is excited to an energy level placed higher than $\mathrm{E}_{\mathbf{kS}}$ by the quantity $\mathrm{E}_{\mathrm{exc}}$:

$$\mathrm{E}^{*}_{\mathbf{kS}} = \mathrm{E}_{\mathbf{kS}} + \mathrm{E}_{\mathrm{exc}} \tag{14}$$

In that way, neighboring walkers have high probability to accept energetically unfavorable moves, repelling each other and increasing their distance in the parameter space, allowing the exploration of other funnels of the PES. Otherwise, isolated walkers accept mainly energetically favorable moves.

References

1. Berzelius, J. J. *Edimburg New Phylos. Journal* **1836**, *XXI*, 223.
2. Somorjai, G. A. *Science* **1985**, *227*, 902.
3. Spencer, N. D.; Somorjai, G. A. *Rep. Prog. Phys.* **1983**, *46*, 1-49.
4. http://www.catalysiscluster.eu/
5. http://gecats.org/en/news.html
6. http://nacatsoc.org/
7. https://www.secat.es/
8. Chorkendorff, I.; Niemantsverdriet, J. W. *Concepts of Modern Catalysis and Kinetics*, WILEY-VCH Verlag GmbH & Co. KGaA, Weinheim, 2003.
9. Kamer, P. C. J.; Vogt, D., Thybaut, J. W. *Contemporary Catalysis: Science, Technology, and Applications*, Royal Society of Chemistry, 2017.
10. Anastas, P. T.; Warner, J. C. *Green Chemistry: Theory and Practice*, Oxford University Press: New York, 1998.
11. Anastas, P. T.; Eghbali, N. *Chem. Soc. Rev.* **2010**, *39*, 301-312.
12. Anastas, P. T.; Kirchhoff, M. M.; Williamson, T. C. *Appl. Catal. A: Gen.* **2001**, *221*, 3-12.
13. Corma, A.; Iborra, S.; Velty, A. *Chem. Rev.* **2007**, *107*, 2411-2502.
14. Rahimi, A.; Azarpira, A.; Kim, H.; Ralph, J.; Stahl, S. S. *J. Am. Chem. Soc.* **2013**, *135*, 6415-6418.
15. Rahimi, A.; Ulbrich, A, Coon, J. J.; Stahl, S. S. *Nature*, **2014**, *515*, 249.
16. Deuss, P. J.; Scott, M.; Tran, F.; Westwood, N. J.; de Vries, J. G.; Barta, K. *J. Am. Chem. Soc.* **2015**, *137*, 7456-7467.
17. Sala, X.; Romero, I.; Rodríguez, M.; Escriche, L.; Llobet, A. *Angew. Chem. Int. Ed.* **2009**, *48*, 2842-2852.
18. Maeda, K.; Domen, K. *J. Phys. Chem. Lett.* **2010**, *1*, 2655-2661.
19. Ahmad, H.; Kamarudin, S. K.; Minggu, L. J.; Kassim, M. *Renewable Sustainable Energy Rev.* **2015**, *43*, 599-610.
20. Teichmann, D.; Arlt, W.; Wasserscheid, P. *Int. J. Hydrogen Energy*, **2012**, *37*, 18118-18132.
21. Yang, M.; Dong, Y.; Fei, S.; Pan, Q.; Ni, G.; Han, C.; Ke, H.; Fang, Q.; Cheng, H. *RSC Adv.* **2013**, *3*, 24877-24881.
22. Yang, Q.; Wang, Q.; Yu, Z. *Chem. Soc. Rev.* **2015**, *44*, 2305-2329.
23. Pingen, D.; Lutz, M.; Vogt, D. *Organometallics* **2014**, *33*, 1623-1629.
24. Lledós, A. *Eur. J. Inorg. Chem.* **2021**, 2547-2555.

25. Vogiatzis, K. D.; Polynski, M. V.; Kirkland, J. K.; Townsend, J.; Hashemi, A.; Liu, C.; Pidko, E. A. *Chem. Rev.* **2019**, *119*, 2453-2523.
26. Ahn, S.; Hong, M.; Sundararajan, M.; Ess, D. H.; Baik, M.-H. *Chem. Rev.* **2019**, *119*, 6509-6560.
27. Besora, M.; Braga, A. A. C.; Ujaque, G.; Maseras, F.; Lledós, A. *Theor. Chem. Acc.* **2011**, *128*, 639-646.
28. Gómez-Orellana, P.; lledós, A.; Ujaque, G. *J. Org. Chem.* **2021**, *86*, 4007-4017.
29. Fey, N. *Dalton Trans.* **2010**, *39*, 296-310.
30. Grimme, S. *J. Chem. Theory Comput.* **2019**, *15*, 2847-2862.
31. Couce-Rios, A.; Lledós, A.; Fernández, I.; Ujaque, G. *ACS Catal.* **2019**, *9*, 848-858.
32. Jia, M.; Bandini, M.; *ACS Catal.* **2015**, *5*, 1638-1652.
33. Ciancaleoni, G.; Belpassi, L.; Zuccaccia, D.; Tarantelli, F.; Belanzoni, P. *ACS Catal.* **2015**, *5*, 803-814.
34. Stirling. A.; Nair, N. N.; Lledós, A.; Ujaque, G. *Chem. Soc. Rev.* **2014**, *43*, 4940-4952.
35. Peltzer, R. M.; Gauss, J.; Eisenstein, O.; Cascella, M. *J. Am. Chem. Soc.* **2020**, *142*, 2984-2994.
36. Besora, M.; Maseras, F.; *WIREs Comput. Mol. Sci.* **2018**, *8*, e1372.
37. Kefalidis, C. E.; Davi, M.; Holstein, P. M.; Clot, E.; Baudoin, O. *J. Org. Chem.* **2014**, *79*, 11903-11910.
38. Guo, W.; Kuniyil, R.; Gómez, J. E.; Maseras, F.; Kleij, A. W. *J. Am. Chem. Soc.* **2018**, *140*, 3981-3987.
39. Astruc, D. *Chem. Rev.* **2020**, *120*, 461-463.
40. Rampino, L. D.; Nord, F. F. *J. Am. Chem. Soc.* **1941**, *63*, 2745–2749.
41. Baletto, F.; Johnston, R. L. *Eur. Phys. J. B* **2019**, *92*, 148.
42. Haruta, M.; Kobatashi, T.; Sano, H.; Yamada, N. *Chem. Lett.* **1987**, *16*, 405–408.
43. Ferrari, P.; Delgado-Callico, L.; Lushchikova, O. V.; Hou, G.-L.; Baletto, F.; Bakker, J. M.; Janssens, E. *Nanoscale Adv.* **2021**, *3*, 6197.
44. Xiang, Y.; Sun, D. Y.; Gong, X. G. *J. Phys. Chem. A* **2000**, *104*, 2746-2751.
45. Zhao, J.; Shi, R.; Sai, L.; Huang, X.; Su, S. *Mol. Simul.* **2016**, *42*, 809-819.
46. Rossi, G.; Ferrando, R. *Chem. Phys. Lett.* **2006**, *423*, 17–22
47. Rossi, G.; Ferrando, R. *J. Phys.: Condens. Matter* **2009**, *21*, 084208
48. Di Paola, C.; Baletto, F. *Phys. Chem. Chem. Phys.* **2011**, *13*, 7701-7707.
49. Jäger, M.; Schäfer, R.; Johnston, R. L. *Adv. Phys. X* **2018**, *3*, 1516514.
50. Ouyang, R.; Xie, Y.; Jiang, D. *Nanoscale*, **2015**, *7*, 14817.
51. Zhao, Y.; Chen, X.; Li, J. *Nano Res.* **2017**, *10*, 3407-3420.
52. Huang, R.; Bi, J.-X.; Li, L.; Wen, Y.-H. *J. Chem. Inf. Model.* **2020**, *60*, 2219-2228.
53. Marínez-Prieto, L. M.; Chaudret, B. *Acc. Chem. Res.* **2018**, *51*, 376-384.

54. Ortuño, M. A.; López, N. *Catal. Sci. Technol.* **2019**, *9*, 5173-5185.
55. Carr, J. A.; Wang, H.; Abraham, A.; Gullion, T.; Lewis, J. P. *J. Phys. Chem. C* **2012**, *116*, 25816-25823.
56. Schrader, I.; Neumann, S.; Sulce, A.; Schmidt, F.; Azov, V.; Kunz, S. *ACS Catal.* **2017**, *56*, 7963.
57. Creus, J.; Drouet, S.; Suriñach, S.; Lecante, P.; Collière, V.; Poteau, R.; Philippot, K.; García-Antón, J.; Sala, X. *ACS Catal.* **2018**, *8*, 11094-11102.
58. Lu, G.; Zhang, P.; Sun, D.; Wang, L.; Zhou, K.; Wang, Z.-X.; Guo, G.-C. *Chem. Sci.* **2014**, *5*, 1082.
59. Fiorio, J. L.; López, N.; Rossi, L. M. *ACS Catal.* **2018**, *8*, 3516.
60. Martínez-Prieto, L. M.; Cano, I.; Márquez, A.; Baquero, E. A.; Tricard, S.; Cusinato, L.; del Rosal, I.; Poteau, R.; Coppel, Y.; Philippot, K.; Chaudret, B.; Cámpora, J.; van Leeuwen, P. W. N. M. *Chem. Sci.* **2017**, *8*, 2931.
61. Fresch, B.; Remacle, F. *J. Phys. Chem. C* **2014**, *118*, 9790-9800.
62. Guedes-Sobrinho, D.; Chaves, A. S.; Piotrowski, M. J.; Da Silva, J. L. F. *J. Chem. Phys.* **2017**, *146*, 164304.
63. Häkkinen, H. *Nat. Chem.* **2012**, *4*, 443.
64. Taylor, M. G.; Mpourmpakis, G. *Nat. Commun.* **2017**, *8*, 15988.
65. González-Gómez, R.; Cusinato, L.; Bijani, C.; Coppel, Y.; Lecante, P.; Amiens, C.; del Rosal, I.; Philippot, K.; Poteau, R. *Nanoscale* **2019**, *11*, 9392.
66. Tang, Q.; Hu, G.; Fung, V.; Jiang, D.-e. *Acc. Chem. Res.* **2018**, *51*, 2793.
67. Ernst, J. B.; Schwermann, C.; Yokota, G.-i.; Tada, M.; Muratsugu, S.; Doltsinis, N. L.; Glorius, F. *J. Am. Chem. Soc.* **2017**, *139*, 9144.
68. Narouz, M. R.; Osten, K. M.; Unsworth, P. J.; Man, R. W. Y.; Salorinne, K.; Takano, S.; Tomihara, R.; Kaappa, S.; Malola, S.; Dinh, C.-T.; Padmos, J. D.; Ayoo, K.; Garrett, P. J.; Nambo, M.; Horton, J. H.; Sargent, E. H.; Häkkinen, H.; Tsukuda, T.; Crudden, C. M. *Nat. Chem.* **2019**, *11*, 419.
69. Turner, M.; Golovko, B.; Vaughan, O. P. H.;Abdulkin, P.; Berenguer-Murcia, A.; Tikhov, M. S.; Johnson, B. F. G.; Lambert, R. M. *Nature* **2008**, *454*, 981.
70. Pei, Y.; Shao, N.; Gao, Y.; Zeng, X. C. *ACS Nano* **2010**, *4*, 2009-2020.
71. Almora-Barrios, N.; Cano, I.; van Leeuwen, P. W. N. M.; López, N. *ACS Catal.* **2017**, *7*, 3949.
72. Cano, I.; Chapman, A. M.; Urakawa, A.; van Leeuwen, P. W. N. M. *J. Am. Chem. Soc.* **2014**, *136*, 2520.
73. Chatterjee, A.; Jensen, V. R. *ACS Catal.* **2017**, *7*, 2543.
74. Chatterjee, A.; Eliasson, S. H. H.; Jensen, V. R. *Catal. Sci. Technol.* **2018**, *8*, 1487.
75. Ortuño, M. A.; López, N. *ACS Catal.* **2018**, *8*, 6138.
76. Studt, F. *Front. Catal.* **2021**, 1:658965.

77. Hansch, C. *Acc. Chem. Res.* **1969**, *8*, 232-239
78. Jover, J.; Fey, N. *Chem. Asian J.* **2014**, *9*, 1714-1723.
79. Zahrt, A. F.; Athavale, S. V.; Denmark, S. E. *Chem. Rev.* **2020**, *120*, 1620-1689.
80. Nørskov, J. K.; Abild-Pedersena, F.; Studta, F.; Bligaard, T. *PNAS*, **2011**, *108*, 937–943.
81. Le, T.; Epa, V. C.; Burden, F. R.; Winkler, D. A. *Chem. Rev.* **2012**, *112*, 2889–2919.
82. a) Li, H.; Zhang, Z.; Liu, Z. *Catalysts* **2017**, *7*, 306. b) Kitchin, J. R. *Nat. Chem.* **2018**, *1*, 230–232. c) Grajciar, L.; Heard, C. J.; Bondarenko, A. A.; Polynski, M. V.; Meeprasert, J.; Pidko, E. A.; Nachtigall, P. *Chem. Soc. Rev.*, **2018**, *47*, 8307. d) Medford, A. J.; Kunz, M. R.; Ewing, S. M.; Borders, T.; Fushimi, R. *ACS Catal.* **2018**, *8*, 7403−7429. e) Goldsmith, B. R.; Esterhuizen, J.; Bartel, C. J.; Sutton, C.; Liu, J.-X. *AIChE J.* **2018**, *64*, 2311−2323. f) Li, Z.; Wang, S.; Xin, H. *Nat. Catal.* **2018**, *1*, 641−642. g) Takahashi, K.; Takahashi, L.; Miyazato, I.; Fujima, J.; Tanaka, Y.; Uno, T.; Satoh, H.; Ohno, K.; Nishida, M.; Hirai, K.; Ohyama, J.; Nguyen, T. N.; Nishimura, S.; Taniike, T. *ChemCatChem* **2019**, *11*, 1146−1152. h) Freeze, J. G.; Kelly, H. R.; Batista, V. S. *Chem. Rev.* **2019**, *119*, 6595−6612. i) Bruix, A.; Margraf, J. T.; Andersen, M.; Reuter, K. *Nat. Catal.* **2019**, *2*, 659–670. j) Gu, G. H.; Noh, J.; Kim, I; Jung, Y. *J. Mater. Chem. A* **2019**, *7*, 17096. k) Lamoureux, P. S.; Winther, K. T.; Garrido-Torres, J. A.; Streibel, V.; Zhao, M.; Bajdich, M.; Abild-Pedersen, F.; Bligaard, T. *ChemCatChem* **2019**, *11*, 3581–3601. l) Zhao, Z. J.; Liu, S.; Zha, S.; Cheng, D.; Studt, F.; Henkelman, G. Gong, J. *Nat. Rev. Mat.* **2019**, *4*, 792–804. m) Zhou, T.; Song, Z.; Sundmacher, K. *Engineering*, **2019**, *5*, 1017–1026. n) Chen, C.; Zuo, Y.; Ye, W.; Li, X.; Deng, Z.; Ong, S. P. *Adv. Energy Mater.* **2020**, *10*, 1903242. o) Gu, G. H.; Choi, C.; Lee, Y.; Situmorang, A. B.; Noh, J.; Kim, Y.-H.; Jung, Y. *Adv. Mater.* **2020**, 1907865. p) Yang, W.; Fidelis, T. T.; W.-H. *ACS Omega* **2020**, *5*, 83−88. q) Toyao, T.; Maeno, Z.; Takakusagi, S.; Kamachi, T.; Takigawa, I.; Shimizu, K.-I. *ACS Catal.* **2020**, *10*, 2260−2297.
83. Tropsha, A. *Mol. Inf.* **2010**, *29*, 476 – 488.
84. Bo, C.; Maseras, F.; López, N. *Nat. Catal.* **2018**, *1*, 809-810.
85. Hummelshøj, J. S.; Abild-Pedersen, F.; Studt, F.; Bligaard, T.; Nørskov, J. K. *Angew. Chem., Int. Ed.* **2012**, *51*, 272−274.
86. Winther, K. T.; Hoffmann, M. J.; Boes, J. R.; Mamun, O.; Bajdich, M.; Bligaard, T. *Sci. Data* **2019**, *6*, 75.
87. www.iochem-bd.org
88. Álvarez-Moreno, M.; de Graaf, C.; López, N.; Maseras, F.; Poblet, J. M.; Bo, C. *J. Chem. Inf. Model.* **2015**, *55*, 1, 95-103.
89. Calle-Vallejo, F.; Martinez, J. I.; Garcia-Lastra, J. M.; Sautet, P.; Loffreda, D. *Angew. Chem., Int. Ed.* **2014**, *53*, 8316−8319.
90. Calle-Vallejo, F.; Tymoczko, J.; Colic, V.; Vu, Q. H.; Pohl, M. D.; Morgenstern, K.; Loffreda, D.; Sautet, P.; Schuhmann, W.; Bandarenka, A. S. *Science* **2015**, *350*, 185−189.

91. Calle-Vallejo, F.; Bandarenka, A. S. *ChemSusChem*, **2018**, *11*, 1824 – 1828.
92. Rossi, K.; Asara, G. G.; Baletto, F. *Phys. Chem. Chem. Phys.* **2019**, *21*, 4888.
93. Ma, X.; Xin, H. *Phys. Rev. Lett.* **2017**, 118, 036101.
94. Wu, D., Dong, C., Zhan, H.; Du, X. W. *J. Phys. Chem. Lett.* **2018**, *9,* 3387–3391.
95. Fung, V.; Tao, F. F.; Jiang, D. E. *J. Phys. Chem. Lett.* **2017**, *8*, 2206–2211.
96. Nørskov, J. K.; Bligaard, T.; Hvolbæk, B.; Abild-Pedersen, F.; Chorkendorff, I.; Christensend, C. H. *Chem. Soc. Rev.* **2008**, *37*, 2163–2171.
97. Hammer, B.; Morikawa, Y.; Norskov, J. K. *Phys. Rev. Lett.* **1996**, *76*, 2141−2144.
98. Jia, C.; Wang, X.; Zhong, W.; Wang, Z.; Prezhdo, O. V.; Luo, Y.; Jiang, J. *ACS Appl. Mater. Interfaces* **2019**, *11*, 9629−9640.
99. Dickens, C. F.; Montoya, J. H.; Kulkarni, A. R.; Bajdich, M.; Nørskov, J. K. *Surf. Sci.* **2019**, *681*, 122–129.
100. Studt, F.; Abild-Pedersen, F.; Bligaard, T.; Sørensen, R. Z.; Christensen, C. H.; Nørskov, J. K. *Science* **2008**, 320, 1320–1322.
101. Studt, F.; Sharafutdinov, I.; Abild-Pedersen, F.; Elkjær, C. F.; Hummelshøj, J. S.; Dahl, S.; Chorkendorff, I.; Nørskov, J. K. *Nat. Chem.* **2014**, *6*, 320–324.
102. Xin, H.; Vojvodic, A.; Voss, J., Nørskov, J. K.; Abild-Pedersen, F. *Phys. Rev. B* **2014**, *89*, 15114.
103. Rossi, K.; Cumby, J. *Int J Quantum Chem*. **2020**, *120*, e26151.
104. Butler, K. T.; Davies, D. W.; Cartwright, H.; Isayev, O.; Walsh, A. *Nature* **2018**, *559*, 547−555.
105. https://www.aspentech.com/en/products/msc/aspen-unscrambler
106. Fraser, C.; McDonald, R. P. *Multivar. Behav. Res.* **1988**, *23*, 263-265.
107. https://scikit-learn.org/stable/index.html
108. https://www.tensorflow.org/
109. https://pytorch.org/
110. https://chainer.org/
111. Van Santen, R. A.; Sengar, A.; Steur, E. *Faraday Discuss.* **2018**, *208*, 35.
112. Van Duin, A. C. T; Dasgupta, S.; Lorant, F.; Goddard, III W. A. *J. Phys. Chem. A* **2001**, *105*, 9396-9409.
113. Senftle, P. T.; Hong, S.; Islam, M. M.; Kylasa, S. B.; Zheng, Y.; Shin, Y. K.; Junkermeier, C.; Engel-Herbert, R.; Janik, M. J.; Aktulga, H. M.; Verstraelen, T.; Grama, A.; van Duin, A. C. T. *Npj Computational Materials* **2016**, *2*, 15011.
114. Shin, Y. K.; Ashraf, C. M.; van Duin A. C. T. *Development and Applications of the ReaxFF Reactive Force Field for Biological Systems.* vol 284. Springer, Cham. 2021.
115. Feng, M.; Jiang, X. Z.; Mao, Q.; Luo, K. H.; Hellier, P. *Fuel* **2019**, *254*, 115643.
116. Wimalasiri, P. N.; Nguyen, N. P.; Senanayake, H. S.; Laird, B. B.; Thompson, W. H. *J. Phys. Chem. C* **2021**, *125*, 23418-23434.

117. Goddard III, W. A.; van Duin, A. C. T.; Chenoweth, K.; Cheng, M.-J.; Pudar, S.; Oxgaard, J.; Merinov, B.; Jang, Y. H.; Persson, P. *Top. Catal.* **2006**, *38*, 93.
118. Chenoweth, K.; van Duin, A. C. T.; Persson, P.; Cheng, M.-J.; Oxgaard, J.; Goddard III, W. A. *J. Phys. Chem. C* **2008**, *112*, 14645-14654.
119. Wei, M.; Wu, S.; Mao, Q.; Wang, Y.; Guo, G.; Zhang, D. *Fuel* **2020**, *275*, 117989.
120. Mao, Q.; van Duin, A. C. T.; Luo, K. H. *Proc. Combust. Inst.* **2017**, *36*, 4339-4346.
121. Hohenberg, P.; Kohn, W. *Phys. Rev.* **1964**, *136*, 864-871.
122. Kohn, W.; Sham, L. J. *Phys. Rev.* **1965**, *140*, 1133-1138.
123. a) Jensen, F. *Introduction to Computational Chemistry*, John Wiley & Sons Ltd, Chichester, West Sussex, England, 2nd Edition, 2007. b) Andrés, J.; Bertran, J. *Theoretical and Computational Chemistry: Foundations Methods and Techniques*, Publicacions Universitat Jaume I, Castelló de la Plana, 2007. c) Lewars, E. G. *Computational Chemistry. Introduction to the Theory and Applications of Molecular and Quantum Mechanics*, Springer, Peterborough, Canada, 2007.
124. Becke, A. D. *Phys. Rev. A* **1988**, *38*, 3098.
125. Lee, C.; Yang, W.; Parr, R. G. *Phys. Rev. B* **1988**, *37*, 785.
126. Perdew, J. P.; Burke, K.; Ernzerhof, M. *Phys. Rev. Lett.* **1996**, *77*, 3865.
127. Tao, J.; perdew, J. P.; Staroverov, V. N.; Scuseria, G. E. *Phys. Rev. Lett.* **2003**, *91*, 146401.
128. Zhao, Y.; Truhlar, D. G. *J. Chem. Phys.* **2006**, *125*, 194101.
129. Zhao, Y.; Truhlar, D. G. *Theor. Chem. Account.* **2008**, *120*, 215-241.
130. Becke, A. D. *J. Chem. Phys.* **1993**, *98*, 5648.
131. Adamo, C.; Barone, V. *J. Chem. Phys.* **1999**, *110*, 6158.
132. Marsman, M.; Paier, J.; Stroppa, A.; Kresse, G. *J. Phys.: Condens. Matter* **2008**, *20*, 064201.
133. Curnan, M. T.; Kitchin, J. R. *J. Phys. Chem. C* **2015**, *119*, 21060-21071.
134. Álvarez, M.; Molina, F.; Fructos, M. R.; Urbano, J.; Álvarez, E.; Sodupe, M.; Lledós, A.; Pérez, P. J. *Dalton Trans.* **2020**, *49*, 14647-14655.
135. Janthon, P.; Luo, S.; Kozlov, S. M.; Viñes, F.; Limtrakul, J.; Truhlar, D. G.; Illas, F. *J. Chem. Theory Comput.* **2014**, *10*, 3832-3839.
136. Rego, C. R. C.; Oliveira, L. N.; Tereshchuk, P.; Da Silva, J. L. F. *J. Phys.: Condens. Matter* **2015**, *27*, 415502.
137. Davis, J. B. A.; Baletto, F.; Johnston, R. L. *J. Phys. Chem. A* **2015**, *119*, 9703-9709.
138. Bursch, M.; Caldeweyher, E.; Hansen, A.; Neugebauer, H.; Ehlert, S.; Grimme, S. *Acc. Chem. Res.* **2019**, *52*, 258-266.
139. Grimme, S.; Antony, J.; Ehrlich, S.; Krieg, H. *J. Chem. Phys.* **2010**, *132*, 154104.
140. Becke, A. D.; Johnson, E. R. *J. Chem. Phys.* **2006**, *124*, 174104.
141. Grimme, S.; Ehrlich, S.; Goerigk, L. *J. Comput. Chem.* **2011**, *32*, 1456-1465.

142. Pisani, C.; Dovesi, R.; Roetti, C. *Hartree-Fock Ab Initio Treatment of Crystalline Systems* Springer-Verlag, Berlin, Heidelberg 1988.
143. Dovesi, R.; Erba, A.; Orlando, R.; Zicovich-Wilson, C. M.; Civalleri, B.; Maschio, L.; Rérat, M.; Casassa, S.; Baima, J.; Salustro, S.; Kirtman, B. *WIREs Comput. Mol. Sci.* **2018**, *8*, e1360.
144. Bloch, F. *Z. Phys.* **1928**, *52*, 555.
145. Dronskowski, R. *Computational Chemistry of Solid State Materials*, WILEY-VCH Verlag GmbH & Co. KGaA, Weinheim, Germany, 1st Edition, 2005.
146. Monkhorst, H. J.; Pack, J. D. *Phys. Rev. B* **1976**, *13*, 5188.
147. Evarestov, R. A.; Smirnov, V. P. *Phys. Stat. Sol.* **1983**, *119*, 9.
148. Chadi, D. J.; Cohen, M. L. *Phys Rev. B* **1973**, *8*, 5747.
149. Cunningham, S. L. *Phys. Rev. B* **1974**, *10*, 4988.
150. Klamt, A. *WIREs Comput. Mol. Sci.* **2018**, *8*, e1338.
151. Cramer, C. J.; Truhlar, D. G. *Acc. Chem. Res.* **2008**, *41*, 760−768.
152. Marenich, A. V.; Cramer, C. J.; Truhlar, D. G. *J. Phys. Chem. B* **2009**, *113*, 6378-6396.
153. a) Tomasi, J.; Persico, M. *Chem. Rev.* **1994**, *94*, 2027. b) Miertus, S.; Scrocco, E.; Tomasi, *J. Chem. Phys.* **1981**, *55*, 117. c) Cammi, R.; Tomasi, J. J. Comput. Chem. 1995, 16, 1449. d) Mennucci, B. *WIREs Comput. Mol. Sci.* **2012**, *2*, 386−404
154. Tomasi, J.; Mennucci, B.; Cammi, R. *Chem. Rev.* **2005**, *105*, 2999-3093.
155. Eyring, H. *J. Chem. Phys.* **1935**, *3*, 107-115.
156. Wachsstock, D. 2007. Tenua: The kinetics Simulator for java. http://bililite.com/tenua/
157. Hoops, S.; Sahle, S.; Gauges, R.; Lee, C.; Pahle, J.; Simus, N.; Singhal, M.; Xu, L.; Mendes, P.; Kummer, U. *Bioinformatics* **2006**, *22*, 3067-3074.
158. Braun, W.; Herron, J. T.; Kahaner, D. K. Acuchem: *Int. J. Chem. Kinet.* **1988**, *20*, 51–62.
159. García-López, D.; Civit, M. G.; Vogels, C. M.; Ricart, J. M.; Westcott, S. A.; Fernández, E.; Carbó, J. J. *Catal. Sci. Technol.* **2018**, *8*, 3617-3628.
160. Iftimie, R.; Minary, P.; Tuckerman, M. E. *Proc. Natl. Acad. Sci. USA* **2005**, *102*, 6654-6659.
161. Marx, D.; Hutter, J. *Ab Initio Molecular Dynamics: Basic Theory and Advanced Methods*, Cambridge University Press, New York, United States of America, 1st Edition, 2009.
162. Car, R.; Parrinello, M. *Phys. Rev. Lett.* **1985**, *55*, 2471-2474.
163. Rappe, A. K.; Casewit, C. J.; Colwell, K. S.; Goddard III, W. A.; Skiff, W. M. *J. Am. Chem. Soc.* **1992**, *114*, 10024-10035.
164. Mackerell, A. D.; Bashford, D.; Bellott, M.; Dunbrack, R. L.; Evanseck, J. D.; Field, M. J.; Fischer, S.; Gao, J.; Guo, H.; Ha, S.; Joseph-McCarthy, D.; Kuchnir, L.; Kuczera, K.; Lau, F. T. K.; Mattos, C.; Michnick, S.; Ngo, T.; Nguyen, D. T.; Prodhom, B.; Reiher, W. E.; Roux, B.; Schlenkrich, M.; Smith, J. C.; Stote, R.; Straub, J.; Watanabe, M.; Wiórkiewicz-Kuczera, J.; Yin, D.; Karplus, M. *J. Phys. Chem. B* **1998**, *102*, 3586-3616.

165. Cornell, W. D.; Cieplak, P.; Bayly, C. I.; Gould, I. R.; Merz, K. M.; Ferguson, D. M.; Spellmeyer, D. C.; Fox, T.; Caldwell, J. W.; Kollman, P. A. *J. Am. Chem. Soc.* **1995**, *117*, 5179-5197.

166. Oostenbrink, C.; Villa, A.; Mark, A. E.; van Gunsteren, W. F. *J. Comput. Chem.* **2004**, *25*, 1656-1676.

167. González, M. A. JDN 18 – Neutrons et Simulations 2011, 12, 169-200.

168. a) LoDis manual: https://github.com/kcl-tscm/LoDiS. b) Baletto, F.; Ferrando, R.; Fortunelli, A.; Montalenti, F.; Mottet, C. *J. Chem. Phys.* **2002**, *116*, 3856. c) Baletto, F.; Mottet, C.; Ferrando, R. *Phys. Rev. Lett.* **2000**, *65*, 245411. d) Baletto, F. *J. Phys.: Condens. Matter* **2019**, *31*, 113001.

169. Rosato, V.; Guillope, M.; Legrand, B. *Philosophical Magazine A* **1989**, *59:2*, 321-336.

170. Stuart, S. J.; Tutein, A. B.; Harrison, J. A. *J. Chem. Phys.* **2000**, *112*, 6472.

171. a) Liang, T *et al. Annu. Rev. Mater. Sci.* **2013**, *43*, 109-129. b) Shin, Y. K. *et al. MRS Rev.* **2012**, *37*, 504-512. c) Fonseca, A. F. *et al. Phys. Rev. B* **2011**, *84*, 075460. d) Shan, T. R. *et al. Phys. Rev. B* **2010**, *82*, 235302. e) Phillpot, S. R., Sinnott, S. B. *Science*, **2009**, *325*, 1634-1635.

172. a) van Duin, A. C. T.; Dasgupta, S. Lorant, F. Goddard, III W. A. *J. Phys. Chem. A* **2001**, *105*, 9396-9409. b) Chenoweth, K.; van Duin, A. C. T.; Goddard, III W. A. *J. Phys. Chem. A* **2008**, *112*, 1040-1053. c) Russo, M. F.; van Duin, A. C. T. *Nucl. Instrum. Methods Phys. Res. B* **2011**, *269*, 1549-1554. d) Senftle, T. P.; Hong, S.; Islam, M. M.; Kylasa, S. B; Zheng, Y.; Shin, Y. K.; Junkermeier, C.; Engel-Herbert, R.; Janik, M. J; Aktulga, H. M.; Verstraelen, T.; Grama, A.; van Duin, A. C. T. *Npj Comput. Mater.* **2016**, *2*, 15011. E) Leven, I.; Hao, H.; Tan, S.; Guan, X.; Penrod, K. A.; Akbarian, D.; Evangelisti, B.; Hossain, M. J.; Islam, M. M.; Koski, J. P.; Moore, S.; Aktulga, H. M.; van Duin, A. C. T.; Head-Gordon, T. *J. Chem. Theory Comput.* **2021**, *17*, 3237-3251.

173. Abell, G. C. *Phys. Rev. B* **1985**, *31*, 6148-6196.

174. Tersoff, J. *Phys. Rev. B* **1988**, *37*, 6991-7000.

175. Tersoff, J. *Phys. Rev. Lett.* **1988**, *61*, 2879-2882.

176. Brenner, D. W. *Phys. Rev. B* **1990**, *42*, 9458-9471.

177. a) Mortier, W. J.; Ghosh, S. K.; Shankar, S. *J. Am. Chem. Soc.* **1986**, *108*, 4315. b) Janssens, G. O. A.; Baekelandt, B. G.; Toufar, H.; Mortier, W. J.; Schoonheydt, R. A. *J. Phys. Chem.* **1995**, *99*, 3251. c) Rappe, A. K.; Goddard, III W. A. *J. Phys. Chem.* **1991**, *95*, 3358.

178. Wales, D. J.; Doye, J. P. K. *J. Phys. Chem. A* **1997**, *101*, 5111-5116.

UNIVERSITAT ROVIRA I VIRGILI
COMPUTATIONAL MODELING TO EXPLORE SOLVENT AND DYNAMIC EFFECTS IN MOLECULAR, NANO AND SOLID CATALYSIS
Antoni Salom Català

Goals of this Thesis

UNIVERSITAT ROVIRA I VIRGILI
COMPUTATIONAL MODELING TO EXPLORE SOLVENT AND DYNAMIC EFFECTS IN MOLECULAR, NANO AND SOLID CATALYSIS
Antoni Salom Català

Goals of this Thesis

Herein we summarize the main goals of this thesis separated by chapters. In general, all of them are devoted to give an explanation to experimental observations of different catalytic processes and to use novel computational tools to provide a guidance to improve the catalysts and the reaction conditions. Chapter 2 concerns the computational rationalization of the regioselectivity observed experimentally in the Pd-catalyzed isoprene telomerization reaction. Chapter 3 deals with the computational study of morphology, energy and electronic structure of several Rh nanoparticles stabilized by P-based capping ligands. Chapter 4 tries to explain the features that govern the selective H/D exchange of different phosphine ligands catalyzed by Rh and Ru nanoparticles. Finally, Chapter 5 is dedicated to obtain a machine learning force field parameterization (ReaxFF) to study the propane dehydrogenation reaction (PDH) catalyzed by Pt.

Regioselective Telomerization of Isoprene: Solvent and Ligand Control (Chapter 2):

Based on the experimental work of Castillón *et al.* on the isoprene telomerization reaction catalyzed by Pd organometallic complexes, we set out to explain the effect of the solvent and the ligands as factors governing the regioselectivity of the reaction. To carry out these investigations we used Density Funtional Theory (DFT) calculations and microkinetic analysis. The study includes the following specific objectives:

- To elucidate the features of the solvent that control the selectivity of the products obtained, and to discover their influence on the reaction mechanism.
- To give an explanation of the control of the ligands on the observed selectivity.
- To provide Pd/Ligand/Solvent systems suitable to obtain selectively one of the four linear telomers.

Computational Modelling of Rh Nanoparticles. Phosphine Adsorption, Electronic Structure and Solvent Effects (Chapter 3):

Nanoparticles have been used as versatile catalysts in several reactions due to their robustness, selectivity and activity. However, an important ingredient of

nanocatalysts are the capping ligands used to prevent sintering, as they can modulate the catalytic properties of the nanoparticles. Based on the nanocatalysts used by Castillón and Godard groups to hydrogenate simple organic compounds, we focused a computational study to rationalize at atomistic level the structural, energetic and electronic characteristics of Rh nanoparticles stabilized by phosphine ligands in solution. The main specific goals of this chapter can be summarized as follows:

- To investigate the morphology and electronic structure of different sized naked Rh nanoparticles by means of the Basin Hopping Parallel Excitable Walkers (BH-PEW) optimization algorithm with classical potentials and DFT calculations.
- To characterize the interaction between bare Rh_{55} nanoparticles and the model PPh_3 molecule as a capping ligand.
- To analyze the nanoparticle size effect on the adsorption of PPh_3.
- To develop a regression model to predict phosphine adsorption energies using the Generalized Coordination Number (GCN) and d-band center as local and global descriptors, respectively.
- To study the influence of PPh_3 coverage on the adsorption energy and the electronic structure of the Rh_{55} nanoparticle.
- To characterize the interaction of a solvent (THF) with Rh_{55} nanoparticle, and its effect on the PPh_3 adsorption.
- To explore the adsorption mode and energy of different P-based ligands, such as P(o-tolyl)$_3$, $P(OPh)_3$ and $OPPh_3$ on Rh_{55} nanoparticle.

Origin of Selective Deuteration of Phosphorous Ligands Catalyzed by Rh and Ru Nanoparticles (Chapter 4):

Castillón and Godard groups conducted selective deuteration experiments of different P-based ligands using Rh and Ru nanoparticles stabilized by Polyvinylpyrrolidone (PVP) and N-heterocyclic carbenes (NHC). Taking those experiments as reference, we aimed to elucidate the origin of the observed selectivity using DFT calculations. Specifically, our efforts were aimed to:

- Propose a plausible mechanism to explain the selective *ortho* deuteration of PPh_3.
- Suggest a suitable mechanism to shed light to the unexpected *meta* and methyl selective deuterations of P(*o*-tolyl)$_3$ ligand.
- Elucidate the different aspects of the nanoparticles and the ligand structure that govern the selective deuteration.
-

Development of ReaxFF Force Field for Propane Dehydrogenation Reaction on Pt Catalysts (Chapter 5):

Propene is a highly valuable building block to obtain several important chemicals. Traditionally, propene has been produced by naphtha cracking methods, with the inherent environmental issues. As a greener alternative, propane dehydrogenation (PDH) catalyzed by Pt-based catalysts is receiving much attention. However, this approach has its own problems, such as low selectivity towards propene and rapid deactivation of the catalyst due to coke formation. To overcome these issues, a good understanding at atomistic level of the whole reaction and conditions is needed. One suitable method that has grown over the last twenty years to study catalytic processes in a realistic environment at low computational cost is force field approach that includes reactive events, as ReaxFF. Within this context, we wanted to:

- Analyze the cost for the development of a ReaxFF force field.
- Develop a suitable ReaxFF force field to study PDH catalyzed by Pt catalysts.
- Study PDH catalyzed by different Pt surfaces, Pt(111) and Pt(211), and the Pt_{55} nanoparticle using the new developed ReaxFF force field.
- Evaluate the performance of the ReaxFF method to simulate large catalytic systems.

UNIVERSITAT ROVIRA I VIRGILI
COMPUTATIONAL MODELING TO EXPLORE SOLVENT AND DYNAMIC EFFECTS IN MOLECULAR, NANO AND SOLID CATALYSIS
Antoni Salom Català

Chapter 2:
Regioselective Telomerization of Isoprene: Solvent and Ligand Control

UNIVERSITAT ROVIRA I VIRGILI
COMPUTATIONAL MODELING TO EXPLORE SOLVENT AND DYNAMIC EFFECTS IN MOLECULAR, NANO AND SOLID CATALYSIS
Antoni Salom Català

Chapter 2
Regioselective Telomerization of Isoprene: Solvent and Ligand Control

*This chapter is devoted to computationally rationalize the regioselective control of the isoprene telomerization catalyzed by Pd-phosphine complexes that was observed in the experimental group of Prof. Castillón at URV. They studied a large set of phosphine-based ligands and different reactions conditions. Two factors had the major impact on the selectivity: the acidity of the solvent and the structure of the ligand. To understand the factors governing the selectivity, we selected two different phosphine ligands (PPh_3 and a sterically hindered monophosphine **P2**), three alcohol solvents with different acidity (TFE, tBuOH and MeOH), an aprotic solvent DMF, for which the effect of traces of water was analyzed, and the Et_2NH as nucleophile. The atomistic and kinetic simulations reveal that the solvent switches the selectivity-determining step as a function of pK_a from C−C oxidative coupling at low pK_a values (preference for telomer head-to-head) to protonation at high pK_a values (preference for telomer tail-to-tail). The selectivity toward tail-to-head telomer can be directed in moderately acidic solvents by selection of the appropriate ligand, which exerts steric control of the protonation step.*

2.1 Introduction

The telomerization of dienes, first disclosed by Smutny[1] and Takahashi[2] in 1967, consists of the dimerization of a diene catalyzed by a transition metal with subsequent addition of a nucleophile, such as an alcohol, an amine, an acid, and water, to form highly valuable intermediates.[3] Butadiene is the most simple and widely studied substrate, and its telomerization can afford three different products, with the linear telomer presenting the most interesting properties (Scheme 2.1).[3a] Butadiene telomerization[4,5,6] is today an industrial process key for 1-octene production.[6] The telomerization reaction can be catalyzed by several organometallic compounds based on Pd, Ni or Pt, and due to the variety of dienes and nucleophiles that can be used, numerous valuable products can be obtained.

Scheme 2.1 Pd-catalyzed butadiene telomerization and proposed mechanism.

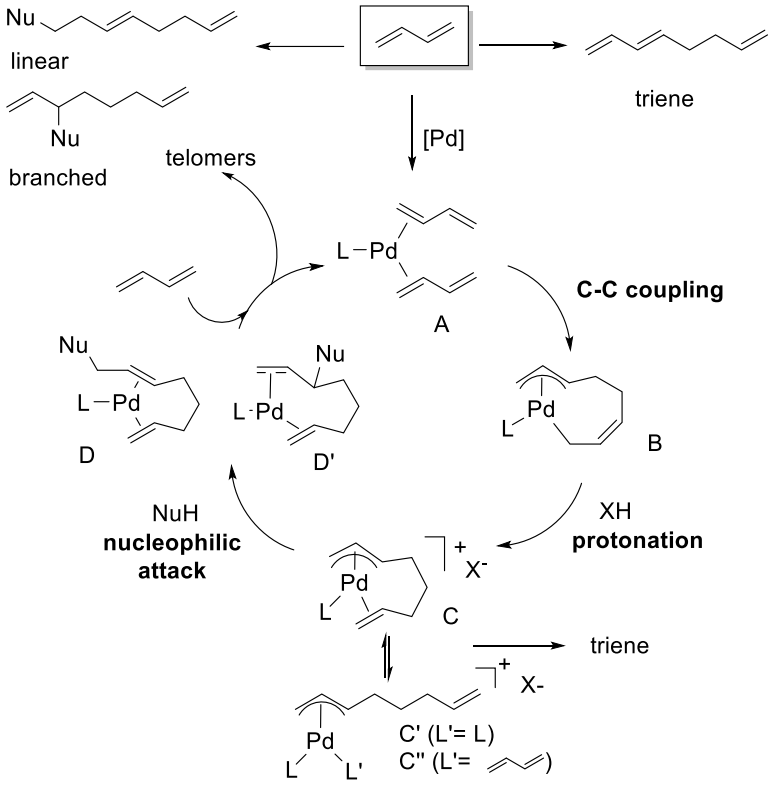

The mechanism of butadiene telomerization[7] involves four different steps (Scheme 2.1): (1) reduction of Pd^{2+} precursor to Pd^{0} and coordination of two butadienes (A), (2) oxidative butadiene coupling (B), (3) protonation at the C6-position (C), and (4) nucleophilic attack (D). Density Functional Theory (DFT) calculations[8,9] completed the mechanistic picture for butadiene telomerization with methanol and trimethylamine as a base and proposed that protonation is fast and Me_3NH^+ species acts as a proton source,[9] although the energy cost of its formation was not evaluated.

A part from 1,3-butadiene, there are other dienes suitable to undergo telomerization, resulting in appreciated products for industry, for instance, isoprene. Isoprene is a diene produced in very large scale and its demand worldwide has increased exponentially due to its value as a building block for important products such as, polyisoprene, styrene-isoprene styrene, isobutylene-isoprene rubber or special fine chemicals, e. g. linear telomers for flavor and fragrance industries.[10]

Nevertheless, isoprene telomerization has been infrequently used due to regioselectivity issues. For isoprene, the simplest example of a non-symmetric diene the telomerization process can yield up to 12 isomers (being the linear telomers (**1**-**4**), shown in Scheme 2.2, the most valuable isomers). Thus, isoprene telomerization represents a formidable challenge in terms of selectivity.

Scheme 2.2 The four linear telomers resulted for the telomerization of isoprene catalyzed by Pd complexes.

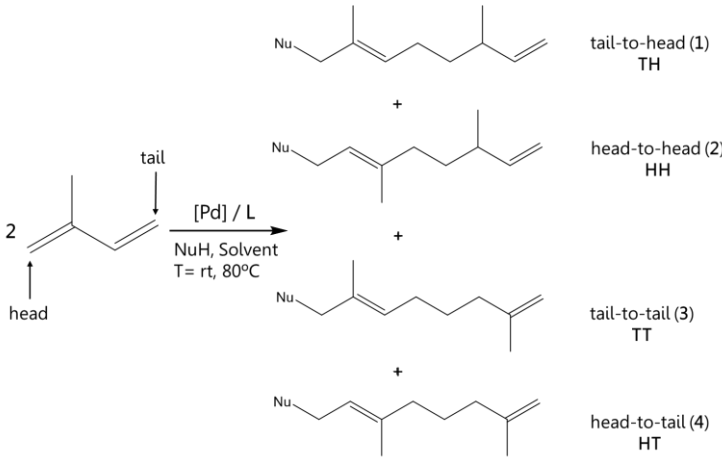

Most strategies to improve the performance and efficiency of catalytic telomerizations implied tuning the steric and electronic properties of the ligand. The most used ligands were those based on N-heterocyclic carbenes (NHCs) and phosphines.

Beller *et al.* reported the study of isoprene telomerization with different Pd-NHC catalysts.[11] They succeeded in performing the reaction with a moderate conversion (up to 69%) for different telomers respect dimer or trimer byproducts, while the selectivity reached up to 76% for telomer **2**. Recently, Asachenko *et al.* also investigated the telomerization of isoprene using a Pd catalyst with several NHC carbenes as ligand, and they improved significantly the conversion ratio (up to 100% with some of the systems investigated) but the selectivity towards one of the telomers was moderate (around 60% in the best cases).[12]

Regarding phosphine-based ligands, the main reported results are summarized in Table 2.1. Maddock and Finn reported excellent results towards telomer **2** (100% of conversion and 96.6% of selectivity) using $[Pd(\eta^3\text{-}C_3H_5)COD]BF_4$/P(2,4,6-tri-OMe-Ph)$_3$ system.[13] In addition, Leca and Réau, studied the reaction using P,N ligands and they obtained excellent selectivities for telomeres **1** and **3** with two different catalytic systems (Table 2.1), but with very low yield.[14] Furthermore, high

selectivity towards telomer **3** (up to 81%) employing $Pd(acac)_2/P(OBu)_3$ as catalytic system was also reported by Röper *et al.*[15] The head-to-tail telomer (**4**), not included in Table 2.1, was always obtained with low selectivity. These results illustrate the difficulty of obtaining both high yield and high selectivity in isoprene telomerization, and in general in non-symmetric dienes telomerization, probably because factors controlling the selectivity of the reaction have not been stablished.

Computationally, the mechanism of isoprene telomerization, even of 1,3-butadiene, has been scarcely studied. In this chapter, the mechanism and the role of the solvent and the ligand controlling the regioselectivity of isoprene telomerization will be elucidated by means of DFT calculations and microkinetic simulations. In collaboration with the experimental group of Prof. Castillón (URV), we provide a complete mechanistic picture of this challenging reaction, in which three of the four most important linear telomers of isoprene were obtained, in high yields and selectivities.

Table 2.1 Main reported results in isoprene telomerization using Pd, phosphine ligands and amines as nucleophile.

Telomer	Ligand	Conditions	Yield Selectivity	Reference
tail-to-head (**1**)	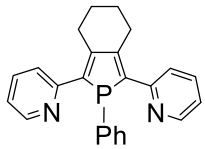 $[Pd(CH_3CN)_4]^{2+}2BF_4^-$	THF 40 ºC	35% y. 100% s.	14
head-to-head (**2**)	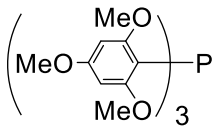 $[Pd(C_3H_5)COD]^+BF_4^-$	MeOH rt	100% c. 96.6% s.	13
tail-to-tail (**3**)	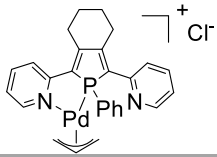	THF 40 ºC	20% y. 92.5% s.	14
	$Pd(acac)_2$ $P(OBu)_3$	CH_3CN 90 ºC	92% y. 81 % s.	15

2.2 Experimental Background

Castillón and co-workers have studied experimentally the telomerization of isoprene with Et_2NH catalyzed by Pd-phosphine complexes, focusing on the influence of different parameters on the selectivity. Scheme 2.2 shows the four possible linear telomers obtained in the telomerization reaction.

Initially, the influence of the solvent was investigated by systematically varying their acidity from 2,2,2-trifluoroethanol (TFE) (pK_a = 12.4) to *tert*-butanol (*t*BuOH) (pK_a = 19.2), including methanol (MeOH) (pK_a = 15.3), ethanol (EtOH) (pK_a = 15.5), propanol (PrOH) (pK_a = 16.1) and isopropanol (*i*PrOH) (pK_a = 17.1), as well as some aprotic solvents such as dimethylformamide (DMF), dimethylacetamide (DMA) or N-methyl-2-pyrrolidone. The reactions of isoprene with Et_2NH were performed using $Pd(OAc)_2/PPh_3$ (**P1**) and Pd/L (1:1.5). The results are summarized in Table 2.2. Interestingly, it was observed a progressive shift of the selectivity from **1** + **2** to **3** + **4** when the acidity of the solvent was increased from TFE to *t*BuOH, and more specifically a shift form telomer **2** (91%) to telomer **3** (80%). When the reaction was carried out in aprotic solvent such as DMF, telomer **3** with a 76% of selectivity and telomer **4** with 24% were obtained while telomers **1** and **2** were not detected.

Table 2.2 Solvent effect in the $Pd(OAc)_2$/**P1**-catalyzed telomerization of isoprene in the presence of Et_2NH.[a]

Solvent	Ratio 1/2/3/4	Ratio (1+2):(3+4)
TFE	9/**91**/0/0	100:0
MeOH	51/29/19/1	80:20
EtOH	39/8/27/26	47:53
PrOH	24/4/36/36	28:72
***i*PrOH**	13/3/80/15	16:84
***t*BuOH**	2/3/**80**/15	5:95
DMF	0/0/**76**/24	0:100

[a]Reactions conditions: [Pd] (0.05 mmol), PPh_3 (0.075 mmol), isoprene (10 mmol), Et_2NH (10 mmol), solvent (2 mL), rt, 24 h.

A second parameter analyzed was temperature. The results showed that the temperature mainly affected the conversion rate rather than the selectivity. On the one hand, when the reaction was carried out in TFE and heated at 50 ºC, the selectivity towards telomer **2** decreased, whereas performing the reaction at -10 ºC increases telomere 2 selectivity at the cost of lower yield. On the other hand,

when the solvent used was DMF and the reaction was heated at 80 ºC, the selectivity towards **3** was slightly improved and its yield was greatly increased.

The experimental group have also investigated the influence of some reaction parameters such as Pd precursor, Pd loading, Et_2NH/isoprene ratio and the structure of the amine. All these tests were carried out in TFE and in DMF. The main results can be summarized as follows: (1) in the absence of the ligands, telomers were not formed in any solvents (2) in TFE, all tested reactions conditions provided high selectivity to **2** (84-92%), (3) in DMF the selectivity notably changed from telomer **2** to **3**, and the use of bulky secondary amines decreased the yield while providing excellent selectivities and, (4) in anhydrous DMF, the reaction did not evolve.

To evaluate whether the selectivity towards telomere **1** (**TH**) and **4** (**HT**) may result from ligand control, 26 phosphine ligands were tested. They included structurally different ligands such as triphenyl phosphine (PPh_3) (**P1**), diphosphines, hemilabile P,N and P,O ligands, electron-poor phosphines and sterically hindered monophosphines. The reactions were conducted at room temperature and in a solvent with an intermediate pK_a, such as MeOH. In most cases, telomer **1** was preferably obtained, but with low yield or selectivity. However, when sterically hindered phosphines, such as **P2** (see Table 2.3), was used as ligand excellent yield and selectivity were obtained towards telomer **1** (85% yield and 92% selectivity with **P2**). For that reason, we hypothesized that selectivity to telomer **1** was governed by ligand control. Nevertheless, when the reaction was performed in TFE using the same ligand, up to 97% of telomer **2** was obtained.

The main conclusions drawn from experimental results are summarized in Table 2.3 and can be numbered as follows:

· Solvent control: i) acidic solvents, like TFE, lead to telomer **2** as main product, ii) telomer **3** was observed as major product when higher pK_a solvents were used, such as *t*BuOH or non-anhydrous DMF, iii) when solvent with an intermediate pK_a was used, a mixture of four telomers was obtain, with some preference towards telomer **1** and, iv) the reaction did not evolve in anhydrous DMF.

· Ligand control: sterically hindered phosphines strongly increases the selectivity and yield towards telomer **1**.

Table 2.3 Summary of the main experimental results and conditions to obtain three of the four main linear telomers **1**, **2** and **3** for the Pd/ligand-catalyzed telomerization of isoprene in the presence of Et_2NH.

Telomer	Ligand	Solvent	Yield Selectivity	Control
tail-to-head (**1**)	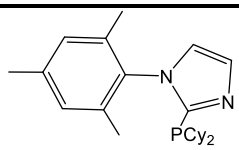 **(P2)**	MeOH[a]	85% y. 92% s.	Ligand Control
head-to-head (**2**)	PPh_3 **(P1)**	TFE[b]	86% y. 91% s.	Solvent Control
tail-to-tail (**3**)	PPh_3 **(P1)**	DMF[c]	63% y. 87% s.	Solvent Control

[a][Pd(η^3-C_3H_5)(COD)]BF_4 (0.05 mmol), ligand (0.075 mmol), isoprene (10 mmol), Et_2NH (9.6 mmol), MeOH (2 mL), rt, 24h. [b][Pd] (0.05 mmol), PPh_3 (0.075 mmol), isoprene (10 mmol), Et_2NH (10 mmol), solvent (2 mL), rt, 24 h. [c]At 80 ºC, Et_3N (20 mmol)

Castillón *et al.* detected intermediates complexes **I**(**HH**), **I**(**TT**) and **I**(**TH**) in operando ^{31}P NMR experiments using $Pd(OAc)_2$/PPh_3/isoprene in TFE and DMF (

Scheme **2.3**). To confirm the assignment of NMR signals, they performed the independent synthesis of these complexes.

Scheme **2.3** shows the procedure followed to obtain the intermediates, previous transformation of the desired telomers to the respective alcohols.

The complexes **I**(**TH**), **I**(**HH**) and **I**(**TT**) were characterized by single crystal X-ray crystallography showing a distorted square planar environment around the Pd center, and that the ligands coordinate in a chelate manner via a η^3-allylic fragment and η^2-olefin tail. The difference among them is the orientation and position of the methyl group. The **I**(**TT**) intermediate showed a *trans-cis-syn* configuration, while **I**(**HH**) intermediate presents a 2-*trans-anti* configuration.

Moreover, these three intermediates were treated with Et_2NH at room temperature, and the corresponding telomers **1**, **2** and **3** were obtained exclusively, indicating that the target telomers are formed via the intermediates shown in

Scheme **2.3** with retention of the regioselectivity. Intermediate **I**(**HH**) was dissolved in DMF, which favors the formation of **I**(**TT**), and heated at 60 ºC,

monitoring the evolution by ^{31}P NMR, but no new signal appeared, discarding the interconversion between intermediates.

Scheme 2.3 Synthesis of intermediate complexes **I(TH)**, **I(HH)** and **I(TT)** from the target telomers.

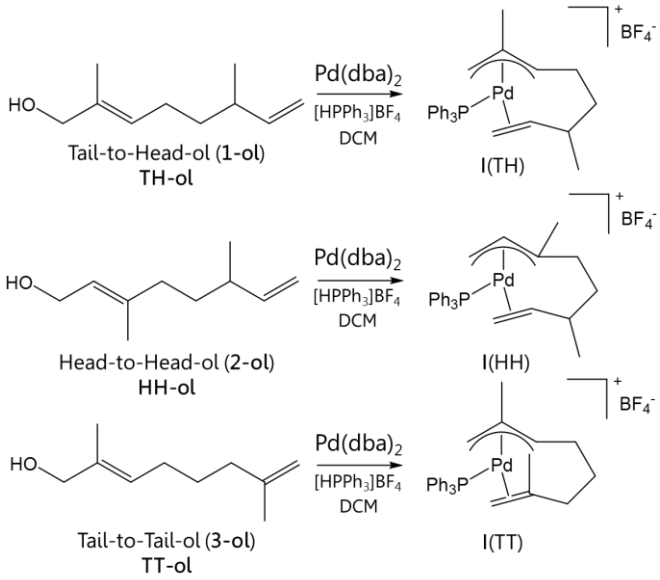

2.3 Results and Discussion

2.3.1 Computational Characterization of the Reaction Mechanism

To understand the factors controlling the selectivity in the palladium-catalyzed telomerization of isoprene with amines, we carried out a systematic DFT study under different solvent conditions and performed kinetic simulations. Based on previous mechanistic studies on butadiene telomerization,[7,8,9] and in the characterization of catalytic intermediates described above, we proposed for the isoprene telomerization with Et_2NH catalyzed by Pd/PPh_3 (**P1**), a catalytic cycle consisting of four main steps as illustrated by Figure 2.1: (1) isoprene coordination and oxidative coupling to form the allyl-alkyl intermediate $\mathbf{B_{P1}}$, (2) protonation of $\mathbf{B_{P1}}$ to yield the cationic allyl-alkene species $\mathbf{C_{P1}}$, (3) nucleophilic amine attack and reductive elimination giving Pd(0) complex $\mathbf{DH_{P1}}$, and (4) hydrogen abstraction to yield $\mathbf{D_{P1}}$. Figure 2.1 also shows the computed free-energy values for the four paths yielding the four telomers in TFE and *t*BuOH solvents.

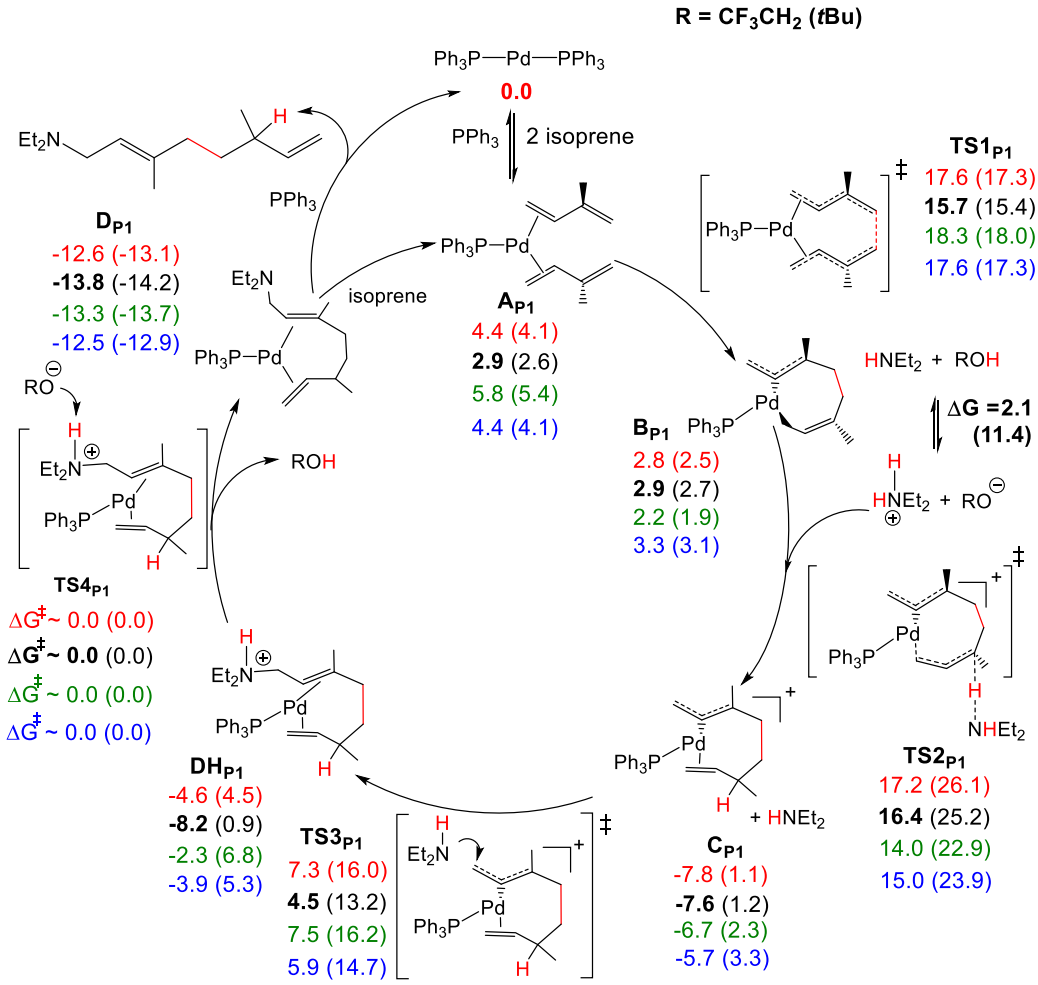

Figure 2.1 Computed catalytic cycle for the telomerization of isoprene with Et_2NH catalyzed by Pd/PPh_3 (**P1**) system, depicting path **HH**. Relative free energies for **TH** (1st row, red), **HH** (2nd row, black), **TT** (3rd row, green) and **HT** (4th row, blue) in TFE and *t*BuOH (shown in parenthesis). Energies are in kcal mol^{-1}.

Among the possible bi- and tricoordinated Pd(0) pre-catalyst species, the $Pd(PPh_3)_2$ complex turned out to be the most energetically favorable. Starting from $Pd(PPh_3)_2$, the reaction is initiated by replacing a phosphine ligand and coordinating two isoprene units to the Pd(0) center, yielding the $\mathbf{A_{P1}}$ structure. The carbon-carbon oxidative coupling in $\mathbf{A_{P1}}$ results in a η^3,η^3-diallyl-Pd(II) intermediate that rearranges to the more stable η^1,η^3-diallyl-Pd(II) complex $\mathbf{B_{P1}}$ via barrierless isomerization.[9] Palladium complexes with η^1,η^3-diallyl ligands have been experimentally isolated and characterized as a potential intermediate in Pd-catalyzed reactions with butadiene.[7a] Note that the η^1- and η^3-allyl moieties can

be formed from either the *tail* or the *head* sides of the original isoprene substrate, allowing us to distinguish between the **TH** and **HT** paths (Figure 2.2). In the **TH** and **TT** isomers of intermediate $\mathbf{B_{P1}}$, the configuration of the methyl groups is *syn*, whereas for the **HH** and **HT** isomers their configuration is *anti*. The relative position of the η^1 and η^3-allyl moieties in **TH** and **HT** isomers determines the protonation site and consequently, the formation of the final telomer, **1** or **4**.

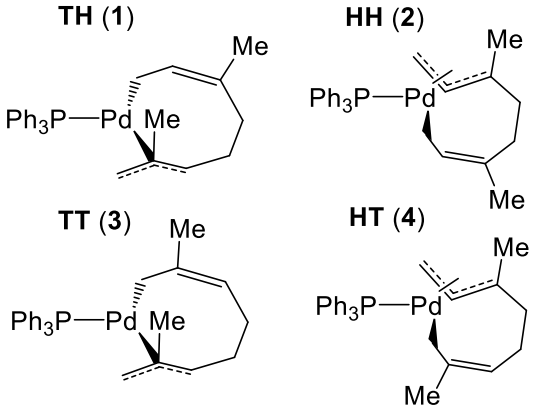

Figure 2.2 Schematic representation of the different possible isomers for intermediate $\mathbf{B_{P1}}$.

The protonation of the intermediate $\mathbf{B_{P1}}$ gives the observed cationic Pd(II) intermediate $\mathbf{C_{P1}}$. Direct protonation by the secondary amine Et_2NH via external attack or via previous coordination to palladium can be discarded because of the high energy associated with the processes (>40 kcal mol^{-1}). Alternatively, as previous DFT studies on butadiene isomerization suggests,[9] the $Et_2NH_2^+$ species, resulting from deprotonation of the acidic hydrogens of the solvents, can act as a proton source (Figure 2.1). We selected the two alcohol solvents with the most extreme acidity, TFE and *t*BuOH. The free energy cost associated with the deprotonation process (ΔG = 2.1 and 11.4 kcal mol^{-1}, respectively) was estimated using the experimental pK_a values (see Table 2.4 and Computational Details). Thus, the calculation of the overall free-energy barrier for protonation can be divided into three additive steps avoiding the calculation of charge separation processes: (1) the free energy cost for deprotonation derived from experimental pK_a values, (2) the entropic term associated with the formation of the hydrogen-bonded adduct between $Et_2NH_2^+$ and $\mathbf{B_{P1}}$ assuming that the hydrogen bonds are similar to those set with the solvent, and consequently, the associated enthalpy can be set to zero, and (3) the free energy cost for the hydrogen transfer from the hydrogen-bonded adduct. Note that the protonation barrier depends strongly on the acidity of the solvent; the higher the pK_a is, the larger the energy

barrier (1.4 kcal mol^{-1} per pK_a unit), resulting in the same increase for all isomeric paths. This reaction step is clearly exergonic, leading to the low-energy intermediate **C_{P1}**, in full agreement to analogous experimentally characterized complexes **I**(**HH**), **I**(**TT**) and **I**(**TH**).

Once the Pd complex is activated via protonation (**C_{P1}**), there is an external nucleophilic attack by Et_2NH at the π-allyl moiety to form the observed linear telomer with moderate free energy barriers. Then, the resulting quaternary amine in **DH_{P1}** is deprotonated by the conjugated base of the solvent (alkoxide) present in the medium to yield the product coordinated to the Pd(0) centre and regenerate the solvent (Figure 2.1). In this case, the analysis of deprotonation of **DH_{P1}** by non-solvated alkoxide molecule indicates a barrierless process. Importantly, from **C_{P1}** intermediates, the forward barriers to give the final product are significantly lower in energy than those in the reverse reaction to give **B_{P1}**, further supporting the irreversibility of protonation.

The overall catalytic cycle depicted in Figure 2.1 reveals two different kinetic scenarios (I and II) for acidic TFE and non-acidic *t*BuOH solvents. In TFE, the protonation step is fast and irreversible, making oxidative addition the selectivity-determining step (kinetic *scenario I*). Accordingly, assuming a Boltzmann distribution of the relative energies of transition states for oxidative addition, **$TS1_{P1}$**, the predicted isomer distribution is 4%, 91%, 1%, and 4% for telomers **1**, **2**, **3** and **4**, respectively, in excellent agreement with the experimental values (Table 2.2, entry 1). The kinetic modelling using the energy parameters of Figure 2.1 gives the same isomer distribution, indicating that the high concentration of solvent as reactant speeds up the protonation step, in a scenario in which the transition states (**$TS2_{P1}$**) have very close energy to those for oxidative coupling (**$TS1_{P1}$**).

In the case of low acidic *t*BuOH solvent, the free-energy cost associated with its deprotonation process rises, resulting in a higher-laying protonation transition states (**$TS2_{P1}$**). Therefore, we might have a different kinetic scenario, slow protonation and reversible oxidative coupling (kinetic *scenario II*), in which protonation is the selectivity-determining step. In this case, the calculated isomer distribution from the relative free-energies of **$TS2_{P1}$** (0.4%, 2%, 83% and 15% for telomers **1**, **2**, **3** and **4**, respectively), also fits very well with the experimental results (Table 2.2, entry 6). Another consequence of reducing solvent acidity is the increase in the overall free-energy barrier by ~6.5 kcal mol^{-1}, which agrees with the observed decrease in reaction rate from TFE to *t*BuOH.

2.3.2 Origin of the Solvent Control of Selectivity

The decrease in solvent acidity causes a continuous shift in the selectivity-determining step from oxidative addition to protonation, therefore, the features of both steps need to be analyzed separately to understand the origin of the selectivity. In the acidic solvent TFE (kinetic *scenario I*), the preferred path **HH** proceeds via coordination of two isoprenes to Pd through the *tail* moieties, adopting an alternate conformation that avoids steric repulsion between the two methyl groups (Figure 2.3) in the corresponding transition state $\mathbf{TS1_{P1}}$. The other possible coordination modes involve the isoprene interaction with Pd through one *tail* and one *head* moieties (**TH** and **HT** paths) and through both *head* moieties (**TT** path). The energy analysis of the different paths in oxidative addition (Figure 2.1 and Figure 2.3) indicates that bringing the substituted alkene fragment (*head*) to the coordination sphere of palladium has a negative impact on the stability of the $\mathbf{A_{P1}}$ and $\mathbf{TS1_{P1}}$ species because of the increase of steric hindrance.

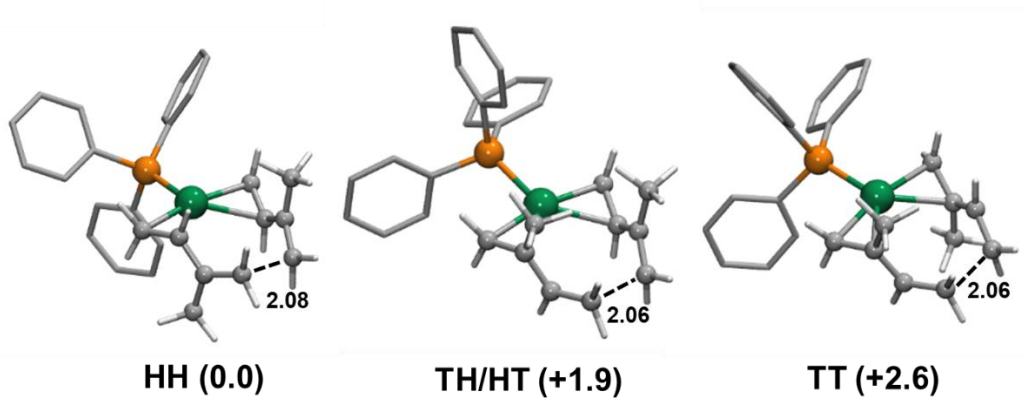

Figure 2.3 Molecular structures of the transition states for oxidative coupling of the two isoprene molecules.

For the low acidity solvent *t*BuOH (kinetic *scenario II*), we analyzed the intermediate $\mathbf{B_{P1}}$, which must be protonated at the alkene, γ-carbon of the η^1-σ-allyl moiety, to yield the intermediate $\mathbf{C_{P1}}$. Following Markovnikov's rule for the addition to non-symmetric alkenes, protonation is favored at the less substituted carbon, as displayed by the **TT** (**3**) and **HT** (**4**) paths, which show lower free-energy barriers than the **TH** (**1**) and **HH** (**2**) isomers (Figure 2.4). Accordingly, the analysis of charge distribution in $\mathbf{B_{P1}}$ demonstrates that Cγ is more negatively charged for isomers **TT** (**3**) and **HT** (**4**). Finally, we attribute the preference of the **TT** path over the **HT** path to the steric factors associated with the different substitution pattern of the η^3-π-allyl moiety, as manifested in their relative energies in the $\mathbf{B_{P1}}$

intermediate or in the **TS2$_{P1}$** transition state shown in Figure 2.5. Isomers **TH** and **HH** are clearly disfavored of about +6.6 and +7.2 kcal mol^{-1}, respectively. In turn, the path **HT** is also disfavored by +2.7 kcal mol^{-1}, leading to **TT** path preference, in agreement with the observed selectivity.

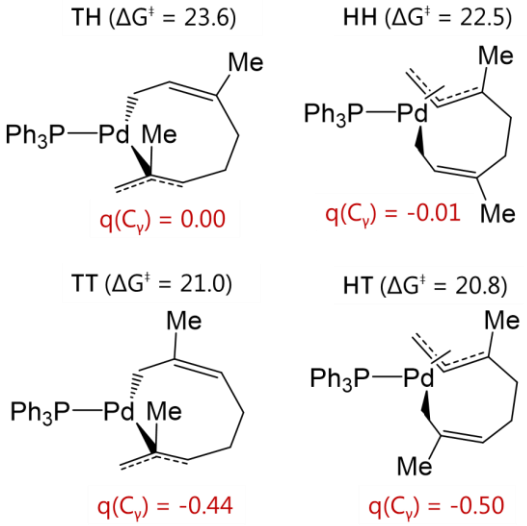

Figure 2.4 Electrostatic based atomic charges (a.u.) for the γ -carbon of η^1-σ -allyl moiety of the **B$_{P1}$** intermediate and free-energy barriers (ΔG‡) for the protonation step in *t*BuOH solvent in kcal mol^{-1}.

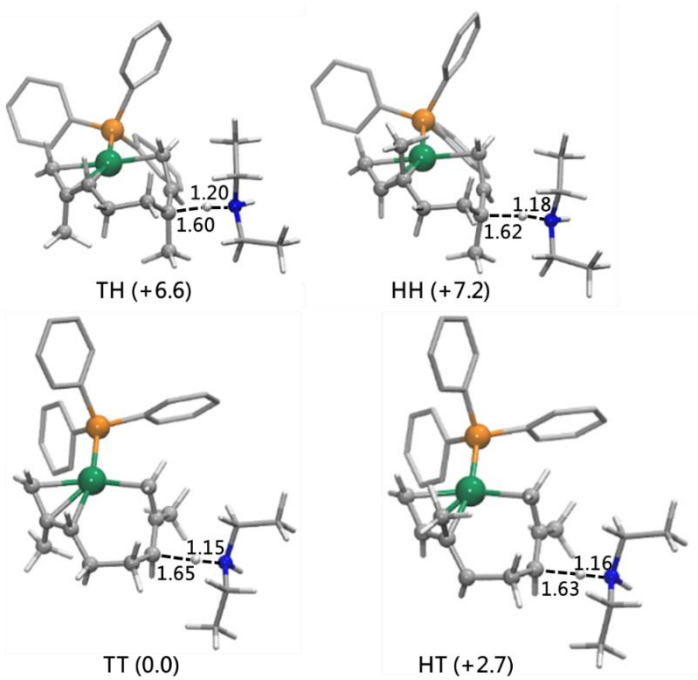

Figure 2.5 Molecular structures of transition states for the isomeric paths of protonation of $\mathbf{B_{P1}}$ by $Et_2H_2N^+$ ($\mathbf{TS2_{P1}}$) in *t*BuOH. Relative free energies in kcal mol^{-1} and distances in Å.

2.3.3 Microkinetic Models

Control of selectivity by the solvent is illustrated in Figure 2.6, which displays the evolution of isomer distribution as a function of the pK_a values derived from kinetic modelling. Note that pK_a values are very sensitive to the media in which they are determined. In this case, using the average values between the tabulated pK_a values in aqueous media and their values for autoprotolysis, we found an excellent fitting of the kinetic model to the experimental selectivity, particularly the percentage of evolution from **1+2** to **3+4** (see Figure 2.6 and Computational Details for detailed discussion on pK_a values). Simulations show that as the pK_a value increases, the percentage of isomer **2** decreases exponentially, while the percentage of isomer **3** increases exponentially.

Isomers **1** and **4** follow a bell-shaped distribution with maximums at intermediate pK_a values. At intermediate pK_a values, the selectivity is not governed by a single step, oxidative coupling ($\mathbf{TS1_{P1}}$) or protonation ($\mathbf{TS2_{P1}}$), but the slowest reaction step depends on the isomer, leading to a more complex kinetic scenario. Thus, our simulations for **3** and **4** are able to reproduce the shape and the position of the evolution curve but not the quantitative proportions of the two isomers.

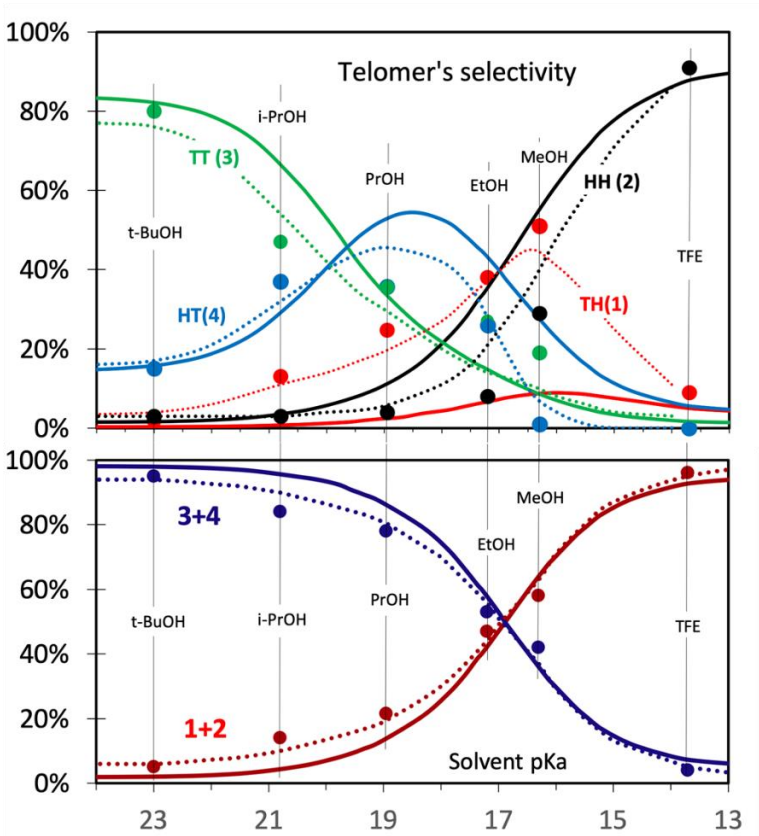

Figure 2.6 Microkinetic modelling of the percentage evolution for each isomer top, and of the percentage evolution for (**1** + **2**) and (**3** + **4**) bottom, as a function of solvent pK_a. Dots and dotted lines correspond to experimental values while solid lines are referred to simulated values.

Another striking observation is that aprotic solvents such as DMF provide **3** as the main isomer in low yield, even when acid-base equilibrium between the solvent and the amine is not possible. Here we propose that water impurities of the solvent catalyze the reaction by generating $Et_2NH_2^+$ species in a similar way as TFE and *t*BuOH.[16] Figure 2.7 plots the simulated variation in isomer distribution as a function of water content obtained by kinetic modelling using the energy parameters from the DFT calculations (Figure 2.8). At low water concentration (< 10^{-4} M), we reproduced **3** as a major isomer; and in this case, we note that including diffusion energy barrier in the kinetic model would also predict isomer **3** for larger amount of water. More interestingly however, the percentage evolution of the isomers as a function of protic solvent content is analogous to that as a function of solvent pK_a (compare Figure 2.6 and Figure 2.7). Additional experiments reducing systematically TFE amount confirm the shift of selectivity

from **2** to **3** and the reduction of catalytic activity, in full agreement with the proposed kinetic model.

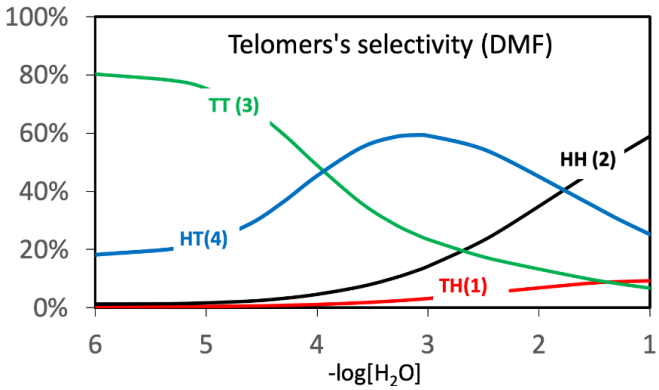

Figure 2.7 Microkinetic modelling of the percentage evolution for each isomer as a function of the amount of water impurities in DMF solvent. Initial simulated conditions: $Pd(PPh_3)_2$ (0.075 mmol), isoprene (10 mmol), Et_2NH (10 mmol), solvent (2 mL), 25ºC, 24 h.

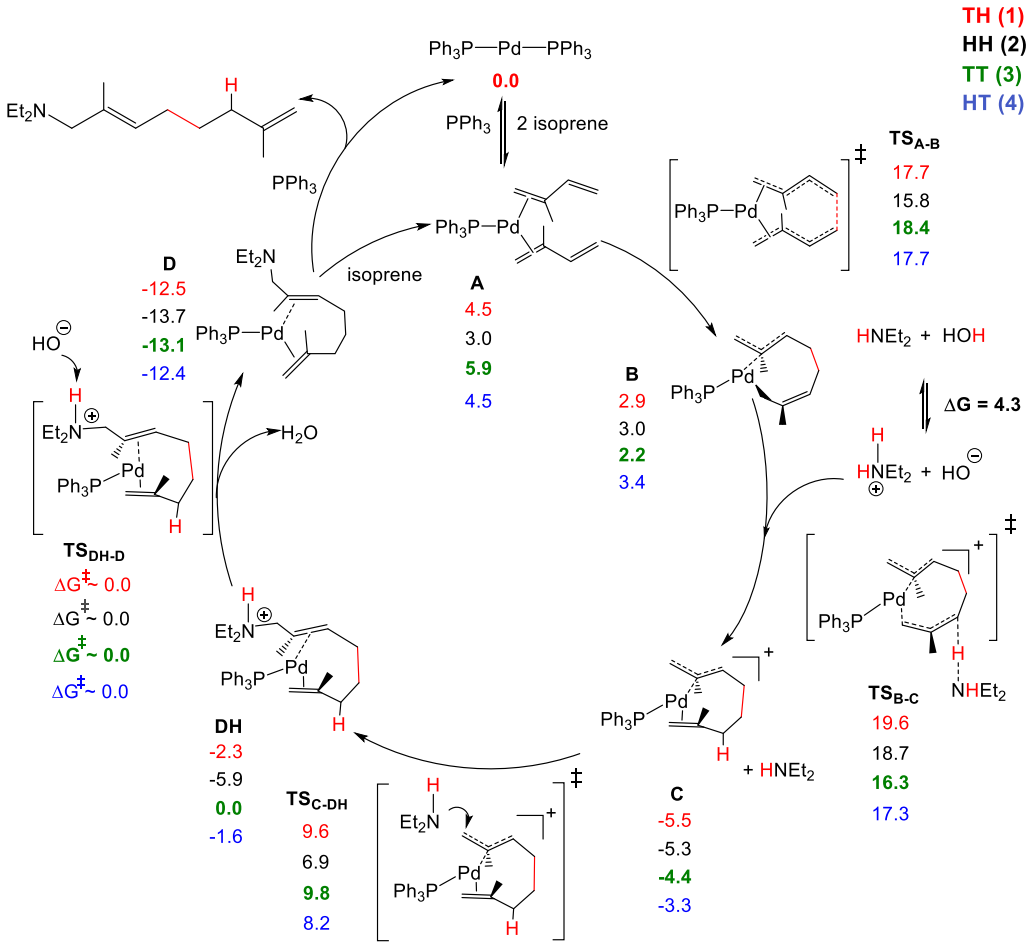

Figure 2.8 Catalytic cycle for the telomerization of isoprene with amine catalyzed by Pd/PPh_3 (**P1**) system in DMF solvent with water impurities. Relative free-energies, in kcal mol^{-1} for **TH** (**1**) (1st row, red), **HH** (**2**) (2nd row, black), **TT** (**3**) (3rd row, green) and **HT** (**4**) (4th row, blue); and structural representation of the **TT** path.

2.3.4 Origin of the Ligand Control of Selectivity

Experimental ligand screening in methanol has shown that using the sterically hindered monophosphine **P2**, the reaction can be directed towards isomer **1**. Interestingly, the same catalytic system gives isomer **2** as the major product in TFE, while the selectivity towards **1** is somewhat reduced in *t*BuOH.

We computed the full catalytic cycle for the Pd/**P2** catalyst (Figure 2.9), and Figure 2.10 shows the molecular structures of the transition states for the key protonation step (**$TS2_{P2}$**). From PPh_3 to **P2** ligand, protonation at the substituted

γ-carbon through **TH** (**1**) path becomes energetically preferred, indicating that the selectivity in the protonation step is not electronically but sterically controlled.

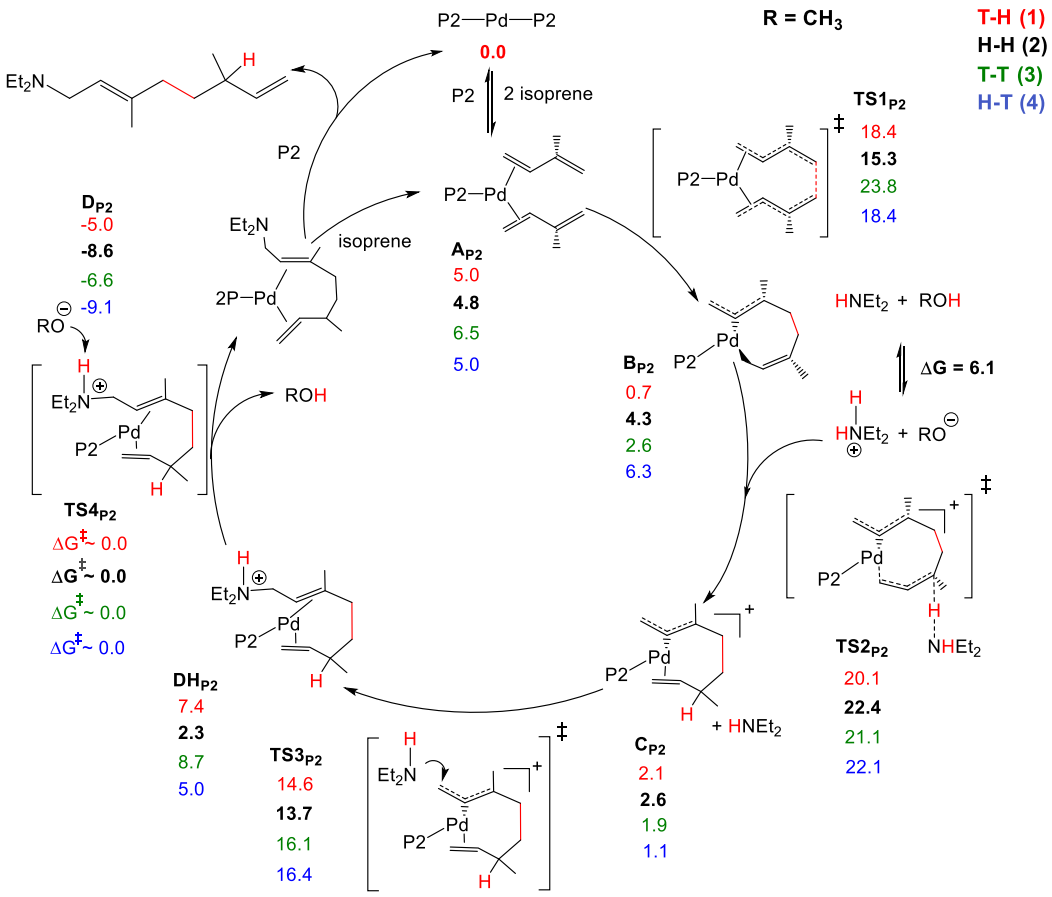

Figure 2.9 Catalytic cycle for the telomerization of isoprene with amines catalyzed by Pd/**P2** system in MeOH solvent. Relative free-energies, in kcal mol^{-1} for **TH** (**1**) (1st row, red), **HH** (**2**) (2nd row, black), **TT** (**3**) (3rd row, green) and **HT** (**4**) (4th row, blue); and structural representation of the **HH** path.

The conformation of the **P2** ligand places the mesityl substituent of the imidazole ring over the metal centre (Figure 2.10), hindering one coordination site and blocking ligand rotation around the Pd-phosphine bond, which provides more rigid Pd-ligand scaffold. Thus, in the **TT** (**3**) and **HT** (**4**) paths, the methyl substituent at the β-carbon of the η^1-σ-allyl moiety suffers a repulsive steric interaction with one cyclohexyl substituent of the phosphine ligand, while in the **HH** (**2**) path, the alternated conformation of the two methyl substituents results

in a destabilizing interaction between the methyl of the π-allyl moiety and the mesityl group of the phosphine (Figure 2.10).

The calculated isomer distributions from the relative free-energies of **TS2$_{P2}$** (0.0, +2.3, +1.0, +2.0 kcal mol^{-1} in Figure 2.10) were 81%, 2%, 14% and 3% for **1**, **2**, **3** and **4**, respectively, while those from **TS1$_{P2}$** (+3.1, 0.0, +8.5 and +3.1 kcal mol^{-1} in Figure 2.11) were 0.5%, 99%, 0% and 0.5%, respectively. Thus, in low-acidity *t*BuOH solvent (76% of **1**), the selectivity is governed by the protonation step (**TS2$_{P2}$**) favoring isomer **1**, while in high-acidity TFE solvent (93% of **2**) it is governed by oxidative C-C coupling (**TS1$_{P2}$**). For MeOH solvent (92% of **1**), we propose that protonation is still the selectivity-determining step but the **TS2$_{P2}$** species become closer in energy to **TS1$_{P2}$**, in which the **TT** (**3**) path is sterically blocked (relative free-energy of +8.5 kcal mol^{-1}), increasing the proportion of **1** at the expense of **3**.

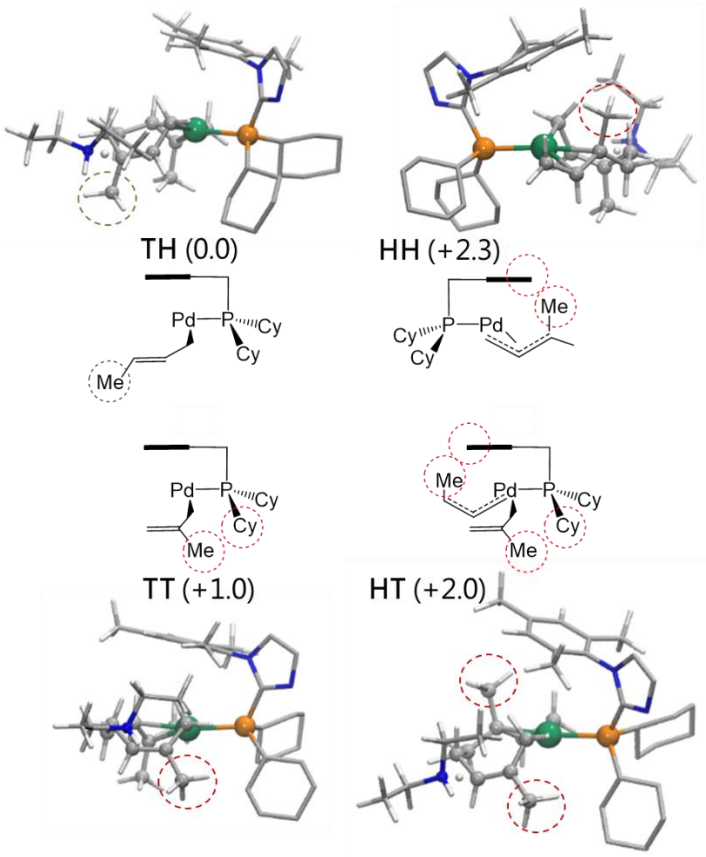

Figure 2.10 3D and schematic representations of the transition state for protonation (**TS2$_{P2}$**) by the Pd/**P2** catalyst, and relative free-energies in kcal mol^{-1}. Repulsive steric interactions are represented in red circles.

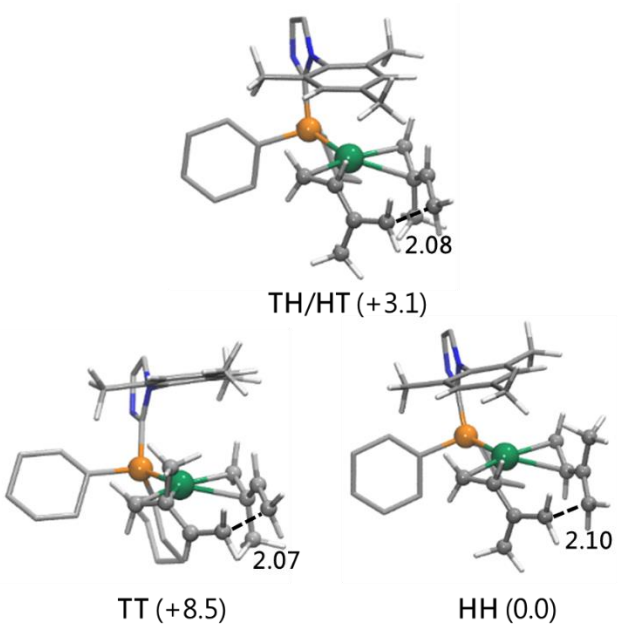

Figure 2.11 Molecular structures of the transition states for the isomeric paths of oxidative coupling of (**TS1**$_{P2}$) with Pd/**P2** catalytic system in MeOH. Distances are in Å and relative energies in kcal mol^{-1}.

2.4 Concluding Remarks

A combined experimental and computational study showed that both solvent and ligand are responsible for controlling the selectivity in isoprene telomerization catalyzed by palladium complexes. The solvent control occurs as a function of its pK_a, which is responsible of a continuous shift of the selectivity-determining step. For acidic solvents (TFE), the protonation step is fast and irreversible (kinetic scenario I), and the selectivity is governed by the C-C oxidative coupling. Under these conditions, the catalyst favors the least sterically demanding **HH** path (telomer **2**), which minimizes substrate-substrate and ligand-substrate repulsive interactions. As solvent acidity decreases (e.g. *t*BuOH), the protonation step becomes slower and more influential in the selectivity (kinetic scenario II), favoring the formation of telomer **3** (**TT**), which is more easily protonated at the non-substituted carbon of the η^1,η^3-diallyl. The ligand **P2** directs the selectivity towards the telomer **1** (**TH**) in moderately acidic solvents though the steric control of the protonation step via the mesityl substituent of the imidazole ring, which generates a more hindered and rigid metal-ligand scaffold. As a consequence of this study, we have been able to rationalize why

depending of reaction conditions telomers **1-3** were obtained in high yields and selectivities (>90%) using palladium catalysts.

2.5 Computational Details

DFT calculations. All calculations were carried out within the Density Functional Theory (DFT) framework, using Gaussian09 package of programs.[17] The correlation-exchange functional used was M06 by Truhlar et al.[18] Heavy atoms, Pd and P, were describe using LanL2DZ effective core potential for their inner shell electrons with its associated double ζ basis set for the outer electrons. Additionally, f- and d-type polarisation functions were included for Pd and P, respectively (exponent = 1.472 for Pd[19] and 0.387 for P[20]). The standard 6-31g(d,p) basis set[21] was used to describe N, C, H and O. The structures of all minima and transition states were optimised without any symmetry constraints and their nature was confirmed by frequency calculations, recognizing the transition states with one imaginary frequency matching the desired normal mode. To simplify the conformational problem, the preferred pathway computed for butadiene telomerization by Budzelaar[22] was taken, and methyl groups were added systematically to build the diisoprene. Solvent effects were introduced by single point calculations performed on the optimised structures in gas phase, using the self-consistent reaction field approach, by means of the integral equation formalism polarizable continuum model (IEFPCM)[23]. Free energy values were calculated at 298.15 K and at 1 mol L^{-1}, the standard state in liquid.

Evaluation of solvent acidity. Computationally, it is very challenging to evaluate accurately chemical processes involving charge separation in solution as the proposed deprotonation of the solvent by the amine ($ROH + Et_2HN \rightarrow RO^- + Et_2HNH^+$). Therefore, we used the experimental pK_a values to estimate the free energy cost associated to deprotonation process. Nevertheless, the best selection of appropriate pK_a value for each solvent is not straightforward because the experimental media is not aqueous and usually, the tabulated data are in such media. Moreover, different values are reported in the literature depending on the specific conditions at which the pK_a's were calculated. In this study we have found that the average values between standard accepted aqueous-media pK_a values and pK_a corresponding to the solvent autoprotolysis give the best fit of the kinetic model to the experimental selectivity (Figure 2.6). Table 2.4 collects the employed pK_a values and the corresponding reference where the values can be found.

Table 2.4 pK_a values of different compounds and solvents depending on the media and the average between both values.

Compound	pK_a		
	Aqueous solution	Autoprotolysis	Average
TFE	12.4[24]	15.0[25]	13.7
MeOH	15.3[24]	17.2[26,27]	16.3
EtOH	15.5[24]	18.9[28,27]	17.2
PrOH	16.1[24]	19.4[28,27]	17.8
***i*PrOH**	17.1[24]	20.8[28,27]	18.9
***t*BuOH**	19.2[24]	26.8[29,27]	23.0
$Et_2NH_2^+$	10.8[30]	11.1[31,27]	11.0

Microkinetic Analysis. Microkinetic modelling permits to introduce concentration effects in computational homogeneous catalysis.[32] It is very helpful when the more efficient reaction path is not obvious, as for example when different isomers with slightly different activation energies in the different steps of the reaction are present, or/and when there is not a clear determinant high energy barrier step, or/and when key species are present in very low concentration. All of these possibilities are present in our study, in which the rate-determining step can switch between the C-C oxidative coupling and the protonation step. Moreover, the reaction rate of this latter step depends on solvent concentration or on water impurities content in the case of DMF solvent, which have significantly higher or lower concentrations, respectively, than the other species involved in the reaction. There are 4 (isomers) by 14 direct steps plus 4 (isomers) by 14 inverse reactions plus 2 corresponding to the amine protonation by the solvent. Thus, a total of 58 elemental reactions are considered with the corresponding rate constants. All rate constants were calculated using Eyring approximation and Transition State Theory (TST). The differential equations are solved using the Acuchem software.[33]

References

1. Smutny, E. J. *J. Am. Chem. Soc.* **1967**, *89*, 25, 6793-6794.
2. Takahashi, S.; Shibano, T.; Hagihara, N. *Tetrahedron Lett.* **1967**, *8*, 2451-2453.
3. a) Fassbach, T. A.; Vorholt, A. J.; Leitner, W. *ChemCatChem* **2019**, *11*, 1153-1166. b) Herrmann, N.; Vogelsang, D.; Behr, A.; Seidensticker, T. *ChemCatChem* **2018**, *10*, 5342-5365. c) Behr, A.; Neubert, P. Applied, *Homogeneous Catalysis*, Wiley-VCH, 2012. d) Behr, A.; Becker, M.; Beckmann, T.; Johnen, L.; Leschinski, J.; Reyer, S. *Angew. Chem. Int. Ed.* **2009**, *48*, 3598-3614. e) Consiglio, G.; Waymouth, R. M. *Chem. Rev.* **1989**, *89*, 257-276. f) Clement, N. D.; Routaboul, L.; Grotevendt, A.; Jackstell, R.; Beller, M. *Chem. Eur. J.* **2008**, *14*, 7408-7420.
4. Tschan, M. J. L.; García-Suárez, E. J.; Freixa, Z.; Launay, H.; Hagen, H.; Benet-Buchholz, J.; van Leeuwen, P. W. N. M. *J. Am. Chem. Soc.* **2010**, *132*, 6463–6473.
5. Harkal, S.; Jackstell, R.; Nierlich, F.; Ortmann, D.; Beller, M. *Org. Lett.*, **2005**, *7*, 541–544.
6. van Leeuwen, P. W. N. M.; Clément, N. D.; Tschan, M. J. L. New processes for the selective production of 1-octene. *Coord. Chem. Rev.* **2011**, *255*, 1499–1517.
7. a) Benn, R.; Jolly, P. W.; Mynott, R.; Scheker, G. *Organometallics* **1985**, *4*, 1136-1138. b) Benn, R.; Jolly, P. W.; Mynott, R.; Raspel, B.; Schenker, G.; Schick, K. P.; Schroth, G. *Organometallics* **1985**, *4*, 1945-1953. c) Jolly, P. W.; Mynott, R.; Raspel, B.; Schick, K. P. *Organometallics* **1986**, *5*, 473-481. d) Völkl, L.; Recker, S.; Niedermaier, M.; Kiermaier, S.; Strobel, V.; Maschmeyer, D.; Cole-Hamilton, D.; Marquardt, W.; Wasserscheid, O.; Haumann, M. *J. Catal.* **2015**, *329*, 547-559.
8. Huo, C. F.; Jackstell, R.; Beller, M.; Jiao, H. *J. Mol. Model.* **2010**, *16*, 431-436.
9. Jabri, A.; Budzelaar, P. H. M. *Organometallics* **2011**, *30*, 1374-1381.
10. Asghar, U.; Masoom, A.; Javed, A.; Abbas, A. *Am. J. Chem. Eng.* **2020**, *8*, 63-69.
11. Jackstell, R.; Grotevendt, A.; Michalik, D.; El Firdoussi, L.; Beller, M. *J. Organomet. Chem.* **2007**, *692*, 4737-4744.
12. Rzhevskiy, S. A.; Topchiy, M. A.; Bogachev, V. N.; Ageshina, A. A.; Minaeva, L. I.; Sterligov, G. K.; Nechaev, S. M.; Asachenko, A. F. *Mendeleev Commun.* **2021**, *31*, 478-480.
13. Maddock, S. M.; Finn, M. G. *Organometallics* **2000**, *19*, 2684-2689.
14. Leca, F.; Réau, R. *J. Catal.* **2006**, *238*, 425-429.
15. Keim, W.; Kurtz, K. R.; Röper, M. *J. Mol. Catal.* **1983**, *20*, 129-138.
16. For an example, see: García-López, D.; Civit, M. G.; Vogels, C. M.; Ricart, J. M.; Westcott, S. A.; Fernández, E.; Carbó, J. J. *Catal. Sci. Technol.* **2018**, *8*, 3617–3628.
17. *Gaussian 09*: Frisch, M. J.; Trucks, G. W.; Schlegel, H. B.; Scuseria, G. E., Robb, M. A.; Cheeseman, J. R.; Scalmani, G.; Barone, V.; Mennucci, B.; Petersson, G. A.; Nakatsuji, H.;

Caricato, M.; Li, X.; Hratchian, H. P.; Izmaylov, A. F.; Bloino, J.; Zheng, G.; Sonnenberg, J. L.; Hada, M.; Ehara, M.; Toyota, K.; Fukuda, R.; Hasegawa, J.; Ishida, M.; Nakajima, T.; Honda, Y.; Kitao, O.; Nakai, H.; Vreven, T.; Montgomery Jr.; J. A.; Peralta, J. E.; Ogliaro, F.; Bearpark, M.; Heyd, J. J.; Brothers, E.; Kudin, K. N.; Staroverov, V. N.; Kobayashi, R.; Normand, J.; Raghavachari, K.; Rendell, A.; Burant, J. C.; Iyengar, S. S.; Tomasi, J.; Cossi, M.; Rega, N.; Millam, J. M.; Klene, M.; Knox, J. E.; Cross, J. B.; Bakken, V.; Adamo, C.; Jaramillo, J.; Gomperts, R.; Stratmann, R. E.; Yazyev, O.; Austin, A. J.; Cammi, R.; Pomelli, C.; Ochterski, J. W.; Martin, R. L.; Morokuma, K.; Zakrzewski, V. G.; Voth, G. A.; Salvador, P.; Dannenberg, J. J.; Dapprich, S.; Daniels, A. D.; Farkas, O.; Foresman, J. B.; Ortiz, J. V.; Cioslowski, J.; Fox, D. J.; Eds., Gaussian Inc.: Wallingford CT (2010).

18. Zhao, Y.; Truhlar, D. *Theor. Chem. Acc*. **2008**, *120*, 215–241.
19. Ehlers, A. W.; Böhme, M.; Dapprich, S.; Gobbi, A.; Höllwarth, A.; Jona, V.; Köhler, K. F.; Stegmann, R.; Veldkamp, A.; Frenking, G. *Chem. Phys. Le*tt. **1993**, *208*, 111–114.
20. A. Höllwarth, A.; Böhme, M.; Dapprich, S.; Ehlers, A.W.; Gobbi, A.; Jonas, V.; Köhler, K. F.; Stegmann, R.; Veldkamp, A.; Frenking, G. *Chem. Phys. Le*tt. **1993**, *208*, 237–240.
21. a) Francl, M. M.; Pietro, W. J.; Hehre, W. J.; Binkley, J. S.; Gordon, M. S.; Defrees, D. J.; Pople, J. A. *J. Chem. Phys*. **1982**, *77*, 3654–3665; b) Hehre, W. J.; Ditchfield, R.; Pople, J. A. *J. Chem. Phys*. **1972**, *56*, 2257–2261; c) Hariharan, P.C.; Pople, J. A. *Theor. Chem. Acc*. **1973**, *28*, 213–222.
22. Jabri, A.; Budzelaar, P. H. M. *Organometallics,* **2011**, *30*, 1374–1381.
23. Mennucci, B. ; Cancès, E. ; Tomasi, J. *J. Phys. Chem. B* **1997**, *101*, 10506–10517.
24. Serjeant, E. P.; Dempsey, B.; *Ionisation Constants of Organic Acids in Aqueous Solution. International Union of Pure and Applied Chemistry* (IUPAC). IUPAC Chemical Data Series No. 23. Pergamon Press: New York, 1979, p. 989.
25. Carre, B.; Devynk J. *Anal. Chim. Acta* **1981**, *131*, 141–1247.
26. a) Kreshkov, A. P.; Aldarova, N. Sh.; Tanganov, B. B. *Russian J. Phys. Chem*. **1970**, *44*, 1186; b) Kreshkov, A. P.; Smolova, N. T.; Aldarova, N. Sh.; Gabidulina, N. A. *Zh. Fiz. Khim*. **1972**, *46*, 667–671.
27. Reichardt, C.; Welton, T. *Solvents and Solvent Effects in Organic Chemistry*, 4th Edition. WILEY-VCH Verlag GmbH & Co. KGaA, Weinheim, 2010.
28. Schaal, R.; Tézé, A. *Bull. Soc. Chim. Fr*. **1961**, 1783–1791.
29. Bykova, L. N.; Petrov, S. I. *Zh. Anal. Khim*. **1972**, *27*, 1076–1079.
30. Marion, N.; Navarro, O.; Mei, J.; Stevens, E. D.; Scott, N. M.; Nolan, S. P. *J. Am. Chem. Soc.* **2006**, *128*, 4101–4111.
31. Perrin D. D. *Dissociation constants of organic bases in aqueous solution*. IUPAC Chem. Data Ser, Buttersworth, London, 1965.

32. Besora, M.; Maseras, F. *WIREs Comput. Mol Sci.* **2018**, *8*, 1–13.

33. Braun, W.; Herron, J. T.; Kahaner, D. K. Acuchem: *Int. J. Chem. Kinet.* **1988**, *20*, 51–62.

UNIVERSITAT ROVIRA I VIRGILI
COMPUTATIONAL MODELING TO EXPLORE SOLVENT AND DYNAMIC EFFECTS IN MOLECULAR, NANO AND SOLID CATALYSIS
Antoni Salom Català

Chapter 3:

Organometallic Rh Nanocatalysts: Phosphine Interaction, Adsorption, and Solvent Effects

UNIVERSITAT ROVIRA I VIRGILI
COMPUTATIONAL MODELING TO EXPLORE SOLVENT AND DYNAMIC EFFECTS IN MOLECULAR, NANO AND SOLID CATALYSIS
Antoni Salom Català

Chapter 3:

Organometallic Rh Nanocatalysts: Phosphine Interaction, Adsorption, and Solvent Effects

This chapter presents a computational study of phosphine-decorated Rh nanoparticles. We used classical approaches to explore shape and size nanoparticle (NP) influence. Then, the interaction of PPh_3 with 55-atom Rh nanoparticles was studied in detail. The PPh_3 ligand was adsorbed through the lone pair electrons of the phosphorous atom, and in some cases PPh_3 bends towards NP surface allowing the interaction of phenyl substituents π-system in η^6- and η^2- modes. We also evaluated the adsorption energy of PPh_3 on different sized NPs, showing a steady decrease with increasing NPs size. In addition, we used the information obtained from the PPh_3 adsorption study to build a simple regression model to predict adsorption energies of PPh_3 on Rh NPs using the Generalized Coordination Number (GCN) and d-band center as local and global descriptors, respectively. Afterwards, we investigated the PPh_3 coverage effects, revealing a constant stabilization of the electronic structures as more molecules were adsorbed, up to 7 PPh_3. At the end, for the first time, we evaluate the solvent effect on PPh_3-adsorbed Rh NPs by means of the ab initio *molecular dynamics (AIMD) technique. Simulations performed using THF as solvent, showed that the adsorption of PPh_3 is stronger than that of THF molecules, and a preference of solvent to interact with corner Rh atoms. Finally, the adsorption of other phosphine molecules (P(*o*-tolyl)$_3$, P(OPh)$_3$ and OPPh$_3$), was analyzed, indicating an influence of the geometry of the molecule on the adsorption mode and strength.*

Part of this project was carried out during a three-month research stay in the group of Dr. F. Baletto at King's College London, under HPC Europa3 mobility program.

3.1 Introduction

Large-scale chemical processes in industry are dominated by heterogeneous catalysis, which offers high activity and recyclability, despite showing a poor selectivity. Since 1941, when the first application of nanoparticles in catalysis was reported,[1] nanocatalysis has emerged as a new field that attempts to combine the advantages of heterogeneous and homogenous catalysis. The development of novel metal nanoparticles (MNPs) can lead to highly active and recyclable, as well as selective catalysts. In addition, they have also shown applications in many

fields including medicine, electronics, sensors, pigments, magnetic and optical materials, etc.[2]

Among nanoparticles, organometallic MNPs constitute an important subclass of compounds[3] with their surface decorated by organic ligands, such as N-heterocyclic carbenes (NHCs), carbodiimides, amidinates, pyridines, thiolates and phosphines. The role of ligands is twofold: they stabilize the nanoparticles in solution and prevent their sintering. One of the current challenges is to elucidate how the presence of ligands affects the catalytic performance of the MNP due to 1) modification of the electronic and steric properties that the nanocatalyst exerts on the reactants; 2) change of the effective number of active sites; 3) a non-innocent role of the ligand in the reaction. The understanding at atomistic level using quantum chemistry is essential to elucidate structure and reactivity allowing a fine-tuning of the ligands-MNP interaction for the design of optimal nanocatalysts. Specifically, phosphine ligands have also revealed to stabilize rhodium NPs that are active catalysts in several processes such as hydrogenations[4] and hydroformylation.[5]

From a computational approach, the interaction of P-donor ligands with quantum sized MNPs and how it affects reactivity is scarcely investigated. These studies include the adsorption of model phosphine PH_3 on Pd nanoparticles,[6] PH_3 on Au_{55} and Pt_{55} nanoclusters,[7] of BINAP diphosphine on Pd surfaces,[8] or of bis(diphenylphosphino) butane on Ru nanoparticles.[9] Other studies analyzed the reactivity on surfaces or nanoparticles functionalized with P-donor ligands including Pd surfaces[10] and gold nanoparticles[11,12].

Phosphine related molecules are frequently used as stabilizer and surface ligand to prevent the sintering of the NPs. However, their interaction has been scarcely investigated at atomistic level. To fill this gap, we investigated the nature of the interaction of phosphines species with different sized and shaped Rh NPs. The aim of the study presented in this chapter is to identify the preferred structures of triphenylphosphine (PPh_3) adsorbed on a Rh_{55} nanoparticle; to analyze the effect of the particle size on the adsorption energy and mode of PPh_3; to propose a structure-adsorption relationship of the phosphine adsorption energies on different nanoparticles using the generalized coordination number (GCN) and the d-band center and to study the effect of the PPh_3 coverage. Finally, we present here, to the best of our knowledge, the first *ab initio* molecular dynamics (AIMD) study on the interaction among nPPh_3-NP moiety and the solvent, paying special attention to: 1) the PPh_3-NP interaction in a dynamic environment; 2) the nature of the solvent-NP interaction and 3) the competition between the PPh_3 surface ligands and the explicit solvent molecules, all taking into account the coverage effect. Furthermore, the adsorption of P(*o*-tolyl)$_3$, $P(OPh)_3$ and $OPPh_3$ was investigated to assess the dependence of adsorption on ligand geometry.

3.2 Results and Discussion

3.2.1 Rhodium Nanoparticles. Size, Shape and Electronic Structure

Initially, we analyzed the morphology of Rh nanoparticles as one of the most important features determining their properties. A recent study synthesizing Rh nanoparticles using triphenylphosphine (PPh_3) as stabilizer resulted in NPs exhibiting small diameter (< 2nm) with narrow size distribution and spherical shape.[13] Therefore, we selected Rh nanoclusters of 49, 55, 75 and 147 that can form highly symmetric structures ranging from 1.0 to 1.6 nm. These clusters, present (100) and (111) faces and well defined corner and edges atoms. We explored the configurational potential energy surface to find possible stable shapes of the studied NPs by means of classical Monte Carlo (MC) simulations within the Basin-Hopping Parallel Excitable Walkers (BH-PEW) method[14] as implemented in the LoDiS software developed by Baletto and co-workers.[15] The atomic interactions are modelled within the second moment approximation of the tight binding theory.[16] Figure 3.1 summarizes the exploration results for the four NPs showing representative structures.

All structures fell in a global minimum corresponding to a high-symmetry geometry in the MC simulations. For Rh_{55} and Rh_{147} NPs the global minimum was an icosahedral (ICO) shape, while for Rh_{75} was the Marks-decahedron form. For Rh_{49}, MC simulation led to an ICO-like geometry with one vertex removed and exposing the first atomic shell. Then, we performed classical molecular dynamics (MD) at 400 K of some local and all global minima structures to ensure their minimum nature, showing all of them having stable character during 500 ps of simulation.

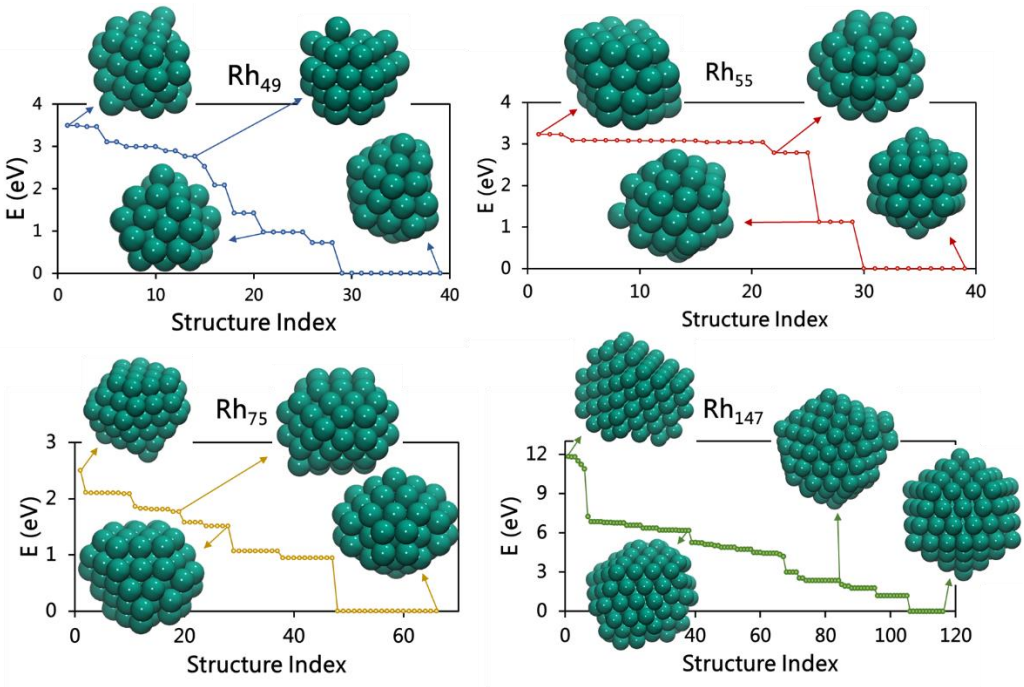

Figure 3.1 Classical Monte Carlo configurational search for Rh NPs with different number of atoms: 49, 55, 75 and 147. The geometries of representative structures are also shown.

Next, we performed periodic Density Functional Theory (DFT) calculations on the obtained global minima for Rh_{49}, Rh_{55}, Rh_{75} and Rh_{147} clusters, and compared them with Rh(111) surface. For Rh_{55} we also considered the cuboctahedron (CUB) structure which will be subsequently employed as a model of 100 facet for the study PPh_3 adsorption. The FCC fragment (FCCf) has been also proposed as a stable configuration for Rh_{55} clusters in gas phase,[17,18,19,20] but here, we selected ICO and CUB configurations as representative structures of phosphine-stabilized NPs in solution since there is experimental evidence[21,22] that the NPs exhibit spherical shapes and the diameters we found were very reasonable (1.5 ± 0.2 vs 1.3 nm experimental and computational, respectively).

Table 3.1 collects the cohesion energy (E_c) for the computed MNPs and surface that is defined in Equation 3.1, where E is the total energy of the NP, n is the total number of atoms and E_a is the atomic energy. The smaller the nanoparticle, the lower (less negative) the cohesion energy, in agreement with the findings obtained by Qi *et al.*, using different models.[23] The Rh(111) surface shows the highest cohesion energy (-4.8 eV), while in Rh clusters it ranges from -4.5 to -4.1 eV, ongoing from Rh_{147} to Rh_{49}, respectively. This trend can explain the tendency for MNPs to sinter if there are not ligands or other species to prevent it.

$$E_c = \frac{E - (n \cdot E_a)}{n} \quad (3.1)$$

Table 3.1 Cohesion energy and d-band center respect the Fermi level for the occupied d states in eV for Rh_n NPs (n = 49, 55, 75, and 147) and Rh(111) surface.

NP	49	55		75	147	Rh(111)
		Ico	Cub			
$E_{cohesion}$	-4.1	-4.1	-4.1	-4.3	-4.5	-4.8
d-band center	-2.24	-2.22	-2.27	-2.37	-2.37	-2.63

To further investigate the electronic structure of the nanoparticles, Table 3.1 reports the energy of the d-band center descriptor. The d-band center is widely used as a descriptor to set correlations with the adsorption strength of ligands and reactants, and with the reactivity of a metal NP or surface. Normally, the larger is the difference between d-band center value and the Fermi level, the less reactive is the MNP.[17,18] In general terms, the evolution of the d-band follows the trend stablished by the cohesion energy, becoming more negative as the size of the NP increases (from -2.24 to -2.63 eV for Rh_{49} to Rh(111), respectively). This means that we expect lower phosphine adsorption energies on going from Rh_{49} to Rh_{147}, and then, to Rh(111).

3.2.2 Interactions of Phosphines with Rhodium Nanoparticles

To obtain an atomistic description of the interaction of phosphines with Rh NPs, we have performed DFT calculations on the cluster described above, as well as an AIMD simulations on phosphine-decorated NPs embedded into THF solvent box. Primarily, we select PPh_3 as a commonly used phosphine for NP stabilization, and then it was compared with other phosphines such as P(*o*-tolyl)$_3$, P(OPh)$_3$ and $OPPh_3$.

Adsorption of PPh_3 on Rh_{55} NPs

The highly symmetric 55-atom Rh nanocluster, was initially selected, as it has been considered extensively both in experimental and computational studies.[19,20,24,25] We have systematically explored the binding sites for PPh_3 phosphine on Rh_{55} clusters with ICO and CUB symmetries. In total, we obtained 6 possible initial structures for ICO nanostructure and 9 for CUB NP. After minimization, three and four final representative structures were obtained for ICO

and CUB NPs respectively, and they are shown in Table 3.2, as well as the respective electronic adsorption energies.

Table 3.2 Possible adsorption modes and energies in eV of PPh_3 on the Rh_{55} icosahedral (top) and cuboctahedral (bottom) symmetries.

Adsorption Modes	P_{edge}-η^6	P_{edge}- η^2	P_{vertex}	P_{face}- η^6
ICO	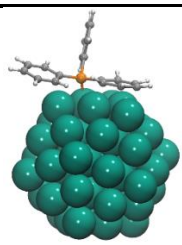 **1A**	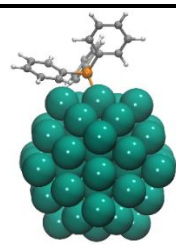 **1B**	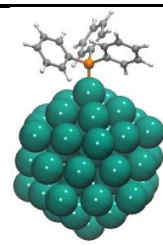 **1C**	-
E_{ads}	-2.96	-1.81	-1.50	-
CUB	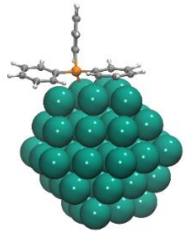 **$1A^{CUB}$**	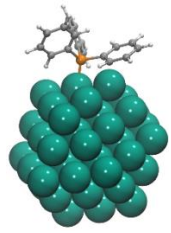 **$1B^{CUB}$**	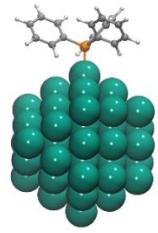 **$1C^{CUB}$**	 **$1D^{CUB}$**
E_{ads}	-2.90	-2.04	-1.64	-2.52

Several important features emerge from these optimized structures: (i) the phosphorus atom interacts with the Rh NP surface in an atop mode at either the vertex or edge Rh atoms, (ii) the phenyl substituents of the phosphine do also interact with the Rh NP surface, and (iii) in both clusters the strongest adsorption is that in which the phosphorus coordinates to an edge Rh atom with phenyl rings oriented on a (111) facet (P_{edge}-η^6 adsorption with -2.96 and -2.90 eV for ICO and CUB, respectively). Figure 3.2A shows in more detail the **1A** adsorption mode, as well as some important geometric parameters that confirms the nature of the interaction between the PPh_3 and the NP.

The phosphorus atom is coordinated to a Rh edge atom through its lone pair electrons (distance P-Rh: 2.25 Å). One of the phenyl rings is fully interacting with the Rh(111) face through the 6 carbon atoms of the π system that gain a sp^3 hybridization. The η^6-phenyl interaction is characterized by short Rh-C distances

(2.17 Å in average) and some pyramidalization of the carbon atoms that breaks the planarity of the aromatic ring lifting the hydrogen atoms out of the ring plane. The other phenyl ring interacts with the corner Rh atom through its *ipso* and *ortho* carbon atoms both of them at distance of 2.30 Å. To confirm the interaction between the ligand and the NP surface a charge density difference analysis was performed (Figure 3.2B). The graph shows charge transfer surfaces (blue-colored) on the Rh atoms interacting with the phosphorus atom and the phenyl rings, while charge depletion (yellow-colored) are located on the C-C bonds of the phenyl rings and close to P.

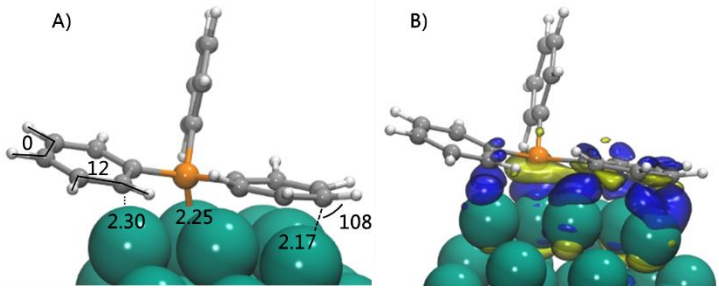

Figure 3.2 Zoom of 3D structure for **1A** adsorption mode on Rh_{55} ICO NP with selected geometrical parameters in Å for distances and degrees for angles (**A**). Charge Density Difference plot where electron accumulation areas are in blue and electron depletion areas are in yellow (**B**).

To rationalize the different contributions to the adsorption energy of PPh_3 phosphine, we have performed a fragment decomposition analysis of the different individual functional groups of the phosphine. From the optimal geometry of the adsorbed phosphine with the lowest energy (**1A**), we built two type of model systems, PH_3 and C_6H_6, by replacing the corresponding substituents by hydrogen atoms. Then the adsorption energy of these individual model fragments is divided into interaction and distortion energies. The interaction energies ($E_{int.}$) were evaluated as the energy difference between the model fragment and the nanoparticle at infinite distance in the geometry of Rh_{55}@PPh_3 minimum. The distortion energies ($E_{dis.}$) accounts for the energy cost from the isolated optimized geometries of model fragments and nanoparticle to the final geometries in Rh_{55}@PPh_3 minimum. The results are schematically shown in Figure 3.3.

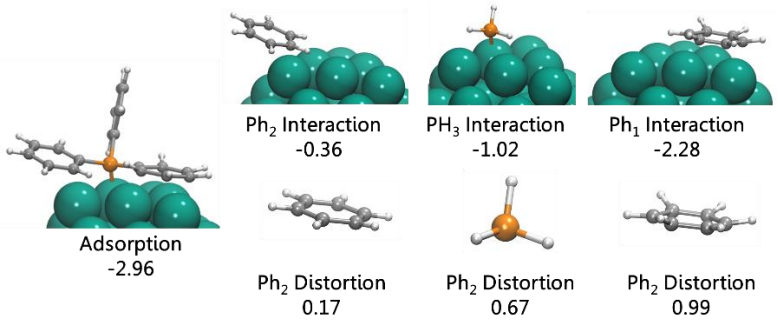

Figure 3.3 Fragment decomposition analysis of the adsorption energy of PPh_3 to Rh_{55}-ICO cluster in **1A**. Energies in eV.

The distortion energies indicate that the NP did not undergo a major structural change, since the icosahedral geometry is maintained and the corresponding distortion energy is only+0.22 eV. The interaction energies of the three functional groups are -1.02, -0.36 and -2.28 eV for the phosphorus, the η^2 and η^6 interacting phenyl, respectively. Interestingly, the η^6 π interaction is significantly larger than the interaction involving the phosphorus lone pair. However, the distortion energy associated to the partial loss of the aromaticity of the phenyl ring counterbalances its strong interaction energy. The other phenyl interacting with the NP vertex through the *ipso* and *ortho* carbons has a lower contribution to the overall adsorption energy. Thus, PPh_3 phosphine adsorbs on the Rh nanoparticle through the phosphorus lone pair but the interaction of the aromatic ring substituents can significantly contribute to the overall adsorption energy.

Nanoparticle size effect on the adsorption of PPh_3

Next we analyze the effect of the size of Rh clusters on the adsorption mode and energy of PPh_3. The selected Rh NPs were those discussed on Section 3.2.1: ICO-like Rh_{49}, Marks-decahedron Rh_{75}, ICO Rh_{147}, as well as the Rh(111) surface. All the Rh clusters possess 111 facets, making possible to define analogous structures to the most stable adsorption mode, **1A**, on Rh_{55} cluster. Thus, we coordinated the PPh_3 molecule through phosphorus lone pair on the edge Rh atom, and then bend it towards the 111 nanoparticle face allowing the interaction of the phenyl substituents. The results are shown in Table 3.3.

Table 3.3 PPh_3 adsorption onto different sized NPs. Energies are in eV.

System	E_{ads}	Figure	System	E_{ads}	Figure
$Rh_{49}@PPh_3$	-3.06	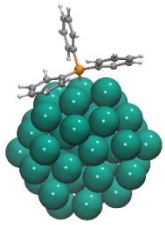	$Rh_{147}@PPh_3$	-2.45	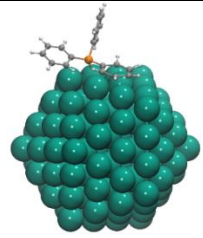
$Rh_{75}@PPh_3$	-2.31	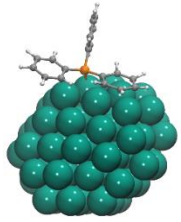	$Rh(111)@PPh_3$	-1.52	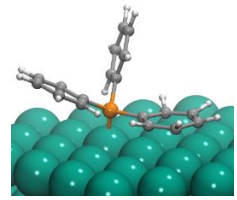

One can stablish a relationship between the adsorption energies and the size of the NP. The bigger is the NP, the lower (less negative) the phosphine adsorption energy is, ranging from -3.06 eV for Rh_{49} to -2.45 eV for Rh_{147}, and then to -1.52 eV for the Rh(111) surface. Again these results agree with the trend of the d-band center of the naked NPs shown in Table 3.1: the more negative is the d-band center, the weaker the adsorption is. In terms of geometries, all nanoparticles maintained the same adsorption mode as in $Rh_{55}@PPh_3$ **1A**, while in Rh(111) surface only one phenyl ring interacts with the Rh surface. This trend is alike the use of phosphines as stabilizers of small-size Rh nanoparticles. Also it is important to note that the geometry of the nanoparticles is important since despite Rh_{147} is bigger than Rh_{75}, higher is the PPh_3 adsorption energy.

Regression model for PPh_3 adsorption mode on Rh nanoparticles

The systematic study of phosphine adsorption on the different Rh nanoparticles has resulted in a total of 16 different structures: 1 for Rh_{49}, Rh_{75} and Rh_{147} and 8 for the Rh_{55}^{CUB} and 5 for the Rh_{55}^{ICO} nanocluster, the most representative of which are shown in Table 3.2 and Table 3.3. This provides a small dataset to attempt regression models correlating the adsorption energies with the structure of the nanoparticle. To map the adsorption sites on nanoparticle surfaces we used the generalized coordination number (GCN) as local topological descriptor, which has been widely and successfully used to predict different nanoparticles properties,[26] and the d-band center as global descriptor. The GCN of a site i is

defined as an average coordination (CN) of the j atoms within a certain cut-off from j, and the maximum coordination (CN_{max}) of the site (Equation 3.4).

$$GCN_i = \sum_{j=1}^{N_i} \frac{CN_j}{CN_{max}} \quad (3.4)$$

The same formalism can be used to characterize the atop, bridge and hollow sites, as CN_{max} varies with the site type. For Rh, CN_{max} can be 12 for the atop site, 18 for the bridge one and 22 for the hollow site. To stablish whether an atom is a neighbor or not, we followed the formulation suggested by Baletto *et al.*, i. e. is nearest neighbor lattice distance times 1.2 to include possible thermal vibrations effects[27]. Thus, we considered all atoms embedded in a sphere of radius 3.227 Å. Building structure-adsorption models based on GCN descriptor is relatively straightforward for the adsorption of atoms and small molecules such as CO and O_2 on nanoclusters.[26,28] However, whether the GCN concept can serve as a simple and effective structure descriptor for more complex adsorbents such as phosphines is still an open question. In addition, the use of the d-band center as a descriptor allow us to distinguish not only between different sized nanoparticles (different number of atoms), but also between different topologies. D-band center has been used to predict the adsorption and catalytic properties of several metal surfaces and nanoparticles,[17,29,30,31] however, the combination of these two local and global, topological and electronic, descriptors has been not used at best of our knowledge. Here we attempt regression models for PPh_3 phosphines that capture the simultaneous interaction of the phosphorus atom and the phenyl substituents with nanoparticle surface. Three different factors were considered to quantify these interactions: (i) the GCN of the Rh atom to which the phosphorous atom is coordinated (GCN_P), (ii) the sum of the two GCN of the sites where the phenyl rings are adsorbed, multiplied by the number of adsorbed carbon atoms (n) for each phenyl, ($nC \cdot GCN_{Ph1} + nC \cdot GCN_{Ph2}$), and (iii) the d-band center of the occupied states of the bare nanoparticle. Figure 3.4 shows the correlation model for the adsorption energies of PPh_3 on Rh NPs obtained after multilinear regression, as well as the comparison between calculated and fitted values. The current regression model showed a good correlation between the GCN and the d-band center and the adsorption energies of PPh_3 on de Rh nanoparticles with a r^2 value of 0.83. These results indicate that the particle size, as well as the particle topology have a large influence on the PPh_3 adsorption energies.

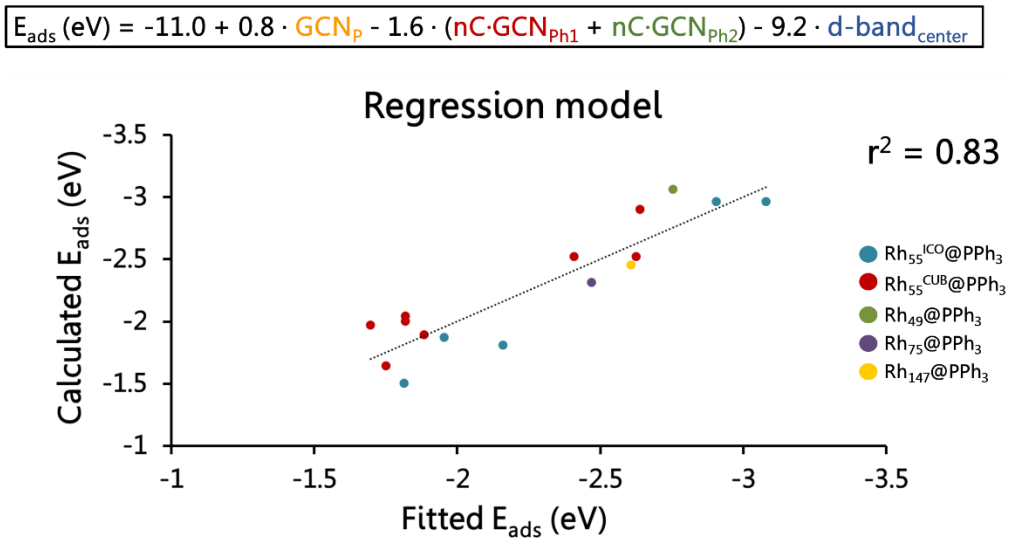

Figure 3.4 Multilinear regression model for the adsorption energy of PPh_3 onto Rh nanoparticles using GCN and d-band center descriptors, and comparison between DFT calculated and fitted values. The r^2 value is = 0.83.

Coverage effect on adsorption energies and nanoparticle electronic structure

Previous computational studies have shown that increasing the coverage value on the nanoparticle surface, the NP-ligand bond strength weakens what was related to the stabilization of the d-band center with respect to the Fermi level.[9,32] Here we systematically investigated the effect of PPh_3 coverage on Rh_{55} nanoparticle by sequentially decorating the surface with 1 to 10 PPh_3 ligands. For all of them, we adopted a **1A** adsorption mode which is characterized by phosphorus coordination on an edge and π-bonding of two phenyl rings with the rhodium surface. Each new ligand on the surface was placed with the maximum separation respect to previous ones in order to minimize ligand-ligand steric repulsions and obtain an uniform distribution. It is important to note that this procedure does not seek to find the ligand configuration for the absolute minimum. The complex, dynamic nature of organometallic nanoparticles under experimental conditions involves particles of different configuration and dynamic adsorption/desorption processes that do not allow to define the system with a single structure. Here we aim to evaluate the fundamental effect of ligand coverage in the adsorption and the electronic signature of the metal core, while in the next section we will explore the dynamic nature of this species in solution through AIMD simulations.

Table 3.4 Effect of Rh_{55} ICO NP PPh_3 coverage on its adsorption energy and electronic structure. Energies and d-band center are in eV.

n PPh_3	av. E_{ads}[a]	total E_{ads} variation[b]	surface Rh d-band center[c]	magnetization
0	0.00	0.00	-1.95	45.8
1	-2.96	-2.96	-2.05	29.3
2	-3.02	-3.08	-2.05	23.0
3	-2.93	-2.76	-2.11	21.0
4	-2.83	-2.53	-2.18	17.3
5	-2.72	-2.24	-2.23	16.8
6	-2.61	-2.08	-2.27	5.0
7	-2.53	-2.02	-2.31	3.6
8	-2.27	-0.46	-2.35	1.4
9	-2.02	-0.02	-2.34	3.2
10	-1.77	+0.49	-2.35	5.3

[a] Average E_{ads}: total adsorption energy divided by the number of PPh_3 molecules. [b] Total E_{ads} variation: $E_{NP@nPPh3} - (E_{NP@(n-1)PPh3} + E_{PPh3})$ [c] Surface Rh d-band center respect to the Fermi level of occupied states.

Table 3.4 shows the most relevant results of the analysis of the coverage effects. On a bare Rh_{55} nanoparticle, the adsorption of PPh_3 in its most stable isomer is largely exothermic by -2.96 eV. As the number of phosphine ligands on the surface increases, the average adsorption energy (column 1 in Table 3.4) is reduced because both the lowering of Rh-P and-phenyl bonding strength, and the mutual ligand hindrance that prevents the π-bonding of phenyl rings. Thus, these averaged energies move from -2.96 to -1.77 eV per absorbed PPh_3 ligand. Column 2 of Table 3.4 collects the variation of the overall adsorption energy upon coordinating one new PPh_3 ligand at a time. This parameter indicates a reduction on the adsorption strength for each new ligand following a non-linear trend. Up to 7 PPh_3 ligands, the increase of adsorption energy is significant with values ranging from -2.96 to -2.02 eV. The addition of the eighth phosphine is clearly less favorable than the others (-0.46 eV), suggesting a dynamic adsorption/desorption process in competition with solvent molecules (see next section). The adsorption of the ninth and tenth phosphine molecules was isothermic, and even endothermic in the latter case. This loss in adsorption strength can be attributed to the steric hindrance that comes up when an eighth

PPh_3 ligand is adsorbed, and to the loss of the π-interactions of one the phenyl rings due to the lack of free space in the surface. Figure 3.5 shows the structure of Rh_{55} nanoparticle saturated with 7 adsorbed PPh_3 ligands, which are optimal number for adsorption onto a 55-atoms icosahedral Rh NP.

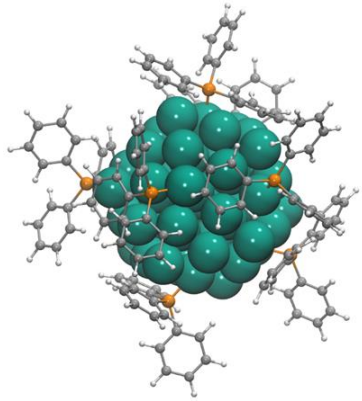

Figure 3.5. Representation of Rh_{55}@$7PPh_3$ system.

The coverage also affects the electronic structure of the Rh NP. To inspect the variation on the electronic structure, two descriptors are shown in Table 3.4: the surface Rh d-band center of occupied states, and the magnetization of the system. The energy of the d-band center constantly decreases due to the stabilization induced by PPh_3 adsorption. Note that the d-band center correlates with the overall adsorption energy, and once the eighth PPh_3 is coordinated the value remains invariant. This trend can also be noted in the density of states (DOS) plot in Figure 3.6. Adding PPh_3 ligands onto the NP surface, shifts down the energy of the occupied d states and decreases the number of states around the Fermi level.

The magnetization also indicates an electronic stabilization going from a state with highly open-shell character (29.3 for Rh_{55}@$1PPh_3$) to almost completely closed-shell system (1.4 for Rh_{55}@$8PPh_3$). Note that the magnetization experiments a large decrease once six PPh_3 ligands are adsorbed, a similar break on the trend as for the variation of total adsorption energy (compare columns 2 and 4 in Table 3.4). Finally, we suggest that the optimal coverage of a naked Rh_{55} icosahedral nanoparticle is between 6 and 7 PPh_3 ligands in terms of geometrical and electronic stabilization.

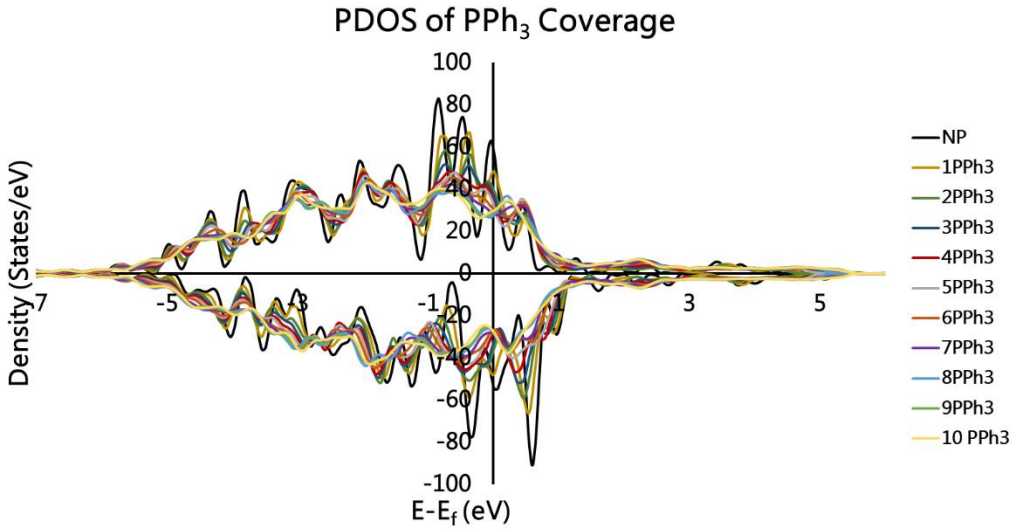

Figure 3.6 PDOS plot as a function of PPh_3 coverage. Note the smearing was changed from 0.05 to 0.2 eV to decrease the fine structure degree for an easier comparison.

Solvent influence on Rh_{55}-ICO-PPh_3 systems. *Ab initio* molecular dynamics study

Over the whole chapter, the adsorption of triphenyl phosphine molecule has been largely analyzed, sampling thoroughly the possible configurations. Similarly, previous computational studies on organometallic nanoparticles have focused on structural impact of the ligands, and more recently, on the role of ligands in controlling the activity and selectivity of catalytic processes (see also Chapter 4).[33] On the other hand, the effect of the solvent has been scarcely investigated, despite of its importance to gauge the nanoparticle reactivity at the interface between homogeneous and heterogeneous catalysis. However, the modelling of nanoparticle/ligand/solvent systems and its dynamic behavior is highly computationally demanding at the frontier of theoretical simulations. Within the context of a high-performing computing project (HPC-Europa3), we performed large AIMD simulations (see Computational Details) on $Rh_{55}@(PPh_3)_n$ nanoparticles embedded into a solvent box in order to explore the influence of the solvent on the ligand adsorption and on the electronic signature of the metal core. Thus, we simulated Rh_{55} icosahedral nanoclusters decorated with 1 and 7 PPh_3 ligands ($Rh_{55}@PPh_3$ and $Rh_{55}@(PPh_3)_7$) in tetrahydrofuran (THF) solvent, which has been commonly used in experimental studies.[13,34] Figure 3.7 shows a snapshot of the two AIMD simulated structures. The analysis of properties was averaged over the 3 ps of the 5 ps simulations at 343 K.

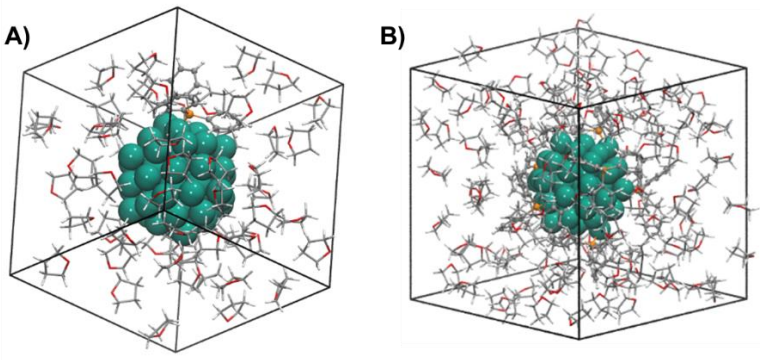

Figure 3.7 Snapshots of AIMD simulated systems: A) Rh_{55} ICO NP with 1 PPh_3 adsorbed and 55 THF solvent molecules; and B) Rh_{55} ICO NP with 7 PPh_3 ligands adsorbed in 112 THF solvent molecules.

Initially, we equilibrated the system using classical MD simulation, and keeping frozen the Rh and P core at the DFT optimized geometry in gas phase (see Computational Details). Then, we selected the final configuration as starting point for AIMD simulations. Figure 3.8 plots the evolution of the rhodium-phosphorous and rhodium-phenyl center of mass (com) distance over 3 ps for Rh_{55}@PPh_3. Figure 3.8 also shows the initial configuration of Rh_{55}@PPh_3, in which the phosphorous atom coordinates to an edge rhodium atom (Rh1) (distance Rh-P = of 2.25 Å) and two carbon atoms of the phenyl ring (*ortho* and *ipso*) are interacting with the NP surface, (distance Rh-phenyl com = 3.45 Å). The P-Rh1 distance did not present significant variations with respect to the initial P-Rh1 distance (2.25 Å) and throughout the simulation it oscillated around 2.2-2.3 Å, indicating a strong covalent-type interaction between P and Rh nanoparticle surface. On the other hand, the phenyl ring (com) approaches to the nanoparticle surface (from 3.5 to 2.2 Å after 1 ps of simulation) forming a π-type, η^6-phenyl interaction, which remains stable during the rest of simulation (av. phenyl-surface = 2.1 Å). This indicates that the π-interaction of phenyl with Rh surface is present during PPh_3 phosphine adsorption in solvent conditions because it overcomes competitive phenyl-solvent and solvent-nanoparticle interactions. Also we can conclude that the interactions characterized previously by static DFT calculations are reliable.

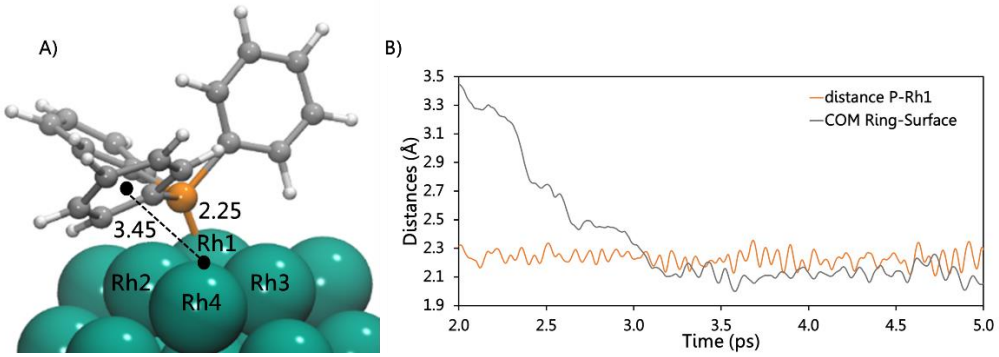

Figure 3.8 A) Initial configuration of AIMD simulation. Distances in Å. B) Evolution of P-Rh1 and $Ring_{com}$-$Surface_{com}$ distances during simulation. Distances in Å and time in ps.

These simulations can be also used to gauge the interface between metal nanoparticle and the solvent (THF). We observed that solvent molecules adsorb on the nanoparticle surface through the covalent interactions of their oxygen atoms with Rh atoms in atop mode. Figure 3.9 shows the radial distribution function (RDF) between the oxygen atoms of THF molecules and the Rh atom at the center of the NP. In the graph, we can identify two sharp peaks in the range from 6.6 to 7.8 Å (highlighted in blue and yellow, respectively). The first peak centered at 6.85 Å corresponds to the coordination of THF molecules to the edge Rh atoms (sum of $Rh_{central}$-Rh_{edge} and Rh_{edge}-O distances, 4.53 and 2.35 Å) and integrates 0.72 THF molecules. The second peak centered 7.25 Å corresponds to the vertex Rh atoms (sum of $Rh_{central}$-Rh_{vertex} and Rh_{vertex}-O distances, 5.09 and 2.26 Å) and has a large integration (3.91 THF molecules) indicating that the THF adsorbs preferentially at the vertex sites of the nanoparticle. There is also a broad peak from 8.8 to 10.8 Å that can be attributed to the first solvation sphere of the NP, where there is not a clear preferred orientation of the solvent molecules. Overall, this simulation, predicts that five THF molecules on average are absorbed on the nanoparticle surface. The interaction of THF molecules is dynamic in nature showing adsorption and desorption process during the simulation as illustrated in Figure 3.10. We selected three THF molecules that represent three different situations, such as adsorbed molecule (red), adsorption process (yellow) and desorption process (green). Accordantly, static DFT calculations on the adsorption of THF molecules on an edge or vertex atom gives modest energies of -0.19 and -0.50 eV, respectively. Moreover, these values are lower than the estimated interaction energies of the phenyl rings of the ligand, suggesting that THF solvent molecules do not compete for adsorption sites with the π-interaction of the phenyl substituents of phosphine.

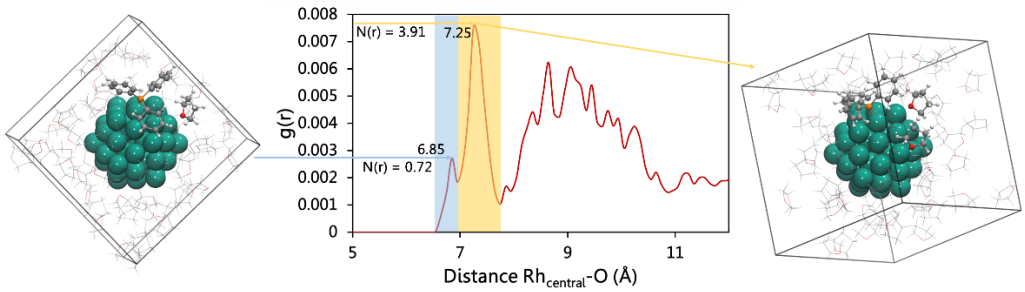

Figure 3.9 AIMD simulations for the Rh_{55}@PPh_3 in THF. Radial Distribution Function (RDF) between the O atom of THF and $Rh_{central}$ atom of NP. Blue zone corresponds to THF adsorbed on Rh edge atoms, and yellow zone to THF adsorbed on Rh corner atoms. The centers of the peaks in Å and integrated number of THF molecules, N(r). Representative snapshots for THF adsorption through the O atom corresponding to the different RDF peaks.

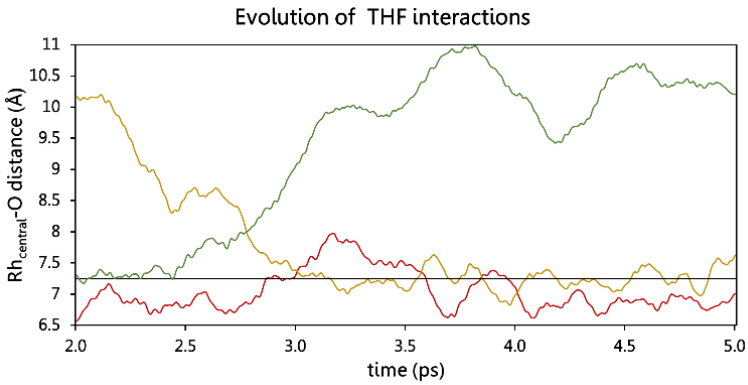

Figure 3.10 Representation of the dynamic nature of the interaction of the THF molecules plotting the evolution of the $Rh_{central}$-O distance of selected representative THF molecules. Each color represents one THF molecule. The black straight line at 7.25 Å indicates the threshold of Rh-THF interaction.

During the simulation of high coverage, Rh_{55}@$(PPh_3)_7$, the seven phosphines remain adsorbed on the Rh surface, showing different types of interactions represented in the RDF plot of Figure 3.11. There are PPh_3 ligands with phenyl rings fully adsorbed on a (111) face of the nanoparticle (peak centered at 6.65 Å and integrating 5 phenyl rings), or interacting with the nanoparticle edge (green zone integrating almost 4 phenyl rings), or only through the P atom (blue zone integrating 12 phenyl substituents). The solvent-NP interaction is represented by the RDF data in Figure 3.12 that shows a peak centered at 7.55 Å and integrating 1.08 THF molecules that indicates that there is only one molecule of THF in the first coordination sphere of the NP, but no more. The high coverage of phosphine

ligands prevents adsorption of the solvent. During the simulation, we observed only one THF molecule interacting with the nanoparticle in a dynamic fashion that suggests weak interaction. This adsorption of THF is illustrated by the snapshot also in Figure 3.12.

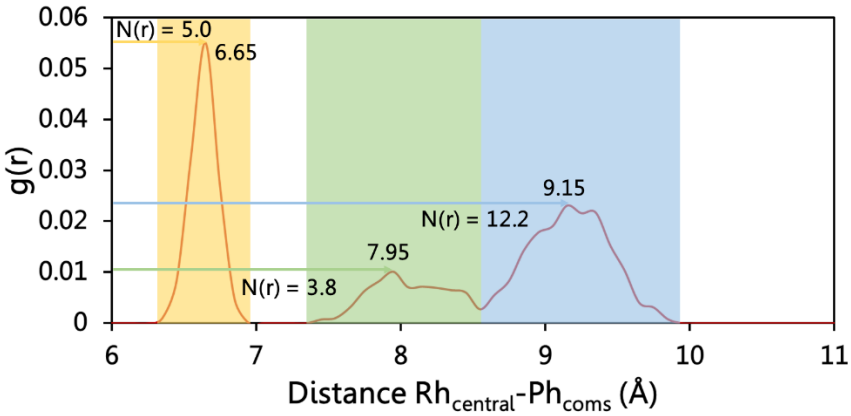

Figure 3.11. RDF between the center of mass of the phenyl rings and the $Rh_{central}$ atom for the NP for AIMD simulation of $Rh_{55}@(PPh_3)_7$ in THF. Yellow zone corresponds to phenyl rings interacting in η^6 mode, green zone corresponds to the phenyl rings interacting in η^2 mode and blue zone corresponds with the phenyl rings that do not interact with the NP. The center of the peak in Å and integrated number of phenyl rings, N(r).

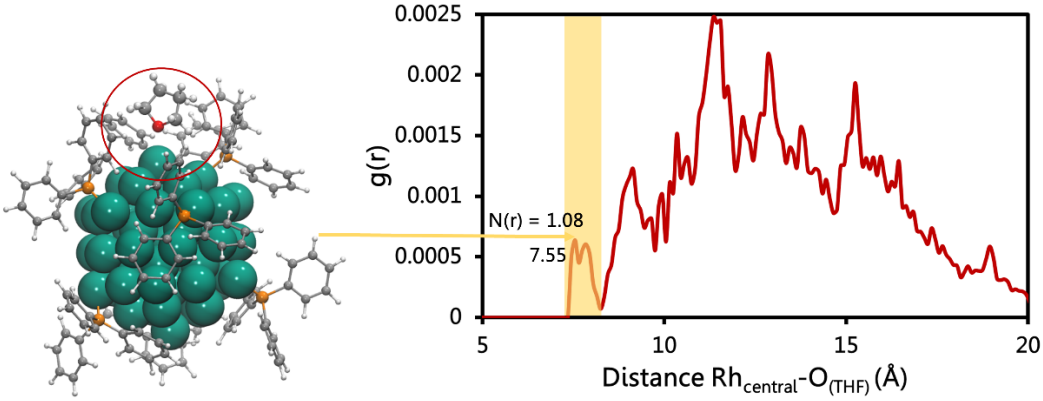

Figure 3.12 Radial Distribution Function between the O atom of the THF and $Rh_{central}$ atom of the NP for AIMD simulation of $Rh_{55}@(PPh_3)_7$ in THF. Yellow zone corresponds to THF adsorbed on Rh corner atoms. The center of the peak in Å and integrated number of THF molecules, N(r). Representative snapshot of the situation corresponding to the highlighted peak (the rest of THF molecules are omitted for clarity).

Overall, AIMD simulations on phosphine-decorated nanoparticles in solution reveals the following features: 1) the π-interaction of phenyl ring substituents with nanoparticle surface is not an artifact of gas phase calculations, but they are also relevant in solution, 2) the solvent molecules (THF) can weakly adsorb on non-protected nanoparticle sites, and 3) increasing the phosphine coverage, maintains its interaction mode in despite of the increase of ligand-ligand repulsion.

3.2.3 Interaction of Rh_{55} NPs with Other Phosphines

The adsorption of other phosphine ligands was investigated and compared to PPh_3. They include tri(*o*-tolyl)phosphine ($P(o\text{-tolyl})_3$) (**2**), triphenyl phosphite ($P(OPh)_3$) (**3**) and triphenyl phosphine oxide ($OPPh_3$) (**4**). Table 3.5 compares the adsorption energies of the studied phosphines for different adsorption modes.

Table 3.5. Adsorption energies of the different studied phosphines for different adsorption modes.

	P/O_{edge}-η^6	P/O_{edge}- η^2	P/O_{vertex}
PPh_3	-2.96	-1.81	-1.50
$P(o\text{-tolyl})_3$	-	-1.03	-1.06
P(OPh)3	-4.15	-	-1.44
$OPPh_3$	-2.43	-	-1.96

$P(o\text{-tolyl})_3$. Placing the phosphine molecule on different possible adsorption sites, three representative structures were obtained, shown in Figure 3.13. As expected, in all cases the P atom is bound in atop mode on both Rh sites, vertex and edge. In the corner adsorption we located one isomer, in which the phosphine substituents do not interact with Rh surface (**2-corner**). For edge adsorption, we found two different interaction modes of the phosphine substituents, **2A-edge** and **2B-edge**. In **2A-edge** the methyl substituents of the tolyl moieties point towards the Rh surface preventing the interaction of the aromatic rings. In **2B-edge**, the phosphine bends towards the 111 face and distorts to allow the interaction of one tolyl substituent with the nanoparticle through *meta* and *ortho* carbon atoms of the aromatic ring (Figure 3.13). This is reflected in the elongation of the C_{meta}-C_{ortho} bond from 1.41 Å to 1.44 Å. The computed adsorption energies are similar for all the isomers ranging from -0.69 and -1.06 eV. The higher adsorption energy in **2-corner** respect to **2A-edge** (-1.06 vs. -0.69 eV) reflect the different coordination sphere of vertex and edge Rh atoms, respectively, while the interaction of one tolyl substituent with Rh surface

in **2B-edge** has a minor impact (-1.03 eV). More interestingly, the adsorption energies of P(*o*-tolyl)$_3$ phosphine are significantly lower than those computed for PPh_3 phosphine (from -1.50 eV in corner adsorption to -1.81 and -2.96 eV in edge coordination, see Table 3.2). As we will describe in next Chapter, this has important consequences on the selectivity of isotope exchange catalyzed by Rh nanoparticles. The steric hindrance between the methyl groups of the tolyl substituents and the Rh surface hinders both the coordination of the P atom to the Rh and the aromatic ring. Thus, the P-Rh distances are larger for P(*o*-tolyl)$_3$ adsorption than for PPh_3 (2.33 vs 2.28 Å and 2.29 vs 2.26 Å in corner and edge sites, respectively).

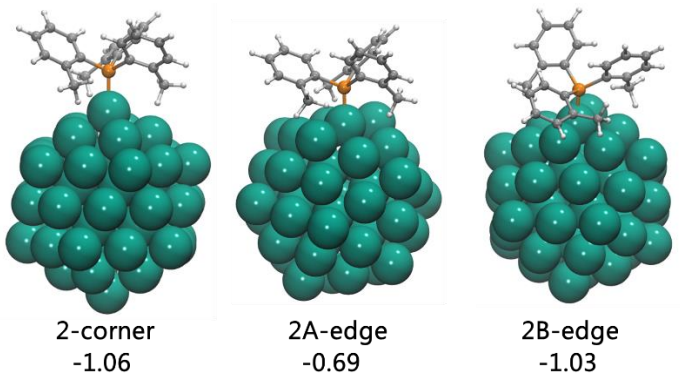

Figure 3.13 Computed structures and adsorption energies for P(*o*-tolyl)$_3$ onto Rh_{55} ICO NP. Energies in eV.

P(OPh)$_3$. In the case of P(OPh)$_3$ phosphite, the P atom was adsorbed onto the vertex and edge Rh atoms and the structures after fully relaxation are represented in Figure 3.14. Compared to PPh_3, phosphine P(OPh)$_3$ is less basic and consequently its adsorption energy on the vertex (-1.44 eV) is somewhat lower than for PPh_3 (-1.50 eV). However, in the adsorption on the edge of P(OPh)$_3$ the flexibility of the O bridge atoms, allows two phenyl rings interacting effectively with a double η^6 mode with two nanoparticle faces that results in a very strong adsorption, -4.15 eV.

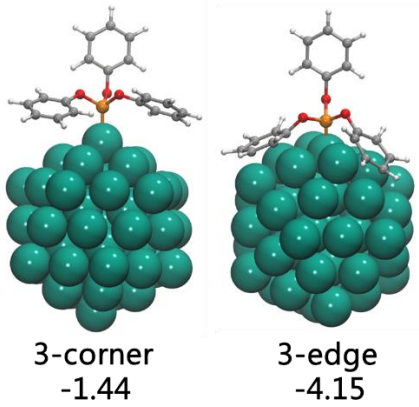

Figure 3.14 Computed structures and adsorption energies for $P(OPh)_3$ onto Rh_{55} ICO NP. Energies in eV.

$OPPh_3$. Finally, we analyzed the phosphine oxide ligand $OPPh_3$, which interacts with Rh through the lone pair of the oxygen atom instead of the P atom. O-coordination on corner and edge Rh atoms are shown in Figure 3.15 (**4-corner** and **4-edge**). In both cases, the phenyl rings can fully interact on one NP face, unlike PPh_3 in which the π-interaction is only possible for coordination on the edge. When O is coordinated to an edge Rh (**4-edge**), two phenyl rings are interacting with NP in a similar adsorption mode than Rh_{55}@PPh_3 (**1A**). However, the adsorption energy drops from -2.96 for PPh_3 to -2.43 eV for $OPPh_3$ mainly due to the weaker O-coordination. Accordantly, the energy decomposition analysis reveals that the P- and O-interaction energies of PH_3 and OPH_3 fragments are -1.02 vs -0.38 eV, respectively.

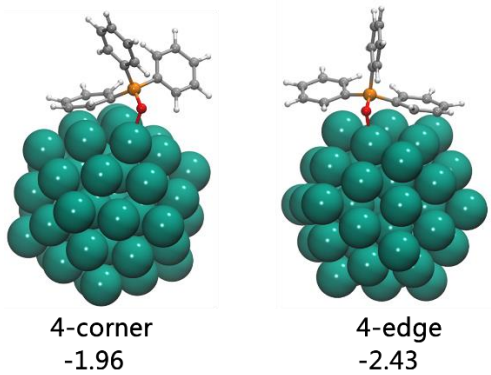

Figure 3.15 $OPPh_3$ adsorption modes and energies depending if the O atom is coordinated to a vertex (left) or an edge (right) Rh atom. Energies are in eV. Distances are in Å.

3.3 Concluding Remarks

In this chapter, we have investigated by means of classical simulations, periodic DFT calculations, and *ab initio* molecular dynamics simulations different aspects of phosphine-decorated Rh nanocatalysts, including the structural and electronic features of the Rh nanoparticle core, the adsorption modes of phosphine ligands correlating them with local and global properties of the nanoparticles, the effect of particle size and coverage, and the role of explicit solvent. First, classical Monte Carlo and MD simulations have explored the possible configurations of Rh_{49}, Rh_{55}, Rh_{75} and Rh_{147} nanoparticles, which then were studied with DFT calculations. As expected, the calculated cohesion energy showed a decreasing trend when the NP size was smaller. The d-band center clearly decreases in energy as the NP size increases, implying a stabilization of the occupied states, and reducing their adsorption strength. These facts indicate that the larger the NP, the less reactive and the less prone to adsorb ligands is.

Second, we studied the interaction of PPh_3 molecule with selected bare Rh_{55} CUB and ICO NPs. The PPh_3 adsorbs on the Rh nanoparticle surface via lone pair electrons of phosphorus atom in an atop mode. By bending the adsorbed phosphine towards the nanoparticle surface, the aromatic rings of phenyl substituents can also interact with the nanoparticle faces and edges. We characterized different type of interaction for the aromatic rings including η^6- and η^2-(C,C), and η^2-(C,H). The adsorption energy decomposition analysis reveals strong coordination of P (-1.02 eV), and even stronger π interaction of the phenyl ring (-2.28 eV), although the latter involve a larger fragment distortion due to the loss of aromaticity. In addition, the PPh_3 adsorption energy depends of the nanoparticle size, ranging from -3.06 eV for Rh_{49} to -2.45 eV for Rh_{147} and shape with an adsorption energy of -2.31 eV for Rh_{75}. Then, with all the information acquired from the previous studies, we built a regression model using the GCN and the d-band center as local and global descriptors, respectively. The model showed a good correlation with $r^2 = 0.83$, indicating a significant influence of the NP size and topology on the PPh_3 adsorption energy.

Increasing the PPh_3 coverage on a Rh_{55} ICO NP from 1 to 10 molecules lowers the adsorption energy of each individual new ligand. However, the overall adsorption energy increases up to the eighth ligand, while adsorption of the ninth and the tenth phosphines are isothermal and endothermal, respectively. Accordantly, both, d-band center and magnetization indicate stabilization of the nanoparticle up to eight PPh_3 molecules. Overall, we propose that the optimal PPh_3 coverage for a bare Rh_{55} ICO NP is about 6-7 PPh_3 ligands.

The effect of explicit solvent molecules was also analyzed using AIMD simulations for Rh_{55}@PPh_3 and Rh_{55}@$(PPh_3)_7$ systems embedded in a THF solvent box. The

THF molecules can weakly adsorb through coordination of the oxygen atoms to Rh atoms free of ligand protection. The adsorption process is reversible reveling a weak interaction that are closer to the physisorption than to the chemisorption. Thus, neither the solvent-nanoparticle nor the solvent-ligand interactions prevents the adsorption mode of PPh_3 ligands involving π interaction of their phenyl rings.

Finally, the adsorption of other phosphine ligands was evaluated and compared to PPh_3. The P(*o*-tolyl)$_3$ phosphine, shows a significant decrease in adsorption energies respect to PPh_3 because the steric hindrance of the methyl groups. In $P(OPh)_3$ phosphine the adsorption occurs by a coordination of the P atom to Rh atom, but the flexibility given by the bridging oxygen atoms, allows a more efficient interaction of the phenyl rings substituents with the nanoparticle, resulting in higher adsorption energies. In $OPPh_3$ phosphine oxide, the ligand can adsorb through the oxygen atom of the oxide group resulting in a geometry analogous to that of the lowest energy isomer for PPh_3. However, the O-interaction is weaker than the P-interaction resulting in lower overall adsorption energy.

3.4 Computational Details

Classical Simulations. Classical Monte Carlo calculations were performed using the BH-PEW[14] algorithm implemented in LoDis software.[15] For all runs, the starting point was a NP with the selected number of atoms, randomly cutting the bulk with different Miller indices planes. The number of Monte Carlo steps was set to 80000 for Rh_{49} and Rh_{55} NPs, 160000 for Rh_{75} and 320000 for Rh_{147} and the number of walkers was 2 in all cases. The temperature was 3000 K, but for Rh_{147} a temperature of 5000 K was needed to obtain the highly symmetric ICO structure. Classical MD simulations performed with LoDis were carried out in a NVT ensemble with a temperature of 400 K. The simulated time was 500 ps in all cases, with a time step of 5 fs. Andersen thermostat[35] was used to equilibrate the temperature during the whole simulation. The potential used to describe Rh-Rh interaction was taken from ref. 36.

Static DFT calculations. All quantum static calculations were performed using the Vienna Ab Initio Simulation Package 5.3.5 (VASP) program[37] within spin polarized Density Functional Theory (DFT) approximation.[38] The exchange-correlation functional used was the revised Perdew-Burke-Ernzenhof (RPBE).[39] The core electrons were described within the Projector Augmented Wave (PAW) approach[40] and the valence states were expanded in a plane-wave basis set with an energy cut-off of 400 eV. Since we were dealing with molecular systems and there was not interaction between replicated cells only the Γ k-point was used.

Geometry convergence criterion was reached when all forces were smaller than 0.01 eV $Å^{-1}$, whereas the convergence criterion for the wave function minimization was set at 10^{-5} eV. The partial occupancies of the orbitals were set by the second order Methfessel-Paxton scheme[41] with a smearing width of 0.05 eV. All Rh clusters were placed in the center of a unit cell of 30 x 30 x 30 $Å^3$, with a vacuum space between NPs of neighbor periodic images of, at least, 10 Å to avoid possible interactions.

The Rh(111) surface was modelled as a four layer slab, of which only the top two layers were allowed to relax. A large p(6x6) supercell was used to avoid possible interactions between adsorbates. A 2x2x1 k-point net generated by Monkhorst-Pack algorithm[42] was used to integrate in the reciprocal space. The partial occupancies of the orbitals were set by Methfessel-Paxton scheme[41], but the smearing used was 0.2 eV.

The adsorption energy of phosphine molecules was defined as: $E_{ads} = E_{mol/NP} - (E_{mol} + E_{NP})$, where E_{mol}, E_{NP} and $E_{mol/NP}$ are the total energy of the phosphine molecules, the total energy of the NP and the total energy of NP-PPh_3 adduct. d-band center values were calculated using the scripts from Vasp Transtition State Tools (VTST) by Henkelman group.[43]

AIMD. The starting point for AIMD was obtained by an equilibration procedure performed with GROMACS 4.5.4 classical MD simulation package.[44] The **1A** structure was placed in the center of an equilibrated cubic box of THF molecules of 25 Å of lattice. First, we performed an energy minimization with a maximum of 10000 steps. Secondly, a first equilibration within a NVT ensemble was carried out. We performed 250 ps of simulation with a time step of 1 fs. The temperature was set at 300 K regularized by Berendsen thermostat[45] and the NP-PPh_3 fragment was kept at the unit cell center. Third, a NPT ensemble was applied to adjust the sizes of the box. As previous NVT simulation, NPT last 250 ps with a time step of 1 fs. A Berendsen thermostat and barostat were used to keep the temperature and the pressure around set values of 300K and 1 bar. After NPT simulation, the unit cell changed its lattice from 25 Å to 20.9744 Å. Finally, second NVT simulation was carried out. It was composed by 250 ps of equilibration, and 20 ns of productive simulation with a time step of 1 fs. Again, Berendsen thermostat was used and the temperature was set at 300 K. The last frame of that simulation was taken as starting point for the AIMD. For $Rh_{55}@(PPh_3)_7$ system, the procedure to get the starting point for AIMD simulation was exactly the same. Only to point out that the initial cubic simulation box was 30 Å of lattice and after NPT run was decreased to 26.7021 Å. The force field used was AMBER99[46]. The bonding parameters for NP-PPh_3 fragments were not realistic and the bond force constant (750000.0 KJ mol^{-1} nm^{-2}) and angle force constant (7500.0 KJ mol^{-1} rad^{-2}) were set as bigger to keep the structure more or less rigid. However, the C-Rh

parameters were not fixed, and, for that reason, the initial structures of the AIMD simulations were not the same that those obtained by static DFT calculations. The non-bonded parameters for Rh was taken from ref. 47 and the values were σ = 0.2929 and ε = 0.221752. All parameters, bonding and non-bonding, for THF solvent molecules, as well as the equilibrated box was taken from ref. 48. AIMD simulations were performed using CP2K program[49] within the Born-Oppenheimer approach[50]. The exchange correlation functional used was the revised Perdew-Burke-Ernzenhof (revPBE)[51]. The basis sets used to describe valence electrons were DZVP-MOLOPT-SR-GTH for Rh atoms and DZVP-MOLOPT-GTH for the rest of the elements,[52] and to describe core electrons GTH-PBE pseudopotential was selected.[53] For all simulations, unrestricted formalism was applied with an energy cut-off for plane waves of 400 eV. In total, two AIMD simulations on two different systems were performed. Both simulations lasted 5 ps, with the first 2 ps considered as equilibration time, and as productive time the remaining 3 ps, with a time step of 0.5 fs. The temperature of both simulations was set at 343 K and the Nose-Hoover thermostat was applied.[54] One system (Rh_{55}@PPh_3) was composed by a Rh_{55} ICO NP with one PPh_3 molecule adsorbed and surrounded by 55 THF molecules as solvent. The dimensions of the periodic simulation box were 20.9744 x 20.9744 x 20.9744 $Å^3$. This simulation was performed in two parts: 1.4 ps of NVT ensemble and 3.6 of NVE ensemble, where 1.4 ps of NVT and 0.6 ps of NVE simulations were considered equilibration time, whereas the rest 3 ps in NVE ensemble were taken as productive time. The other system (NP-7PPh_3) was composed by Rh_{55} ICO NP with 7 PPh_3 molecules interacting with it, surrounded by 112 THF solvent molecules in a cubic box of 26.7021 Å of lattice. In this case the whole simulation was performed within NVT ensemble.

References

1. Rampino, L. D.; Nord, F. F. *J. Am. Chem. Soc.* **1941**, *63*, 2745-2749.
2. Chakraborty, I.; Pradeep, T. *Chem. Rev.* **2017**, *117*, 8208-8271.
3. Ibrahim, M.; Poreddy, R.; Philippot, K.; Riisager, A.; Garcia-Suarez, E. J. *Dalt. Trans.* **2016**, *45*, 19368-19373.
4. Castelbou, J. L.; Szeto, K. C.; Barakt, W.; Merle, N.; Godard, C.; Taoufik, M.; Claver, C. *Chem. Commun.* **2017**, *53*, 3261-3264.
5. Garcia, M. A. S.; Ibrahim, M.; Costa, J. C. S.; Corio, P.; Gusevskaya, E. V.; dos Santos, E. N.; Philippot, K.; Rossi, L. M. *Appl. Catal. A: Gen.* **2017**, *548*, 136-142.
6. Fresch, B.; Remacle, F. *J. Phys. Chem. C* **2014**, *118*, 9790-9800.
7. Guedes-Sobrinho, D.; Chaves, A. S.; Piotrowski, M. J.; Da Silva, J. L. F. *J. Chem. Phys.* **2017**, *146*, 164304.
8. Reimann, S.; Urakawa, A.; Baiker, A. *J. Phys. Chem. C* **2010**, *114*, 17836-17844.
9. Cusinato, L.; Del Rosal, I.; Poteau, R. *Dalt. Trans.* **2017**, *46*, 378-395.
10. Ortuño, M. A.; López, N. *ACS Catal.* **2018**, *8*, 6138-6145.
11. Almora-Barrios, N.; Cano, I.; van Leeuwen, P. W. N. M.; López, N. *ACS Catal.* **2017**, *7*, 3949-4954.
12. Pei, Y.; Shao, N.; Gao, Y.; Zeng, X. C. *ACS Nano* **2010**, *4*, 2009-2020.
13. Castelbou, J. L.; Blondeau, P.; Claver, C.; Godard, C. *RSC Adv.* **2015**, *5*, 97036.
14. Rossi, G.; Ferrando, R. *Chem. Phys. Lett.* **2006**, *423*, 17-22.
15. a) LoDis manual: https://github.com/kcl-tscm/LoDiS. b) Baletto, F.; Ferrando, R.; Fortunelli, A.; Montalenti, F.; Mottet, C. *J. Chem. Phys.* **2002**, *116*, 3856. c) Baletto, F.; Mottet, C.; Ferrando, R. *Phys. Rev. Lett.* **2000**, *84*, 5544. d) Baletto, F. *J. Phys.: Condens. Matter* **2019**, *31*, 113001.
16. Rosato, V.; Guillope, M.; Legrand, B. *Philosophical Magazine A* **1989**, *59:2*, 321-336.
17. a) Hammer, B.; Norskov, J. K. *Surf. Sci* **1995**, *343*, 211-220. b) Hammer, B.; Morikawa, Y.; Norskov, J. K. *Phys. Rev. Lett.* **1996**, *76*, 2141-2144. c) Hammer, B.; Norskov, J. K. *In Impact of Surface Science on Catalysis*; Gates, B. C., Knozinger, H., Eds.; Advances in Catalysis; Academic Press: San Diego, CA, 2000; Vol. 45, pp 71-129.
18. a) del Rosal, I.; Mercy, M.; Gerber, I. C.; Poteau, R. *ACS Nano* **2013**, *7*, 9823-9835. b) Cusinato, L.; del Rosal, I.; Poteau, R. *Dalton Trans.* **2017**, *46*, 378.
19. Piotrowski, M. J.; Ungureanu, C. G.; Tereshchuk, P.; Batista, K. E. A.; Chaves, A. S.; Guedes-Sobrinho, D.; Da Silva, J. L. F. *J. Phys. Chem. C* **2016**, *120*, 28844–28856.
20. Kappes, M. M.; Rapps, T.; Schooss, D.; Waldt, E.; Ahlrichs, R. *Angew. Chemie Int. Ed.* **2013**, *52*, 6102–6105.

21. Ibrahim, M.; Garcia, M. A. S.; Vono, L. L. R.; Guerrero, M.; Lecante, P.; Rossi, L. M.; Philippot, K. *Dalt. Trans.* **2016**, *45*, 17782–17791.
22. Martinez-Espinar, F.; Blondeau, P.; Nolis, P.; Chaudret, B.; Claver, C.; Castillón, S.; Godard, C. *J. Catal.* **2017**, *354*, 113–127.
23. a) Qi, W. H.; Wang, M. P.; Xu, G. Y. *Chem. Phys. Lett.* **2003**, *372*, 632-634. b) Qi, W. H.; Wang, M. P.; Hu, W. Y. *Mater. Lett.* **2004**, *58*, 1745-1749. c) Qi, W. H.; Wang, M. P.; Zhou, M.; Shen, X. Q.; Zhang, X. F. *J. Phys. Chem. Solids* **2006**, *67*, 851-855. d) Qi, W. H.; Wang, M. P. *Mater. Chem. Phys.* **2004**, *88*, 280-284. e) Qi, W. H.; Huang, B. Y.; Wang, M. P.; Li, Z.; Yu, Z. M. *Phys. Lett. A* **2007**, *370*, 494-498. f) Qi, W. H. *J. Mater. Sci.* **2006**, *41*, 5679-5681.
24. Bae, Y. C.; Kumar, V.; Osanai, H.; Kawazoe, Y. *Phys. Rev. B - Condens. Matter Mater. Phys.* **2005**, *72*, 1–6.
25. Deushi, F.; Ishikawa, A.; Nakai, H. *J. Phys. Chem. C* **2017**, *121*, 15272–15281.
26. a) Calle-Vallejo, F.; Martínez, J. I.; García-Lastra, J. M.; Sautet, P.; Loffreda, D. *Angew. Chem. Int. Ed.* **2014**, *53*, 8316–8319. b) Calle-Vallejo, F.; Tymoczko, J.; Colic, V.; Vu, Q. H.; Pohl, M. D.; Morgenstern, K.; Loffreda, D.; Sautet, P.; Schuhmann, W.; Bandarenka, A. S. *Science* **2015**, *350*, 185–189. c) Asara, G. G.; Paz-Borbjn, L. O.; Baletto, F. *ACS Catal.* **2016**, *6*, 4388 – 4393. d) Tymoczko, J.; Calle-Vallejo, F.; Schuhmann, W.; Bandarenka, A. S. *Nat. Commun.* **2016**, *7*, 10990. e) Calle-Vallejo, F.; Pohl, M. D.; Bandarenka, A. S. *ACS Catal.* **2017**, *7*, 4355–4359.
27. Rossi, K.; Asara, G. G.; Baletto, F. *Phys. Chem. Chem. Phys.* **2019**, *21*, 4888-4898.
28. Xu, H.; Cheng, D.; Gao, Y.; Zeng, X. C. *ACS Catal.* **2018**, *8*, 9702-9710.
29. Hammer, B.; Norskov, J. K. *Nature* **1995**, *376*, 238-240.
30. Toyoda, E.; Jinnouchi, R.; Hatanaka, T.; Morimoto, Y.; Mitsuhara, K.; Visikovskiy, A.; Kido, Y. *J. Phys. Chem. C* **2011**, *115*, 43, 21236-21240.
31. Prabowo, W. A. E.; Khoiroh, N.; Wibisono, S.; Supardi, A. *J. Phys.; Conf. Ser.* **2020,** *1445,* 012011.
32. Cusinato, L.; Martínez-Prieto, L. M.; Chaudret, B.; del Rosal, I.; Poteau, R. *Nanoscale* **2016**, *8*, 10974-10992.
33. Ortuño, M. A.; López, N. *Catal. Sci. Technol.* **2019**, *9*, 5173-5185.
34. a) Castelbou, J. L.; Szeto, K. C.; Barakat, W.; Merle, N.; Godard, C.; Taoufik, M.; Claver, C. *Chem. Commun.* **2017**, *53*, 3261. b) Martínez-Espinar, F.; Blondeau, P.; Nolis, P., Chaudret, B.; Claver, C.; Castillón, S.; Godard, C. *J. Catal.* **2017**, *354*, 113-127.
35. Andersen, H. C. *J. Chem. Phys.* **1980**, *72*, 2384.
36. Soon, Y. Y.; Lim, T. L.; Yoon, T. L. *AIP Conf. Proc.* **2015**, *1657*, 110001.
37. a) Kresse, G.; Hafner, J. *Phys. Rev. B* **1993**, *47*, 558. b) Kresse, G.; Furthmüller, J. *Comput. Mat. Sci.* **1996**, *6*, 15-50. c) Kresse, G.; Furthmüller, J. *Phys. Rev. B* **1996**, *54*, 11169.

38. a) Hohenberg, P.; Kohn, W. *Phys. Rev.* **1964**, *136*, 864-871. b) Kohn, W.; Sham, L. J. *Phys. Rev.* **1965**, *140*, 1133-1138.
39. Hammer, B.; Hansen, L. B.; Norskov, J. K. *Phys. Rev. B* **1999**, *59*, 7413.
40. Kresse, G.; Joubert, D. *Phys. Rev. B* **1999**, *59*, 1758.
41. Methfessel, M.; Paxton, A. T. *Phys. Rev. B* **1989**, *40*, 3616.
42. Monkhorst, H. J.; Pack, J. D. *Phys. Rev. B* **1976**, *13*, 5188.
43. VTSTTools, Henkelman group, University of Texas, Austin, TX, USA. https://theory.cm.utexas.edu/vtsttools/index.html#
44. a) Berendsen, H. J. C.; van der Spoel, D.; van Drunen, R. *Comp. Phys. Comm.* **1995**, *91*, 43-56. b) Lindahl, E.; Hess, B.; van der Spoel, D. *J. Mol. Model.* **2001**, *7*, 306-317. c) van der Spoel, D.; Lindahl, E.; Hess, B.; Groenhof, G.; Mark, A. E.; Berendsen, H. J. C. *J. Comput. Chem.* **2005**, *26*, 1701-1718. d) Hess, B.; Kutzner, C.; van der Spoelen, D.; Lindahl, E. *J. Chem. Theory Comput.* **2008**, *4*, 435-447. e) Pronk, S.; Páll, S.; Schulz, R.; Larsson, P.; Bjelkmar, P.; Apostolov, R.; Shirts, M. R.; Smith, J. C.; Kasson, P. M.; van der Spoelen, D.; Hess, B.; Lindahl, E. *Bioinformatics* **2013**, *29*, 845-854. f) Páll, S.; Abraham, M. J.; Kutzner, C.; Hess, B.; Lindahl, E. *Proc. Of EASC 2015 LNCS* **2015**, *8759*, 3-27. g) Abraham, M. J.; Murtola, T.; Schulz, R.; Páll, S.; Smith, C. J.; Hess, B.; Lindahl, E. *SoftwareX* **2015**, *1-2*, 19-25.
45. Berendsen, H. J. C.; Postma, J. P. M.; van Gunsteren, W. F.; DiNola, A.; Haak, J. R. J. *Chem. Phys.* **1984**, *81*, 3684.
46. Wang, J.; Cieplak, P.; Kollman, P. A. *J. Comput. Chem.* **2000**, *21*, 1049-1074.
47. Prasanth, K. P.; Pillai, R. S.; Bajaj, H. C.; Jasra, R. V.; Chung, H. D.; Kim, T. H.; Song, S. D. *Int. J. Hydrog. Energy* **2008**, *33*, 735-745.
48. Parameters of THF and equilibrated solvent box were taken from: http://virtualchemistry.org/index.php, and those parametres were refered to : a) Caleman, C.; van Maaren, P. J.; Hong, M.; Hub, J. S.; Costa, L. T.; van der Spoel, D. *J. Chem. Theory Comput.* **2012**, *8*, 61-74. b) Fisher, N. M.; van Maaren, P. J.; Ditz, J. C.; Yildirim, A.; van der Spoel, D. *J. Chem. Theory Comput.* **2015**, *11*, 2938-2944. c) Zhang, J.; Tuguldur, B.; van der Spoel, D. *J. Chem. Inf. Model.* **2015**, *55*, 1192-1201.
49. Kühne, T. D.; Iannuzzi, M.; Ben, M. D.; Rybkin, V. V.; Seewald, P.; Stein, F.; Laino, T.; Khaliullin, R. Z.; Schütt, O.; Schiffmann, F.; Golze, D.; Wilhem, J.; Chulkov, S.; Bani-Hashemian, M. H.; Weber, V.; Borstnik, U.; Taillefumier, M.; Jakobovits, A. S.; Lazzaro, A.; Pabst, H.; Müller, T.; Schande, R.; Guidon, M.; Andermatt, S.; Holmberg, N.; Schenter, G. K.; Hehn, A.; Bussy, A.; Belleflamme, F.; Tabacchi, G.; Glöss, A.; Lass, M.; Bethune, I.; Mundy, C. J.; Plessl, C.; Watkins, M.; VandeVondele, J.; Krack, M.; Hutter, J. *J. Chem. Phys.* **2020**, *152*, 194103.
50. Born, M.; Oppenheimer, J. R. *Ann. Phys*, **1927**, *84*, 457-484.
51. Zhang, Y.; Yang, W. *Phys. Rev. Lett.* **1998**, *80*, 890.

52. VandeVondele, J.; Hutter, J. *J. Chem. Phys.* **2007**, *127*, 114105.

53. a) Goedecker, S.; Teter, M.; Hutter, J. *J. Phys. Rev. B* **1996**, *54*, 1703. b) Hartwigsen, C.; Goedecker, S.; Hutter, *J. Phys. Rev. B.* **1998**, *58*, 3641. c) Krack, M. *Theor. Chem. Acc.* **2005**, *114*, 145.

54. a) Nosé, S. *J. Chem. Phys.* **1984**, *81*, 511. b) Nosé, S. *Mol. Phys.* **1984**, *52*, 255-268. c) Hoover, W. G. *Phys. Rev. A* **1985**, *31*, 1695. d) Evans, D. J.; Holian, B. L. *J. Chem. Phys.* **1985**, *83*, 4069.

UNIVERSITAT ROVIRA I VIRGILI
COMPUTATIONAL MODELING TO EXPLORE SOLVENT AND DYNAMIC EFFECTS IN MOLECULAR, NANO AND SOLID CATALYSIS
Antoni Salom Català

Chapter 4:

Origin of Selective Deuteration of Phosphorus Ligands Catalyzed by Rh Nanoparticles

UNIVERSITAT ROVIRA I VIRGILI
COMPUTATIONAL MODELING TO EXPLORE SOLVENT AND DYNAMIC EFFECTS IN MOLECULAR, NANO AND SOLID CATALYSIS
Antoni Salom Català

Chapter 4

Origin of Selective Deuteration of Phosphorous Ligands Catalyzed by Rh Nanoparticles

Castillón et al. *selectively deuterated specific positions of different phosphine ligands using Rh- and Ru-based metal nanoparticles decorated by N-heterocyclic carbenes (NHC) or polyvinylpyrrolidone (PVP) as catalysts. Based on those experimental results, we used Density Functional Theory (DFT) approach to understand the observed selectivity. By quantum mechanical (QM) calculations, we proposed a plausible mechanism for the Hydrogen Isotope Exchange (HIE) reaction, showing a high influence of the phosphine geometry on the selectivity, and the need of defects on the nanoparticle surface, such as corner and edges, to make the C-H activation feasible.*

4.1 Introduction

C-H activation has become a powerful technique for the synthesis and functionalization of complex organic compounds via the subsequent formation of a large variety of C-C, C-N, C-O, C-B and C-D bonds.[1] The formation of C-D bonds provides rapid access to deuterium labelled compounds, which are of interest in basic research on C-H bond activation[2] or in mechanistic investigations on catalysts and reaction pathways.[3]

In this context, several methodologies based on H/D exchange using homogeneous and heterogeneous metal catalysts have been reported.[1a,4] Currently, the use of well-defined heterogeneous catalysts, and particularly metal nanoparticles (MNPs), is of high interest for academic and industrial chemists.[5] Regarding the H/D exchange using MNPs, the labelling of N-containing compounds has been mainly studied. For instance, Sullivan *et al.* reported the application of Pd NPs stabilized by 4-dimethylaminopyridine (DMAP) for the selective H/D exchange of pyridine-based compounds using D_2O as deuterium source.[6] This catalytic system promoted selective H/D exchange of protons in α position of the endocyclic N atom of DMAP. The use of Pd NPs stabilized by polyvinylpyrrolidone (PVP) was also investigated for the deuteration of N-based molecules such as pyridines, N-methylimidazole and quinoline, indicating interactions between the NPs surface and the N atom in all cases. [7,8,9]

Mobile and reactive hydride species at the surface of Ru NPs stabilized by hexadecylamine (HDA) undergo H/D exchange when exposed to a D_2 atmosphere.[10] H/D exchange in pyridine[11] derivatives and phosphine oxides[12] used as stabilizers was also observed by ^{2}D MAS NMR after exposure to D_2.

Later, the application of Ru NPs stabilized by PVP for the regioselective and stereospecific deuteration of N-containing substrates under mild reaction conditions using D_2 as deuterium source was reported (Scheme 4.1).[15] The D-labelling of pyridines, quinolines, indoles and alkyl amines, with high isotopic enrichment in positions close to the N atom suggested the direct coordination of the N atom to the surface of the Ru NPs. Rosseau, Chaudret *et al.* have reported the enantiospecific deuterium incorporation at the stereogenic center of amino acids following the same methodology.[13] Recently, water soluble Ru NPs stabilized by sulfonated N-heterocyclic carbine (NHC) ligands were also reported in the H/D exchange of L-Lysine and variation of the pH showed to directly affect the selectivity of the reaction.[14]

Scheme 4.1. Deuteration of amino derivatives reported by Chaudret *et al.*[12,15]

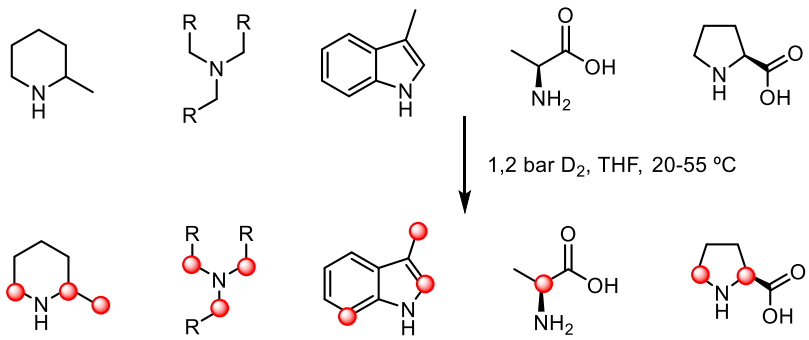

Catalytic deuterium incorporation in phosphorus based ligands has not been reported and only stoichiometric labelling in molecular complex has been informed.[16] In this context, Castillón's group at URV has developed the catalytic labelling of such ligands using NPs, also aiming at gaining information on their coordination mode at metallic surfaces.[17] Specifically, they reported that Ru NPs stabilized by PVP (**Ru@PVP**) efficiently catalyze the selective deuteration of phosphines through H/D exchange in *ortho*-position of aryl phosphines such as PPh_3 and derivatives, while the alkyl group of phenyl-alkylphosphines remained unaltered.[18] Interestingly, when $O{=}PPh_3$ was used as substrate, the reduction of the aromatic rings was observed. Next, Castillón *et al.* have extended this study to a wider range of P-ligands deuterated using D_2 by ruthenium and rhodium NPs stabilized by PVP (**Ru@PVP**) and NHC (**Ru@NHC** and **Rh@NHC)** ligands.

This will allow to evaluate whether, as in molecular systems, it is possible to tune the selectivity of this reaction either using other metal or through modification of the coordination sphere around the nanoparticle. In collaboration with the experimental group, this chapter aims to report a DFT study on the mechanism and the origin of selectivity of deuteration of selected phosphine ligands over the surface of rhodium and ruthenium NPs decorated by NHC carbenes, providing also additional information of the phosphine coordination with respect to previous Chapter.

4.2 Experimental Background

In a previous work, Castillón *et al.* reported the full deuteration of PPh_3 phosphine at ortho position using Ru metal nanoparticles (NPs) stabilized with PVP (**Ru@PVP**) as catalyst.[18] More recently, the experimental work has been extended to the study of rhodium and ruthenium nanoparticles stabilized by N-heterocyclic carbenes, **Rh@NHC** and **Ru@NHC**, comparing the results with those obtained with **Ru@PVP**, in order to assess the influence in the reaction of the ligand shell and of the nature of the metal. The use of **Rh@PVP** was discarded due to its low solubility under the working conditions.

Structurally different phosphines were also selected as shown in Figure 4.1. They include aryl phosphines (**1**-**3**), mixed aryl/alkyl phosphines (**4**), phosphines with heteroatoms (**5**-**7**) and diphosphines (**8**,**9**).

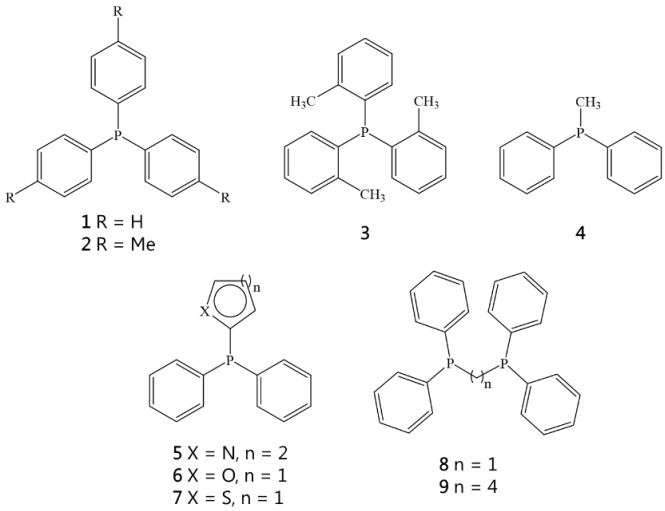

Figure 4.1. Selected phosphines for the experimental deuteration study using **Ru@NHC** and **RhNHC** nanoparticles as catalyst.

Table 4.1 collects the results for phosphines **1** and **2**, for which only deuteration in ortho positions of the phenyl rings was detected. The Ru NPs showed higher activity than those of Rh. Thus, the reaction with Ru-based NP afforded full conversion after 48h with fully ortho deuterated product **f** (6 positions) as major product, showing up to 92 and 87 % selectivity for phosphine **1** and **2**, respectively (Table 4.1, entries 1-3 and 5-7). For **Rh@NHC** NPs, the reaction led to conversions up to 87% or 69% for phosphines **1** and **2**, respectively, while major products showed deuteration at only 1, 2, or 3 ortho C-H bonds (products **a**-**c** Table 4.1, entries 4 and 8). The methyl substituent in para position did not affect neither the selectivity or conversion rate, since phosphine **2** presented very similar results than phosphine **1**, and in any case, the H/D exchange in alkyl positions was not observed.

Table 4.1. Experimental results for H/D exchange on phosphines **1** and **2** using Ru and Rh NPs. Number of deuterated ortho sites ranges from 1 to 6 (**a** to **f** labels). The order of deuteration is first one C-H bond of each ring, and then the second ortho position. Percentage of products after 48h.[a]

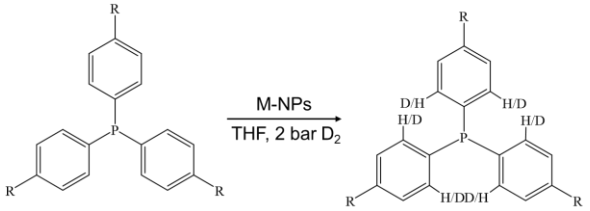

Entry	PR_3	NPs	Prod	a[b]	b[b]	c[b]	d[b]	e[b]	f[b]
1[18]	1	Ru@PVP[c]	1a-f	0	0	2	12	35	51
2[18]	1	Ru@PVP[c,e]	1a-f	0	0	0	0	8	92
3	1	Ru@NHC[d]	1a-f	0	0	0	1	16	83
4	1	Rh@NHC[d]	1a-f	19	23	18	12	7	8
5[18]	2	Ru@PVP[c]	2a-f	0	0	0	1	12	87
6[18]	2	Ru@PVP[c,e]	2a-f	0	0	0	0	9	91
7	2	Ru@NHC[d]	2a-f	0	0	0	1	12	87
8	2	Rh@NHC[d]	2a-f	22	20	10	7	3	7

[a]Conditions: NPs, solvent = THF. D_2 pressure = 2 bar. T = 55ºC. t = 48h; [b]NMR yield of deuterated products; [c]3 mol% cat.; [d]5 mol% cat.; [e]80 ºC.

Phosphine **3** was chosen to study the effect of methyl substituent on ortho position. When the reaction was performed with **Ru@NHC** catalyst the

deuteration of methyl groups was detected, and surprisingly, also the hydrogens of meta positions of the rings were exchanged (Scheme 4.2). Furthermore, the H/D exchange between meta positions was not equitable, being the deuteration rate on meta position 3 (close to methyl substituent) higher than on meta position 5. After 12 days of reaction, approximately 66% of H/D exchange for protons in meta position 3 and 33 % in position 5 were detected. Changing the stabilizer from **Ru@NHC** to **Ru@PVP**, the reaction only yielded traces of deuterated product.

Rh@NHC catalyst afforded similar results to **Ru@NHC** on the selectivity, but deuteration of aromatic positions is faster than of the CH_3 protons. After 48h of reaction, the $D_{aromatic}/D_{aliphatic}$ ratio was 47:53 for **Ru@NHC** catalyst, whereas this ratio shifted to 17:83 for **Rh@NHC** catalyst.

Scheme 4.2. Deuteration of phosphine **3** in presence of Ru and Rh NPs.

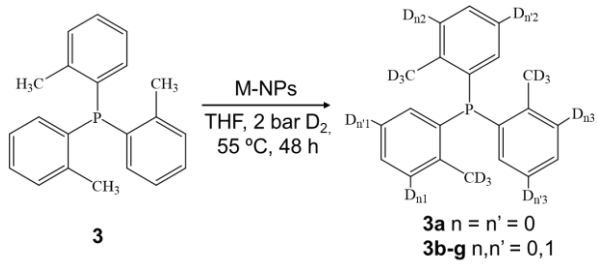

3

3a n = n' = 0
3b-g n,n' = 0,1

Mixed aryl/alkyl phosphine **4**, with a methyl group directly linked to the P atom, resulted in complete ortho deuterated positions of phenyl rings, with a progressive deuteration of methyl group. Deuteration reaction with **Ru@NHC** catalysts was fast, while using **Ru@PVP**, only ortho phenyl deuteration product **4a** was observed. In the case of **Rh@NHC**, partially deuterated products at the aromatic rings and methyl group was observed after 8 days of reaction at 55 °C indicating a lower reactivity than for **Ru@NHC**.

Replacement of methyl group in phosphine **4** by a ring containing a heteroatom such as N, O and S gives phosphines **5**, **6** and **7**, respectively. The deuteration experiments were performed using **Ru@NHC** and **Rh@NHC** catalysts under the same reaction conditions used in previous experiments, but in none of the cases, deuteration was detected.

Diphosphines **8** and **9**, differing in the length of the aliphatic linker (Figure 4.1), showed differences in the selectivity, but the overall deuteration pattern is analogous to monophosphines. Deuteration occurs at the ortho positions of the

phenyl groups and at the aliphatic carbons bound to phosphorus. For bis(diphenylphosphino)methane (dppm, **8**), no H/D exchange was observed with **Ru@NHC**, even after 8 days of reaction, while the use of **Rh@NHC** as catalyst produced selective deuteration of methylene hydrogens. On the other hand, for bis(diphenylphosphino)butane (dppb, **9**), the product resulted from exclusive deuteration on *ortho* position of phenyl rings, using either Ru or Rh NPs.

The experimental results can be summarized as follows:

1) Ru NPs are more reactive than Rh NPs towards aromatic positions.
2) Rh NPs deuterate faster alkylic C atoms than aromatic ones, and also faster than Ru NP catalysts.
3) β positions to P atom (normally ortho positions of phenyl rings) are selectively deuterated, but with two exceptions. Phosphine **3** is deuterated on methyl groups and aromatic meta position, and in case of diphosphine **8**, only alkylic positions suffer H/D exchange.
4) No reaction was observed when a heteroatom is added in a phosphine fragment.

4.3 Results and Discussion

DFT calculations were performed to understand the origin of the observed selectivity in the H/D exchange of phosphine ligands, and to set a correlation between the coordination mode and the selectivity. In general, Ru and Rh nanoparticles show similar selectivity for all phosphines, although for dppm, the isotope exchange is not observed for Ru NPs due to their low reactivity towards the aliphatic C-H bonds. Here, we have selected Rh NPs for the main study. As a model for metal NPs we used a 55-atom icosahedron (ICO) structure with a diameter of 1.29 nm (See Chapter 3). The size and the shape of the model cluster are consistent with the experimental observations in which all nanoparticles exhibited small sizes (<2nm) and spherical shapes.[17b,18] Moreover, the icosahedral structure is 1.8 eV lower in energy than other symmetric, spherical-type cuboctahedron structure, and it constitutes a simple model with only one type of face (111) and two possible adsorption sites, vertex and edge (see Figure 4.2). We have based our study in naked models in order to reduce complexity and provide fundamental understanding of the interaction of phosphines with different structural motifs of nanoparticle. However, we have compared key species with more realistic models including hydrides and NHC carbenes stabilizers on the metal surface. We selected phosphines **1** and **3** as representative ligands because

they undergo activation at two different aromatic C-H sites (*ortho* and *meta*) and at aliphatic C-H bonds.

4.3.1 Origin of selectivity towards aromatic *ortho* C-H bonds in PPh_3.

The possible coordination modes of PPh_3 phosphine (**1**) on the surface of icosahedral Rh_{55} nanoparticle have been analyzed in detail in Chapter 3. Figure 4.2 shows three representative coordinations and the corresponding adsorption energies, highlighting the specific interactions with the C-H *ortho* bonds for which deuteration is observed. To sum up, the phosphine adsorbed in atop mode through the coordination of phosphorus lone pair to a rhodium atom. In the most stable structure, the phosphine coordinates through phosphorus lone pair on the edge Rh atom, and then, it bends towards one of the nanoparticle faces allowing the interaction of two phenyl substituents. One of the phenyls interacts with the Rh(111) face through the six carbon atoms of the π system. The η^6-phenyl interaction is characterized by short Rh-C distances (2.18 Å in average) and some pyramidalization of the carbon atoms that breaks the planarity of the aromatic ring lifting the hydrogen atoms out of the ring plane. The other phenyl interacts with a vertex Rh atom, displaying a η^2-phenyl interaction with the ipso and ortho carbon atoms at distances of 2.34 and 2.35 Å, respectively.

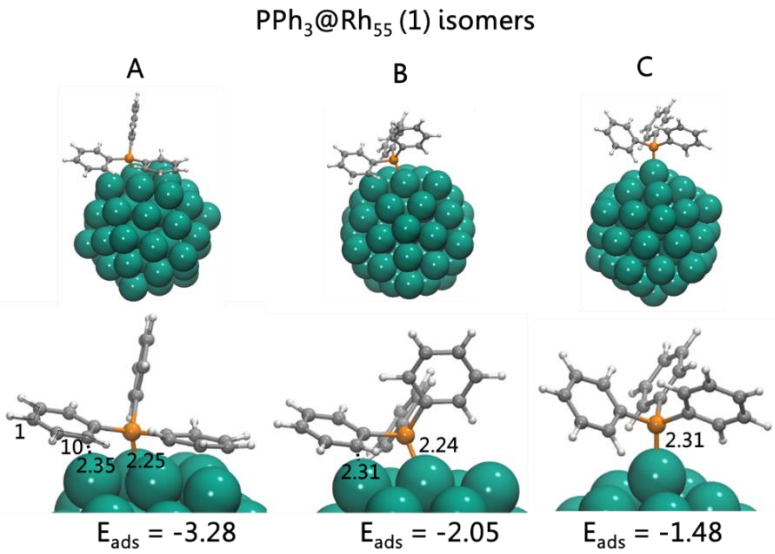

Figure 4.2. Representative adsorption modes of PPh_3 onto Rh_{55} ICO NPs. Adsorption energies are in eV and distances in Å. For detailed discussion on the adsorption of PPh_3 we refer to Chapter 3.

These two types of phenyl interactions with Rh nanoparticle in adsorbed phosphine suggest that there are two possible paths for C-H activation, the *face* and the *edge* activations. Figure 4.3 shows the computed transition states and the resulting intermediates for all the possible pathways for C-H activation of PPh_3 phosphine on Rh_{55} surface from structure **1A** (Rh_{55}@PPh_3 isomer **A** in Figure 4.2).

For the phenyl group interacting in η^6-mode, the computed energy barriers were relatively high for all the possible activations: 1.5, 2.3 and 2.1 eV for *ortho*, *meta*, and *para* C-H bond types, respectively. In the corresponding transition states, as the bond breaks, the carbon atom has to be lifted out of the ring plane in order to place the Rh atom in valence position (see Figure 4.3). This results in a large geometric distortion of the phenyl ring that losses resonance, and consequently, the energy penalty causes a prohibitively high energy barrier and high-energy laying intermediates. For instance, the C_{ortho}-C_{ipso}-C_{ortho}-C_{meta} torsion angle in $\mathbf{1TS_{ortho\text{-}f}}$ and $\mathbf{1I_{ortho\text{-}f}}$ was around 10º while in **1A** was 4º, or in the case of meta activation, the C_{meta}-C_{ortho}-C_{ipso}-P dihedral was decreased from 172º in **1A** to 165º or 162º in $\mathbf{1TS_{meta\text{-}f}}$ and $\mathbf{1I_{meta\text{-}f}}$, respectively. The distortion in *para* activation is less pronounced as reflected in the change in the P-C_{ipso}-C_{para} angle from 167º in **1A** to 165º in $\mathbf{1TS_{para\text{-}f}}$ and $\mathbf{1I_{para\text{-}f}}$. It is likely that this description is a good approximation of the behavior of aromatics compounds over larger 111 metal surfaces in extended models,[19,20] for which C-H activations have not been observed to the best of our knowlege.[21]

On the other hand, the *ortho* C-H bond interacting with the edge of the nanoparticle can be activated with a moderate energy barrier (0.6 eV) while the phenyl ring is not significantly distorted along the process (see structures $\mathbf{1TS_{ortho\text{-}e}}$ and $\mathbf{1I_{ortho\text{-}e}}$ in Figure 4.3). In fact, the resulting intermediate could be described as an ortho-metalated phosphine dirhodium fragment which is a well-known complex type in coordination chemistry. Moreover, the resulting intermediate is similar in energy than reactants, and then, the H* atom can easily exchange its position with deuterides (D*), and then, can back to the adsorbed PPh_3 phosphine with isotope exchange. The other *ortho* C-H bonds becomes accessible for activation through rotations of the phenyl rings and bending of the phosphorus atom. It is also worth to note that similar energy schemes have been reported in computational studies of H/D exchange on N-containing substrates.[12,15,22]

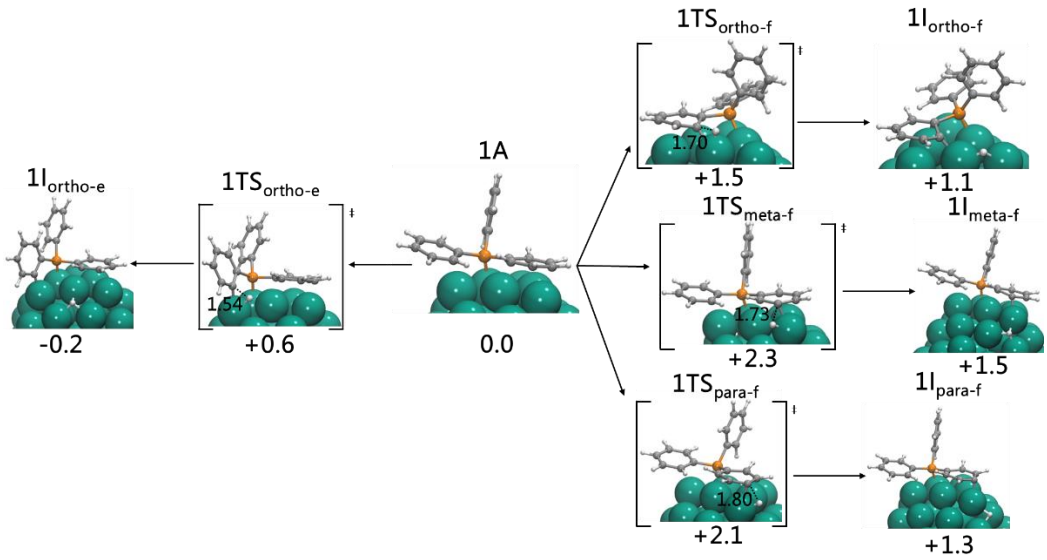

Figure 4.3. Possible C-H activation pathways of PPh_3 onto Rh_{55} ICO NPs. Right: a) *ortho*-, b) *meta*-, and c) *para*-activations of C-H bond on the 111 face (**1TS$_{ortho-f}$**, **1TS$_{meta-f}$**, **1TS$_{para-f}$** and **1I$_{ortho-f}$**, **1I$_{meta-f}$** and **1I$_{para-f}$**, respectively). Left: ortho-activation on the edge (**1TS$_{ortho-e}$** and **1I$_{ortho-e}$**). Energy barriers and relative energies in eV, and distances in Å.

Experimentally it was observed that for phosphine oxides these NPs catalyse the reduction of aromatic rings. Thus, one can envisage a different mechanism for H/D exchange in which D* species present at the surface reduce the phenyl ring, it rotates, and then the H of the reduced carbon moves to the Rh surface. Nevertheless, the computed barrier for the reduction of the *ortho* position by one hydrogen at the surface (1.1 eV) is significantly larger than the corresponding C-H activation (see Figure 4.4), and therefore, this associative mechanism can be discarded for phosphine **1**. Overall, we can conclude that for PPh_3 phosphines the H/D exchange occurs through C-H activation at nanoparticle edges where activation of *ortho* C-H bonds does not involve significant distortion of phenyl ring. In contrast, the interaction of *meta* and *para* C-H bonds with the Rh surface involve phenyl arrangements that are not suitable for smooth activations at the aromatic ring.

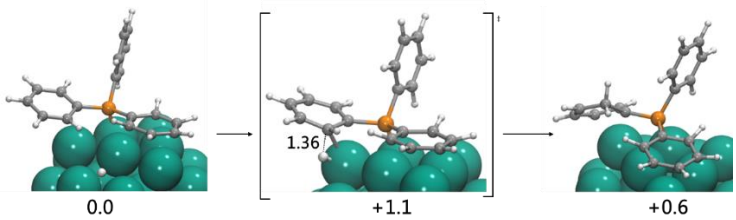

Figure 4.4. Associative mechanism for deuteration of the aromatic rings of phosphine **1**. Energies in eV and distance in Å.

4.3.2 Origin of selectivity towards aliphatic and aromatic *meta* C-H bonds in P(*o*-tolyl)$_3$.

Next we turned our attention to P(*o*-tolyl)$_3$ phosphine (**3**), in which H/D exchange is observed at aliphatic C-H bonds and at a different position of the aromatic ring, meta, compared with phosphine **1**. Using as reference the structures obtained for the adsorption of **1**, we tried to build analogous interactions between Rh_{55} and phosphine **3** (see also Chapter 3). However, the adsorption energy for **3** (-1.2 eV) is significantly lower than for **1** because the presence of a methyl group prevents η^2- and η^6-interactions of the aromatic rings. As shown in Figure 4.5, **3** adsorbs onto Rh surface through coordination of the phosphorus lone pair on an edge rhodium atom, and through one of the tolyl substituents where the methyl group and the aromatic *meta* carbon are directly interacting with the (111) face and the Rh atom at the vertex.

Figure 4.5 illustrates also the possible pathways for C-H bond activation from P-adsorbed phosphine. The computed energy barriers were 0.4 and 1.9 eV for aliphatic and aromatic *meta* C-H activations, respectively. This agrees with the relative rates of aliphatic and aromatic carbons observed experimentally, but the barrier of the aromatic C-H activation is too high to be feasible under current experimental conditions. Alternatively, the *meta* C-H bond could be activated through a sequential mechanism. After initial activation of the methyl group, the resulting intermediate could undergo a second C-H activation at *meta* position, but the computed energy barrier for the second step is even higher (2.3 eV).

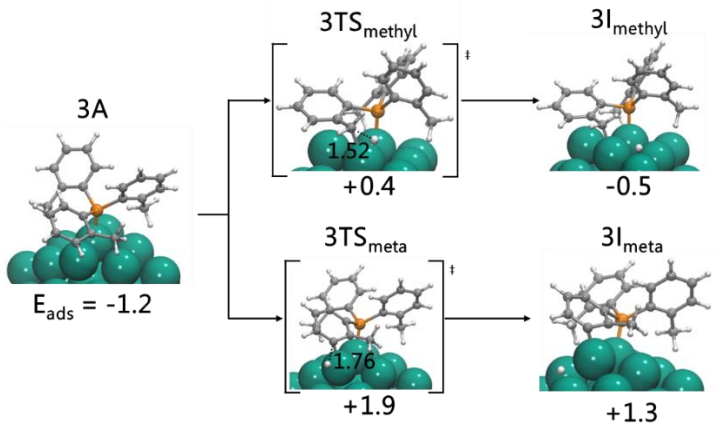

Figure 4.5. Adsorption of phosphine **3** onto Rh_{55} ICO NP (for more details, see Chapter 3). C-H activation transition states and intermediates for experimentally observed deuterated C atoms, methyl group and aromatic *meta* position. Energies in eV and distances in Å.

To explain the selectivity observed for phosphine **3**, we propose a dissociative mechanism as illustrated in Figure 4.6. Firstly, the phosphine detaches the phosphorus atom from the Rh surface, resulting in a weakly phosphine-bonded intermediate in which the phosphine interacts only through the methyl group and *meta* and *para* carbons of the aromatic ring, species **3A'**. From this adduct, the activation of the C-H bonds of methyl groups has a low energy barrier (0.2 eV), yielding the alkyl-rhodium intermediate **$3I'_{methyl}$** with the *meta* carbon interacting with one rhodium in the vertex. Then, the *meta* C-H bond can be activated with a moderate energy barrier of +0.9 eV, resulting in a 5-membered ring dirhodium metallacycle intermediate with an energy of 0.2 eV below **3A'** (Figure 4.6). The overall energy barrier for the double C-H activation is 1.3 eV, still accessible at working conditions.

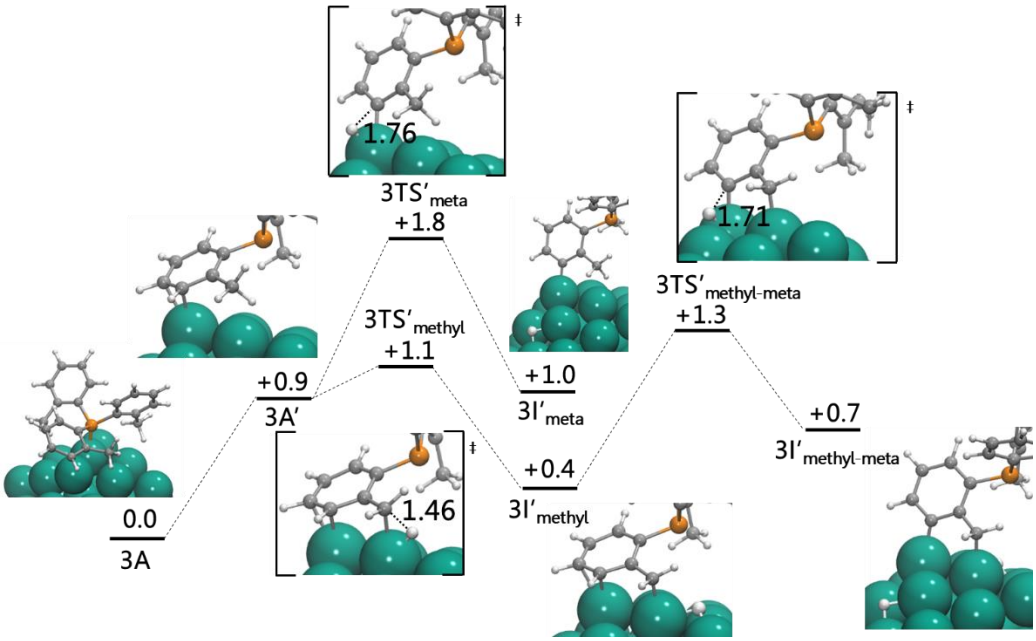

Figure 4.6. Energy profile (eV) for the proposed dissociative mechanism for deuteration of phosphine **3** at methyl and aromatic *meta* positions.

We also investigated the activation of the other C-H bonds in the aromatic ring (see Figure 4.7). Here, the reaction starts with phosphine **3** adsorbed through the *meta* and *para* positions of tolyl substituent to a Rh vertex atom. The computed energy barrier for C-H activation is 0.9 eV for *meta* position opposite to methyl group and 1.1 eV for *para* position, while *ortho* C-H bond is not accessible to the rhodium surface. These trends agree with the experimental observations since the second *meta* position is slower deuterated than the methyl group and the adjacent *meta* position, as well as the deuteration of the *para* position was not observed. Nevertheless, the overall energy cost of the processes starting with the phosphine **3** adsorbed through phosphorus atom is still high. Therefore, here we evaluate the effect on phosphine adsorption of the hydrides and NHC carbene stabilizers on the Rh surface by building a more realistic model of Rh NP (see Figure 4.8). Adding 0.6 H atoms and 0.1 NHC *per* Rh surface atom, we observed a significant reduction of adsorption energy for **3** that becomes only -0.2 eV. This can be attributed to two factors: (1) the electronic stabilization of Rh_{55} cluster (the d band center shifts from -1.95 to -2.17 eV) reduces the Rh-P interaction, and (2) the large cone angle of phosphine **3** causes some steric repulsion between phosphine substituents and other species at the Rh surface. Thus, we can assume that the computed stabilization of species **3A** in Figure 4.6 is lower than for real

system, and therefore, the energy barriers are somewhat lower making the activation of the *meta* position non-adjacent to methyl group affordable. Although the access to accurate energy barriers is difficult because the structural complexity of organometallic nanoparticle, we succeeded in reproducing relative rates of C-H activations and explaining the different selectivities of phosphines. Phosphine **3** adsorbs weakly than **1** because the larger cone angle and the methyl substituents preventing the π-interaction of aromatic substituents, giving access to other interaction modes between phosphine **3** and Rh_{55} surface.

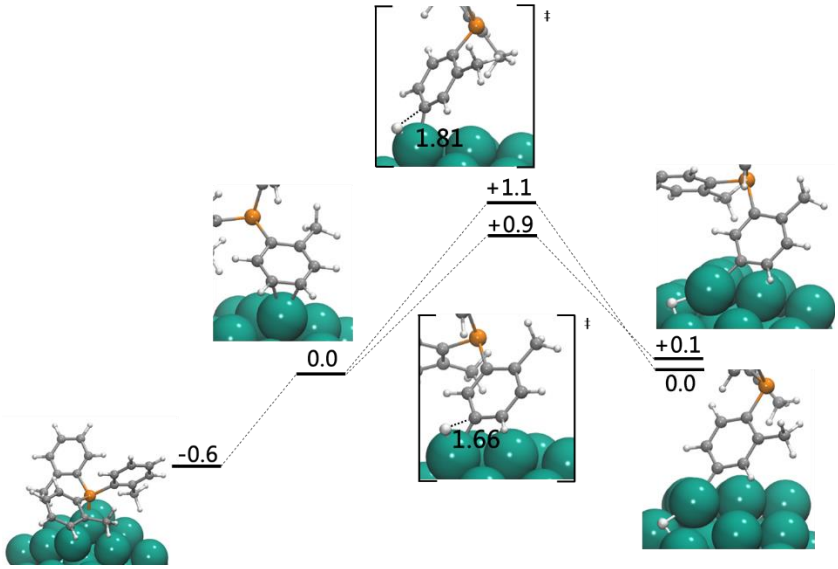

Figure 4.7. Energy profile (eV) for the activation of *meta*-5 and *para* positions of phosphine **3**.

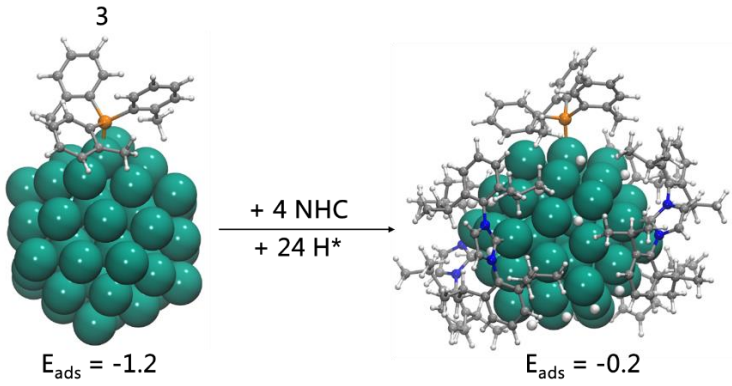

Figure 4.8. Comparison of the adsorption of phosphine **3** onto naked and functionalized (4 NHCs ligands and 24 Hs) Rh_{55} ICO nanoparticles. Adsorption energies in eV.

4.4 Concluding Remarks

This chapter aimed to study the application of metal nanoparticle catalysts to a specific reaction: the hydrogen isotope exchange. The investigation was based on the experimental observations of Castillón *et al.* PPh_3 was selectively deuterated only on the *ortho* positions of the phenyl rings, but when P(o-tolyl)$_3$ was used, the *meta* and methyl hydrogens were exchanged. Another interesting example was the selective aliphatic deuteration of biphosphine **8**, but only with a Rh-based NP (with Ru no deuteration was detected).

DFT calculations have elucidated the origin of the observed selective H/D exchange on several phosphines using Rh nanoparticles stabilized by NHC or PVP as catalysts. Selecting PPh_3 (**1**) and P(*o*-tolyl)$_3$ (**3**) phosphines and Rh_{55} cluster as nanoparticle model, we have found that the selectivity and its differences can be related to the different interaction modes of phosphines and their substituents with the nanoparticle surface.

The PPh_3 phosphine **1** adsorbs to Rh NPs through P lone pair electrons, while the phenyl substituents can simultaneously interact with the Rh surface in two different modes: in η^6 mode via π system, and the second in η^2 mode through *ortho* and *ipso* C atoms. When phenyl ring is attached via η^6 mode, the C-H activation is kinetically and thermodynamically unfeasible (computed energy barriers: 1.5, 2.7 and 2.1 eV for *ortho*, *meta* and *para* positions, respectively). However, the activation of the *ortho* C-H bond, when the phenyl substituent interacts in a η^2 mode on an edge of the nanoparticle, proceeds with a moderate energy barrier (+0.6 eV) leading to an unstressed five membered dimetallacycle. This indicates that isotope exchange via C-H activation is favored in nanoparticles where edges and surface defects are present. The activation of *meta* and *para* C-H bonds on a nanoparticle edge would require phosphorus decoordination of the ligand with the concomitant energy penalty. In addition, an associative mechanism, in which a deuteride insertion proceeds previous C-H bond breaking was also evaluated, but it was discarded due to a higher energy barrier.

The P(*o*-tolyl)$_3$ phosphine **3**, showing H/D exchange on aromatic meta positions and methyl C-H bonds, also adsorbs through P but the adsorption energy is lower than for **1** because the presence of methyl substituents prevents the π-interaction of aromatic rings and the larger cone angle might induce some repulsion of the methyl groups with the functionalized NP surface. The activation of aliphatic C_{sp3}-H bonds at the Rh NP has a lower energy barrier (0.2 vs 0.6 eV). To explain also the exchange at C-H *meta*, we propose a mechanism in three steps: 1) the P atom is detached from NP surface, to avoid the ring distortion after activation, 2) activation of the C-H methyl bonds at NP edge, and 3) the *meta* C-H bond of the aromatic ring activation resulting in an overall energy barrier of +1.3 eV. The 5-

meta position activation was also evaluated, but the energy barrier resulted too high to be affordable at working conditions (1.5 eV). However, we observed a significant drop of the adsorption energy (of about 1 eV) when phosphine **3** was adsorbed onto a more realistic NP, covered by hydrides and NHC species, making the energy barrier for the activation processes lower.

4.5 Computational Details

All calculations were performed within the periodic Density Functional Theory approach[23] using the plane-wave based Vienna ab Initio Simulation Package (VASP).[24] The exchange correlation functional used was revised Perdew-Burke-Ernzerhof (RPBE)[25] with an energy cut-off for the plane-waves basis set of 400 eV. The core electrons were simulated by the Projector Augmented Wave method.[26] The wave function was considered to converge when the energy difference between one electronic step and the previous one was less than $1 \cdot 10^{-5}$ eV, whereas the minimum geometry was obtained when all forces were smaller than 0.01 eV A^{-1}. To set the partial occupancies the Methfessel-Paxton scheme[27] was used with smearing of 0.05 eV. The system under study was placed at the center of a 30 Å lattice cubic box with a minimum vacuum space between two neighboring systems of more than 10 Å to avoid possible interactions between periodic images. Since we were dealing with a molecular system only the Γ k-point was taken into account in the integration of the Brillouin zone. The Improved Dimer method[28] was employed to locate the transition states. Once the transition state was found, we performed a frequency calculation to ensure the TS character, and then displacements of the frequency was applied to the transition state, in both directions, forward and reverse, to guarantee the connection between reactants, transition and intermediate states. All the calculations had been performed within the non-spin polarized approach to reduce the computational cost. However, we computed the associative and dissociative transition states of PPh_3 with spin polarization, and we did not observe important discrepancies between both calculations (0.59 vs 0.61 eV for non-spin and spin polarization, respectively, of dissociative transition states and 1.11 vs 1.07 eV for non-spin and spin polarization, respectively, of associative transition states).

References

1. a) Atzrodt, J.; Derdau, V.; Kerr, W. J.; Reid M. *Angew. Chem. Int. Ed.* **2018**, *57*, 3022-3047. b) Arockiam, P. B.; Bruneau, C.; Dixneuf, P. H. *Chem. Rev.* **2012**, *112*, 5879-5918. c) Mkhalid, I. A. I.; Barnard, J. H.; Marder, T. B.; Murphy, J. M.; Hartwig, J. F. *Chem. Rev.* **2010**, *110*, 890-931. d) Shilov, A. E.; Shul'pin, G. B.; *Chem. Rev.* **1997**, *97*, 2879-2932. e) Zhang, S.-Y.; Zhang, F.-M.; Tu, Y.-Q. *Chem. Soc. Rev.* **2011**, *40*, 1937-1949. f) Song, G.; Wang, F.; Li, X.; *Chem. Soc. Rev.* **2012**, *41*, 3651-3678. g) Engle, K. M.; Mei, T.-S.; Wasa, M.; Yu, J.-Q. *Acc. Chem. Res.* **2012**, *45*, 788-802.
2. a) Crabtree, R. H. *J. Organomet. Chem.* **2004**, *689*, 4083-4091. b) Periana, R. A.; Bhalla, G.; Tenn, W. J.; Young, K. J. H.; Liu, X. X.; Mironov, O.; Jones, C.; Ziatdinov, V. R. *J. Mol. Catal. A.* **2004**, *220*, 7-25. c) Ribas, X.; Xifra, R.; Parella, T.; Poater, A; Sola, M.; Llobet, A. *Angew. Chem. Int Ed.* **2006**, *45*, 2941-2944.
3. Marcus, D. M.; McLachlan, K. A.; Wildman, M. A.; Ehresmann, J. O.; Kletnieks, P. W.; Haw, J. F. *Angew. Chem. Int. Ed.* **2006**, *45*, 3133-3136.
4. a) Bhatia, S.; Spahlinger, G.; Boukhumseen, N.; Boll, Q.; Li, Z.; Jackson, J. E. *Eur. J. Org. Chem.* **2016**, *24*, 4230-4235. b) Atzrodt, J.; Dernau, V.; Fey, T.; Zimmermann, J. *Angew. Chem. Int. Ed.* **2007**, *46*, 7744-7765.
5. a) Liu, L.; Corma A. *Chem. Rev.* **2018**, *118*, 4981-5079; b) Zhao, M.; Yuan, K.; Wang, Y.; Li, G.; Guo, J.; Gu, L.; Hu, W.; Zhao, H.; Tang, Z. *Nature* **2016**, *359*, 76-80. C) Zhang, Y.; Guo, J.; Shi, L.; Zhu, Y.; Hou, K.; Zheng, Y.; Tang, Z. *Sci. Adv.* **2017**, *3*, e1701162.
6. a) Sullivan, J. A.; Flanagan, K. A.; Hain, H. *Catal. Today* **2008**, *139*, 154-160. b) Flanagan, K. A.; Sullivan, J. A.; Müeller-Bunz, H. *Langmuir* **2007**, *23*, 12508-12520.
7. Guy, K. A.; Shapley, J. R. *Organometallics* **2009**, *28*, 4020-4027.
8. For a review about C-H activation using nanoparticles see: Pla, D.; Gómez, M. *ACS Catal.* **2016**, *6*, 3537-3552.
9. Philippot, K.; Chaudret, B. *C. R. Chemie* **2003**, *6*, 1019-1034.
10. Pery, T.; Pelzer, K.; Buntkowsky, G.; Philippot, K.; Limbach, H.-H.; Chaudret, B. *ChemPhysChem*, **2005**, *6*, 605-607.
11. Favier, I.; Massou, S.; Teuma, E.; Philippot, K.; Chaudret, B.; Gómez, M. *Chem. Commun.* **2008**, 3296-3298.
12. Rafter, E.; Gutmann, T.; Löw, F.; Buntkowsky, G.; Philippot, K.; Chaudret, B.; van Leeuwen, P. W. N. M. *Catal. Sci. Technol.* **2013**, 3, 595-599.
13. Taglang, C.; Martínez-Prieto, L. M.; del Rosal, I.; Maron, L.; Poteau, R.; Philippot, K.; Chaudret, B.; Perato, S.; Lone, A. S.; Puente, C.; Dugave, C.; Rousseau, B.; Pieters, G. *Angew. Chem. Int. Ed.* **2015**, *54*, 10474-10477.

14. Martínez-Prieto, L. M.; Baquero, E. A.; Pieters, G.; Flores, J. C.; de Jesús, E.; Nayral, C.; Delpech, F.; van Leeuwen, P. W. N. M.; Lippens, G. ; Chaudret, B. *Chem. Commun.* **2017**, *53*, 5850-5853.

15. Pieters, G.; Taglang, C.; Bonnefille, e.; Gutmann, T.; Puente, C.; Berthet, J.; Dugave, C.; Chaudret, B.; Rousseau, B. *Angew. Chem. Int. Ed.* **2014**, *53*, 230-234.

16. a) Campos, J.; Espada, M. F.; López-Serrano, J.; Carmona, E. *Inorg. Chem.* **2013**, *52*, 6694-6704. b) Grellier, M.; Mason, S. A.; Albinati, A.; Capelli, S. C.; Rizzato, S.; Bijani, C.; Coppel, Y.; Sabo-Etienne, S. *Inorg. Chem.* **2013**, *52*, 7329-7337. c) Chaudret, B.; Poilblanc, R. *Organometallics* **1985,** *4*, 1722-1726. d) Borowski, A. F.; Sabo-Etienne, S.; Christ, M. L.; Donnadieu, B.; Chaudret, B. *Organometallics* **1996**, *15*, 1427-1434. f) Clague, A. D. H.; Masters, C. *J. Chem. Soc., Dalton Trans.* **1975**, 858-861.

17. a) Bresó-Femenia, E.; Chaudret, B.; Castillon, S. *Catal. Sci. Technol.* **2015**, *5*, 22741-2751. b) Llop-Castelbou, J.; Blondeau, P.; Claver, C.; Godard, C. *RSC Adv.* **2015**, *5*, 97036-97043. c) Llop-Castelbou, J.; Bresó-Femenia, E.; Blondeau, P.; Chaudret, B.; Castillon, S.; Claver, C.; Godard, C. *ChemCatChem* **2014**, *6*, 3160-3168. d) Llop-Castelbou, J.; Gual, A.; Mercadé, E.; Claver, C.; Godard, C. *Catal. Sci. Technol.* **2013**, *3*, 2828-2833. e) Gual, A.; Godard, C.; Philippot, K.; Chaudret, B.; Denicourt-Nowicki, A.; Roucoux, A.; Castillon, S.; Claver, C. *ChemSusChem* **2009**, *2*, 769-779. f) Axet, M. R., Castillon, S.; Claver, C.; Philippot, K.; Lecante, P.; Chaudret, B. *Eur. J. Inorg. Chem.* **2008**, *22*, 3460-3466.

18. Bresó-Femenia, E.; Godard, C.; Claver, C.; Chaudret, B.; Castillón, S. *Chem. Commun.* **2015**, *51*, 16342-16345.

19. Garfunkel, E. L. *Surf. Sci.* **1986**, *167*, 177-197.

20. a) Treanor, M.-J.; Torres, J. A. G.; Bromley, C. J.; Früchtl, H. A.; Schaub, R. *J. Phys. Chem. C* **2018**, *122*, 11890-11904. b) Lakshmikanth, K. G.; Ayishabi, P. K.; Chatanathodi, R. *Comput. Mater. Sci.* **2017**, *137*, 10-19. c) Garcia-Pintos, D.; Voss, J.; Jensen, A. D.; Studt, F. *J. Phys. Chem. C* **2016**, *120*, 18529-18537. d) Carrasco, J.; Liu, W.; Michaelides, A.; Tkatchenko, A. *J. Chem. Phys.* **2014**, *140*, 084704. e) Jasen, P. V.; González, E. A.; Brizuela, G.; Juan, A. *J. Mol. Catal. A Chem.* **2010**, *323*, 23-27. f) Morin, C., Simon, D.; Sautet, P. *J. Phys. Chem. B* **2004**, *108*, 5653-5665.

21. Saeys, M.; Reyniers, M.-F.; Neurock, M.; Marin, G. B. *J. Phys. Chem. B* **2003**, *107*, 3844-3855.

22. Pfeifer, V.; Certiat, M.; Bouzouita, D.; Palazzolo, A.; Garcia-Argote, S.; Marcon, E.; Buisson, D.; Lesot, P.; Maron, L.; Chaudret, B.; Tricard, S.; del Rosal, I.; Poteau, R.; Feuillastre, S.; Pieters, G. *Chem. Eur. J.* **2020**, *26*, 4988-4996.

23. a) Hohenberg, P.; Kohn, W. *Phys. Rev.* **1964**, *136*, 864-871. b) Kohn, W.; Sham, L. J. *Phys. Rev.* **1965**, *140*, 1133-1138.

24. a) Kresse, G.; Hafner, J. *Phys. Rev. B* **1993**, *47*, 558. b) Kresse, G.; Furthmüller, J. *Comput. Mat. Sci.* **1996**, *6*, 15-50. c) Kresse, G.; Furthmüller, J. *Phys. Rev. B* **1996**, *54*, 11169.
25. Hammer, B.; Hansen, L. B.; Norskov, J. K. *Phys. Rev. B* **1999**, *59*, 7413.
26. Kresse, G.; Joubert, D. *Phys. Rev. B* **1999**, *59*, 1758.
27. Methfessel, M.; Paxton, A. T. *Phys. Rev. B* **1989**, *40*, 3616.
28. Dimer method: Henkelman, G.; Jonsson, H. *J. Chem. Phys.* **1999**, *111*, 7010. Improved Dimer method: Heyden, A.; Bell, A. T.; Keil, F. J. *J. Chem. Phys.* **2005**, *123*, 224101.

Chapter 5:

Development of ReaxFF Force Field for Propane Dehydrogenation Reaction on Pt Catalysts

UNIVERSITAT ROVIRA I VIRGILI
COMPUTATIONAL MODELING TO EXPLORE SOLVENT AND DYNAMIC EFFECTS IN MOLECULAR, NANO AND SOLID CATALYSIS
Antoni Salom Català

Chapter 5:

Development of ReaxFF Force Field for Propane Dehydrogenation Reaction on Pt Catalysts

In this chapter, we present the development of a new ReaxFF force field tailored to study the Propane Dehydrogenation reaction (PDH) catalyzed by Pt surfaces and nanoparticles (NPs): ***2022-Pt/C/H****. The process of ReaxFF force field re-parametrization is an iterative procedure where the developer must validate, identify, and fix the points where the force field fails, and start a new cycle of training and validation. The development from an initial* ***2021a-Pt/C/H*** *force field to the last version* ***2022-Pt/C/H*** *is presented, exposing the improvements and the fragilities during the development, and the strategies used to fix the force field debilities such as, changing the starting set of parameters (****2021b-Pt/C/H****), adding more entries and structures in the training set (****2021c-Pt/C/H****) or tuning the force field parameters (****2021d-Pt/C/H****). Also, the validation of* ***2022-Pt/C/H*** *force field is shown in terms of thermodynamic, kinetic, and MD simulations analysis. The comparison of the new* ***2022-Pt/C/H*** *force field with DFT reference data indicates a very promising results, with a maximum Mean Absolut Error (MAE) for the relative energies of the intermediates of 3.4 kcal mol^{-1} or not higher than 5 kcal mol^{-1} for the energy barriers and 0.2 Å for the key C-H or C-C distance of several reaction processes. The force field also shows encouraging results with external validations, and it was able to describe processes not included in the training set with a MAE for the energy barriers and key distances of 2.3 kcal mol^{-1} and 0.08 Å, respectively. We also performed productive reactive MD simulations of PDH catalyzed by Pt(111) and Pt(211) surfaces and Pt55 icosahedral (ICO) NP. The results show a higher reactivity on Pt(211) with a conversion of 0.88 % of propane against 0.5 % of conversion on Pt(111). Moreover, the simulations with Pt(211) reveal that the active site are the edge Pt atoms since all processes undergo on that positions, and the preferential propene formation mechanism goes through 1-propyl (****I1****) formation. In the case of Pt$_{55}$ NP, the propane conversion is even higher, up to 2.6%, indicating a higher catalytic performance. At the end of the chapter we show the assessment of the ReaxFF force field parameter optimization with Covariance Matrix Adaptation Evolution Strategy (CMA-ES) optimization algorithm, pointing out an important influence of the proper algorithm and the job performed on each structure during the Error Function Evaluation (EFE), and the assessment of the ReaxFF performance in reactive MD simulations, showing a very high capability to carry out long simulations with large systems with low computational cost.*

5.1 Introduction

Over the last years, the demand of light olefins has increased exponentially because of their extensive use as chemical building blocks employed in the production of a vast array of important chemicals such as polymers, oxygenates and other important chemical intermediates such as ethylbenzene and propionaldehyde. Among different possible olefins, propene has become one of the most valuable chemical precursors, with a continuous growing demand, used to synthesize polypropylene, acrylonitrile and propylene oxide.[1]

Typically, light olefins were obtained by steam cracking or fluid catalytic cracking methods of naphtha, light diesel, and other oil by-products. However, there are some limitations using these methods: high-energy demanding, low selectivity towards the desired olefin, dwindling petroleum reserves or rising oil prices. For these reasons, more economical feedstock and more efficient conversion methods and technologies are mandatory. Within this context, the catalytic dehydrogenation of short alkane molecules emerged as a promising approach to derive selective alkene production. In case of propane to obtain propene, the reaction is called Propane Dehydrogenation reaction, and it can be oxidative if an oxidant is employed during the dehydrogenation, or direct if no other reagent is used.[2]

Nevertheless, despite PDH overcome most of the issues of traditional synthetic routes, it is not free of its own limitations. Propane (and other short alkanes) are very stable and nonpolar molecules, and the C-H bond energies can vary from 410.4 to 439.3 kJ/mol,[3,4,5] making the process endothermic, and as consequence, temperatures around 500-700 ºC and the presence of a catalyst are needed. Catalysts for these processes are metal oxides, typically based on chromia (Cr_xO_y), and Pt-based catalysts.[1,6] During the last years, there was an increasing interest in Pt-based catalysts due to the rapid coking and sintering of chromia-based catalysts and the significant health issues derived from possible chromium spilling or exposure.[7,8,9] However, Pt-based catalysts also suffer fast deactivation due to coke formation and sintering at the high temperatures used in the process.[10]

One way to overcome the problem of coke formation is the formulation of new and more efficient catalysts that it has been the subject of numerous studies (see ref. 9 and references herein). Another way to improve the performance of the reaction could be the analysis and optimization of the reaction conditions, such as, temperature, pressure, gas feed composition, surface coverage, among many others, but an appropriate approach to study the system at atomistic level in realistic reaction conditions is required.

Classical Molecular Dynamics (MD) simulations are of great interest due to the ability of simulate very big systems at low computational cost, but contrary to the *ab initio* MD, Classical MD is not able to reproduce some important phenomena in chemistry: bond breaking and formation. During the last years, some Reactive MD approaches, such as ReaxFF,[11] AIREBO[12] or COMB[13,14,15,16,17] have gained an important attention due to their capacity to combine the low computational cost to simulate large systems and the possibility to observe chemical reactions. Within this framework, ReaxFF has shown very interesting and promising results in fields such as catalysis, biology or material science. For instance, as illustrated in Figure 5.1, ReaxFF was used to study carbon nanotubes growth catalyzed by Ni,[18] the conformational dynamics of biomolecules,[19] or the oxidation of metal surfaces,[20] among many other applications.[21]

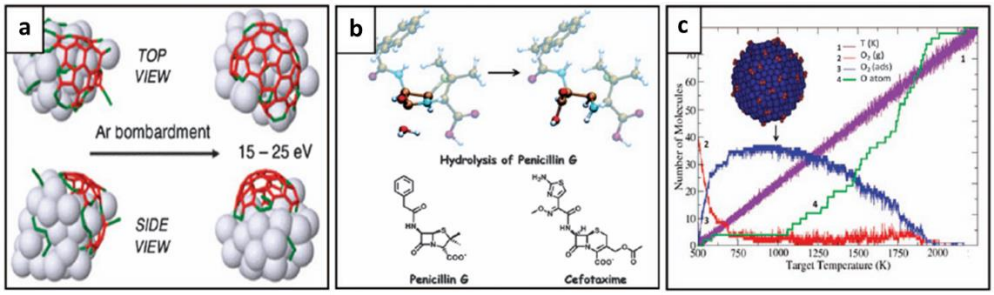

Figure 5.1. Examples of applications were a ReaxFF study was applied successfully. (a) Ni-catalysed CNT growth, (b) conformational dynamics of biomolecules and (c) Pd surface oxidation. The images and the examples were taken from reference 21.

ReaxFF formulation, beyond DFT, seems to be a very promising tool to study PDH catalyzed by Pt atomically. ReaxFF[11,21,22,23] is a program developed by Adri van Duin in 2001 that uses the called Bond Order Formalism allowing reactive MD simulations, gathering the advantages of Classical MD (simulations of large systems with low computational cost) and *ab initio* MD (reactive events). The development of the empirical force-field parameters is not a simple process and it can become the bottle neck of the overall modelling study. The ReaxFF functional form does not employ the "atom type" concept of traditional force-fields. There is only one atom type for each element in the periodic table allowing the transferability of the empirical parameters between phases (solid/gas) and between related chemical systems. According to the developers, the parameters are transferable within the same development branch (combustion or aqueous), but one cannot simply combine parameters coming from different elements, then, the user must assess the transferability before performing productive work with ReaxFF force fields.

In this chapter, the steps followed to re-optimize a ReaxFF force field to study the PDH reaction catalyzed by Pt surfaces and NPs are presented, as well as the internal and external validations of the final force field (**2022-Pt/C/H**) and the potential applications of the ReaxFF approach to study PDH on different Pt catalysts, such as Pt(111) and Pt(211) surfaces and Pt_{55} nanoparticles. At the end, we provide a suitable ReaxFF force field starting point to develop other ReaxFF potentials for more complex systems.

5.2 Results and Discussion

5.2.1 ReaxFF Force Field Development Strategy

The development of a ReaxFF force field is not one step, straightforward procedure, but an iterative, trial and error strategy, identifying the weaknesses and strengths of your new force field, and improving them. The general workflow for ReaxFF force field development is depicted in Figure 5.2.

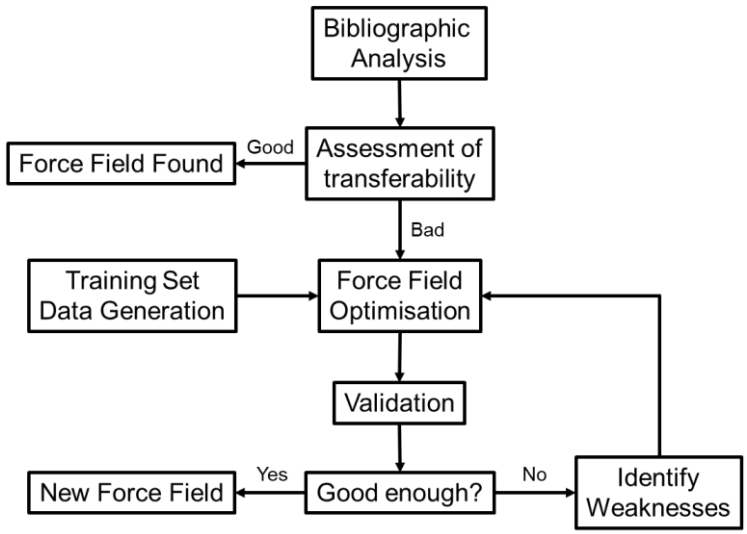

Figure 5.2. General workflow for ReaxFF force field development.

Firstly, one must perform a bibliographic search, and look for force fields that include the maximum number of elements of the system under study, and if it is possible, force fields used in similar reactions, processes, or conditions. Once potential candidates are selected, if they contain all the elements involved in our system, the transferability needs to be assessed by geometry optimizations and

Molecular Dynamic (MD) simulations using the selected force fields, and then checking the degree of agreement between ReaxFF results and quantum mechanics/experimental data from literature or own experiments.

After transferability evaluation, if selected force fields were not suitable to describe properly the target system, one needs to re-optimize one of these force fields. The optimization of parameters of a ReaxFF force field is carried out by one of the available function minimization algorithms such as, Genetic Algorithms (GAs), Monte-Carlo approaches (MC) or Evolution Strategies (ES). In this work, the optimization algorithm used to obtain the best force field was the Covariance Matrix Adaptation Evolution Strategy (CMA-ES). Basically, this algorithm tries to minimize the called Error Function (EF) looking for the parameters set that allows the best fitting between properties calculated by ReaxFF and the reference ones. The EF has the following form:

$$\text{Error} = \sum_{i=1}^{n} \left(\frac{x_{i,ref} - x_{i,ReaxFF}}{\sigma_i} \right)^2 \quad (1)$$

Where $x_{i,ref}$ is the property reference value, $x_{i,ReaxFF}$ is the property value calculated by ReaxFF, and σ_i is the weight given to each property and could be considered as a measure of the accuracy, or importance of that property. The reference data can come from several sources, but the most commonly used is high quality quantum mechanics calculations, mostly based on DFT. Then, to optimize or train a new force field, reference data set must be generated previously, and depending on the system, and the size of the training set desired, it can take a lot of time, and for that reason, the reference data set generation represents a bottle neck for ReaxFF force field development.

Next step is the validation of the new set of parameters obtained after force field training. It can be divided in two parts: internal and external validation. On one hand, internal validation consists in comparison of geometrical and energetic results of systems included in the training set calculated with the new set of parameters and reference data. On the other hand, external validation means to check the agreement degree between systems calculated by ReaxFF and DFT on systems not present in the training set. Finally, it is also important to perform ReaxFF MD simulations to test the behavior of target system in dynamic environment.

Finally, if the new set of parameters reproduce properly the nature of the system, a new reactive force field is obtained and productive simulations can be

performed. If the properties of the reaction are not well reproduced, one must identify the points were the force field failed, such as, too short or long distances, energies not fitted with the corresponding reference, etc. Then, modifications must be applied in the training set (adjust weights, add more entries in the training set, etc.), and finally start another cycle of force field optimization and validation, until adequate parameters are found.

5.2.2 Transferability of Pt/C/H ReaxFF Force Fields

The target reaction we wanted to study is the direct PDH reaction on Pt catalysts, so the elements on which we are interested in are Pt, C and H. In the literature, we found three possible force field candidates suitable to study PDH catalyzed by Pt surfaces:

1- **2016-Pt/Ni/C/O/H** force field.[24] This force field was developed for heterogeneous catalysis applications of PtNi alloys. It was training using DFT data, consisting in the equations of state of Pt_3Ni, $PtNi_3$ and PtNi alloys, the surface energy of $Pt_xNi_{1-x}(111)$, and binding energies of small molecular and atomic species such as O, H, C, CH, CH_2, CH_3, CO, OH and H_2O.

2- **2016-Pt/H/O** force field.[25] Here, the authors built a force field to study the adsorption behavior of O and H atoms over Pt surfaces and nanoparticles. They re-optimized a previous developed Pt/H force field[26] using DFT data, like the binding energy of H on Pt(111) surface at all possible sites (fcc, hcp, bridge and top) and first- and second-subsurfaces (tetrahedral and octahedral sites) at 0.25 ML of coverage, as well as the thermodynamic stability of adsorbed hydrogen on Pt(111) at different coverages, and then, it was combined to another existing Pt/O force field[27] trained with the structures of different Pt bulk faces (fcc, hcp, bcc, sc, diamond and β-tungsten), small Pt clusters up to 35 atoms, the equations of state of various bulk platinum-oxide phases such as α-PtO_2, β-PtO_2, PtO and Pt_3O_4, and adsorption energies of O on different flat and stepped Pt and Pt-Oxide surfaces. Note these force fields were not optimized for applications where carbon was involved, but C parameters were present in the force field.

3- **2008-Pt/C/H** force field.[28] This force field was developed to investigate the interaction and the structure of a Pt_{100} nanoparticle adsorbed on three different sides of carbon platelet. It was optimized against a set of binding structures and adsorption energies calculated by DFT of the chemisorption of all CH_x and C_2H_y species onto Pt(111) surface.

To assess the transferability of the selected force fields, some static ReaxFF calculations were carried out on different model systems, and the results were compared with other theoretical results from the literature. First, we assessed the transferability of the reference force fields to describe the adsorption of two important species in the PDH reaction: propane and propene. In Table 5.1 are shown the main results. On one hand, **2008-Pt/C/H** parameterization was able to reproduce the adsorption energies of propane and propene onto Pt(111) surface, but the optimized geometry of propene deviates significantly from DFT reference. Probably, it is because the data used to train the **2008-Pt/C/H** did not include C_3 species or chemisorption involving double bond breaking, mostly noted on the short C_1-C_2 bond of 1.39 Å on propene or the high Pt-C distances of 2.45 and 2.47 Å. On the other hand, the **2016-** force fields showed a completely opposite behavior. They provide good geometrical description mostly for propene (C_1-C_2 bond distance of 1.51 Å), but the C/H-Pt interactions look to be overestimated showing shorter Pt-C and Pt-H distances, and extremely high adsorption energies for both, propane and propene. Again, the effect of the training of these force fields can be noted, since they were not trained to reproduce the adsorption of that molecules (only small molecules with one C atom, or even no carbon species), leading to unrealistic adsorption energies.

Table 5.1. Assessment of transferability of selected ReaxFF force fields of propane and propene adsorptions on Pt(111) surface. Distance are in Å. Energies are in kcal mol^{-1}.

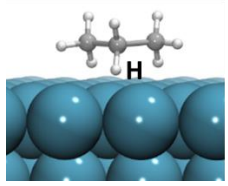

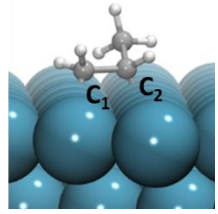

		DFT[29]	2008-Pt/C/H	2016-Pt/H/O	2016-Pt/Ni/C/O/H
Propane	E_{ads}	-0.2/-0.6	-0.7	-23.0	-25.2
	Pt-H	2.95/3.02	2.96	2.19	2.19
Propene	E_{ads}	-12.9/-24.4	-23.0	-41.6	-50.9
	Pt-C_1	2.11	2.45	1.92	1.86
	Pt-C_2	2.13/2.14	2.47	1.92	1.86
	C_1-C_2	1.50/1.51	1.39	1.49	1.51

Furthermore, we selected some PDH intermediates, and all of them were optimized using the reference parameter sets. We selected representative intermediates of three well know processes occurring during PDH reaction, including 1-propyl (**I1**) and 2-propyl (**I2**) to obtain propene adsorbed on Pt(111) surface with two H atoms (**I3**) as dehydrogenation steps, 1-propenyl (**I6**) as deep dehydrogenation intermediate and methyl/ethyl (**I10**) and methylene/ethylene (**I11**) to represent C-C bond breaking reactions. All of them are depicted in Figure 5.3, and the resulting relative energies respect propane physisorbed on Pt(111) surface are presented in Table 5.2. In line with the results presented in Table 5.1, **2016-** parameterization overestimates the relative energy of the intermediates, leading to a very strong and unrealistic relative energies despite the fact that in some studies, the thermodynamic trends agree with the **2016-** force field results.[30] Probably, the large Pt-C adsorption energy was not accurately counterbalanced by the energy cost of C-C and C-H bond breaking. **2008-Pt/C/H** set of parameters, showed most of the selected intermediates are higher in energy than propane adsorption, but with a pronounced deviation of relative energy values from DFT reference data.[31] Interestingly however, the different parameterization sets identify propene intermediate **I3** as the most stable intermediate among the series. Moreover, it should be noted that DFT reference data differ from one study to another, and the results depend on the computational methodology used, giving for the same reaction opposite results.

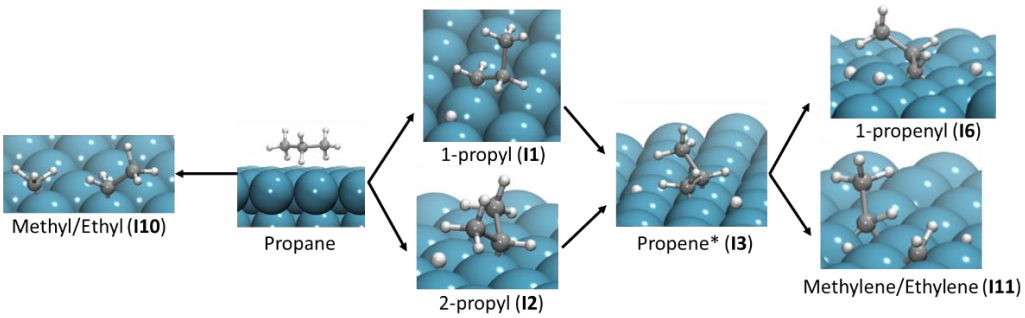

Figure 5.3. PDH reaction intermediates. **I1**, **I2**, **I3** and **I6** corresponds to C-H bond breaking processes. **I10** and **I11** refer to C-C bond breaking products.

Table 5.2. Relative energies of PDH intermediates respect propane physisorbed on Pt(111) surface in kcal mol^{-1}. NF = Not Found.

E_{rel}	DFT[30]	DFT[31]	2008-Pt/C/H	2016-Pt/H/O	2016-Pt/Ni/C/O/H
I1	-1.8	+27.4	+2.4	-27.0	NF
I2	-1.6	-	+2.9	-30.0	-37.4
I3	-	-	+3.0	NF	-36.3
I4	-6.2	+18.6	-1.5	-28.1	-40.3
I5	-3.9	+16.8	NF	-30.9	-37.4
I6	-	-	+9.0	NF	NF

Finally, we conducted ReaxFF MD simulations to evaluate the performance of the reference force fields in a more realistic PDH and dynamic environment. All the simulations were performed with a Pt(111) 5-layer slab p(9x9) supercell. The temperature was 873 K and the number of propane molecules per unit cell was varied modelling different coverages and pressures. Coverage of 1/9 ML corresponds to 18 propane molecules and coverage of 2/9 ML corresponds to 36 propane molecules. Table 5.3 shows the simulated time (t) and the distribution of species at the end of the simulation. Again, significant differences between parameterizations can be observed. On one hand, **2008-Pt/C/H** shows large reaction evolution, even in a short time, with preference for deep dehydrogenation and coke precursors species formation for both coverage situations. On the other hand, using **2016-** force fields, the reaction notably slows down, and in some cases (1/9 and 2/9 ML coverage for **2016-Pt/Ni/C/O/H** and **2016-Pt/H/O**, respectively) it was not observed, even at those high pressures, or at maximum, only the first C-H bond breaking intermediate **I1** was detected (1/9 and 2/9 ML coverage for **2016-Pt/H/O** and **2016-Pt/Ni/C/O/H**, respectively).

Table 5.3. Summary of reactive molecular dynamics simulations. The species are those present at the end of the simulation.

	2008-Pt/C/H		2016-Pt/H/O		2016-Pt/Ni/C/O/H	
θ (ML)	**t (ns)**	**species**	**t (ns)**	**species**	**t (ns)**	**species**
1/9	7	15 C_3H_8 2 $H_3C(ads)_3$ 14 H(ads) 1 H_2 1 $H_2C(ads)_3$	7	17 C_3H_8 1 $C_2H_7C(ads)$ 1 H(ads)	7	18 C_3H_8
2/9	3	27 C_3H_8 40 H(ads) 3 $H_3C(ads)_3$ 2 $CH_4C(ads)_3$ 1 $CH_3C(ads)_2$ 1 $H_4C(ads)_3$ 2 H_2 2 $H_2C(ads)_3$	5	36 C_3H_8	4	35 C_3H_8 1 $C_2H7C(ads)$ 1 H(ads)

Overall, the assessment of the transferability of selected **2008-Pt/C/H** and **2016-** force fields reveals that:

1) The assessment of any force field got from literature is mandatory, and they cannot be used directly from the source in most of cases.
2) The training set used in the parameterization of a ReaxFF force field is crucial, and it has a strong effect on force field behavior and determines the application on that force field can be used.
3) The ReaxFF force fields selected to investigate the PDH reaction showed notable differences between them, and with DFT data, indicating the need of further re-optimization.

5.2.3 Development of 2021-Pt/C/H Force Field

The transferability assessment revealed that any of the selected force fields from the literature was suitable to accurately describe PDH reaction, and a re-parameterization was needed to perform productive analysis of PDH. Thus, we generated our own quantum mechanical data to build the training set used to

re-optimize the force field. The quantum mechanical data was composed by Density Functional Theory (DFT) calculations of key species and potential energy scans of bond breakings to emulate the energy barriers, based on the reaction scheme proposed by Saerens *et al.*[32] and shown in Figure 5.4. In addition, the re-parameterization procedure is a complex and not straightforward process. The user cannot expect to obtain the desired set of parameters in the first attempt of re-parameterization, and in most cases some variables must be adjust after getting the right parameterization. Table 5.4 shows a summary of the training set and the initial guess used in each development step.

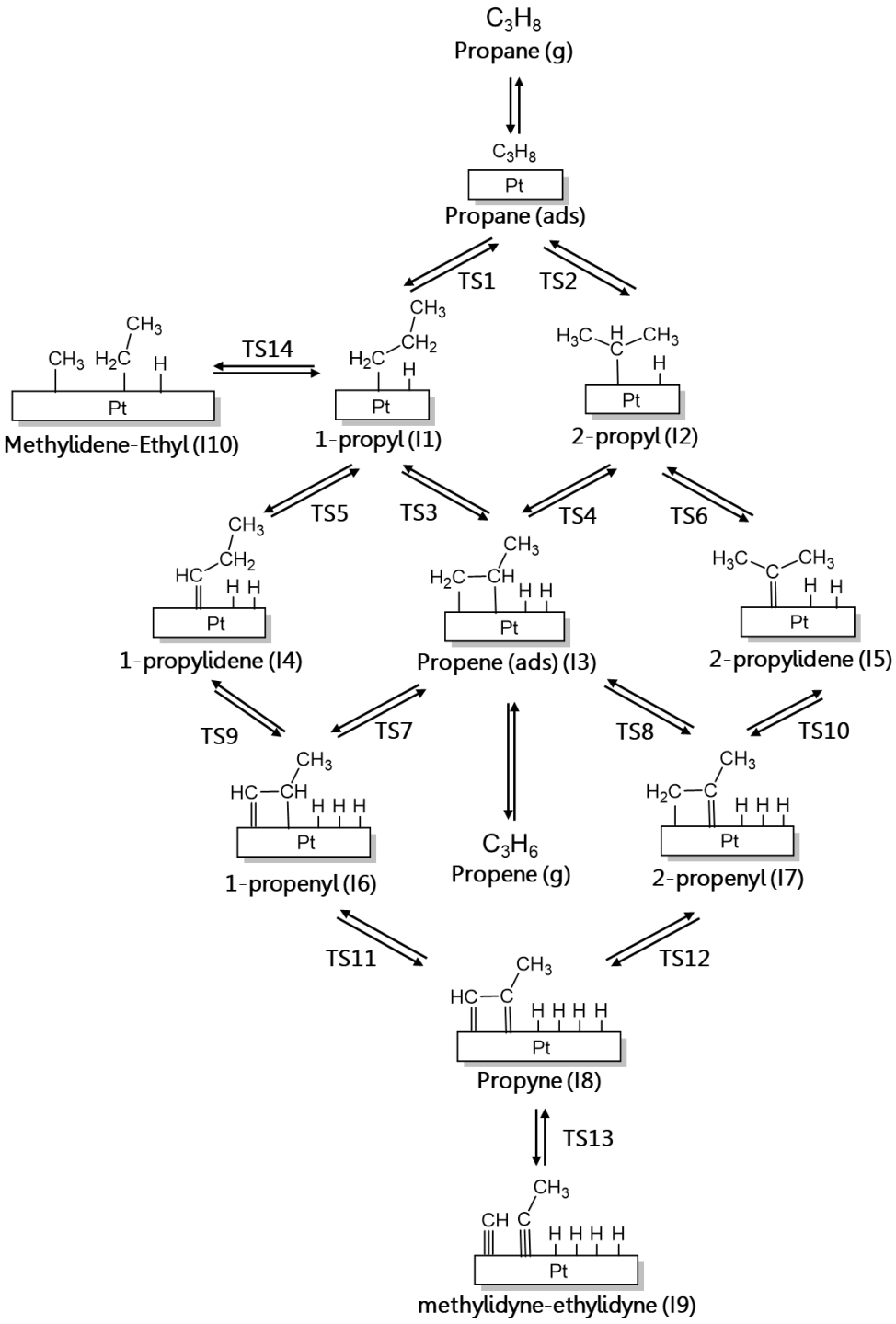

Figure 5.4. Schematic representation of the proposed reaction mechanism for PDH catalyzed by Pt(111) surface based on the mechanism suggested by Saerens *et al.*[32]

Table 5.4. Development stages of ReaxFF **2021-Pt/C/H** force field to describe PDH catalyzed by Pt(111) surface. Entries included in the training set and the initial force field used are specified. Blue-highlighted features are the modifications conducted from previous version.

Version	Training Set	Initial Force Field
2021a-Pt/C/H	Geometries, E_{rel} intermediates, 2 E profiles (single point calculations: 1 C_3H_6 adsorption, 1 C-H bond breaking of propane in gas phase)	2016-Pt/H/O
2021b-Pt/C/H	Geometries, E_{rel} intermediates, 2 E profiles (single point calculations: 1 C_3H_6 adsorption, **1 C-H bond breaking of propane on Pt(111) surface)**	2008-Pt/C/H
2021c-Pt/C/H	Geometries, E_{rel} intermediates, **7** E profiles (single point calculations: 1 C_3H_6 adsorption, 5 C-H and 1 C-C bond breaking processes)	2021b-Pt/C/H
2021d-Pt/C/H	Geometries, E_{rel} intermediates, 7 E profiles (**partial optimisation calculations**: 1 C_3H_6 adsorption, 5 C-H and 1 C-C bond breaking processes). *Pt-Pt E_σ parameter set at 122.1396 kcal mol^{-1}*	2008-Pt/C/H
2022-Pt/C/H	Geometries, E_{rel} intermediates, 7 E profiles (partial optimisation calculations: 1 C_3H_6 adsorption, 5 C-H and **2** C-C bond breaking processes).	2021d-Pt/C/H

2021a-Pt/C/H

2021a-Pt/C/H set of parameters was the first version parameterized to specifically describe PDH reaction on Pt catalysts. The initial force field selected was **2016-Pt/H/O**, which provided the best definition of Pt-Pt and Pt-H parameters. The training set was composed by: 1) geometries of propane, propene and all intermediates considered by Saerens *et al.*[32] shown in Figure 5.4, 2) their relative energies to propane physisorbed on Pt(111) surface and the adsorption energies of propane and propene, and 3) two energy profiles (propene adsorption and $C_{primary}$-H bond breaking in gas phase). After the force field optimization, the adsorption energy of propene was decreased from -41.8 to -19.8 kcal mol^{-1}, very close to DFT reference value of -19.1 kcal mol^{-1}. The reaction thermodynamics was evaluated computing the elementary reaction energies of the mechanism proposed by Saerens *et al.*[6] and calculating the MAE between ReaxFF and DFT

values and it was 9.7 kcal mol^{-1}. If only the intermediates in the assessment of the transferability (see Figure 5.3 and Table 5.2) are considered, the MAE of the relative energies dropped from 25.6 to 4.5 kcal mol^{-1}.

Also, we checked the behavior of **2021a-Pt/C/H** force field on dynamic simulations, but in all dynamics performed, any reaction was observed. Analyzing the reaction kinetics (Figure 5.5), we realized that it was not well reproduced, with very high energy barrier of almost 75 kcal mol^{-1}, in the case of **TS1**. However, at the same time, it was logic, since the C-H bond breaking profile in the training set was on gas phase and not assisted by Pt(111) surface. For that reason, we decided there was room for improvement of **2021a-Pt/C/H** set of parameters, and the efforts in the next step were focused to improve the adsorption energy of propane molecule and to improve the reaction kinetics.

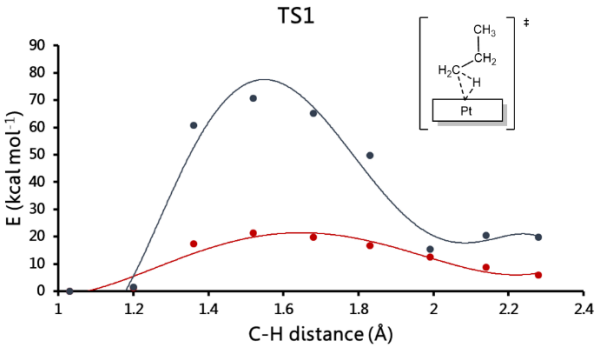

Figure 5.5. Energy evolution as a function of C-H distance of **TS1**. Red: DFT reference profile. Blue: **2021a-Pt/C/H** force field profile.

2021b-Pt/C/H

After several attempts, the adsorption energy of propane on Pt(111) (around -11 kcal mol^{-1} with the initial force fields **2016-Pt/H/O** and **2021a-Pt/C/H**, while reference value was 0.1 kcal mol^{-1}) did not change. Therefore, the initial force field was replaced by **2008-Pt/C/H** force field. The training set was the same used to train **2021a-Pt/C/H** changing the first C-H activation energy profile of propane in gas phase by the same bond breaking profile mediated by Pt(111) (**TS1**).

The results of the validation process were: 1) the adsorption energy of propane was improved form -11.6 kcal mol^{-1} with **2021a-Pt/C/H** to -0.8 kcal mol^{-1} with **2021b-Pt/C/H**, 2) the thermodynamics of the reaction also suffered a big improvement, decreasing the MAE in elementary reaction energies from 9.7 kcal mol^{-1} with **2021a-Pt/C/H** to 3.1 kcal mol^{-1} with **2021b-Pt/C/H**, 3) the reaction kinetics did not fit with DFT results. Despite the energy barrier for the first C-H

bond activation of propane on Pt(111) was improved, the shape was not what expected. Moreover, inspecting the profiles of other key processes, such as **TS3** or **TS13**, both, energy barrier and the shape of the profiles did not fit with reference profiles, and more efforts were needed to improve the reaction kinetics provided by ReaxFF. Figure 5.6 shows the profiles of the commented processes **TS1**, **TS3** and **TS13**.

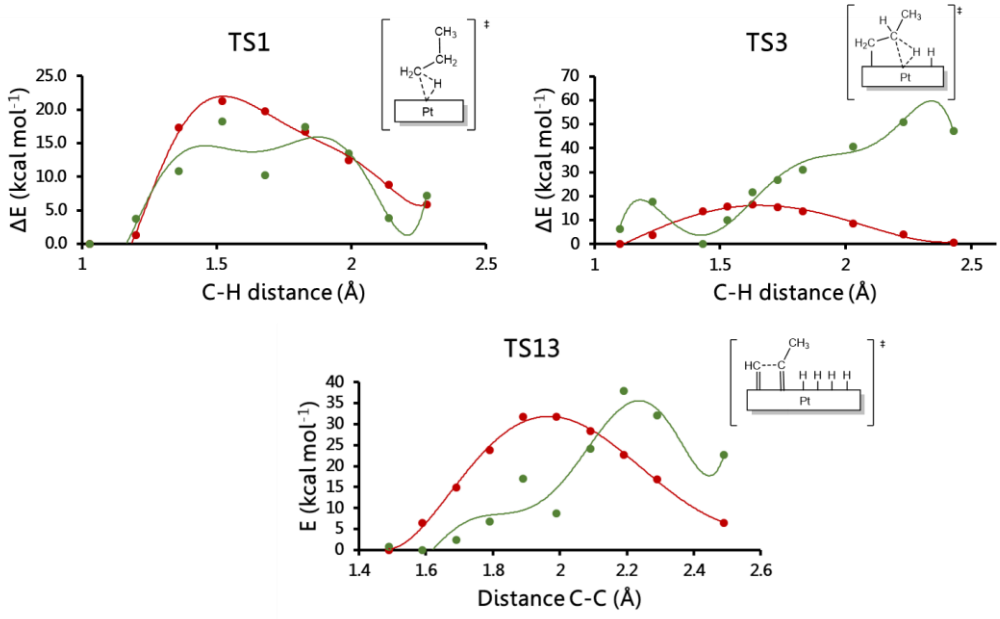

Figure 5.6. Energy evolution as a function of C-H and C-C bond distances of **TS1**, **TS3** and **TS13**. Green: profiles computed with ReaxFF **2021b-Pt/C/H** force field. Red: reference DFT profiles.

2021c-Pt/C/H

To improve the reaction kinetics, more C-H and C-C bond breaking profiles were added in the training set. A part of the two energy profiles **TS1** and propene adsorption, 5 more processes were included: **TS2**, **TS3** and **TS4** as dehydrogenations, **TS7** as deep dehydrogenation and **TS13** as C-C bond breaking. Analyzing the evolution of the potential energy respect the C-H or C-C distance for the three energy profiles inspected in Figure 5.6, the results shown in Figure 5.7 were obtained. Clearly, more energy profiles in the training set, improved the reaction kinetics description in two ways, the shape of the curves, as well as the geometries and energies of the transition states: 25.3 (1.52), 14.6 (1.63) and 30.7 (1.99) kcal mol^{-1} (Å) vs 24.0 (1.52), 16.6 (1.63) and 31.8 (1.99) kcal

mol^{-1} (Å) for the energies (key C-H and C-C bond distances in parenthesis) with ReaxFF and DFT for **TS1**, **TS3** and **TS13**, respectively.

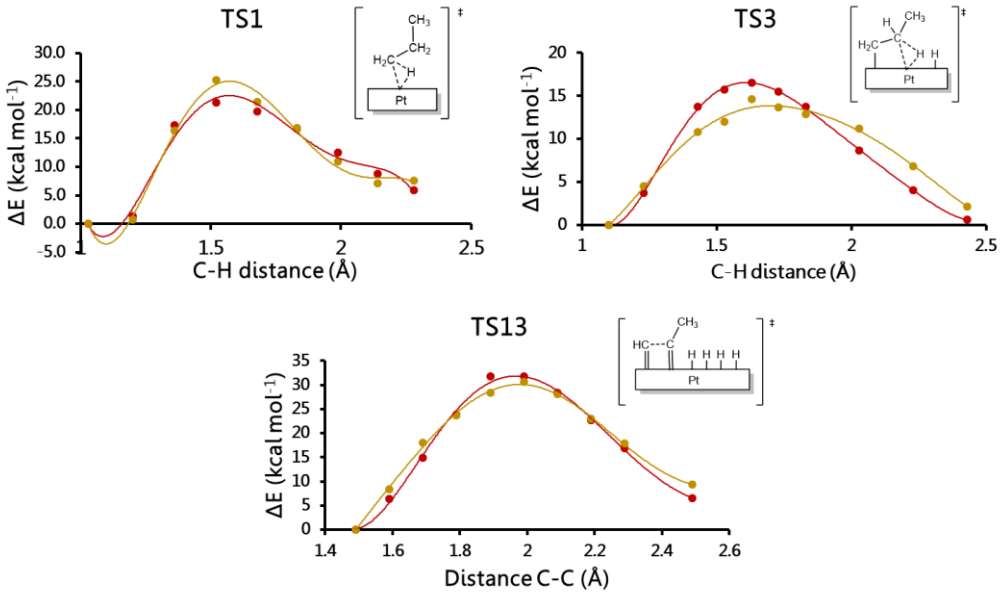

Figure 5.7. Energy profiles of **TS1**, **TS3** and **TS13**. Yellow curve represents the ReaxFF **2021c-Pt/C/H** force field results. Red curve corresponds to DFT reference data.

Finally, a molecular dynamics simulation was carried out. We performed a 2 ns simulation on a system composed of a p(6x6) supercell, 5-layer Pt(111) surface and 2 C_3H_8, 1 **I1**, 1 **I3** and 3 hydrides adsorbed species and the temperature was set at 873 K. At the beginning, any reaction like deep dehydrogenation or C-C bond breaking was detected. However, at 25.2 ps, the Pt atom on which **I1** was attached was split from the surface, diffusing within the gas phase. Later, the 1-propyl molecule was highly deep dehydrogenated due to the high reactivity of the atomic Pt. Finally, around 551 ps, more Pt atoms were split in the gas phase, forming Pt-hydride clusters, and atomic C species were detected on the deformed surface. Figure 5.8 shows some snapshots about the commented molecular dynamic simulation.

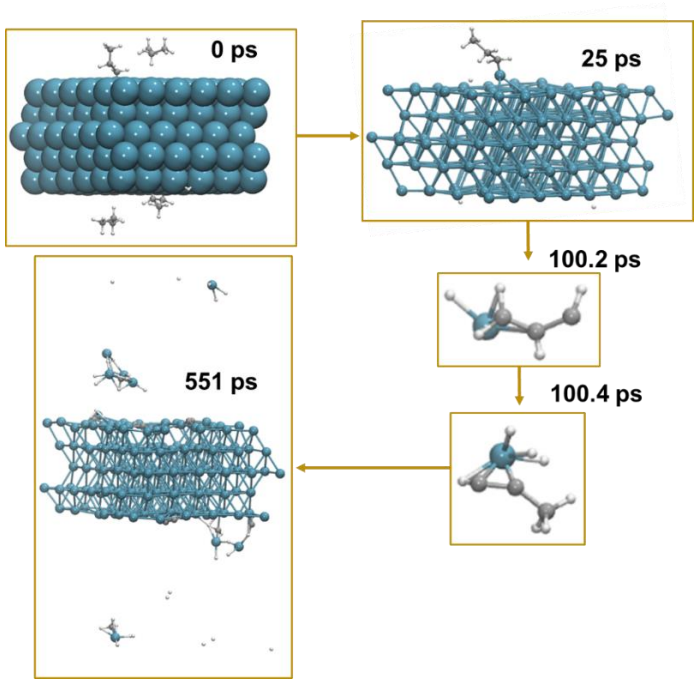

Figure 5.8. Snapshots of the molecular dynamics simulation test preformed with ReaxFF **2021c-Pt/C/H** force field.

2021d-Pt/C/H

The next version was devoted to solve the problem of Pt diffusion. Thus we set the Pt-Pt E_σ parameter at 122.1396 kcal mol^{-1} as in **2016-Pt/H/O**, to make the Pt-Pt bond stronger. Also, we changed the jobs performed on the points of the energy profiles during the force field optimization from single points to partial optimizations, freezing the critical bonds, and including their geometrical parameters in the training set. The MAE of the elementary reactions energies decreased from 4.6 to 4.1 kcal mol^{-1} for **2021c-Pt/C/H** and **2021d-Pt/C/H**, respectively. In addition, the energies and distances (in parenthesis) of the transition states **TS1**, **TS3** and **TS13** shown in Figure 5.6 and Figure 5.7 were 21.3 (1.52), 16.6 (1.63) and 31.8 (1.99) kcal mol^{-1} (Å) vs 19.8 (1.68), 18.0 (1.43) and 30.9 (2.19) kcal mol^{-1} (Å), with DFT and **2021d-Pt/C/H** ReaxFF force field, respectively. At the end of the validation we performed a MD simulation with the same model used for **2021c-Pt/C/H** (6x6 supercell, 5-layer Pt(111) surface and 2 C_3H_8, 1 **I1**, 1 **I3** and 3 hydrides adsorbed species). The total simulation time was 2 ns. During the whole simulation the two propane molecules did not react, but the two adsorbed species (**I1** and **I3**) rapidly decomposed via C-C single bond breaking and deep-dehydrogenation starting at 2 ps, leading to a final distribution of 3 CH_3, 1 CH_2, 1 C_2H_2 and 1 H as adsorbed species, and 2 C_3H_8 and 1 H_2 as free

molecules. Figure 5.9 shows a snapshot of the end of the simulation, where one can observe a highly decomposition of the adsorbed species. That fact could suggest an extremely weak C-C single bond supported by a decrease of the C-C E_σ force field parameter from 139.8093 kcal mol^{-1} in **2008-Pt/C/H** to 60.6377 kcal mol^{-1} in **2021d-Pt/C/H**.

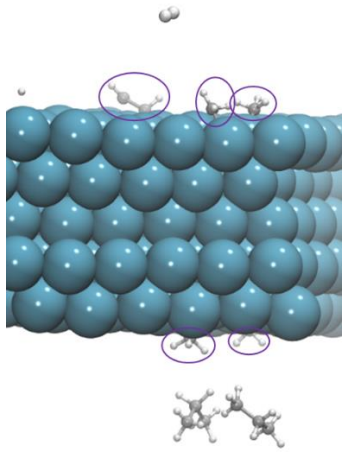

Figure 5.9. Snapshot of the end of the simulation at 2 ns. The marked molecules are the highly degraded products.

5.2.4 Development of 2022-Pt/C/H Force Field

To improve the description of the C-C sigma bong dissociation energy we did two things: 1) we added one more C-C energy profile, corresponding to the C-C bond breaking from 1-propyl (**I1**) to methylidene and ethyl (**I10**), and 2) we set the initial C-C E_σ force field parameter value at 130.0 kcal mol^{-1}, and we narrowed the ranged in which it was allowed to move during the optimization to avoid a drastic fall. The initial guess for this version was **2021d-Pt/C/H**, and after optimization we obtained the last set of parameters that we called **2022-Pt/C/H**.

Internal validation

Firstly, we inspect the thermodynamics of the reaction using static ReaxFF calculations. We calculated the adsorption energy for the propane physisorption and for the propene chemisorption. For propane, ReaxFF gave an adsorption energy of -0.7 kcal mol^{-1} in front the +0.1 of DFT, whereas the adsorption energy for propene was -17.5 and -19.1 kcal mol^{-1} for ReaxFF and DFT, respectively. Then we computed the reaction energies for all the processes in Figure 5.4, and they are shown in Figure 5.10. The MAE was 3.4 kcal mol^{-1}, and represents an

improvement of the reaction thermodynamics of 0.7 kcal mol^{-1} respect **2021d-Pt/C/H** (**2021d-Pt/C/H** MAE = 4.1 kcal mol^{-1})

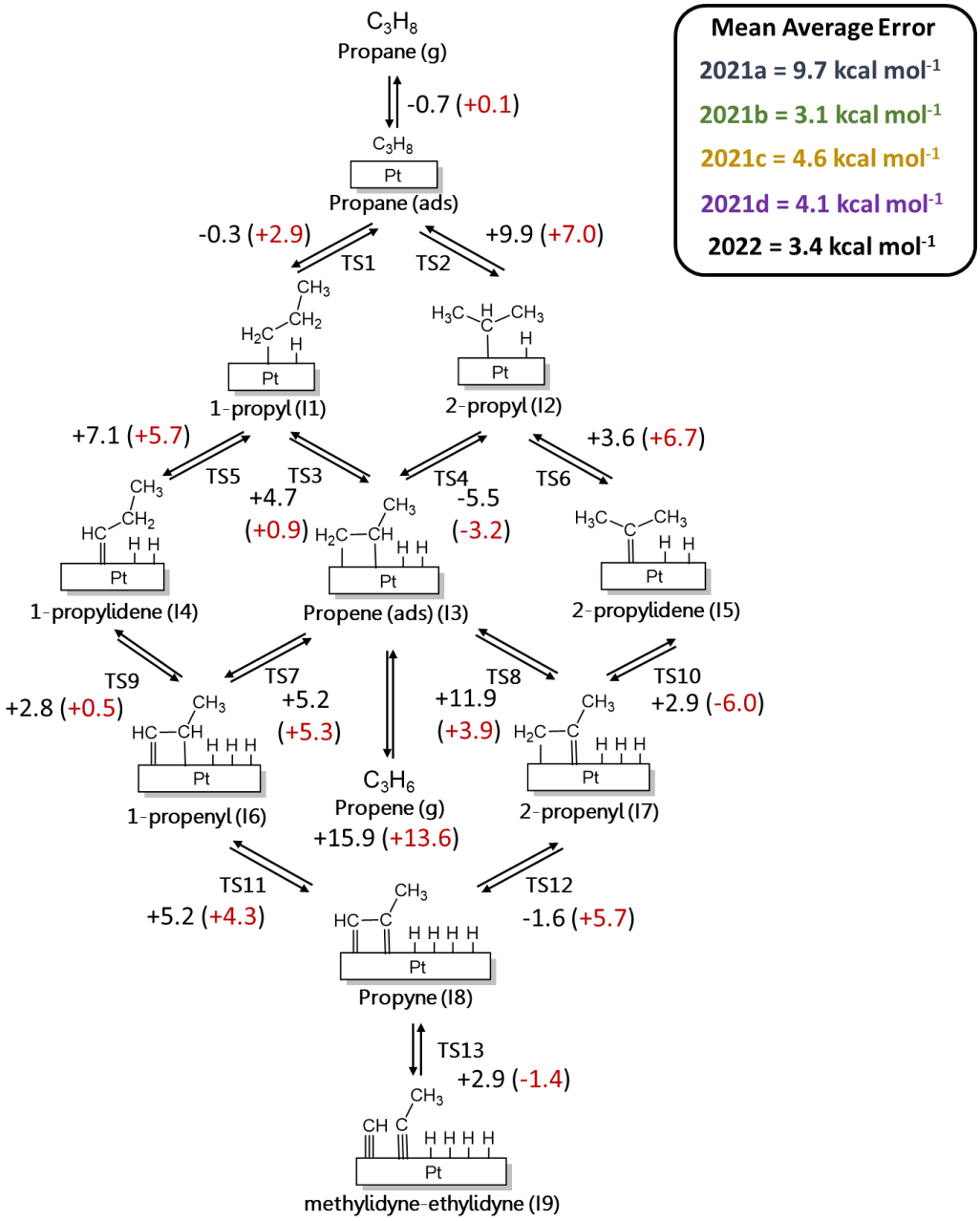

Figure 5.10. PDH reaction profile scheme and correspondent computed elementary reaction energies. Black: ReaxFF **2022-Pt/C/H**. Red: DFT. On the right top corner are shown the MAE for all the force field versions.

Secondly, we checked the kinetics of the reaction computing some of the energy profiles included in the training set: the four C-H bond activations leading to **I3** (**TS1**, **TS2**, **TS3** and **TS4**) and two C-C bond breaking (**TS13** and **TS14**) shown in Figure 5.11. The highest points of the plots represent the structures close to the transition states, and the energies and the key distances (C-H or C-C) are printed in Table 5.5. In most cases the MAE for the energies was not higher than 5 kcal mol^{-1}, and for the distances it was not higher than 0.2 Å. This indicates a good fitting between the DFT reference data and the ReaxFF **2022-Pt/C/H** force field, and a good description of the kinetics of the reaction. Moreover, the force field is able to distinguish between the first and second C-H activations, being the first ones higher in energy, and also, is able to distinguish between the higher energy barriers for a C-C rather than a C-H bond breaking. In addition, with the current ReaxFF AMS engine, it is possible nowadays to calculate transition states, and the energy barriers for the different elemental processes are also shown in Table 5.5, and they are in good agreement with the energy barriers computed by Su *et al.*[5] Unfortunately, TS14 was not found.

Table 5.5. Relative energies and key C-H and C-C distances of the highest point structures of the profiles shown in Figure 5.11, and the energy barriers calculated by ReaxFF engine of AMS program. Energies in kcal mol^{-1} and key distances in (Å). NF = Not Found.

	Energy profiles				Energy barriers			
	DFT		ReaxFF 2022-Pt/C/H		DFT[5]		ReaxFF 2022-Pt/C/H	
	E	Key distances	E	Key distances	E	Key distances	E	Key distances
TS1	21.3	1.52	25.0	1.52	21.2	1.52	25.8	1.55
TS2	24.9	1.61	23.4	1.61	21.2	1.61	22.9	1.57
TS3	16.6	1.63	16.9	1.53	20.8	1.62	22.1	1.56
TS4	13.6	1.46	14.7	1.56	21.7	1.56	18.7	1.53
TS13	31.8	2.09	36.6	2.19	33.0	1.99	29.9	2.21
TS14	41.2	2.18	36.1	2.18	42.0	2.08	NF	NF

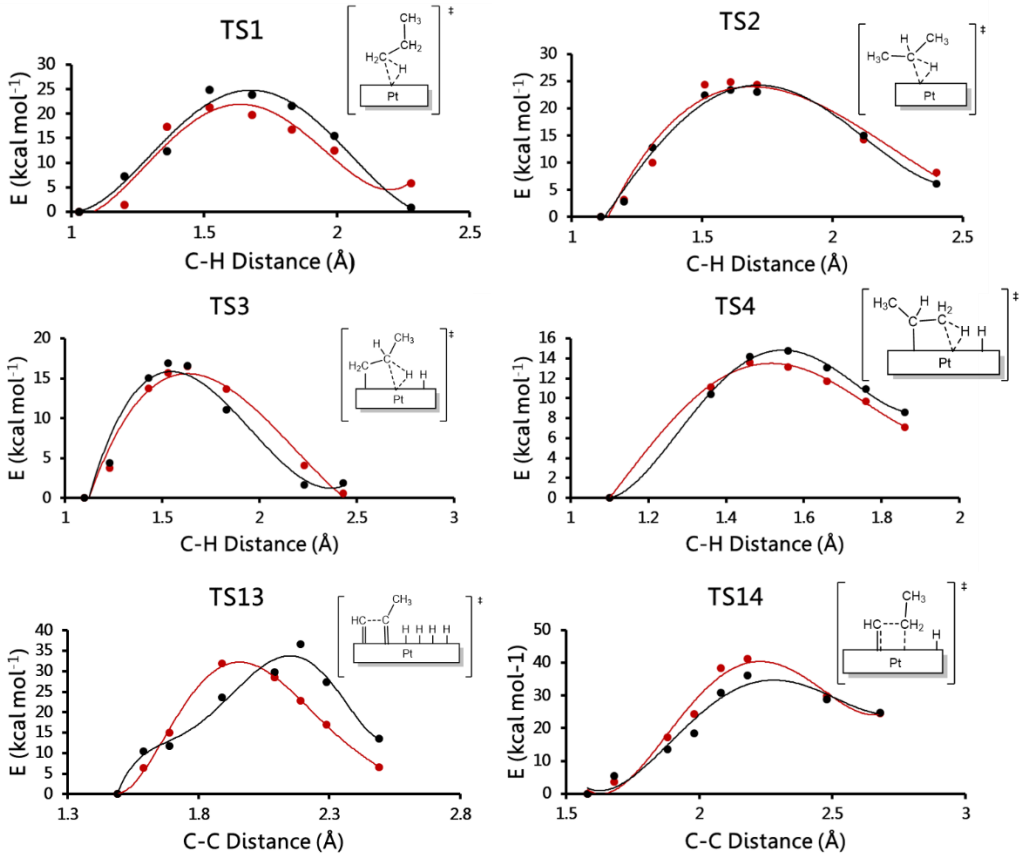

Figure 5.11. Energy profiles of processes involved in the PDH reaction and coke precursors formation. Red: DFT reference data. Black: ReaxFF **2022-Pt/C/H** results.

External Validation

As external validation, we computed the respective C-H bond breaking profiles of **TS6** and **TS9**. They are plotted in Figure 5.12. The energies and key C-H distances of the respective highest points, as well as the energy barriers and C-H distances of the transition states calculated with the ReaxFF AMS engine and their comparison with the bibliographic data are shown in Table 5.6. The MAE for the energies of **TS6** and **TS9** are 3.2 and 2.2 kcal mol^{-1} and 0.1 Å for the distances in the energy profiles, respectively. Furthermore, the MAE of the energy barriers and the C-H distances (in parenthesis) of the TS calculated by the ReaxFF program developed by SCM for **TS6** and **TS9** respect the work of Su *et al.* are 2.3 (0.05) and 0.4 (0.08) kcal mol^{-1} (Å), respectively. That indicates a good description of processes not included in the training set.

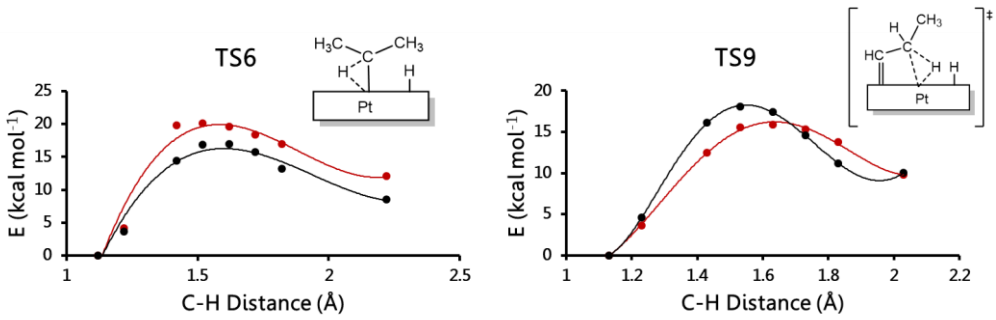

Figure 5.12. Energy profiles of the selected processes for the external validation, **TS6** and **TS9**. Red: DFT reference data. Black: ReaxFF **2022-Pt/C/H** results.

Table 5.6. Relative energies and key C-H distances of the highest point structures of the profiles shown in Figure 5.12, and the energy barriers calculated by ReaxFF engine of AMS program. Energies in kcal mol^{-1} and key distances in (Å).

	Energy profiles				Transition States			
	DFT		ReaxFF 2022-Pt/C/H		DFT[5]		ReaxFF 2022-Pt/C/H	
	E	Key distances	E	Key distances	E	Key distances	E	Key distances
TS6	20.2	1.52	17.0	1.62	24.4	1.62	22.1	1.57
TS9	15.9	1.63	18.1	1.53	18.5	1.63	18.9	1.55

A ReaxFF MD simulation was carried out with a model system to expand the external validation. The model was composed by a p(6x6) supercell, 5-layer Pt(111) surface and 2 C_3H_8, 1 **I1**, 1 **I3** and 3 hydrides adsorbed species. The temperature was set at 873 K and the total simulated time was 2 ns with equilibration, non-reactive 100 ps. The two propane molecules did not react during the whole simulation, in agreement with the endothermic character of the reaction. However, **I1** rapidly desorbs when the reactive time of the simulation just started and remained in the gas phase until the end of the simulation. In the case of **I3**, around 1.4 ns, a C_3H_6 molecule is formed via **TS3**, and after 2.8 ps it is desorbed. At the end, the product distribution was: 2 C_3H_8, 2 C_3H_6 and 4 H atoms adsorbed onto the Pt surface. Figure 5.13 shows some snapshots of the processes commented. With the results of the internal and external validations in hand, we think that the ReaxFF **2022-Pt/C/H** force field is suitable to describe properly the propane dehydrogenation reaction catalyzed by Pt surfaces, and it is ready to perform productive reactive MD.

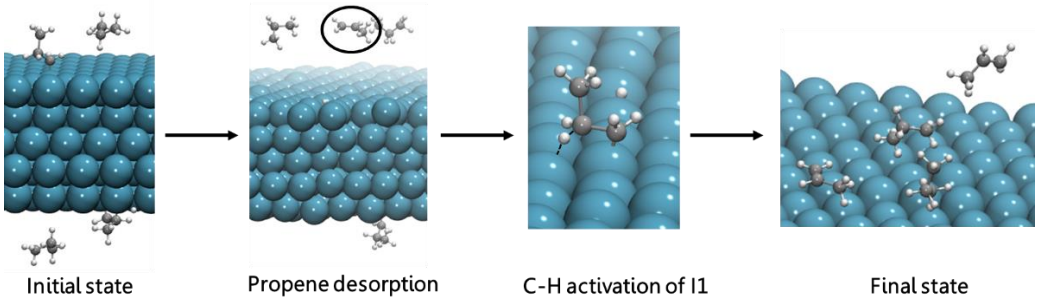

Figure 5.13. Snapshots of reactive MD simulation of the model system used in the external validation of the ReaxFF **2022-Pt/C/H** force field.

5.2.5 Study of PDH Catalyzed by Pt with ReaxFF MD Simulations

We used our newly developed ReaxFF **2022-Pt/C/H** force field to study the PDH reaction catalyzed by Pt surfaces and NPs, and the effect that the presence of defects could have on this reaction. Thus, we selected two Pt surfaces, the flat Pt(111) slab and the stepped Pt(211) one and the Pt_{55} icosahedral NP. We performed 5 simulations per system, and in all simulations the reactant was propane, without any species already adsorbed on the surfaces, and all of them were of 2 ns of duration at 1000 K. Table 5.7 summarize the results obtained in the PDH ReaxFF MD analysis. In the case of Pt(111), one C_3H_7 (**I1**) molecule was detected only in one of the five simulations representing an average of 0.5% of conversion. The first C-H activation undergoes via **TS1** at 911 ps of simulation. In the case of Pt(211) two different products were observed for two different simulations: C_3H_6 (**I3**) and a deep-dehydrogenated product C_3H_5 (allyl). In both simulations, the formation of propene undergoes via **TS1** and subsequent **TS3** at 1.68 and 1.98 ns for one simulation and at 633 and 848 ps for the second simulation. However, in the second simulation, at 1.47 ns, a third C-H bond activation is observed on the CH_3 group of propene, leading to a deep-dehydrogenated allyl product. The average conversion of propane catalyzed by Pt(211) surface was 0.88 % with a selectivity towards propene of 20 %. Figure 5.14 shows some snapshots where the intermediates commented previously can be appreciated. That simulations agree with the endothermicity of the reaction, showing low propane conversion in the simulated times. Also, they indicate that the Pt(211) surface is more reactive than Pt(111), where the steps are crucial to increase the propene conversion, but they also favor undesired side reactions such as deep-dehydrogenations in agreement with Zhou *et al.*[33] Finally, the preferential pathway of **2022-Pt/C/H** force field for the formation of propene is through **I1** prior a second C-H activation via **TS3**. The Pt_{55} NP catalyst presented

higher reactivity than the surfaces with a 2.6 % of propane conversion. However, more reactivity also means a higher proportion of deep dehydrogenation side reactions. The distribution of products shows a large variety of activated products such as, propene and the deep dehydrogenated species C_3H_5 (allyl), C_3H_2, C_3H_3, C_3H_4 (**I8**) and one H_2 molecule, representing a selectivity of 37 % towards propene.. Again, the preferred propene pathway is through **I1** followed by a second C-H activation (**TS3**). The further dehydrogenations that lead to **I9** goes via primary carbon C-H activation (**I6**). Figure 5.14 shows some of the different products detected in the simulations of PDH catalyzed by Pt_{55} NP.

Table 5.7. Simulation conditions and product distribution of PDH for the three systems studied with ReaxFF MD simulations.

Catalyst	Simulated time (ns)	n propane (estimated P in atm)	T (K)	Products	Conversion
Pt(111)	10 (5 x 2 ns)	40 (912)	1000	*1-propyl	0.5 %
Pt(211)	10 (5 x 2 ns)	46 (912)	1000	*propene *CH_2=CH-CH_2	0.9 %
Pt_{55} ICO	10 (5 x 2 ns)	100 (516)	1000	propene *CH_2=CH-CH_2 *C_3H_2 *C_3H_3 *C_3H_4 H_2	2.6 %

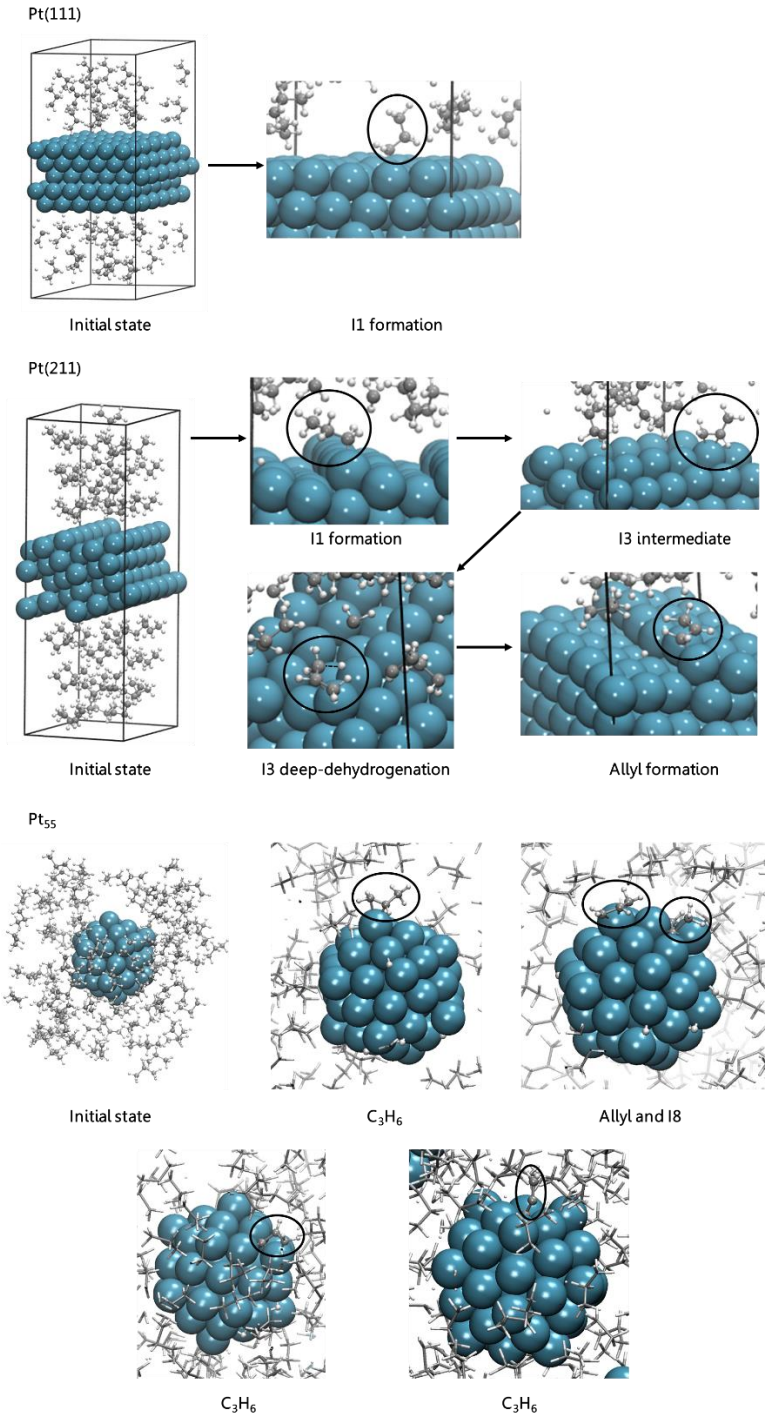

Figure 5.14. Snapshots of the reactive MD simulations performed with the ReaxFF **2022-Pt/C/H** force field for the PDH catalyzed by Pt(111), Pt(211) and Pt_{55}.

5.2.6 Evaluation of the performance of ReaxFF

In this last section we want to analyze the cost in terms of computational time of: 1) the optimization of a ReaxFF force field with CMA-ES algorithm, and 2) the performance of ReaxFF with reactive MD simulations. On one hand, the results for the assessment of the ReaxFF force field optimization are shown in Table 5.8. The computational cost of a ReaxFF force field optimization depends on several parameters, such as the number of entries in the training set, the number of Error Function Evaluations (EFE) or the numbers of CPUs used. However, the parameters that have a major impact on the cost of a ReaxFF force field optimization are: 1) the intrinsic algorithm performance, noted for instance with the versions **2021a-Pt/C/H**, **2021b-Pt/C/H** and **2021c-Pt/C/H**, that despite in **2021b-Pt/C/H** had much less entries in the training set than **2021a-Pt/C/H** and more EFE than **2021c-Pt/C/H**, it took around 5 times more time to reached the maximum number of EFE, and 2) the job performed on the structures for each EFE, that changing from single point (sp) to partial or full optimization the time required to reach the number of EFE can be switched from hours to date. Nevertheless, it is important to point out that the error function value has an exponential decrease during the force field parameters optimization with a drastic falling until the point where the improvement is minimum. After that point, the optimization can be killed without losing in force field parameters quality. This procedure is known as "early stopped". Figure 5.15 shows the evolution of the error function value in the **2022-Pt/C/H** force field optimization.

Table 5.8. Assessment of the ReaxFF force field optimization with CMA-ES multivariable optimization algorithm. EFE = Error Function Evaluations, sp = single point and par-opt = partial optimization. Job EFE is the type of calculation performed on the energy profiles structures in each error function evaluation.

FF version	n structures	Entries in training set	Job EFE	n EFE	Cores	time
2021a	40	75897	sp	160000	32	~10 h
2021b	35	1292	sp	320000	32	~48 h
2021c	88	1339	sp	400000	40	~17 h
2021d	88	13645	par-opt	600000	60	10 days
2022	98	1358	par-opt	600000	64	15 days

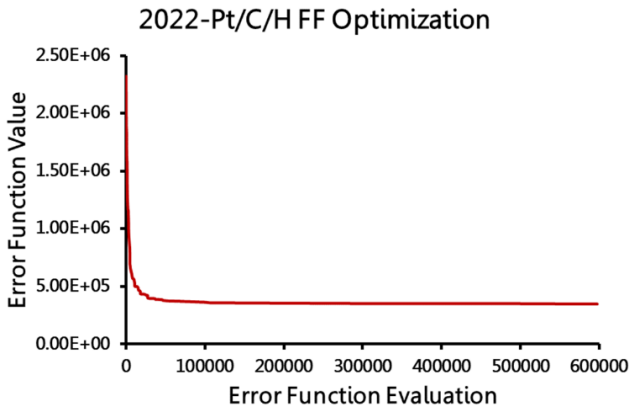

Figure 5.15. Evolution of the Error Function Value during the 2022-Pt/C/H force field optimization using the CMA-ES algorithm.

On the other hand, the results of the evaluation of the ReaxFF performance are shown in Table 5.9. The values indicate that ReaxFF approach is a very powerful tool to perform long reactive MD simulations with very large systems with very low computational cost, because a reactive simulation of 2 ns with a system of more than one thousand atoms with AIMD is unthinkable, even more in 43 hours. In addition, the parallelization of the ReaxFF scm program is exceptional, because only increasing the number of CPU cores in 4, the time required is reduced to the half.

Table 5.9. Performance analysis of ReaxFF program in reactive MD simulations.

System	n atoms	Simulated time (ns)	Time step (fs)	Wallclock time[1]	Wallclock time[2]
Pt(111) + 40 C_3H_8	620	2	0.1	36 h	70 h
Pt(211) + 46 C_3H_8	650	2	0.1	38 h	79 h
Pt_{55} + 40 C_3H_8	1155	2	0.1	44 h	-

[1] average time of the simulations performed on 64 CPU cores.
[2] average time of the simulations performed on 60 CPU cores.

5.3 Concluding Remarks

In this Chapter we developed a new ReaxFF force field to study the Propane Dehydrogenation reaction catalyzed by Pt surfaces and NPs: ReaxFF **2022-Pt/C/H** force field. First, we assessed the transferability of three different force fields obtained from the literature (**2016-Pt/Ni/C/O/H**, **2016-Pt/H/O** and **2008-Pt/C/H**). All of them were trained for different purposes, and they show notable discrepancies describing the geometries and relative energies of some key intermediates of PDH catalyzed by the Pt(111) surface, even with different DFT data from the bibliography. This fact pointed out the importance of the training set used in the development of a ReaxFF force field, and the need to re-parameterize one of these set of parameters to study PDH reaction catalyzed by Pt.

The ReaxFF force field parameterization is a non-straightforward procedure, based on an iterative strategy where the user must identify the weak points of the force field, and solve them by increasing the entries in the training set, manipulating the force field parameters or adjust the weights of the parameters in the error function, among others, until a suitable force field is achieved. We used the CMA-ES algorithm to optimize the force field and fit the parameters to home-produced DFT reference data. To obtain the first version of the force field, called **2021a-Pt/C/H**, we used the **2016-Pt/H/O** force field as initial guess, because it reproduced quite well the geometries of some key species, but not the energies. The training set was composed by the geometries and relative energies of all the elementary processes shown in Figure 5.4, and two energy profiles: propene adsorption and propane C-H bond breaking in the gas phase. After re-parameterization, the energies were improved. For instance, the adsorption energy of propane was decreased from -41.8 to -19.8 kcal mol^{-1}. However, during a MD simulation, we did not observe any kind of reaction, due to the high energy barrier of a C-H bond breaking of ~75 kcal mol^{-1}. For that reason, the second version (**2021b-Pt/C/H**) was devoted to decrease that energy barrier. To do that, we change the C-H bond breaking energy profile in gas phase, for the equivalent catalyzed by Pt(111) surface. The energy barrier for **TS1** was greatly decreased from 70 to 17 kcal mol^{-1}, but the kinetics of other C-H and C-C activations were not well reproduced. Thus, we added more C-H and C-C energy profiles in the training set, and after optimization we got the third version of the force field, **2021c-Pt/C/H**. In that case the geometries and the relative energies were well described, with a MAE for the elementary processes of 4.6 kcal mol^{-1}, and the reaction kinetics showed almost an excellent fitting with the reference DFT data. However, when reactive MD simulations were performed, we observed a surface degradation, forming Pt-hydride clusters diffusing within the gas phase. That fact revealed a too weak Pt-Pt bond, thus, for the next **2021d-**

Pt/C/H force field version we set the Pt-Pt E_σ parameter from 98.9857 kcal mol^{-1} in **2021c-Pt/C/H** to 122.1396 kcal mol^{-1}, as in the reference **2016-Pt/H/O** force field. Doing that, we solved the issue of Pt diffusion, without decreasing the accuracy on the geometries, relative energies and kinetics, even they were improved indicated by a reduction of the MAE of the elementary reaction energies from 4.6 to 4.1 kcal mol^{-1}. Nevertheless, in the reactive MD simulations, the main products detected were CH_3 and CH_2, formed by a single C-C bond breaking, before any C-H activation, revealing a bad description of the C-C single bond. Finally, we obtained the last version of the force field, called **2022-Pt/C/H**, adding one more C-C bond breaking energy profile in the training set.

The internal validation of the **2022-Pt/C/H** force field indicated a good fitting between the DFT and ReaxFF values. The MAE of the relative energies was 3.4 kcal mol^{-1}, and the maximum MAE of the highest point energies and key distances was less than 5 kcal mol^{-1} and not higher than 0.1 Å, respectively. Moreover, the energy barriers and distances for **TS1**, **TS2**, **TS3**, **TS4**, **TS13** and **TS14** calculated with the ReaxFF engine of AMS package of programs agree with the results provided in the literature, with a maximum MAE of 4.6 kcal mol^{-1} for **TS1** and 0.22 Å for the C-C distance of **TS13**. For the external validation, **TS6** and **TS9** were selected, and also matched with the DFT reference data, with MAE for the relative energies in the energy profiles of 3.2 and 2.2 kcal mol^{-1}, respectively, and 0.1 Å for the key C-H distances in both cases. The reactive MD simulation performed as external validation test, shows the formation of 2 C_3H_6 molecules, without the issues of the previous versions, such as Pt diffusion or C-C single bond breaking. With all of that, we think that the **2022-Pt/C/H** force field is ready to be used in productive MD simulations.

To study the PDH with the new ReaxFF **2022-Pt/C/H** force field we selected two different surfaces (Pt(111) and Pt(211)) and the Pt_{55} icosahedral NP. In the case of Pt(111) at the end of the simulation we detected only the intermediate **I1** as product, representing a conversion of 0.5 % of propane. With Pt(211) we observed the formation of two different species: one propene and one allyl, leading to a 0.9 % of conversion with a 20 % of selectivity towards propene. The simulations showed that the Pt(211) surface is more reactive than the Pt(111) surface. In addition, all reactive events observed with Pt(211) undergo on the edged Pt atoms. The analysis of the mechanism reveals that the formation of propene takes place via **I1** preferentially, rather than **I2** with **2022-Pt/C/H** force field. The Pt55 NP presented higher activity with a 2.6 % of propane conversion, but also with higher proportion of deep dehydrogenated products with a 37 % of selectivity towards propene.

Finally, we assessed the cost of parameterize a ReaxFF force field with CMA-ES algorithm and the performance of ReaxFF to simulate large systems and long

times. The cost of parameterize a ReaxFF force field depends on several parameters, such as the number of entries in the training set or the number of EFE. Nevertheless, the variables that have a major impact on the computational cost are the algorithm used and the job performed on each structure for each EFE, switching the time required from hours to days. However, once the force field is obtained, ReaxFF is a very powerful tool to simulate long times and large systems at low computational cost. For instance, it is able to simulate 2 ns on a system of more than a thousand atoms with less than two days, something impossible to achieve with AIMD techniques.

5.4 Computational Details

Static Quantum Chemical Calculations. The quantum chemical reference dataset to train the different force fields was generated in the URV facilities. All reference data was calculated using the 5.3.5 version of Vienna Ab Initio Simulation Package (VASP)[34] within the Density functional Theory (DFT) approach.[35] The Generalized Gradient Approximation (GGA) functional used was revised-PBE (RPBE)[36] with a cut-off energy for the plane waves basis set of 400 eV to describe the valence electrons, whereas the core electrons was defined using the Projector Augmented Wave (PAW) method.[37] The Monkhorst-Pack[38] 3x3x1 k-point mesh was used for the integration in the reciprocal space. The convergence criterion for the electronic minimization was set at 10^{-7} eV, while the geometry was optimized when the forces over all atoms were smaller than 0.03 eV $Å^{-1}$. The partial occupancies of the orbitals were stablished using the Methfessel-Paxton scheme[39] with a smearing of 0.2 eV. The model surface was taken from IoChem-BD database[40] used in the work from López *et al.*[41] It was composed by a p(3x3) 5-layer Pt surface in a unit cell of 8.44295 x 8.44293 x 22.1673 $Å^3$.

ReaxFF force field Optimization. The optimizer used to find the best fitting between ReaxFF and quantum data was the Covariance Matrix Adaptation Evolution Strategy (CMA-ES)[42,43] implemented in SCM package of programs[44] Since CMA-ES is a stochastic method, for each force field optimization we performed 5 different runs. For each run the number of iterations was set to 10000 with a sample size of 60, giving a total number of error function evaluations of 600000. The optimization procedure was stopped when the total number of function evaluations was reached or if the step-size became smaller than 10^{-6} for each parameter.

Static ReaxFF Calculations. The minimization method to perform static ReaxFF calculations was L-BFGS with a maximum number of iterations of 10000 and with a force convergence criterion of 1 kcal mol^{-1} $Å^{-1}$.

ReaxFF Dynamic Simulations.

Assessment of the transferability: all simulations were performed with a 5-layer slab of the Pt(111) surface in a p(9x9) supercell. The temperature was set at 873 K. The number of propane molecules per unit cell was varied modelling different coverages and pressures. Coverage of 1/9 ML corresponds to 18 propane molecules and hence a pressure of 206 atm. Coverage of 2/9 ML corresponds to 36 propane molecules and a pressure of 412 atm. These high pressures were set to ensure the reactivity in the available short simulation times. The simulations were done within a NVT ensemble, using a Hoove-Nose thermostat[45]. The time step for all simulations was 0.1 fs.

External validations: the model was composed by a p(6x6) supercell, 5-layer Pt(111) surface and 2 C_3H_8, 1 **I1**, 1 **I3** and 3 hydrides adsorbed species. The temperature was set at 873 K in a NVT ensemble using Berendsen thermostat[46] with a damping constant of 100 fs, and using a Velocity-Verlet integration method. The total simulated time was 2 ns with equilibration non-reactive 100 ps with a time step of 0.1 fs.

Productive MD simulations: we performed 5 simulations for each catalyst, Pt(111), Pt(211) and Pt_{55} NP. The total simulation time for all of them was 2 ns with 100 ps of non-reactive time to equilibrate the system, with a time step of 0.1 fs. The temperature was set at 1000 K in a NVT ensemble using Berendsen thermostat with a damping constant of 100 fs, and using a Velocity-Verlet integration method. The system for Pt(111) simulations was composed by a 5-layered p(6x6) supercell, and 40 propane molecules representing a total pressure of 795 atm. These high pressures were set to ensure the reactivity in the available short simulation times. The system for Pt(211) simulations was composed by a 5-layer p(6x6) supercell in a box of 13.58966 x 16.64388 x 40.0 $Å^3$ of lattice, and 46 propane molecules, keeping the total pressure at the same value than for the Pt(111) simulations. The system for the simulation with the nanocatalyst was composed by the Pt_{55} icosahedral nanoparticle in a cubic box of 30 x 30 x 30 $Å^3$, with 100 propane molecules.

References

1. Sattler, J.; Ruiz-Martinez, J.; Santillan-Jimenez, E.; Weckhuysen, B. M. *Chem. Rev.* **2014**, *114*, 10613-10653.
2. Bhasin, M. M.; McCain, J. H.; Vora, B. V.; Imai, T.; Pujadó, P. R. *Appl. Catal. A* **2001**, *221*, 397-419.
3. Dobis, O.; Benson, S. W. *Int. J. Chem. Kinet.* **1987**, *19*, 691-708.
4. Russell, J. J.; Seetulam J. A.; Gutman, D. *J. Am. Chem. Soc.* **1988**, *110*, 3092-3099.
5. Lian, Z.; Ali, S.; Liu, T.; Si, C.; Li, B.; Su, D. S. *ACS Catal.* **2018**, *8*, 4694–4704.
6. Saerens, S.; Sabbe, M. K.; Galvita, V. V; Redekop, E. A. *ACS Catal.* **2017**, No. 111, 1–32.
7. Davis, R. J.; Griffith, R. H.; Marsh, J. D. F. *Adv. Catal.* **1957**, *9*, 155-168.
8. Tinnemans, S. J.; Kox, M. H. F.; Nijhuis, T. A.; Visser, T.; Weckhuysen, B.M. *Phys. Chem. Chem. Phys.* **2005**, *7*, 211-216.
9. Liu, G.; Zeng, L.; Zhao, Z. J.; Tian, H.; Wu, T. F.; Gong, J. L.; Platinum-Modified ZnO/Al_2O_3 for Propane Dehydrogenation: Minimized Platinum Usage and Improved Catalytic Stability. *ACS Catal.* **2016**, *6*, 2158-2162.
10. Iglesias-Juez, A.; Beale, A. M.; Maaijen, K.; Weng, T. C.; Glatzel, P.; Weckhuysen, B. M. *J. Catal.* **2010**, *276*, 268-279.
11. Van Duin, A. C. T; Dasgupta, S.; Lorant, F.; Goddard, III W. A. *J. Phys. Chem. A* **2001**, *105*, 9396-9409.
12. Stuart, S. J.; Tutein, A. B.; Harrison, J. A. *J. Chem. Phys.* **2000**, *112*, 6472–6486.
13. Liang, T.; Shin, Y. K.; Cheng, Y. T.; Yilmaz, D. E.; Vishnu, K. G.; Verners, O.; Zou, C.; Phillpot, S. R.; Sinnott, S. B.; Van Duin, A. C. T. *Annu. Rev. Mater. Res.* **2013**, *43*, 109–129.
14. Shin, Y. K.; Shan, T.-R.; Liang, T.; Noordhoek, M. J.; Sinnott, S. B.; van Duin, A. C. T.; Phillpot, S. R. *MRS Bull.* **2012**, *37*, 504–512.
15. Fonseca, A. F.; Lee, G.; Borders, T. L.; Zhang, H.; Kemper, T. W.; Shan, T. R.; Sinnott, S. B.; Cho, K. *Phys. Rev. B* **2011**, *84*, 34–36.
16. Shan, T. R.; Devine, B. D.; Hawkins, J. M.; Asthagiri, A.; Phillpot, S. R.; Sinnott, S. B. *Phys. Rev. B - Condens. Matter Mater. Phys.* **2010**, *82*, 1–9.
17. Phillpot, S. R.; Sinnott, S. B. *Science.* **2009**, *325*, 1634–1635.
18. Neyts, E. C.; Ostrikov, K.; Han, Z. J.; Kumar, S.; Van Duin, A. C. T.; Bogaerts, A. *Phys. Rev. Lett.* **2013**, *110*, 1–5.
19. Monti, S.; Corozzi, A.; Fristrup, P.; Joshi, K. L.; Shin, Y. K.; Oelschlaeger, P.; Van Duin, A. C. T.; Barone, V. *Phys. Chem. Chem. Phys.* **2013**, *15,* 15062–15077.
20. Deng, L.; Miura, H.; Shishido, T.; Wang, Z.; Hosokawa, S.; Teramura, K.; Tanaka, T. *J. Catal.* **2018**, *365*, 277–291.

21. Senftle, P. T.; Hong, S.; Islam, M. M.; Kylasa, S. B.; Zheng, Y.; Shin, Y. K.; Junkermeier, C.; Engel-Herbert, R.; Janik, M. J.; Aktulga, H. M.; Verstraelen, T.; Grama, A.; van Duin, A. C. T. *Npj Computational Materials* **2016**, *2*, 15011.
22. Chenoweth, K.; van Duin, A. C. T.; Goddard, III W. A. *J. Phys. Chem. A* **2008**, *112*, 1040-1053.
23. Leven, I.; Hao, H.; Tan, S.; Guan, X.; Penrod, K. A.; Akbarian, D.; Evangelisti, B.; Hossain, M. J., Islam, M. M.; Koski, J. P.; Moore, S.; Aktulga, H. M.; van Duin, A. C. T.; Head-Gordon, T. *J. Chem. Theory Comput.* **2021**, *17*, 3237-3251.
24. Shin, Y. K.; Gai, L.; Raman, S.; van Duin, A. C. T. *J. Phys. Chem. A* **2016**, *120*, 8044-8055.
25. Gai. Y.; Shin, Y. K.; Raju, M.; van Duin, A. C. T.; Raman, S. *J. Phys. Chem. C* **2016**, *120*, 9780-9793.
26. Ludwig, J.; Vlachois, D. G.; van Duin, A. C. T.; Goddard, W. A. *J. Phys. Chem. B* **2006**, *110*, 4274-4282.
27. Fantauzzi, D.; Bandlow, J.; Sabo, L.; Mueller, J. E.; van Duin, A. C. T.; Jacob, T. *Phys. Chem. Chem. Phys.* **2014**, *16*, 23118-23133.
28. Sanz-Navarro, C.; Astrand, P-O.; Chen, D.; Ronning, M.; van Duin, A. C. T.; Jacob, T.; Godard III, W. A. *J. Phys. Chem. A* **2008**, *112*, 1392-1402.
29. Lian, Z.; Ali, S., Liu, T.; Chaowei, S., Li, B.; Su, D. S. *ACS Catal.* **2018**, *8*, 4694-4704.
30. Yang, M-L.; Zhu, Y-A.; Fan, C.; Sui, Z-J.; Chen, D.; Zhou, X-G. *J. Mol. Catal. A Chem.* **2010**, *321*, 42-49.
31. Sun. G.; Zhao, Z-J.; Mu, R.; Zha, S.; Li, L.; Chen, A.; Zang, K.; Luo, J.; Li, Z.; Purdy, A. C., Kropf, A. J., Miller, J. T.; Zeng, L.; Gong, J. *Nat. Commun.* **2018**, *9*, 4454.
32. Saerens, S.; Sabbe, M. K.; Galvita, V. V.; Redekop, E. A.; Reyniers, M-F.; Marin, G. B. *ACS Catal.* **2017**, *7*, 7495-7508.
33. Zhang, W.; Wang, H.; Jiang, J.; Sui, Z.; Zhu, Y.; Chen, D.; Zhou, X. *ACS Catal.* **2020**, *10*, 12932-12942.
34. a) Kresse, G.; Hafner, J. *Phys. Rev. B* **1993**, *47*, 558. b) Kresse, G.; Furthmüller, J. *Comput. Mat. Sci.* **1996**, *6*, 15-50. c) Kresse, G.; Furthmüller, J. *Phys. Rev. B* **1996**, *54*, 11169.
35. a) Hohenberg, P.; Kohn, W. *Phys. Rev.* **1964**, *136*, 864-871. b) Kohn, W.; Sham, L. J. *Phys. Rev.* **1965**, *140*, 1133-1138.
36. Hammer, B.; Hansen, L. B.; Norskov, J. K. *Phys. Rev. B* **1999**, *59*, 7413.
37. Kresse, G.; Joubert, D. *Phys. Rev. B* **1999**, *59*, 1758.
38. Monkhorst, H. J.; Pack, J. D. *Phys. Rev. B* **1976**, *13*, 5188.
39. Methfessel, M.; Paxton, A. T. *Phys. Rev. B* **1989**, *40*, 3616.
40. https://www.iochem-bd.org/
41. Navarro-Ruiz, J.; Cornu, D.; López, N. *J. Phys. Chem. C* **2018**, *122*, 25339-25348.
42. Hansen, N.; Müller, S. D.; Koumoutsakos, P. *Evol. Comput.* **2003,** *11*, 1-18.

43. c-cmaes library: https://github.com/CMA-ES/c-cmaes

44. a) https://www.scm.com/ b) https://www.scm.com/product/reaxff/

45. a) Nose, S. *J. Chem. Phys.* **1984**, *81*, 511. B) Nose, S. *Mol. Phys.* **1984**, *52*, 255. C) Hoover, W. G. *Phys. Rev. A* **1985**, *31*, 1695.

46. Berendsen, H. J. C.; Postma, J. P. M.; van Gunsteren, W. F.; DiNola, A.; Haak, J. R. J. *Chem. Phys.* **1984**, *81*, 3684.

Conclusions

UNIVERSITAT ROVIRA I VIRGILI
COMPUTATIONAL MODELING TO EXPLORE SOLVENT AND DYNAMIC EFFECTS IN MOLECULAR, NANO AND SOLID CATALYSIS
Antoni Salom Català

Conclusions

This last chapter summarizes the main achievements and conclusions that have emerged from the studies carried out in this thesis. They are divided into chapters and are presented point by point, trying to relate them to the corresponding objectives.

Regioselective Telomerization of Isoprene: Solvent and Ligand Control (Chapter 2).

- The acidity is the responsible of the solvent control on the selectivity, which shifts the selectivity-determining step, from the protonation step, to a C-C oxidative coupling step. For acidic solvents, such as TFE, the C-C oxidative coupling is the selectivity-determining step, due to the fast and irreversible protonation, while for less acidic solvents, such as *t*BuOH, the protonation step becomes slower and more influential in the selectivity.
- The ligand exerts its influence on the selectivity due to its steric control. For instance, in the case of ligand **P2**, the mesityl substituent of the imidazole ring generates a more hindered and rigid metal-ligand scaffold, that changes the preference path of the protonation step.
- Thanks to the combined experimental and computational studies, we understand the factors that govern the selectivity and we can formulate suitable Pd/Ligand/Solvent combinations to obtain selectively three of the four linear isomers of isoprene telomerization. To obtain telomer **1** (**TH**) is needed a sterically hindered ligand, such as **P2**, and moderate acidic solvents, such as MeOH. To synthesized telomer **2** (**HH**), is required non-bulky ligands, such as **P1**, and more important, high acidic solvents. Finally, non-bulky ligands and low acidic solvents, such as *t*BuOH, are good candidates to obtain telomer **3** (**TT**) selectively.

Computational Modelling of Rh Nanoparticles. Phosphine Adsorption, Electronic Structure and Solvent Effects (Chapter 3).

- The Basin Hopping Parallel Excitable Walkers (BH-PEW) optimization algorithm with the Gupta classical potential was used to find the global minimum structure of naked Rh nanoparticle (NP) with different number of atoms. I all cases, the global minimum was highly symmetric structures, being quasi-icosahedral for Rh_{49}, Icosahedron (ICO) for Rh_{55} and Rh_{147} and

Marks-Decahedron for Rh_{75}. Density Functional Theory (DFT) was used to calculate their cohesion energy and the d-band center of the d occupied states. When the size of the NP increases, the cohesion energy also increases, whereas the d-band center became smaller, indicating a general stabilization.

- PPh_3 is adsorbed on a Rh_{55} ICO NP, preferentially, through the lone pair electrons of the P to an edge Rh atom, one phenyl ring interacting with a (111) face in a η^6 mode, and a second phenyl substituent via η^2 coordination of the *ortho* and *ipso* C atoms. The resulted adsorption energy was -2.96 eV, where an adsorption energy decomposition analysis revealed that the main contributions came from the π interaction of the first phenyl ring and the P atom.
- The adsorption energy of PPh_3 decrease as a function of nanoparticle size, going from -3.06 eV for Rh_{49} to -2.45 eV for Rh_{147}, in agreement with the trend of the d-band center of the naked nanoparticles. Moreover, we found that the edges are fundamental to adsorb two phenyl substituents at once, because this adsorption was not found for PPh_3 adsorbed on the Rh(111) surface.
- We successfully built a simple regression model using the generalized coordination number (GCN) as structural descriptor and the d-band center as electronic descriptor, to predict PPh_3 adsorption energies on Rh nanoparticles.
- The adsorption energy of PPh_3 decreases when the coverage increases. Up to 8 PPh_3 molecules, the adsorption is exothermic, but above that number, the adsorption is unfavorable due to the high steric repulsion between ligands. Regarding the electronic effects, the d-band center of the occupied states of the surface Rh atoms decreases continuously up to eight PPh_3, and we think that the optimal PPh_3 coverage for a bare Rh_{55} ICO NP is 6-7 PPh_3 ligands.
- Ab initio molecular dynamic (AIMD) simulations showed that the adsorption of PPh_3 is as stronger as static DFT calculations revealed, because any decoordination is observed. The THF solvent molecules did not affect the adsorption of PPh_3. Moreover, the THF molecules weakly interact with the NP, with a continuous adsorption and desorption, and they do that, preferentially, with the corner Rh atoms rather than the edges.
- P(*o*-tolyl)$_3$ is adsorbed preferentially to a Rh_{55} ICO NP through the lone pair electrons of the P atom to a vertex or edge Rh atom, allowing, in the latter mode, the coordination of one tolyl moiety via η^2 of the *ortho* and *meta* ring positions. In the case of $P(OPh)_3$, the P atom was linked to an edge Rh atom, and two phenyl rings were adsorbed in a η^6 mode to two

different (111) faces, thanks to the flexibility gained by the bridge O atoms, leading to a high adsorption energy of -4.15 eV. The adsorption of $OPPh_3$ is similar to that shown by PPh_3, but the anchoring point was changed to the lone pair electrons of the O atom. Despite the same adsorption mode, the adsorption energy of $OPPh_3$ is lower than PPh_3 (-2.43 vs -2.96 eV, respectively). An adsorption energy decomposition analysis indicated a lower strength of O-Rh than P-Rh interaction.

Origin of Selective Deuteration of Phosphorous Ligands Catalyzed by Rh and Ru Nanoparticles (Chapter 4).

- Taking as reference the strongest adsorption of PPh_3 found in Chapter 3, we determine that the *ortho* C-H activation undergo on the position adsorbed in a η^2 manner on a corner Rh atom, via a dissociative mechanism with a moderate energy barrier of +0.6 eV leading to a five membered dimetallacycle intermediate. The energy barriers for the activation of the *ortho*, *meta* and *para* positions of the phenyl ring adsorbed in η^6 mode onto a 111 face of +1.5, +2.3 and +2.1, respectively, are unaffordable at working conditions.
- The adsorption of P(*o*-tolyl)$_3$ also requires the coordination of the P atom to a Rh edge. However, the activation of the *meta* C-H bond implies a high distortion of the tolyl ring, making the bond breaking unfeasible, unless a P decoordination occurs first. The activation of a methyl C-H bond is easy and fast with an activation barrier of +0.2 eV. We propose a mechanism for the *meta* C-H activation in three steps: 1) P decoordination, 2) methyl C-H bond activation, and 3) meta C-H bond breaking. The 5-*meta* position is activated with a higher energy barrier than the 3-*meta* position (+1.5 vs +1.3 eV), in agreement with the experiments. Despite to be too high to be affordable in working conditions, we think that these barriers decrease when P(*o*-tolyl)$_3$ is adsorbed onto a more realistic NP, covered by hydrides and NHC species.
- The selectivity of the deuteration is closely related with the interaction mode of phosphines and their substituents with the nanoparticle surface. We also found that the defects, such as edges and corner atoms, are crucial to easily activate the C-H bonds.

Development of a ReaxFF Force Field for Propane Dehydrogenation Reaction on Pt Catalysts (Chapter 5).

- A machine learned ReaxFF force field is highly dependent of the application for it was developed, and hence, of the training set used to obtain the parameters. Before using a ReaxFF force field from the literature, its transferability must be assessed and in most cases, re-parameterization is necessary. We took three different force fields from the literature to study the propane dehydrogenation reaction (PDH) catalyzed by Pt surfaces and nanoparticles (**2016-Pt/Ni/C/O/H**, **2016-Pt/H/O** and **2008-Pt/C/H**), and all of them showed discrepancies in terms of geometry, reaction energies or reaction kinetics between them and DFT data. Thus, we decide to re-optimize one of these force fields. We obtained five different set of parameters (**2021(a to d)-Pt/C/H**) before achieve the final force field, able to properly reproduce the features of PDH (**2022-Pt/C/H**). The re-optimization procedure is not straightforward, and we followed a trial and error strategy, identifying the weakest points of each version of the force field, and trying to solve them adding more entries in the training set or changing some force field parameters. The costliest steps of a ReaxFF force field parameterization are the DFT reference data generation and the parameter optimization procedure, the latter depending on several aspects, such as the size of the training set, the job to perform on each structure during the error function evaluation, or the optimization algorithm used.
- We developed a ReaxFF force field to study PDH catalyzed by Pt called **2022-Pt/C/H**. The internal validation shows a good fitting between DFT reference data and ReaxFF results with a mean absolute error (MAE) of 3.4 kcal mol^{-1} on the relative energies of the reaction intermediates, and a maximum MAE on the energy barriers of 5 kcal mol^{-1} and 0.1 Å on the C-H and C-C key transition state distances. The external validation further supports the capability of the force field describing PDH over the Pt(111) surface, and we observed the formation of two propene molecules in a molecular dynamics (MD) simulation of a model system.
- We used the new ReaxFF **2022-Pt/C/H** force field to study PDH catalyzed by Pt(111) and Pt(211) surfaces, and a Pt_{55} NP by means of reactive MD simulations. MD simulation showed that the Pt(211) surface was more reactive than the Pt(111) with a 0.88 % and 0.50 % of propane conversion. Moreover, we observed that all reaction events on Pt(211) surfaces undergo on the steps, and in all cases the preferential pathway to obtain propene was via 1-propyl intermediate. The Pt_{55} NP presented higher activity than the Pt surfaces with a 2.6 % of propane conversion, but also

with a higher probability to undergo deep dehydrogenation side reactions, with a 37% of selectivity towards propene.

- ReaxFF method is a powerful tool to perform long reactive MD simulations on very large systems at low computational cost. To perform 2 ns of simulation on a system with 620 atoms, it took 36 hours, or on even bigger systems, such as the Pt_{55} system, it took 44 days, magnitudes unaffordable to be simulated with AIMD techniques.

Overall, we have taken a step forward in modeling catalysis, combining traditional and novel methodologies to explain experimental observations, and proving the power of computational chemistry to predict and guide researchers in all scientific areas.

UNIVERSITAT ROVIRA I VIRGILI
COMPUTATIONAL MODELING TO EXPLORE SOLVENT AND DYNAMIC EFFECTS IN MOLECULAR, NANO AND SOLID CATALYSIS
Antoni Salom Català

UNIVERSITAT ROVIRA I VIRGILI
COMPUTATIONAL MODELING TO EXPLORE SOLVENT AND DYNAMIC EFFECTS IN MOLECULAR, NANO AND SOLID CATALYSIS
Antoni Salom Català

UNIVERSITAT ROVIRA I VIRGILI
COMPUTATIONAL MODELING TO EXPLORE SOLVENT AND DYNAMIC EFFECTS IN MOLECULAR, NANO AND SOLID CATALYSIS
Antoni Salom Català

Collaborations

The projects of this thesis have been carried out in collaboration with other research groups. Hereunder, they are listed grouped by institutions:

Universitat Rovira I Virgili

- Prof. Cyril Godard
- Prof. Sergio Castillón

King's College London

- Dr. Francesca Baletto

TotalEnergies

- Dr. Daniel Curulla Ferré
- Dr. Kamila Maria Kazmierczak

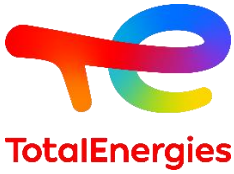

Universidad de Alcalà de Henares

- Dr. Cristina Santamaría

UNIVERSITAT ROVIRA I VIRGILI
COMPUTATIONAL MODELING TO EXPLORE SOLVENT AND DYNAMIC EFFECTS IN MOLECULAR, NANO AND SOLID CATALYSIS
Antoni Salom Català

Acknowledgements/Agraïments

Aquesta tesi, i no tan sols l'escriptura, sinó també els quatre anys passats a Tarragona han representat un llarg camí, no sempre de roses, però que totes i cada una de les vivències, i sobretot les persones que he conegut i m'han ajudat a recórrer-lo ja formen i formaran part del que ja és una de les experiències més importants de la meva vida. Per això, aquestes pàgines van per elles.

Primer de tot, a les dues persones que probablement representin el dos pilars principals de tota aquesta història. Jordi i Josep Manel, m'agradaria agrair-vos de tot cor, la confiança que em vàreu depositar a l'inici i m'heu seguit depositant durant tot aquest temps i que sense a això res hauria estat possible. Moltes gràcies també pels coneixements transmesos, discussions científiques i per fer-me, dia rere dia, un científic un poc més gran. Gràcies a vosaltres he descobert què és realment la recerca, i m'heu infós el vostre interès i la vostra passió per aquesta professió. Però, a part de tot això, i fins i tot més important, moltes gràcies per ser així com sou, per la vostra immensa qualitat humana que ha fet que mai m'hagi sentit a disgust a Tarragona i a la URV. Sincerament, si pogués triar, us tornaria a escollir per que fóssiu els meus directors.

Seguidament, voldria donar les gràcies al meravellós grup de química quàntica, que des del primer moment ja em va donar una càlida benvinguda i sempre m'hi he sentit com un més de la família, com a casa. Coen, Josep Maria, Rosa, Mar, Toni, Maria, Anna i Xavi, moltes gràcies per tota l'ajuda i consells durant aquests anys i per tots els cafès i calçotades tant necessàries per fer l'estada molt més lleugera. Gràcies a tots vosaltres m'he sentit tarragoní durant quatre anys.

Almudena, Roser, Marc, Antonio, Albert i Jianfang vosaltres realment heu estat la meva família tarragonina. Moltes gràcies per tots els moments divertits, birres, festes i demés que ha aportat una mica d'aire a aquest viatge i l'han fet bastant més lleuger del que hauria estat sense vosaltres. Gràcies per acceptar-me des del primer moment i per fer-me sentir que tinc un grup d'amics a terres catalanes. Albert, Yannick, Fei, Ricardo, Jie, Gonzalo i Gerard, a vosaltres us considero la meva segona família, la que m'han ajudat a suportar la segona i possiblement més difícil etapa del doctorat. Moltes gràcies per les nits de jocs, rialles i cubates, però això sí, hauríeu d'entrenar un poc, sobretot amb els futbolins i els bolos...i per molts schytes més!

Yeamin, gràcies per la teva hospitalitat. Evgenii, thanks for your help and advices during this hard period. Jordi, acabes d'arribar, i el consell que et dono és que no desisteixis que ho pots tot i més i et desitjo el millor pel futur. També estic molt agraït a totes les persones del King's College London que em varen acollir, ajudar i fer gaudir de la *amazing* vida que una ciutat com Londres et pot oferir, sobretot

Francesca i Laia, moltíssimes gràcies i grazie mille! Laura, Magda, Irene, Arnau que no es digui tampoc, que per poc que hagi estat també, heu contribuït a millorar aquesta travessia.

Evidentment, unes paraules dirigides a Mallorca són estrictament obligatòries. Moltes gràcies a tots, Costa, Josep, Aina, Cate i pràcticament a tota sa gent que passa pes Casino a fer un cafè. Moltes gràcies per donar-me aquella alenada d'aire que tant necessito, per estimar-me no només durant aquesta etapa sinó durant tota sa meva vida, i per fer de Petra casa meva, encara que estigui llargues temporades sense posar-hi ni un peu. Sense vosaltres no seria res ni el que soc, i encara que diuen que els amics és sa família que un tria, jo us tornaria a triar una i mil vegades. Simplement, vos estim.

Finalment, moltes gràcies monpare, mamare i germà. Vosaltres sí que sou els artífex reals de tot això, de tota la història i de tota la meva vida. Sense vosaltres segur que no seria aquí. Sense la vostra confiança incondicional...i paciència. Gràcies a les vostres ensenyances, valors i sobretot estima, no seria ni d'enfora el que soc avui. No existeixen paraules al diccionari per dir-vos lo molt que us estic agraït ni lo molt que us estimo.

Segur que m'oblido d'algú, però per favor no em jutgeu i perdoneu-me, però unes quantes paraules escrites a un paper que possiblement caiguin a l'oblit no significa l'ajuda real rebuda durant aquest temps, sinó que la vostra ajuda està plasmada en la persona amb la que m'he convertit. Per tot això moltes gràcies i molt més a tothom.

UNIVERSITAT ROVIRA I VIRGILI
COMPUTATIONAL MODELING TO EXPLORE SOLVENT AND DYNAMIC EFFECTS IN MOLECULAR, NANO AND SOLID CATALYSIS
Antoni Salom Català

UNIVERSITAT ROVIRA I VIRGILI
COMPUTATIONAL MODELING TO EXPLORE SOLVENT AND DYNAMIC EFFECTS IN MOLECULAR, NANO AND SOLID CATALYSIS
Antoni Salom Català

UNIVERSITAT ROVIRA I VIRGILI
COMPUTATIONAL MODELING TO EXPLORE SOLVENT AND DYNAMIC EFFECTS IN MOLECULAR, NANO AND SOLID CATALYSIS
Antoni Salom Català

UNIVERSITAT
ROVIRA i VIRGILI